Experimental studies of multifractality and topological phase transitions in microwave resonator lattices

Mattis Reisner

UNIVERSITÉ CÔTE D'AZUR

ÉCOLE DOCTORALE
SCIENCES FONDAMENTALES ET APPLIQUÉES

THÈSE DE DOCTORAT

Études expérimentales de la multifractalité et des transitions de phase topologiques dans des réseaux de résonateurs micro-ondes

Mattis Reisner

Institut de Physique de Nice (INPHYNI)

Présentée en vue de l'obtention du grade de docteur en Physique d'Université Côte d'Azur

Soutenue le : 01 Mars 2023

Devant le jury, composé de :

Jaqueline Bloch, Directrice de recherche CNRS C2N, Université Paris-Saclay	Rapporteure
Anuradha Jagannathan, Professeure LPS, Université Paris-Saclay	Rapporteure
Ulrich Kuhl, Professeur INPHYNI, Université Côte d'Azur	Co-directeur de thèse
Fabrice Lemoult, Maître de conférences Institut Langevin, ESPCI Paris | PSL	Examinateur
Fabrice Mortessagne, Professeur INPHYNI, Université Côte d'Azur	Directeur de thèse
Patrizia Vignolo, Professeure INPHYNI, Université Côte d'Azur	Examinatrice

Études expérimentales de la multifractalité et des transitions de phase topologiques dans des réseaux de résonateurs micro-ondes

Mattis Reisner

Jury :

Rapporteures

Jaqueline Bloch
Directrice de recherche CNRS
C2N, Université Paris-Saclay

Anuradha Jagannathan
Professeure
LPS, Université Paris-Saclay

Examinateurs

Fabrice Lemoult
Maître de conférences
Institut Langevin, ESPCI Pairs | PSL

Patrizia Vignolo
Professeure
INPHYNI, Université Côte d'Azur

Directeur de thèse

Fabrice Mortessagne
Professeur
INPHYNI, Université Côte d'Azur

Co-directeur de thèse

Ulrich Kuhl
Professeur
INPHYNI, Université Côte d'Azur

Études expérimentales de la multifractalité et des transitions de phase topologiques dans des réseaux de résonateurs micro-ondes

Les systèmes micro-ondes jouent un rôle moteur dans l'étude des systèmes uni- ou bidimensionnels relevant du très actif domaine de la photonique topologique. En utilisant des résonateurs diélectriques placés entre deux plaques métalliques, nous étudions des réseau complexes dont on maîtrise la description simplement par la connaissance de la force de couplage entre les résonances propres individuelles. Les couplages peuvent être contrôlés par les distance séparant les résonateurs et leurs orientations relatives. Nous montrons que les structures ainsi construites sont bien décrites par un formalisme de liaison forte, même en présence de modes de résonance d'ordre supérieur, puis nous utilisons cette plate-forme polyvalente pour étudier deux systèmes en détail.

Le premier est constitué de chaînes quasi-périodiques de résonateurs, ordonnés selon des séquences de Fibonacci. Par définition, les structures quasi-périodiques ne présentent ni périodicité ni symétrie globale de translation, mais possèdent un certain ordre et une certaine autosimilarité à différentes échelles. Cela se manifeste par une multifractalité du spectre et des fonctions d'onde. Nous montrons que cette fractalité de la densité d'état locale mesurée est révélée lorsque les sites sont réarrangés en fonction des similitudes de leur environnement local, ce faisant nous introduisons la notion de "conumbers". Cela nous permet de vérifier expérimentalement des schémas de construction récursifs de la densité d'état pour les deux cas de couplages forts dominants et faibles dominants, qui peuvent être formulés en utilisant une méthode de renormalisation. Nous calculons les dimensions fractales des fonctions d'onde mesurées et trouvons un bon accord avec les formulations théoriques de la multifractalité basées sur une description perturbative dans la limite quasi-périodique.

La deuxième structure étudiée est celle formée de réseaux en zigzag, où nous observons une transition de phase topologique en présence d'une symétrie chirale. Par rapport au modèle SSH classique, où la transition topologique est induite par l'alternance des distances (donc des couplages), nous utilisons la même distance entre les résonateurs, mais nous exploitons le couplage anisotrope entre les modes résonants d'ordre supérieur de type "orbitale p" des résonateurs pour induire la dimérisation. En changeant l'angle de liaison de la structure zigzag, déformant ainsi continuellement une chaîne linéaire en une chaîne zigzag à angle droit, une transition de phase topologique se produit à un angle critique, qui dépend du rapport des deux couplages différents entre les modes p polarisés de façon parallèle ou orthogonale. Nous suivons expérimentalement cette transition en mesurant le spectre et en extrayant ses fonctions d'onde. Comme attendu, à la transition, nous observons la nette ouverture d'un bandgap et la formation d'états de bords à énergie nulle aux deux extrémités des chaînes caractérisés par leur extension spatiale.

Mots clés: topologie, multifractalité, micro-ondes, quasi-periodicité

Experimental studies of multifractality and topological phase transitions in microwave resonator lattices

In the vivid domain of topological photonics, microwave setups are a driving force in the experimental study in one or two-dimensional systems. Using small dielectric resonators, sandwiched between two metallic plates, we study complex lattice-like structures, that are essentially described by the coupling strength between the resonances of the resonators. These couplings can be controlled via their distance and orientation. We show that these structures can be well described by a tight-binding formalism, even in the presence of higher order resonance modes and later-on use this versatile platform to study two systems in detail.

The first one are quasiperiodic chains of resonators, that are arranged according to Fibonacci-sequences. Due to fact that quasiperiodic structures lack periodicity and a global translational symmetry, while still showing some order and self-similarity on different scales, we expect multifractality in the spectrum and wavefunctions. We show that the fractality of the measured local density of state (LDoS) is best understood when the sites are rearranged according to the similarities in their local surrounding, i.e., their conumbers. This allows us to experimentally verify recursive construction schemes for the LDoS for the two cases of dominant strong and dominant weak couplings, that can be formulated using a renormalisation group method. We calculate the fractal dimensions of the measured wavefunctions and find good agreement with theoretical formulations for the multifractality based on a perturbative description in the quasiperiodic limit.

The second one are zigzag arrays, where we observe a topological phase transition in the presence of a chiral symmetry. Compared to the classical SSH model, where the topological transition is induced by staggered distances, we use the same distance in between the resonators, but exploit the anisotropic coupling in between the higher order p-orbital-like resonant modes of the resonators to induce the dimerisation. Upon changing the zigzag bond angle in between the resonators, thereby continuously deforming a linear chain into a right angle zigzag chain, a topological phase transition occurs at a critical angle, that depends on the ratios of the two different couplings in between the co- and cross-polarised p-modes of the resonators. We experimentally follow this transition by measuring the systems spectrum and extract its wave functions. As expected, at the transition, we observe the clear opening of a bandgap and the formation of zero-energy edge states on both ends of the chains, that we further characterize by their inverse participation ratio.

Keywords: topology, quasiperiodicity, multifractality, microwaves

Acknowledgments

I would like to express my deep gratitude and appreciation to all the people who have supported me during this research journey.

First and foremost, I would like to thank my two supervisors, Fabrice Mortessagne and Ulrich Kuhl. You have been essential in realizing this work with your guidance and continuous support during my PhD, and I could not have asked for better mentors. You both always had an open door for me and always supported me with your immense expertise and patience, sometimes even discussing questions with me late at night or shortly before submission deadlines. In addition, and this is something I appreciated very much, I have always been able to come to you, even with private problems.

Fabrice, you showed me an impressive amount of trust by letting me work independently while always recognizing at the right moments when help or criticism was needed. You helped me understand the role and importance of our work in the overall field while still encouraging me to form and follow my own ideas. However, you not only supported my actual research with your expertise and guidance but also helped to greatly improve my presentation and communication skills.

Ulle, you reached out to me during my ERASMUS year at the University of Nice, thereby introducing me to this field of research and especially the experimental side of it. You motivated me to continue my studies and research in this direction, and since then, you have always accompanied me with your kind and friendly manner. You always encouraged me to deepen my understanding of the experiment and go further with my research but also guided me to not lose myself within details.

I would also like to thank the other colleagues and fellow researchers in the Waves in Complex Systems group whose discussions and collaborations have contributed significantly to my research experience. I especially thank my fellow PhD students Junjie, Alberto, and Leo, with whom I not only shared office and lab space but also had great discussions during lunchtime. I always enjoyed the rare but stimulating discussions with Olivier Legrand. Finally, the fellow researcher, besides my two supervisors, that I am most grateful for is

Geoffroy Aubry. We became good friends when he joined me on my rusty motorcycle across Corsica on the way home from a scientific conference. If it wasn't for you and your great hospitality in the final week before my defense, which allowed me to fully focus on my presentation, I am confident to say that it may not have lived up to the expectations.

I would like to thank the members of my thesis follow-up committee for their time and their insightful feedback during our annual meetings. I additionally thank you, Laurent Labonté, for introducing me to quantum optics during my master's internship. Although I finally decided to pursue my PhD in another group, you have never stopped mentoring me. I additionally thank you, Patrizia Vignolo, for readily agreeing to be the president of my thesis jury.

I would like to extend my gratitude to the other members of the jury as well, who all agreed to support me in my PhD. I thank Fabrice Lemoult for coming to Nice and asking his intriguing questions. I especially want to thank the two rapporteurs, Jacqueline Bloch and Anuradha Jagannathan, for their detailed reports, in which I could recognize my work, and their constructive criticism, which allowed me to finalize this manuscript with all its essential sections.

Building experimental setups often involves complicated custom-machined parts. Luckily, the Institut de Physique de Nice had an in-house machine shop, and I am grateful for its skilled mechanics Sandra Bosio, Christophe Pitiot, and Florian Zumbo. I was definitely not an easy client with my impossible ideas, but you always managed to come up with clever mechanisms and exceed my expectations.

I would like to extend my heartfelt thanks to my family and friends. With both my parents being enthusiastic physicists, I have the feeling that our conversations during dinnertime, which often turned into some sort of scientific discussions of daily life physical phenomena, had a great influence on my career choice. You always showed me unconditional love and supported me in my private and professional activities. While I was spending my weeks in the lab, the weekends I went camping, climbing, slacklining, and mountain biking in the Mediterranean Alps with this wonderful group of friends. You provided the necessary balance and compensation to have a physically tired but mentally fresh start every Monday. We also managed to build up a successful and lively slackline association that I am particularly proud of.

Last but not least, I want to thank my amazing partner, who stood by me on every single step of this journey and made my life so much more enjoyable. Alina, I thank you immensely for all the effort and sacrifices you had to make to come live with me in Nice, whether it was only for days, weeks, or months at a time.

In conclusion, this thesis would not have been possible without the collective effort and contribution of all those mentioned above and many others.

Your support, guidance, and encouragement have been invaluable in my academic journey, and for that, I am truly grateful.

Contents

Chapter 1

Introduction

The discovery of the integer quantum Hall effect [1, 2] in 1980 has triggered an extensive research in the field of topology in condensed matter physics. Von Klitzing et al. observed for the first time that the transverse Hall resistance of a 2D electron gas at very low temperatures and extremely high magnetic fields showed plateaus that are appearing very accurately at levels that only depend on the fine-structure constant and some integer, associated to topological invariants of the system. The existence of these plateaus was already theoretically predicted [3] and experimentally measured [4] before. But it was only with their improved experimental technique, that Von Klitzing et al. where able to precisely measure the positions of these plateaus, leading to the discovery that these plateaus are indeed quantized with an extraordinary great precision, which was not expected. The plateaus are associated to topologically protected surface modes, that, as such, are immune to backscattering induced by disorder and imperfections, which in turn made the positions of these plateaus independent on impurities or the actual material of the sample. The positions of these plateaus are since then widely used to determine with great precision the fine-structure-constant and to precisely calibrate resistance measuring devices.

Motivated by this new discovery, and especially the robustness provided by topological protection, which also directly found application, topology in condensed matter, and in particular, topological insulators, have gained huge interest [5–7] in the following years. Topological insulators are crystals that are insulating in the bulk, but due to topological protected surface-modes become perfectly conducting at the edges.

Almost 30 years after the discovery of of the integer quantum Hall effect, Haldane and Raghu [8] first noted in 2008 that the concept behind such topological protection is not limited to electron wavefunctions, but can be transferred to the propagation of electromagnetic waves inside photonic crystals as

well [9]. Indeed, topological considerations can be applied to various types of waves propagating in specifically arranged arrays or meta- materials [9–13]. A year later, the scatter-free propagation of edge states in a magneto-optical photonic crystal was experimentally observed in the microwave range [14], hereby marking a starting point for topological photonics. Later, similar behaviors were reported in the IR and visible optical domains [15, 16]. Since then, a wide variety of phenomena directly inspired by topological insulators have been experimentally investigated (see the quasi exhaustive bibliography in the recent review [17]). In addition to the direct analogies of the wave's equations, properties such as loss, gain or nonlinearity, which are intrinsic to photonic systems, can be controlled to create extraordinary systems beyond simple analogies. In this regard, topological lasers [18–20] and topological solitons [21–23], recently reported in the literature, are prominent examples of the remarkable success of various teams around the world.

Typical lattice building blocks in topological photonics can range from the nanometer (visible light) to centimeter scale (RF waves) and can be made out of different material types. The first experiment in the context of topological photonics [14] used small gyromagnetic ferrit cylinders, which allowed to break time-reversal symmetry via a constant, external magnetic field. By now, the most common material used are dielectrics, which allow to generate structures that range from laser written nano-structures, to ceramic microwave resonators of a few mm in size. Intrinsic material properties like the non-linearity of silicon can e.g. readily be exploited to generate higher order harmonics [24] or to generate correlated photon pairs [25] in topological nanostructures. Other structures are e.g. metallic [26] and plasmonic structures [27], and highly engineered systems like polaritons, which were used in the the first demonstration of topological lasing [18]. Note here, that we do not want to be exhaustive with the examples of topological systems that we give. We have chosen to cite a few works of special interest and as mentioned earlier, a quasi exhaustive bibliography can be found in the recent review [17].

To summarize, the field of topological photonics studies wave propagation in complex systems, with the aim of exploiting the robustness provided by topological protection to improve the performances of photonic devices from laser sources to waveguides and sensors.

In this field, microwave setups are a driving force in the experimental studies in one or two-dimensional systems [17]. Microwaves components, such as sources, detectors and high refractive-index ceramic or metallic lattice building blocks are routinely accessible and the typical wavelengths are in the order of cm. This makes implementing systems operating in the microwave range rather easy while providing a high sub-wavelength precision. Additionally, complex fields (amplitude and phase) can be measured with the use of vec-

tor network analyzers. A sketch of a typical experiment setup for microwave photonics can be seen in figure 1.1(a). In order to reduce losses through radiation and effectively reduce the systems dimensions to 2D, most microwave experiments in the framework of topological photonics, make use of a cavity made of two parallel metallic plates. The lattice structure is placed in the cavity and arranged along (x, y), see figure 1.1(a).

For our experimental platform, we use dielectric cylindrical resonators with a high refractive index made of ceramics (from Exxelia Temex manufacturer) as lattice building blocks. Throughout this manuscript we only use resonators from the Exxelia serie E6000 ($\epsilon_r \approx 45$, TiZrNbZnO) with height $h = 5\,\text{mm}$ and two different diameters $D = 6\,\text{mm}$ and $D = 8\,\text{mm}$. In the past, resonator from other Series (e.g. E3000,ZrSnTi, $\epsilon_r \approx 37$) and with different diameters (from 5 mm to 8 mm) were also used with great success. We decided to work with the resonators of the E6000 Series since they have the highest quality factors of $Q \approx 8000$ (given by the manufacture [1]), which lead to sharp resonance peaks and thus a high spectral resolution upon data treatment. To distinguish each resonator (we use between a few tens and up to 500 resonators in our experiments), they are all numerated and individually characterized. A selection of resonators can be seen in Fig. 1.1). The use of dielectric resonators have a lot of advantages in comparison to other photonic structures. With our setup we have total flexibility in the arrangement of the resonator. We position the resonators in the $(x$-$y)$ plane according to specific lattices and geometries with a precision of 0.05 mm using a movable arm that is controlled by an Universal Motion Controller (Newport, Model ESP301, Newport IMS600CC). With our setup it is relative easy to induce additional absorption at specific sites and to change the eigenfrequency of resonators, just by replacing them with other ones. It is also possible to couple the resonators to short-circuited diodes, hereby inducing a non-linearity that acts on both the resonance width and frequency. This is not only useful to create self induced non-hermiticity in topological lattices or sublattices, but already a single resonator coupled to a diode can be used to implement interesting systems. Tuning the non-linearity of such a simple resonant system, one can for example observe the broadband persistence of self-induced coherent perfect absorption [28].

We excite the system of resonators using different antennas. A detailed presentation of the different antennas we use can be found in section 2.2. Depending on which component of the electromagnetic field we want to excite, we use either loop-antennas that excite the z component of the magnetic field B_z, kink-antennas that excite electric field components the (x, y)-plane $E_\perp$ and

1. In experiments with additional ohmic losses in the metallic plates we typically find $Q \approx 3000$

monopole antennas that excite the z component of the electric field E_z. Beside using fixed mounting points in the bottom plate, the different antennas can also be attached to the top-plate and can be moved in the (x-y) plane above the resonators, to scan the system. We can measure either the reflection at one antenna and/or the transmission between two antennas using a Rhode & Schwarz Vector-Network-Analyzer ZVA 24.

The two metallic plates forming the cavity reduce the systems dimension, thereby acting as a wave guide for the electromagnetic fields. This allows us to approximately describe and excite the fields inside in terms of two very distinct types of modes. Transverse magnetic TM modes, where the magnetic field vector $\vec{B}$ is solely in-plane with the cavity and transverse electric TE modes, where the electric field vector $\vec{E}$ has solely in-plane components. We mainly work with the latter type of modes, where the empty cavity has a cut-off frequency $f_c = c_0/(2h)$, where c_0 is the vacuum speed of light, that depends on the height h of the cavity. Below this frequency no propagating TE modes are supported. When resonators are placed inside the cavity, on the other hand, due to their high refractive index, they allow the fields to propagate inside their dielectric medium. This leads to the appearance of sharp Mie resonances, where the fields are essentially confined inside the resonators. For the typically height $h = 8\,\text{mm}$ to $16\,\text{mm}$ between the metallic plates, we work below the cutoff frequency in a frequency range of $6\,\text{GHz}$ to $9\,\text{GHz}$, and hence the fields outside of resonators decay exponentially. This leads to an evanescent coupling in between resonates, then can be controlled by their separation. The system can thus be described with the use of simple tight-binding (TB) Hamiltonians as detailed in Ref. [29] and in chapter 4 of this manuscript. Details on the electromagnetic description of modes can be found in section 2.

Along this manuscript we will work exclusively in this configuration of the experiment, modeled by a TB description, where the setup has already been used with great success to study various systems. Starting with the investigation of graphene-like lattices [30, 31], experimental realization of various systems followed, ranging from Dirac oscillator [32] to transport in molecules [33] and nanoribbons [34] to experimental implementation of quantum search algorithms [35]. It was also used to study quasiperiodic systems [36]. These experiments have been complemented by research on non-Hermitian topological structures in 1D (Su-Schrieffer-Heeger (SSH) chain [37]) and 2D (Lieb lattice [38]). The defect mode of the SSH chain, was also exploited to implement photonic limiters [39, 40]. Further, topological phase transition [41], edge state manipulation [42] and pseudo-magnetic Landau levels [43] have been also reported in strained honeycomb lattices and a relation between phase singularities and topological insulators was experimentally observed [44].

Using the other types of modes, the transverse magnetic TM modes, one can perform a complete set of different interesting experiments. Below the cut-off frequency of the empty cavity, only one type of TM modes is supported, which is the so called TM_0 mode and the vector nature of the electromagnetic waves can be reduced to a scalar description. Compared to the tight-binding modeling, that uses the transverse electric TE modes, the TM_0 modes are always propagating. Thus referring to the dielectric cylinders as scatterers, that interact with the propagating fields becomes more appropriate. They nevertheless still exhibit Mie resonances, leading to a strong frequency dependence of their scattering function. In this regard the experimental platform was used to observe different transport regimes in correlated hyperuniform distributions [45], or to study localization in disorder systems [46].

A huge part of the work during this theses was to further push the limits of the experimental platform in the TB modeling. Moreover, several mechanical improvements in the experimental setup, combined with the development of new sophisticated data-treatment methods, made quantitative interpretations of the systems wavefunctions possible. Analytical calculations and finite-difference time-domain (FDTD) simulations helped us understand, identify and control higher-order resonance-modes of the resonators. With the appropriate adaptions of the experimental setup, we are now able to perform TB experiments with higher order resonance modes, allowing us to exploit their rich anisotropic properties, to study a new family of TB Hamiltonians.

Hence, we start this manuscript by providing the theoretical background, including a detailed electromagnetic description of a single resonator for the experiment in chapter 2. In order to better understand our system, we then continue with a detailed experimental characterization of the single resonator in chapter 3. We then begin building first small test systems using a few resonators, that allow us to investigate in detail the limits of the TB modelling in chapter 4, before we finally tackle more interesting physical systems. As such, in chapter 5 we investigate the multifractal properties of 1D Fibonacci quasiperiodic structures, and in chapter 6 we study a topological phase transition induced by the continuous deformation of linear chains into zigzag arrays employing the higher order p-orbital-like mode of the resonators.

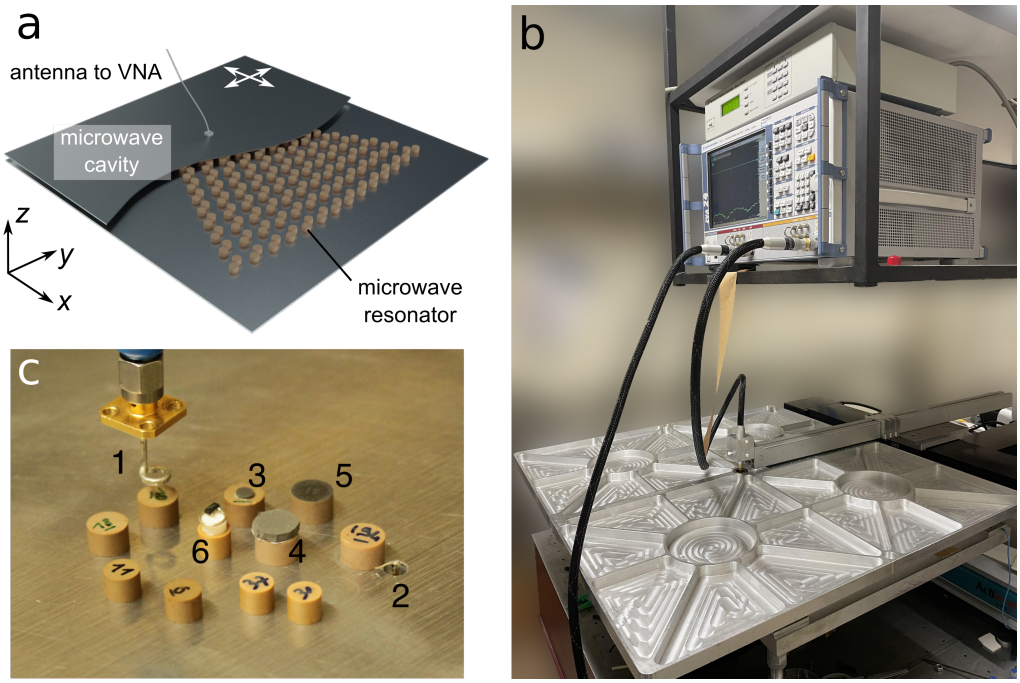

Figure 1.1 – (a) Typical configuration for microwave photonics. A photonic lattice, that in general can be made of dielectric, metallic, ferritic, or gyro-magnetic materials, is inserted in a microwave cavity made of two metallic plates. Antennas can excite and collect the microwave signal via a vector network analyzer (VNA) including phase and amplitude information. They can be mobile to spatially resolve the electromagnetic field in the cavity along the (x, y) plane. (b) Photo of the experimental setup, including the VNA and the microwave cavity (mostly covered by the large top plate). The VNA is connected to one antenna attached to the movable top plate and to another antenna embedded in the bottom plate. The top plate is larger than the bottom plate in order to fully cover the lattice structure in all positions, even when moved to scan the system. (c) Typical microwave components used in the setup. The dielectric cylindrical resonators have the same height (5 mm) but their diameter range from 6 to 8 mm. Different kind of antennas (loop, 1 and dipole, 2) allow to excite the TE polarization. On-site losses can be controlled via absorbing patches (3, 4) or sprayed graphite (5) placed on top of the resonators. Nonlinear losses are added via a Schottky diode short-circuited by a metallic loop and placed on a Teflon spacer (6).

Chapter 2

Theoretical description of the system

In this chapter we provide the theoretical framework of the experiment. We mainly describe the experiment with a tight-binding formalism, but microwaves and dielectric resonators are primarily assigned to electrodynamics and the fields inside/outside the resonators follow Maxwell-equations. Before introducing the tight-binding formalism in chapter 4 we therefore start this chapter by presenting a detailed electromagnetic description of a single resonator using an analytic approach and finite-difference time-domain (FDTD) simulations. We then present how we couple to the system using different antennas and show how the measured scattering matrix is linked to the resonant modes of the system, before we finally discuss different methods of data treatment in order to extract as much information as possible out of the measured spectra.

Contents

2.1 Electromagnetic description of a single resonator

The fields inside and outside of a single resonator with relative permittivity ϵ_r^{reso} and relative permeability $\mu_r^{\text{reso}} = 1$ sandwiched between two metallic plates are described by Maxwell equations

$$\vec{\nabla} \cdot \vec{D} = 0 \tag{2.1}$$

$$\vec{\nabla} \cdot \vec{B} = 0 \tag{2.2}$$

$$\vec{\nabla} \times \vec{E} = -\frac{\partial \vec{B}}{\partial t} \tag{2.3}$$

$$\vec{\nabla} \times \vec{H} = \frac{\partial \vec{D}}{\partial t} \tag{2.4}$$

For linear material laws the displacement $\vec{D}$ and the magnetic induction $\vec{B}$ are related to the fields via

$$\vec{D} = \epsilon \vec{E}$$
$$\vec{B} = \mu \vec{H}\,,$$

where $\epsilon = \epsilon_0 \epsilon_r$ is the dielectric constant and $\mu = \mu_0 \mu_r$ the permeability of the medium. Assuming periodic time dependence $e^{i\omega t}$ we derive the Helmholtz equation for $\vec{E}$ and $\vec{B}$:

$$\left(\Delta + \frac{\omega^2}{c^2}\right)\vec{E} = 0\,, \tag{2.5}$$

$$\left(\Delta + \frac{\omega^2}{c^2}\right)\vec{B} = 0\,, \tag{2.6}$$

where $c = 1/\sqrt{\mu\epsilon} = c_0/n$ is the speed of light in a medium with index of refraction $n = \sqrt{\mu_r \epsilon_r}$ and c_0 the speed of light in vacuum. For the derivation we used the vector identity $\vec{\nabla} \times (\vec{\nabla} \times A) = \vec{\nabla}(\vec{\nabla} \cdot A) - \Delta A$. Although the relative permeability changes at the boundary of the resonator, we can suppose locally linear, homogeneous and isotropic media for both inside and outside of the resonator and therefore $\vec{\nabla} \cdot \vec{E} = 0$ [47]. In general one then can solve the Helmholtz equation individually for the two regions, inside and outside of the resonator, and then combine the found solutions so that they respect the continuity conditions at the interface resonator-air and the boundary conditions at the metallic surfaces.

The boundary conditions at the metallic surfaces (top and bottom plate) with the normal vector $\vec{n}$ are

$$\vec{n} \times \vec{E} = 0\,, \tag{2.7}$$

$$\vec{n} \cdot \vec{B} = 0. \tag{2.8}$$

The magnetic field is tangential while the electric field is perpendicular to the metallic boundary surface. The continuity conditions for field components at the interface of the dielectric resonator and air are given by

$$\vec{n}_{12} \times \left(\vec{E}_2 - \vec{E}_1\right) = 0\,, \tag{2.9}$$

$$\vec{n}_{12} \cdot \left(\vec{D}_2 - \vec{D}_1\right) = 0\,, \tag{2.10}$$

$$\vec{n}_{12} \times \left(\vec{H}_2 - \vec{H}_1\right) = 0\,, \tag{2.11}$$

$$\vec{n}_{12} \cdot \left(\vec{B}_2 - \vec{N}_1\right) = 0\,, \tag{2.12}$$

where $\vec{n}_{12}$ is the normal vector directing from medium 1 to medium 2. For the dielectric material we use, $\mu_r^{\text{reso}} = 1$, which means that all field components of $\vec{E}$ and $\vec{B}$ are continuous, except for the normal component of the electric field at the resonator-air interface, that gets multiplied by ϵ_r^{reso} upon the transition from the inside of the resonator to the air outside.

2.1.1 Analytic approach

We will now solve the the Helmholz equation of $\vec{E}$ and $\vec{B}$ in cylindrical coordinates (r, φ, z) in order to find all resonant modes of the dielectric cylinder (radius r_0, height h_{reso} and relative permittivity ϵ_r^{reso}) with harmonic time dependence $\exp(-\mathrm{i}\omega t)$ [48, 49]. In systems with continuous rotational symmetry, by an analogue of Bloch's theorem, the angular dependence of the fields can always be chosen in the form $\exp(\mathrm{i}n\varphi)$ for some integer $n = 0, 1, 2, 3, \ldots$ [9]. To make the analytic description possible, we suppose that there is no gap underneath or above the resonator and the resonator is in perfect electric contact with the parallel bottom and top plates, in other words the total height of the cavity h_{total} corresponds exactly to the height of the resonator $h_{\text{reso}} = h_{\text{total}}$. This allows us to additionally separate the z-dependency and we will find solution of the form $F(z)G(r)\exp(\mathrm{i}(n\varphi - \omega t)$ for all 6 components of the fields.

Due to the boundary conditions at the metallic surfaces, we have $B_z(z = 0) = B_z(z = h) = 0$ and $E_{x/y}(z = 0) = E_{x/y}(z = h) = 0$. Since the dielectric constant $\epsilon_r(\vec{r}) = 1 + (\epsilon_r^{\text{reso}} - 1)\theta(r_0 - r)$ (where $\theta(r)$ is the Heaviside step function) does not depend on z, the z-component of the fields form a standing

wave in z-direction. We therefore decide to describe the fields using the z-components of $\vec{E}$ and $\vec{B}$ as basis

$$B_z = B_0 \sin\left(\frac{m\pi}{h} \cdot z\right) G(r) \exp\left(\mathrm{i}(n\varphi - \omega t)\right), \quad \text{for } m = 1, 2, 3, \ldots \tag{2.13}$$

$$E_z = E_0 \cos(\frac{m\pi}{h} \cdot z) G(r) \exp(\mathrm{i}(n\varphi - \omega t)), \quad \text{for } m = 0, 1, 2, 3, \ldots \tag{2.14}$$

B_0 and E_0 are constant factors, n the azimuthal mode number and the wavenumber in z-direction $k_z = \frac{m\pi}{h_{\text{total}}}$ is defined by the axial mode number m.

The solution for $G(r)$ are solutions to the Bessel differential equation. Considering that the solutions should neither diverge for $r = 0$ nor for $r \to \infty$ we find

$$G(r) = \begin{cases} J_n(q_{\text{in}} r) & \text{for } r < r_0 \\ J_n(q_{\text{in}} r_0)/H_n^{(1)}(q_{\text{out}} r_0) \cdot H_n^{(1)}(q_{\text{out}} r) & \text{for } r > r_0, \end{cases} \tag{2.15}$$

where J_n and $H_n^{(1)}$ are Bessel- and Hankel-functions of the first kind, respectively. $q_{\text{in}} = \sqrt{k^2 - k_z^2} = \sqrt{k_0^2 \epsilon_r^{\text{reso}} - k_z^2}$ and $q_{\text{out}} = \sqrt{k^2 - k_z^2} = \sqrt{k_0^2 - k_z^2}$ are the wave numbers in the (r, φ)-plane for the regions inside and outside the resonator, respectively. $k_0 = \frac{\omega}{c_0}$ is the vacuum wavenumber, c_0 is the vacuum speed of light, and ϵ_r^{reso} is the permittivity inside the resonator.

From E_z and B_z, all other field components can be derived:

$$(k^2 - k_z^2) E_\varphi = \frac{1}{r} \frac{\partial^2 E_z}{\partial \varphi \partial z} - \mathrm{i}\omega \frac{\partial B_z}{\partial r} \tag{2.16}$$

$$(k^2 - k_z^2) E_r = \frac{\partial^2 E_z}{\partial r \partial z} + \frac{\mathrm{i}\omega}{r} \frac{\partial B_z}{\partial \varphi} \tag{2.17}$$

$$(k^2 - k_z^2) B_\varphi = \mathrm{i}\frac{k^2}{\omega} \frac{\partial E_z}{\partial r} + \frac{1}{r} \frac{\partial^2 B_z}{\partial z \partial \varphi} \tag{2.18}$$

$$(k^2 - k_z^2) B_r = \frac{\partial^2 B_z}{\partial r \partial z} - \mathrm{i}\frac{k^2}{\omega r} \frac{\partial E_z}{\partial \varphi} \tag{2.19}$$

Taking into account the boundary conditions of the different fields components at the interface resonator-air at $r = r_0$ we can derive the characteristic equation

$$(\alpha - \alpha_0)(\epsilon_r^{\text{reso}} \alpha - \alpha_0) = a^2, \tag{2.20}$$

where

$$\alpha = \frac{1}{q_{\text{in}} r_0} \frac{J_n'(q_{\text{in}} r_0)}{J_n(q_{\text{in}} r_0)}, \quad \alpha_0 = \frac{1}{q_{\text{out}} r_0} \frac{H_n^{(1)\prime}(q_{\text{out}} r_0)}{H_n^{(1)}(q_{\text{out}} r_0)}, \quad a = \frac{k_0 k_z n}{q_{\text{in}}^2 q_{\text{out}}^2 r_0^2} (1 - \epsilon_r^{\text{reso}}). \tag{2.21}$$

The complex frequencies $\omega_p = \omega_p' - \mathrm{i}\omega_p''$ ($\omega_p'' \geq 0$) that solve the characteristic equation for a given azimuthal and axial mode number n and m respectively are the resonance frequencies associated with different oscillation modes of the resonator. The subscript p orders the different solution found to the characteristic equation with fixed n and m. p is an integer value, starting at 1 and is ordered according to the real part of the solution ω_p.

The different modes are classed by their subscript npm and further regrouped into different types. TE modes, where $E_z = 0$ and the only non-zero field components are (B_z, B_r, E_φ), TM modes where $B_z = 0$ and the only non-zero field components are (E_z, E_r, B_φ) and hybrid modes, where both B_z and E_z are nonzero and thus all 6 field components are nonzero. TE and TM modes are only appearing for $a = 0$. That is the case for $m = 0$ and $n = 0$. The characteristic equation then simplifies to

$$\epsilon_r \alpha - \alpha_0 = 0 \tag{2.22}$$

for the TM_{0pm} and TM_{np0} modes, and

$$\alpha - \alpha_0 = 0 \tag{2.23}$$

for the TE_{0pm} modes. There is no TE_{np0} mode since for $m = 0$, the z-component of the magnetic field B_z cannot fulfil the boundary conditions at the metallic interface (expect for the trivial solution $B_z = 0$).

If neither $m = 0$ or $n = 0$, there exists only hybrid modes, so no separation in TE and TM modes is possible. By rewriting 2.20 into

$$\frac{a}{\alpha - \alpha_0} = \frac{\epsilon_r^{\mathrm{reso}} \alpha - \alpha_0}{a} = P \tag{2.24}$$

we introduce a new function P, which allows us to further class the hybrid modes into EH and HE modes. For each mode the constants E_0 and B_0 are then related by

$$B_0 = -P E_0 / c_0 \tag{2.25}$$

For HE modes $|P| < k_z/k_0$ and the TM mode is dominant, for EH modes, $|P| > k_z/k_0$ and the TE mode is dominant.

One can further distinguish between trapped and leaky modes. For trapped modes ($\omega_p'' = 0$) q_{in} is real while q_{out} is purely imaginary. That is the case for $\sqrt{\epsilon_r^{\mathrm{reso}}} > (\lambda_0 m/2h) \geq 1$, where λ_0 is the free-space wavelength corresponding to the resonance frequency ω. The other case is $1 > (\lambda_0 m/2h) > 0$, where the resonances are in a leaky state and $\omega_p'' > 0$. $(\lambda_0 m/2h) = 1$ is called the cutoff-condition, $f_c = c_0 m/2h$ is then the cutoff frequency. Below that frequency a mode is trapped, since the fields outside are decaying exponentially, but above

that frequency a mode can radiate energy away, due to the now propagating fields outside of the resonator. Since $m = 0$ for the TM_{np0}-modes, they are always in the leaky state.

The calculated resonance position for the first few modes up to $\nu = 18\,\mathrm{GHz}$ for both type of resonators that we use ($\epsilon_r^{\mathrm{reso}} = 45$, $h = 5\,\mathrm{mm}$, with diameters $D = 6\,\mathrm{mm}$ and $D = 8\,\mathrm{mm}$) can be seen in figure 2.1. We calculate them by numerically finding the zeros of the characteristic equation 2.20. As one would expect the resonance frequencies for the smaller diameter resonator are generally higher. Further one can notice that for increasing frequency ν the density of resonances increases strongly.

For the typical tight-binding experiment one would choose to work with a mode with azimuthal mode number $n = 0$, further referred to as s-modes [1]. Since it does not have an angle dependency the mode is completely rotational symmetric. The coupling between the resonators is then isotropic and depends only on the distance between the resonators and not on the angle between them as well. One further is in search of a mode whose energy is well localized within the resonator and is not leaking away through radiation (which insures a small resonance width). We want the fields outside of the resonator to decay exponentially. This automatically eliminates all the leaky modes of the resonator.

In contrast to the geometry we used to calculate the analytic frequencies and modes, in our experiment we have an additional air gap between the resonator and the top plate. All resonance-frequencies are sensitive to the contact conditions at the resonator-metal interface, but to different extents. A detailed study of the sensitivity of different modes can be found in section 2.1.2 and experimental findings can be found in section 3.3. When the resonators are in contact with the metallic plates, a small air gap remains due to the surface roughness ($\approx 1\,\mu m$) of the two materials. Upon the re-placement of the same resonator at the same position, the air gap is not the same and due to the low refractive index of air, resonance-frequencies will slightly change. There are techniques to avoid this that are used for experiments where the precise determination of the resonance-position is crucial, e.g. experiments that characterize the dielectric properties of a resonator's material via its resonance-positions. They consist, e.g. of using least amounts of water (which has an high refractive index for waves in the RF range) to fill the small air gap [48] or to apply a thin layer of gold directly onto the end faces of the resonator [50].

1. The azimuthal index n can be interpreted in a similar way as the quantum number l, that is used to describe the quantified angular momentum of atomic orbitals. There the use of letters $s, p, d, f, \ldots$ is common to distinguish atomic orbitals with different quantum numbers $l = 0, 1, 2, 3, \ldots$ We adopted this nomenclature, and modes with $n = 0$ will be further referred to as s-modes, modes with $n = 1$ as p-modes, etc.

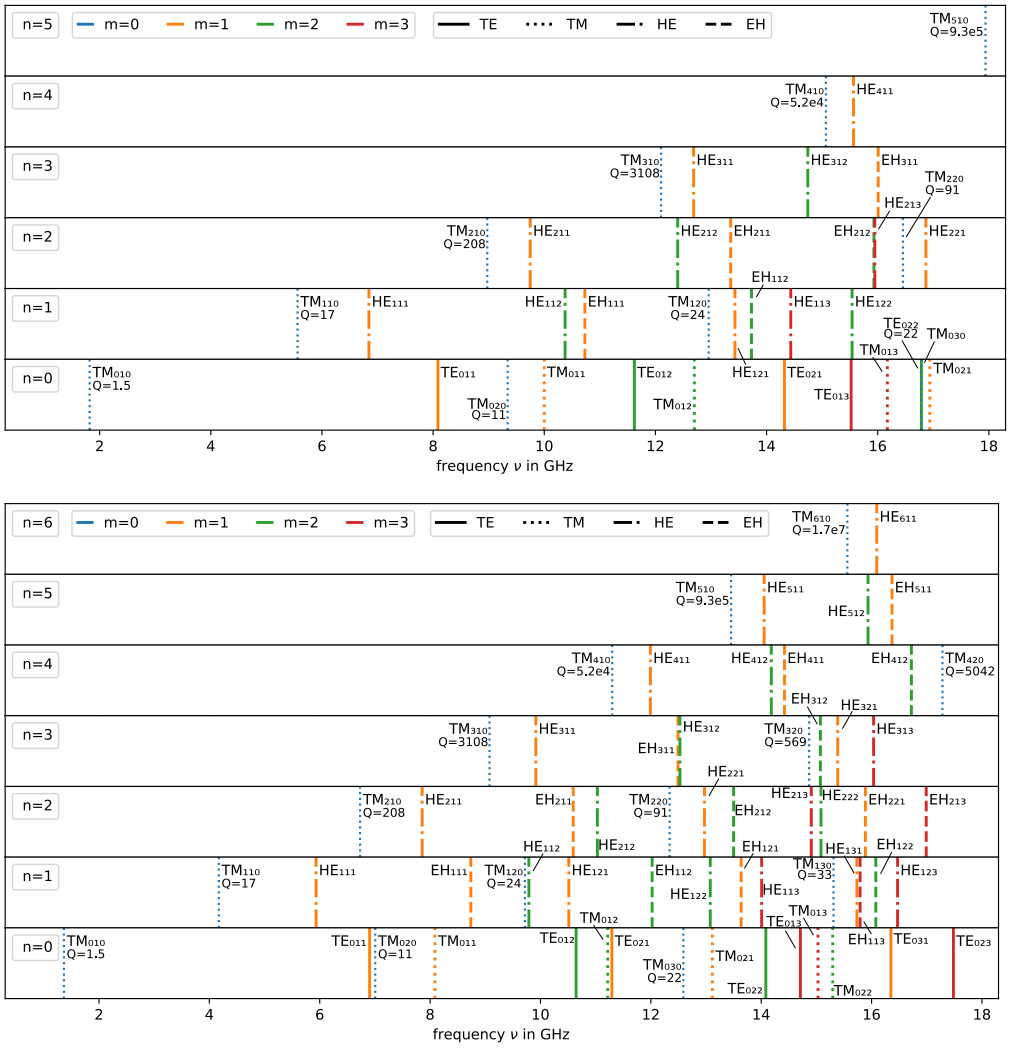

Figure 2.1 – Calculated resonance frequencies of different modes for the resonators with $D = 6\,\text{mm}$ (top) and $D = 8\,\text{mm}$ (bottom). In order to facilitate the identification of different modes, different subplots are used for the azimuthal mode number n, different colors for the axial mode number m and different line styles for the different classes of modes. For the leaky modes we additionally give the quality factor Q.

Unfortunately we cannot make use of this techniques, since we use a large number of resonators. They are arranged on the (x-y) plane and the slightest imperfection in the planarity of the top and bottom plates will result in an uneven distribution of the top plate's weight onto the different resonators, which alters their contact condition and thus their resonance frequency. So in order to avoid the air gap problem in our experiments we leave a big enough air gap above the resonators ($\approx$ 3 mm to 10 mm), so the resonance frequencies are not sensitive to contact condition, at least for the top plate. We further make use of the additional space above the resonators to probe the system with our antennas. We additionally try to reduce the sensitivity of the resonance frequencies to the remaining contact between the bottom plate and the resonators, by applying a small uniform pressure down on to the resonators upon placing. More information on this procedure and the resulting improvements on the variations of the resonance frequencies can be found in section 3.3.

In order to come back to the original problem of choosing the right resonances for our tight biding experiments we have to investigate the effect that an air gap of a couple of mm thickness above the resonators has on the modes. First of all, due to the increased cavity height, the cutoff frequencies become smaller. For a cavity height of $h_{\text{total}} = 16\,\text{mm}$, which is the largest height that we use in experiments, the cutoff frequency for $m = 1$ is at $f_c = 9.4\,\text{GHz}$, we thus want to use a mode with a lower resonance frequency. In order to investigate how the field patterns of the modes are changing upon the introduction of the gap, we first consider that the symmetries of the system are reasonable well maintained so we can still separate the z-dependency. For $r > r_0$ (i.e. outside the resonator) we still have the set of $F(z) = \cos(k_z z)$ or $F(z) = \sin(k_z z)$ with $k_z = \frac{m\pi}{h_{\text{total}}}$. But for $r < r_0$, we would have an altered function $F_{\text{eff}}(z)$. Inside of the resonator, i.e. $z < h_{\text{reso}}$, the z-dependence will be similar to the original z-dependency $F(z) = \cos(k_z^{\text{eff}} z)$ or $F(z) = \sin(k_z^{\text{eff}} z)$ with an $k_z^{\text{eff}} \sim \frac{m\pi}{h_{\text{reso}}}$ but above the resonator the fields will be exponentially decaying. In case of a perfect geometry ($h_{\text{total}} = h_{\text{reso}} = h$), the same orthogonal basis $F(z) = \sin(\frac{m\pi}{h} \cdot z)$ and $F(z) = \cos(\frac{m\pi}{h} z)$ inside ($r < r_0$) and outside ($r > r_0$) the resonator describes the fields. Thus a mode with a certain axial mode number m^* inside the resonator can only couple to a mode outside with the same axial mode number m^*. Once an air gap above the resonator exists, the modes inside the resonator will still be defined by their axial mode number m^*. But since the effective z-dependency $F_{\text{eff}}^{m^*}(z)$ is not orthogonal anymore to the modes outside ($r > 0$), any mode will couple to all modes outside. Considering a mode with axial

mode number m^* inside the resonator, for the magnetic field B_z we get

$$F(z) = \begin{cases} F_{\text{eff}}^{m^*}(z) & \text{for } r < r_0 \\ \sum_{m=1} C_m^{m^*} \cos(\frac{m\pi}{h_{\text{total}}} z) & \text{for } r > r_0\,, \end{cases} \tag{2.26}$$

where the $C_m^{m^*}$ are determined by the mode overlap at $r = r_0$. For the electric field E_z we get

$$F(z) = \begin{cases} F_{\text{eff}}^{m^*}(z) & \text{for } r < r_0 \\ \sum_{m=0} D_m^{m^*} \sin(\frac{m\pi}{h_{\text{total}}} z) & \text{for } r > r_0, \end{cases} \tag{2.27}$$

where the $D_m^{m^*}$ are equally determined by the mode overlap at $r = r_0$, but this time the sum starts at $m = 0$. As for $m = 0$ there is no cutoff frequency outside the resonator, the internal modes that can couple to this mode, i.e. all hybrid (EH and HE) and TM modes, are thus radiating and become leaky modes. Therefore TE modes are preferable for our tight-binding experiment. If the coupling to the $m = 0$ mode outside is sufficiently weak the other modes might still be used as well.

Since we additionally need a well isolated mode, so that we have a clean baseline for our experiments, it limits our choices down to the TE_{011} mode, since for the higher order TE modes the density of resonances becomes to high and we additionally have to stay below the cutoff frequency that itself will depend on the actual height h_{total} of the cavity. It is this mode that was exclusively used in the various different tight-binding experiments performed with the experimental platform (see paragraph in the Introduction for an overview), thus it is worthwhile to at least shortly discuss its spatial profile.

The calculated field pattern of the TE_{011} mode in the case of $h_{\text{total}} = h_{\text{reso}} = h$ can be seen in figure 2.2. One can see that the magnetic field has its maximum at the center of the resonator, whereas the electric field is maximal at the edge of the resonator. The energy is well localized inside the resonator while outside the fields are decreasing fast with increasing distance from the center.

For most tight-binding experiments this *s*-mode is well suited and has already proven itself in multiple experiments. One part of this thesis was to realize an experimental setup for *p*-modes ($n = 1$, term adopted form the nomenclature of atomic orbitals) and perform first experiments. This opens up the path to a whole set of new experiments that use anisotropic coupling between the resonators.

As we just have learned, in the presence of the air gap above the resonators, there are only leaky modes with $n = 1$, making it quite challenging to find suitable modes, that still maintain a high quality factor Q. Possible candidates would be the HE_{111} and EH_{111} modes.

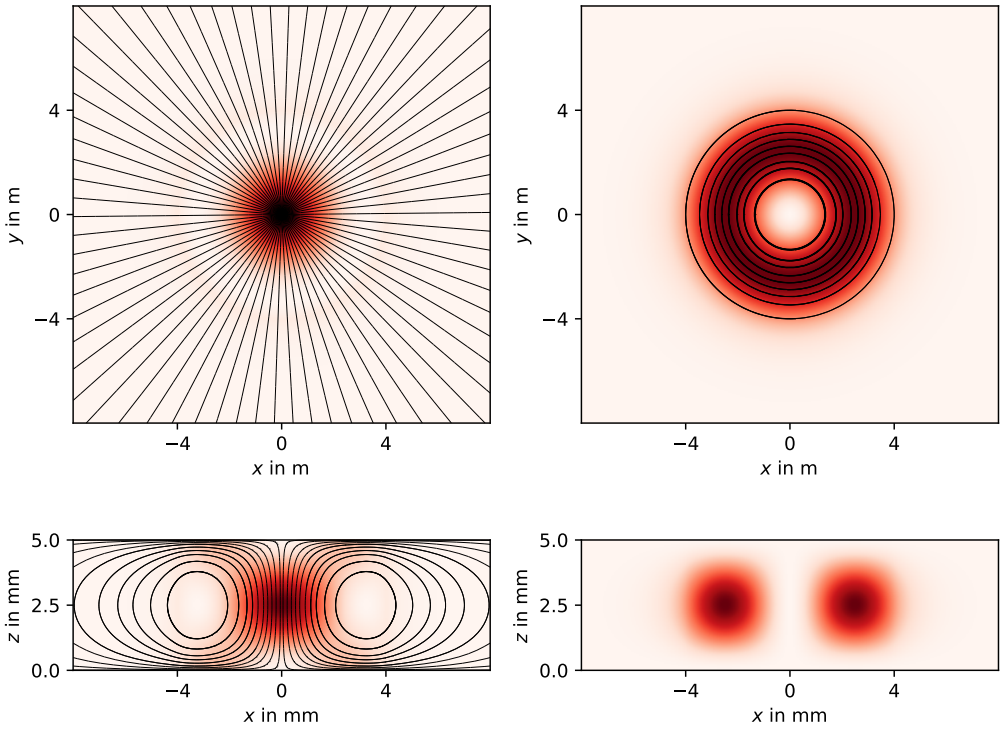

Figure 2.2 – Calculated field pattern of the TE_{011} mode in the case of $h_{\text{total}} = h_{\text{reso}} = h = 5\,\text{mm}$, $\epsilon_r^{\text{reso}} = 45$ and $D = 8\,\text{mm}$. The magnetic field components can be seen on the (left), while the electric field components can be seen on the (right). The (top) figures show the field pattern in the (x, y)-plane, calculated at $z = h/2 = 2.5\,\text{mm}$, while the (bottom) figure show the field pattern in the (x, z)-plane, calculated at $y = 0$. We plot the combined field intensity of the in- and out-of-plane components using a linear color scale from white (corresponding to zero intensity) to a dark red (corresponds to the maximum intensity for each subplot). On top of the color plots we plot the field lines of the in-the-plane components of the fields, to visualize the vectorial character of the electromagnetic fields. For the electric field in the (x, z)-plane (bottom,right) there are no in-the-plane, but only out-of the plane components. For the sake of a better visibility and clarity, we purposely did not add the outline of the resonator into the plots, but using the axis-ticks at $\pm 4\,\text{mm}$ on can easily imagine its contour.

Solving the Helmholtz equation analytically in the presence of an air gap above the resonators is something that to our knowledge has not yet been done [51]. We thus decide to perform Finite-difference time-domain (FDTD) simulations to further inspect how different modes are affected when an air gap above the resonator is introduced. For this particular problem there may be more efficient ways, like mode-matching methods or approaches based an a perturbation theory, but they all need some prior knowledge about modes. We decide to go with the "brute force" method simulating numerically Maxwell's equation.

2.1.2 FDTD simulations using MEEP

In order to perform the FDTD Simulations we use the program package MEEP developed by researchers at the Massachusetts Institute of Technology [52]. MEEP was developed to provide a full-featured open-source software for researchers that needed the flexibility provided by complete access to the source code. For us, the use of MEEP is specially interesting since in experimental physics we only occasionally need FDTD simulation and buying a commercial solution would not be worth it. Additionally it comes with an object-orientated python interface, that made it easier to get started and use simulations results for further calculations/plotting tasks since by far the biggest part of programming within our research group is written in python. Compared to other free software packages MEEP offers a greet amount of features, like built in calls to external libraries such as a Harminv Filter Diagonalization package [53, 54] and supports parallel computation. MEEP additionally supports simulation in cylindrical coordinates which in our case speeds up the simulation by a huge amount.

We want to simulate the single cylindrical resonator sandwiched between two metallic plates with a varying air gap above the resonator. The system is therefore rotational symmetric. Similar to Bloch's theorem for translational symmetries, when a rotational symmetric system is rotated by an angle φ the fields transform as $e^{in\varphi}$ for some integer value n [9]. MEEP thus allows us to simulate Maxwells equations in a reduced (r,z)-plane with cylindrical coordinates, and solve the φ dependency analytically for a given n. Although one needs to perform multiple simulation for different n, each simulation is reduced by one dimension which still results in a much faster simulation time.

A sketch of the used computational cell can be seen in figure 2.3. The resonator is placed at the center of the cell. MEEP supports either periodic or perfectly conducting metallic boundary conditions. Since we are interested in simulating a single resonator we use the metallic boundary conditions. For the z-direction this corresponds well to the metallic bottom and top plates that

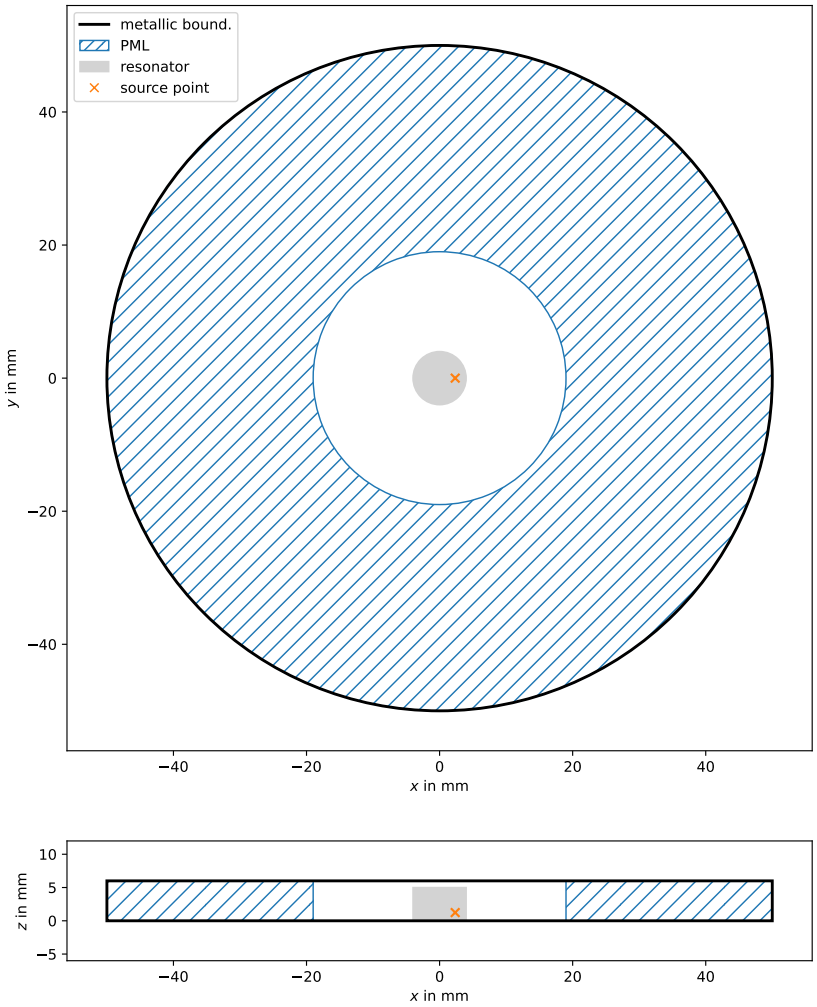

Figure 2.3 – Layout of the computational cell for the FDTD Simulations in the (x, y)-plane (top) and (x, z)-plane (bottom). The resonator (gray shaded) is surrounded by a layer of air (white) and a perfectly matched layer (PML, blue). The cross indicates the position of the source.

we use to form our 2D cavity. Since ideally our cavity is infinitely extended in the (x, y)-plane, we use perfectly matched layers (PML) that are placed in front of the metallic boundaries in the (x, y)-plane to suppress any reflection. PMLs are artificial absorbing layers, often used in FDTD or Finite-Elements methods to simulate problems with open boundary condition. The key property of the PML that distinguishes it from ordinary absorbing materials is that it is designed so that waves incident upon the PML from a non-PML medium do not reflect at the interface, i.e. no impedance mismatch at the interface. This allows the PML to strongly absorb outgoing waves from the interior of the computational region without reflecting them back into the interior. We make sure to have a sufficient layer of air (15 mm) around the resonator before the PML starts, so that we can still characterize the unperturbed decay of modes outside of the resonator. Next we place a broad-band point-source inside of the resonator, making sure that it does not lay on any nodal lines of the modes that are within our frequency-window. We excite both the electric and magnetic field in z-direction and use a Gaussian shaped pulse centered around 8 GHz with a width of 6 GHz. As one can see in figure 2.1, this should cover all modes of interest since lower frequency modes are only of the leaky nature and for higher frequencies the density of modes becomes too high to use them for our type of experiment. The Gaussian pulse is cut off at 5 times its width, both at its start and end.

The documentation of MEEP gives some conservative minimal values for the thickness of the PML, being at least half the maximal wavelength. We chose a PML layer thickness of 31 mm, which should be enough since the analytic calculation in section 2.1.1 predicts the first modes of interest at around 6 GHz.

We chose a resolution of 40 points per mm. For the maximum frequency of $\approx$ 11 GHz, this corresponds to $\approx$ 180 points per wavelength inside of the resonator, which is more than enough. We actually have to use such a high resolution since we are interested in precisely following the resonance-positions upon intruding a small gap above and later also underneath of the resonator. The resolution thus has to match with the smallest gap that we want to introduce. If we would use Cartesian Coordinates, for a total cavity height of $h_{\text{total}} = 8$ mm (which is the smallest height that we use in the experiments) the computational cell consists of (4000 x 4000 x 320) points, which would already need around 500GB of memory to store all 6 field components at only one instance. The use of cylindrical coordinates reduces the computational cell to (2000 x 320) which significantly reduces the amount of memory to store all field components at one instance to around 64MB.

After the source signal has decayed, ($t = 1.43$ ns), we let the fields evolve for additionally $T = 167$ ns (50000 timesteps in MEEP units). The Fourier transformation the time-evolution of the fields, then gives a spectral resolu-

tion of $\Delta\nu = 6\,\mathrm{MHz}$. This value is not so small, especially considering the high quality factors of the resonances that we expect. But it is a good compromise, since upon the variation of parameters like the total height h_{total} of the cavity, the computational time for a single realization becomes an important parameter to optimize. We run our simulation parallel on multiple processors at once, making use of the calculation cluster *Azzurra* of the Université Côte d'Azur. The average runtime for one simulation is thus reduced to approximately 4 hours.

A first important step before varying parameters such as the total height h_{total}, is to verify that with the chosen resolution and PML thickness the simulation has sufficiently converged and the numerical error is within the desired accuracy. We do this by doubling the resolution and PML thickness and checking for eventual discrepancies in the simulated fields. We find that the chosen values are sufficient for our needs, knowing that the numerical error is the highest for the simulation where h_{total} is close to h_{reso} and the air gap measures only a few pixels in thickness.

Another straightforward way to verify the accuracy of the simulations is to compare the found resonance-positions to the analytic predictions. In figure 2.4 one can see the space-averaged Fourier transform of the simulated fields (E_z and B_z) for the case $h_{\mathrm{reso}} = h_{\mathrm{total}} = 5\,\mathrm{mm}$ for both types of resonators $D = 6\,\mathrm{mm}$ (top) and $D = 8\,\mathrm{mm}$ (bottom), together with their analytically calculated resonance-positions (vertical lines). We average only over the space inside the resonator. The agreement is generally very good, although some peak positions, especially of higher order/frequency modes of TE or dominant TE nature (EH modes), correspond only within 2 percent with the analytically calculated resonance frequencies. Upon further investigation it showed that doubling the layer of air or/and PML did not influence the peak-positions at all (considering our spectral resolution of 6 MHz) but doubling the resolution to 80 point per mm reduces the difference within the resonance-positions to about 1 percent, but actually increases the computational time by an factor 8 (2x2=4 times more points and 2 times more timesteps compared to a resolution of 40 points per mm). This is only a small improvement, considering the huge increase in computational time and we stick with the resolution of 40 points per mm for all further simulations.

The main purpose of the FDTD simulation is to bridge the gap between the analytic solution in the case of the perfect geometry ($h_{\mathrm{total}} = h_{\mathrm{reso}}$) and the experimental conditions with an air gap above the resonator in order to fully understand the transition. Therefore, we next vary the total height h_{total} of the cavity while maintaining the resonators height $h_{\mathrm{reso}} = 5\,\mathrm{mm}$ constant and the resonator itself in contact with the bottom plate. Fourier transforming the simulated fields gave us a limited spectral resolution of $\Delta\nu = 6\,\mathrm{MHz}$. Instead us increasing to total runtime T of the simulation in order to increase the spectral

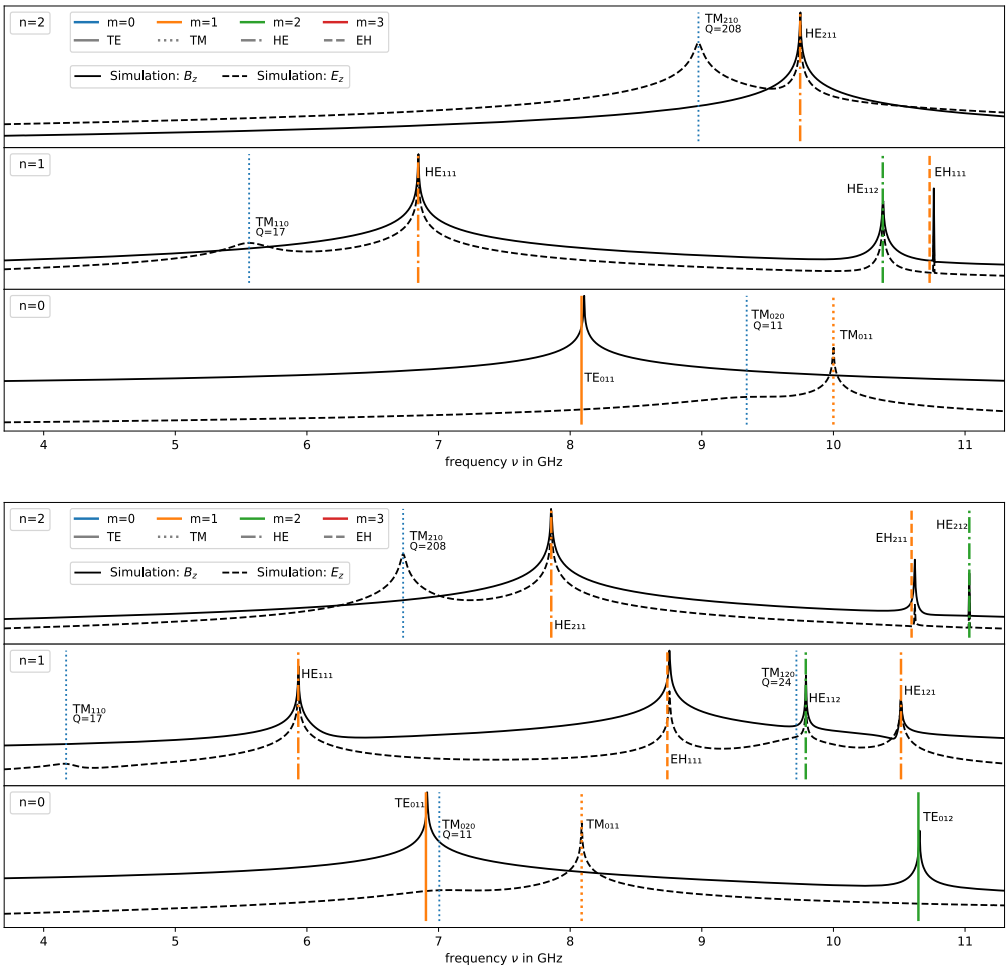

Figure 2.4 – Log-scale plot of the space-averaged Fourier transform $\left\langle |\mathrm{FT}(\nu)|^2 \right\rangle$ inside the resonator of the simulated fields (E_z as dashed black line, B_z as black solid line) for the resonators with $D = 6\,\mathrm{mm}$ (top) and $D = 8\,\mathrm{mm}$ (bottom) and $h_{\mathrm{total}} = h_{\mathrm{reso}}$. For different azimuthal mode numbers n we use different subplots. In order to compare the position of the peaks with the analytically found resonance-positions according to equation (2.20), we plot them as vertical lines with the same colors and styles as in figure 2.1

resolution, we now make use of the built in external package Harminv [54], that uses a harmonic inversion filter diagonalization technique [53], to extract resonance positions and widths. This technique can achieve much greater spectral resolutions and better estimates for the quality factors Q even for very slowly decaying resonances with a high quality factor, since it assumes that the spectrum is only composed of Lorentz-lines, whereas Fourier transformations do not use any prior knowledge of the spectrum's compositions. For more details on this method, also see section 2.2, where we use the same approach in order to extract resonance amplitudes and frequencies form our experimental spectra. A further advantage of this method is that it takes significant less time-steps, even for resonances with a very long lifetime to get precise results.

In figure 2.5 the extracted resonance positions as a function of the air gap height $h_{\text{air}} = h_{\text{total}} - h_{\text{reso}}$ are presented for the two resonator diameters.

One can see that the resonance-positions are strongly shifting for small air gaps, while the variations drastically decrease for $h_{\text{air}} > 3\,\text{mm}$. This corresponds to total cavity height of $h_{\text{cavity}} > 8\,\text{mm}$, which actually is the minimal height that we use in our experiments as the moving antenna needs a few mm space in order to be positioned above the resonators. One may further notice, that the induced frequency-shifts are not monotonic and some modes seem to be more sensitive than others.

On can further notice that for $n > 1$, the TM_{110} and TM_{210} do not have any B_z component for $h_{\text{air}} = 0\,\text{mm}$, but as soon as the smallest air gap is introduced this symmetry is broken and both modes now have a non zero B_z, transforming them into hybrid modes. This is not the case for $n = 0$, where the separation in TE and TM modes is still valid for all $h_{\text{air}} \geq 0$. This further confirms the TM_{011} mode as the perfect candidate for tight-binding experiments, since it does not couple at all to the radiating $\text{TM}(m = 0)$ mode. Additionally for both types of resonators the TM_{011} is well isolated and has a sufficient distance to its neighbouring modes. Generally all TE modes stay lossless until the cutoff-condition for the $m = 1$ mode is reached and they start to couple to the now radiating $TE(m = 1)$ mode outside of the resonator. Since the cutoff frequency for $h_{\text{air}} = 11\,\text{mm}$ is 9.4 GHz, in figure 2.5 one can see that the TE_{012} becomes lossy for $h_{\text{air}} = 11\,\text{mm}$. Modes with $n > 0$ are less affected from this transition since they already couple to the radiating $TM(m = 0)$ mode.

Although not clearly visible (due to the global scale that includes lossless TE modes and leaky TM modes and thus spans 5 orders of magnitude), the resonance-widths of all other resonances is changing as well as a function of the air gap height. This is due to the changing coupling strength between the internal resonator modes and the external radiating $TM(m = 0)$ mode (and for $h_{\text{air}} = 11\,\text{mm}$ and $\nu > 9.4\,\text{GHz}$, the radiating $TM(m = 1)$ and $TE(m = 1)$ modes as well). This is especially important for the selection of the right

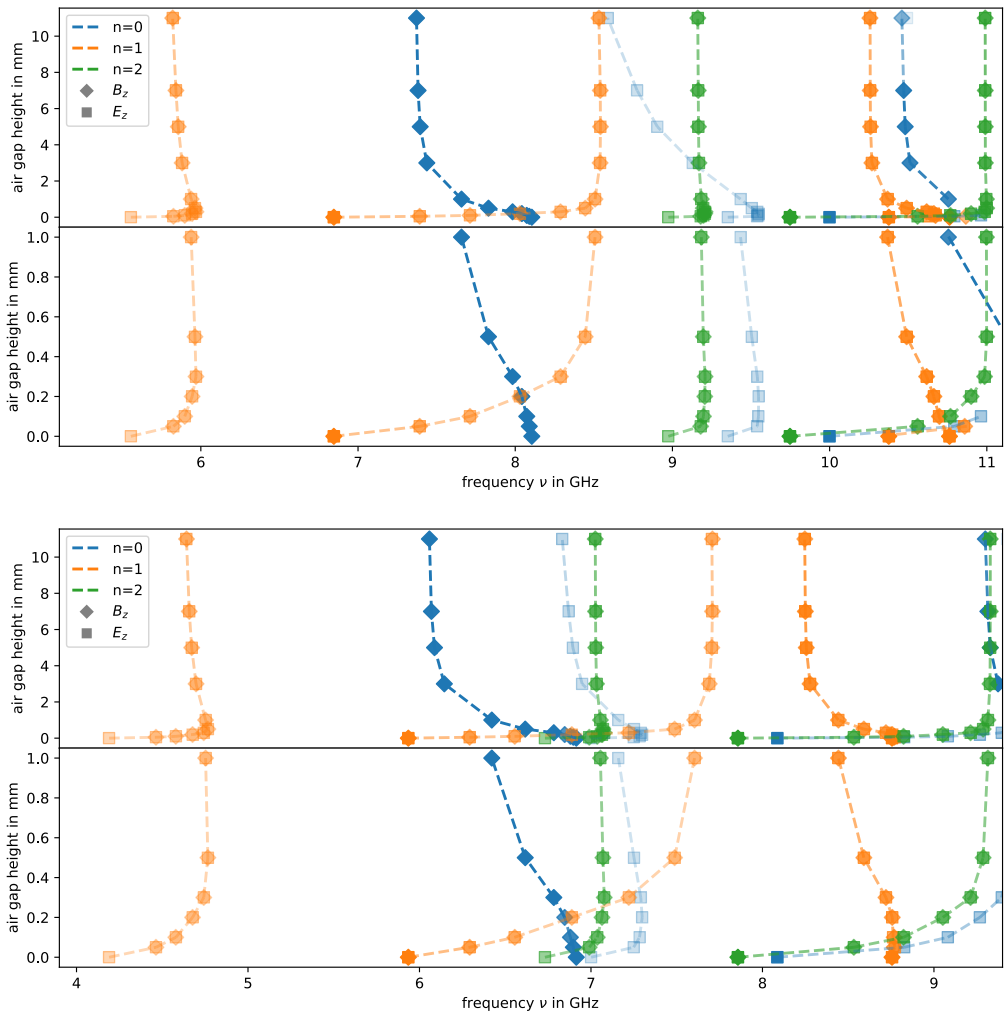

Figure 2.5 – Extracted resonance-positions for different air gap heights h_{air} for the resonators with diameter $D = 6\,\text{mm}$ (top) and diameter $D = 8\,\text{mm}$ (bottom). Resonance frequencies and width were extracted using the Harminv algorithm in MEEP on the E_z (B_z) component and are presented as squares (diamonds). We connect the data points with dashed lines to make it easier to follow a mode's evolution. Compared to the previous figures we now use one color for each different azimuthal mode number n. The transparency of a datapoint corresponds to the quality factor Q of the corresponding resonance. The quality factor Q of a resonance is defined as the ratio between the resonance frequency and its width. In order to map the different quality factors Q to different transparency values we use a log-scale, where the maximal value $Q_{max} \simeq 10^8$ and minimal value $Q_{min} \simeq 2$ correspond to a transparency of 1 and 0.1, correspondingly). The top part shows the full range of h_{air} from 0 mm to 11 mm, which corresponds to a total height h_{total} of 5 mm to 16 mm, while the bottom part shows a zoomed in region of $h_{\text{air}} = 0\,\text{mm}$ to $1\,\text{mm}$.

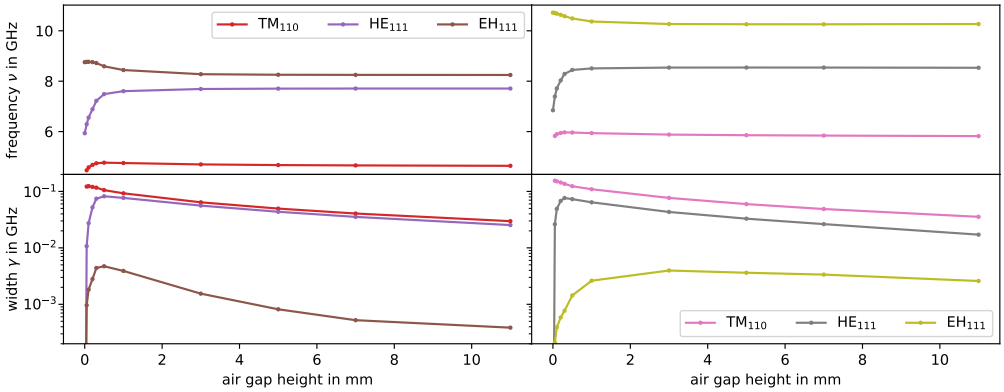

Figure 2.6 – Extracted resonance-positions (top) and width (bottom) as a function of the air gap heights h_{air} for a resonator with diameter $D = 8\,\text{mm}$ (left) and $D = 6\,\text{mm}$ (right) for modes with $n = 1$.

mode for the p-mode tight-binding experiments. To further investigate this, in figure 2.6, one can see the extracted resonance width for the three p-modes with $n = 1$ (orange data points in figure 2.5) for both resonator diameters as a function of the air gap height.

Here it becomes evident, that there is only one suitable p-mode for promising tight-binding experiments. It is the EH_{111} mode of the resonator with a diameter of $D = 8\,\text{mm}$. Compared to the other modes of that resonator it has a resonance width that is smaller by two orders of magnitude. The EH_{111} mode of the resonator with a diameter of $D = 6\,\text{mm}$ has also a significant smaller resonance width than the other p-modes of that resonator, but overall its width is about one order of magnitude greater than for the resonator with $D = 8\,\text{mm}$. Additionally, as one can see in figure 2.5, for the resonator with $D = 6\,\text{mm}$, the EH_{111} is not well isolated, i.e. too close to the TE_{012} mode (not shown, see figure 2.5).

2.2 Mode excitation and S-Matrix

Before presenting the first measurements in chapter 3, we still have to introduce the kind of antennas we will use to couple to the different modes, a theoretical description of the measured quantities and the extraction of the resonance parameters from the measured quantities.

2.2.1 Different antennas

In order to couple to different resonance modes, we need different antennas that will excite different field components. Photos of the different antenna can be seen in figure 2.7.

Although not used for tight-binding experiments, monopole antennas are included. They couple to TM modes since they excite the z-component of the the electrical field E_z. By adjusting the length of the monopole antennas we can vary their coupling strength to modes with different m.

In order to couple mainly to TE modes we use two different kind of antennas: loop antennas and kink antennas. The loop antenna consists of a coaxial cable, where the inner conductor is soldered to the outer one, forming a ring. The loop antenna is placed above the resonators, with the plane of the loop parallel to the (x, y)-plane in order to excite the z-component of the magnetic field B_z. The vertical part of the loop antennas measures typically 11 mm to 14 mm, while the diameter of the loops ranges from 2 mm to 5.5 mm. Since its dimensions are of the same order of magnitude as the wavelengths that we use, the antennas will exhibit resonances due to standing waves inside of the antenna. The position of those unwanted resonances can be tuned by the size of the antenna/loop. We thus use different loop antennas with slightly changed geometries. The loop antenna with the bigger loop has a flat usable frequency window from 5 GHz to 8 GHz, while the loop antenna with the smaller loop size has an usable frequency range of 7 GHz to 10 GHz. While a smaller loop size and the thus reduced area of the loop, results in a overall reduced antenna-coupling, it increases the possible spatial resolution since the fields are integrated within a smaller area. The kink antennas that we use have a short vertical part and horizontal part that is placed tangential to the resonators. The horizontal part thus couples to the angular component of the electric field E_φ. The stronger coupled antennas have a longer horizontal part and might be as well curved around the resonators, so that the current inside the antenna $\vec{j}$ covers a greater arc length in the direction of $\vec{e}_\varphi$. The kink antennas are placed at the side of the resonators, since the electrical field is maximal at the edge of the resonator (see figure 2.2). In order to couple to p-modes, which are hybrid modes, we theoretically could use all of the above mentioned antennas. But since the most promising p-mode for tight-binding measurements is of the EH-type, its TE-components are dominant therefore loop and kink-antennas are better suited.

Typically we scan the system with the loop antenna fixed through a whole to the center of the movable top plate and use the kink antennas as stationary antennas fixed to the bottom plate. Since kink antennas cannot get rid of their vertical part, they are less selective in exciting only TE modes, therefore

Figure 2.7 – Pictures of the different antennas that we use. From left to right: Two different loop antennas with big loops, a loop antenna with a small loop, a strongly coupled curved kink antenna, a weakly coupled straight kink antenna and a short monopole antenna.

sometimes the use of a stationary loop antenna can be useful.

Coupling with two antennas (ports) to the system the transmittance T between the antennas and the reflectance R at each antenna is then measured using a vectorial network analyser (VNA) by means of a 2 x 2 Scattering Matrix (S-Matrix), where the matrix elements will be denoted by S_{ij}.

2.2.2 The scattering matrix

In the following we call $V^1_{\text{in}}, V^2_{\text{in}}$ the input signals at antenna 1 and 2, and $V^1_{\text{out}}, V^2_{\text{out}}$ the received signals at antenna 1 and 2. The relation between them is given by

$$\begin{pmatrix} S_{11} & S_{12} \\ S_{21} & S_{22} \end{pmatrix} \begin{pmatrix} V^1_{\text{in}} \\ V^2_{\text{in}} \end{pmatrix} = \begin{pmatrix} V^1_{\text{out}} \\ V^2_{\text{out}} \end{pmatrix}. \tag{2.28}$$

$|S_{11}|^2$ ($|S_{22}|^2$) is the reflectance R at port 1 (port 2) and $|S_{21}|^2 = |S_{12}|^2$ is the transmittance T between the 2-ports assuming time-reversal symmetry of our system, i.e. $S_{21} = S^*_{12}$.

Considering now a system with a discrete spectra of frequencies ν_n and corresponding eigenfunctions $\Psi_n(\vec{r})$ (of the closed system), that are proportional to the field-components that are excited by the different antennas. $\Psi \propto B_z$ for both loop and kink antennas since for TE modes $E_\varphi \propto B_z$. From now on we will mainly use the notation of using eigenfunctions, often also referred to as wavefunctions $\Psi(\vec{r})$ instead of the individual field components.

Assuming point-like weakly coupled antenna, where we further neglect the influences of the antennas on the spectral positions of the resonances, the Breit-Wigner approximation can be applied once the eigenfrequencies ν_n are sufficiently separated. Thus the S-matrix as a function of the frequency ν can be written as [42, 55–57]

$$S_{ij}(\nu) = \delta_{ij} - \mathrm{i}\sqrt{\sigma_i \sigma_j} \sum_n \frac{\Psi_n(\vec{r}_i)\,\Psi^*_n(\vec{r}_j)}{\nu - \nu_n + \mathrm{i}\Gamma_n/2} \quad \text{for } i,j \in 1,2\,, \tag{2.29}$$

where δ_{ij} is the Kronecker delta, $\vec{r}_1$ is the position of antenna 1, $\vec{r}_2$ the position of antenna 2 and Γ_n the spectral width of n-th resonance, mainly due to ohmic losses. σ_1 (σ_2) is the antenna coupling strength for antenna 1 (2), that is slowly varying with frequency. The choice of the antenna guarantees that in the small frequency range ($\approx 0.4\,\mathrm{GHz}$) of interest for the specifique experiment, σ_1 and σ_2 can be considered constant.

The spectra that we measure are thus superpositions of Lorentzian-shaped resonances with resonance amplitudes $\Psi_n(\vec{r}_i)\Psi_n^*(\vec{r}_j)$. When resonances are strongly overlapping, the interpretation of $\Psi_n(\vec{r})$ as wavefunctions of the closed system is not possible anymore, but the spectrum $S_{ij}(\nu)$ is still a superposition of Lorentzian-shaped resonances as long as parameters like global absorption, and antenna couplings σ_i can be assumes to be constant within the line-width of the individual Lorentz-lines.

By moving one antenna and extracting the resonance amplitudes one can thus directly access the eigen-/wavefunctions $\Psi_n(\vec{r})$ of the (open) system. Of course often this is not an easy task and in the past different methods were found to efficiently extract that information based on different types of measurements (i.e. reflection with the use of only one antenna and transmission measurements using two antennas).

2.3 Extracting wave functions from S-Matrix measurements

In this section we will present the basic ideas and theoretical background for extracting wavefunctions out of the measured spectra. We decide to not provide figures as illustration or explicit examples on how we apply the different methods in this chapter, but rather reference to the different sections throughout this manuscript where the methods are actually applied and one finds a details illustration covering different steps.

First of all one has to distinguish between transmission and reflection measurements. For transmission spectra

$$S_{1,2}(\nu, \vec{r}_1, \vec{r}_2) = -\mathrm{i}\sqrt{\sigma_i \sigma_j} \sum_n \frac{\Psi_n(\vec{r}_1)\Psi_n^*(\vec{r}_2)}{\nu - \nu_n + \mathrm{i}\Gamma_n/2} \tag{2.30}$$

with $\vec{r}_1$ the position of stationary antenna and $\vec{r}_2$ the position of the scanning antenna, one can extract the wavefunctions $\Psi_n(\vec{r})$ by re-scaling the resonance-amplitudes in order to get rid the constant factor $\Psi_n(\vec{r}_1)$ (since antenna 1 is not moving). Since $\Psi_n(\vec{r}_1)$ is not known this is done by enforcing the normalization $\int |\Psi_n(\vec{r})|^2 \mathrm{d}r = 1$ on all wave functions.

For reflection spectra

$$S_{ii}(\nu, \vec{r}) = 1 - i\sigma \sum_n \frac{|\Psi_n(\vec{r})|^2}{\nu - \nu_n + i\Gamma_n/2} \tag{2.31}$$

one can access only the wavefunction intensities $|\Psi_n(\vec{r})|^2$ and the phase/sign-information of wavefunctions is not accessible.

At first it thus seems that transmission experiments are superior to reflection measurements, but this actually depends on the specific measurement, since transmission experiments also have disadvantages. The antennas that we use are non negligible perturbations of the system. Since holes have to be drilled in the metallic bottom and top plate and the antennas themselves are big metallic object that are brought close to the resonators, they affect the resonance-frequencies, -width and coupling strength between the resonators. Under this aspect, reflection measurement using only a single antenna are less invasive and thus often preferred.

The methods that we present in the following are generally applicable on both types of spectra, reflection or transmission, but often work better on one or the other.

2.3.1 Direct curve-fitting

The most straight forward and precise method consist of directly fitting either the reflection or transmission spectrum with a sum of complex Lorentz-lines including a linear frequency dependent complex background. For isolated resonances this is by far the preferred method, since the fit converges well in this case. It still works well for systems that consist of up to $N \approx 10$ resonators, when the resonances are still sufficiently isolated. For overlapping resonances the fit only converges when the initial guess of parameters is very close to the actual values. Additionally, for reflection spectra the theoretical baseline of 1 is often not constant in the experiments and changes with the frequency ν. One often has to use reference measurements, i.e. reflection measurements of the empty cavity without resonators, to adjust the spectra before fitting, which still does not get totally rid of baseline effects [2]. Therefore the performance is slightly better for transmission spectra, where the baseline is zero. During this thesis this method is used for the benchmarking measurements with *s*- and *p*-modes in order to verify how well they can be described by a tight-binding formalism. The test systems are typically small, therefore the few resonance peaks are sufficiently isolated and fits converge reasonably well.

2. See Appendix A for more details on the reference measurements and the corrections that can significantly improve the baseline of reflection measurements

2.3.2 Harmonic inversion

When fitting due to strongly overlapping resonances within the spectrum is not possible anymore, we use another method based on the harmonic inversion of time-signals [53, 58, 59].

The harmonic inversion method is based on the fact that in the time-domain a complex Lorentz-line is given by an exponential function. Supposing that a time-signal of $2N$ datapoints only consists of N exponential functions with different complex amplitudes and exponents. One can then establish a set of non-linear equations in order to determine all the complex parameters of the exponential functions. We thus Fast Fourier Transform the spectrum in a discrete time-signal and further select the first N_{trunc} data-points. N_{trunc} typically ranges from 200 to 650 for a total of 2000-6000 points (we typically measure with a step size of 100 kHz to 300 kHz and the total frequency range is typically 200 MHz to 600 MHz). Due to the typical resonance-widths of a few MHz, that is at least one order of magnitude larger than the step size in the spectral measurements, the time signals decay rapidly and we chose N_{trunc} the smallest possible, while still containing most of the exponential decay.

We then establish the set of non-linear equations and obligatorily find $N_{\text{trunc}}/2$ "resonances". A huge portion of these "resonances" have vanishing amplitudes and/or are "resonances" that form the baseline or mimic the small variations in the spectra induced by noise. We thus have to proceed and filter out resonances according to their width, frequency, phase and intensity to reduce the result to real resonances only. We choose the parameters such that we typically still find more resonances than actually should be present in the spectra. We thus use a clustering algorithms [60] that regroup resonances that are appearing for different antenna positions around one frequency with similar width and assign them to a state.

This method needs a significant amount of time varying parameters like N_{trunc} and parameters of the clustering algorithm, but once optimal parameters found for a certain family of experiments, it is a fast and great performing method to extract both the resonance complex frequencies and amplitudes.

While the effect of the cleaner baseline of transmission spectra compared to reflection spectra was small for the direct curve fitting method, it is unfortunately strongly affecting the results of the harmonic inversion method. The variations in the baseline of reflection spectra have similar depth and width as some of the smaller and wider resonances, we therefore cannot filter them out. We then often use more complicated clustering procedures, coming at the price of a reduced robustness and often have to manually verify that no "false" resonances are assign to the clusters. We apply this method to analyse the reflection spectra in chapter 5 and transmission spectra in chapter 6.

2.3.3 Integrating the density of states

The next method is mainly applicable on reflection spectra, but could probably be adapted for well isolated resonances in transmission spectra as well. It consist of integrating peaks in the local density of states $\rho(\vec{r}, \nu)$, that can be directly derived from reflection spectra. Starting from the reflection spectrum $S_{ii}(\vec{r}, \nu)$, we can derive the local density of states

$$\rho(\vec{r}_i, \nu) = \frac{1}{\pi\sigma}[1 - \Re S_{ii}(\vec{r}_i, \nu)] = \sum_n |\Psi_n(\vec{r}_i)|^2 f_{\nu_n,\Gamma_n}(\nu), \tag{2.32}$$

where $f_{\nu_n,\Gamma_n}(\nu)$ are normalized Cauchy distributions around ν_n with width Γ_n ($\int_{-\infty}^{+\infty} f_{\nu_n,\Gamma_n}(\nu)d\nu = 1$). $\Re S_{ii}(\vec{r}_i, \nu)$ is the real part of the complex reflection spectrum, measured at position $\vec{r}_i$.

In the case of vanishing resonance-widths Γ_n, $\rho(\vec{r}_i, \nu_j) \xrightarrow{\{\Gamma_j\}\to 0} \sum_n |\Psi_n(\vec{r}_i)|^2 \delta(\nu - \nu_n)$, the density of states becomes a sum of delta Dirac function at frequency ν_n, with amplitudes $|\Psi_n(\vec{r})|^2$. Here it is straightforwards that integrating ρ around ν_n one would directly get $|\Psi_n(\vec{r})|^2$. But since our resonances have non vanishing widths Γ_n, the delta Dirac peaks are actual Cauchy distributions. Integrating around a single isolated peak we still get $|\Psi_n(\vec{r})|^2$, since the Cauchy distributions are normalized.

For weakly overlapping resonances one could still chose integration boundaries around each peak and thus extract $|\Psi_n(\vec{r})|^2$ with some error due to the overlapping peaks and finite integration windows. For this case of weakly overlapping resonances, curve fitting or harmonic inversion would be better suited to extract precise wavefunctions, but the direct integration of the density of states remains an important tool. It stands out of the other techniques by its simplicity and robustness and is not prone to numerical problems upon its calculation, like non converging fits or wrong parameters for the harmonic inversion method, where eventually actual resonances of the system could get filtered-out or noise can make clustering problematic. It is therefore the method of choice to quickly check if a measurement behaves as expected before starting tedious data treatment procedures to extract precise wavefunctions.

But actually this method is really useful when resonances are to dense to extract them by direct fitting or harmonic inversion. Directly integrating the density of states stills remains possible and can give at least an estimate of $|\Psi_n(\vec{r})|^2$, although one has to consider that the stronger the resonance are overlapping the higher the error will be.

We make use of an adoption of this technique in chapter 5, where we employ over 100 resonators and the spectrum becomes to dense to extract individual resonances by other means.

Since we typically artificially impose the normalization of the wavefunctions by rescaling them, the prefactor $1/(\pi\sigma)$ is not important and one can directly use $1 - \Re S(\vec{r}, \nu)$. Sometimes it can also be practical to use the approximation $1 - |S(\vec{r}, \nu)|^2$, that neglects term of the order $\mathcal{O}(\sigma^2)$, which is a valid simplification since we often work with weakly coupled antennas. The advantage of using the absolute value instead of the real part is that the raw experimental reflection spectra have a global frequency-dependent phase factor $\approx e^{-i2\pi\nu L/c_0}$. While the phase-factor that arises due to the propagation within the cables from and back to the VNA can get corrected via a calibration, the phase factor that arises due to the propagation within the antennas cannot be corrected via a simple calibration and L is approximately two times the effective antenna length. If one would want to use $1-\Re S(\vec{r}, \nu)$ one first would have to divide the raw measured spectrum by a reference measurement (reflection measurement of the empty cavity without resonators), to get rid of the constant phase factor. In Appendix A more details on the reference measurement can be found.

Chapter 3

Measurements of a single resonator

In this chapter we present the first measurements of single resonators. We compare their spectra with the resonance-frequencies found by the FDTD simulations. We continue by presenting the measured wavefunctions of the *s*- and *p*-mode, which we compare to analytic expressions. We end this chapter by characterizing the most important experimental incertitudes, the variance of the resonance frequencies upon replacing the same resonator and the precision with which we can position the resonators.

Contents

3.1 Spectrum of a single resonator

We measure simultaneously the resonator's reflection spectrum using monopole and kink antennas. We use these two different antennas, since they mainly couple to different families of modes, which then allows use to confidently identify the different modes in the spectrum. As one can see in the insets in figure 3.1, the resonators are positioned in the middle between the two antennas. We then proceed to measure the full 2 x 2 *S*-matrix in order to extract the

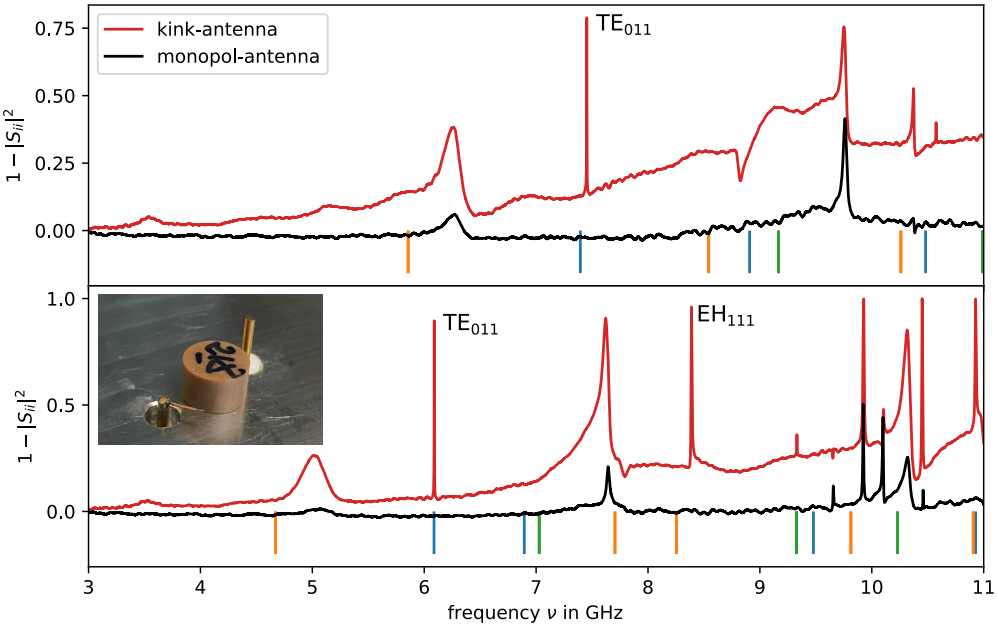

Figure 3.1 – Measured reflection spectrum with different antennas for both types of resonators with $D = 6\,\text{mm}$ (top) and $D = 8\,\text{mm}$ (bottom). The inset in the (bottom) plot shows the experimental configuration, where a single resonator is simultaneously coupled to a kink- and monopole antenna. The legend in the (top) plot also applies for the (bottom) one. The total height of the cavity is fixed at $h_{\text{total}} = 10\,\text{mm}$. The colored vertical bars mark the resonance-positions obtained numerically using MEEP. The colors follow the same scheme as in figure 2.5: s-modes in blue, p-modes in orange and d-modes (with azimuthal mode number $n = 2$) in green.

reflectance $R = |S_{ii}|^2$ at each port. The result can be seen in figure 3.1 for the two diameters.

First of all one can see that the experimentally found peaks do not correspond exactly with their simulated positions. This can have various reasons. First of all the measured dimensions of the resonators corresponds only up to a few hundreds of a mm with the dimensions stated from the manufacturer. This actually is totally acceptable, since the relative dimensional differences within the series of resonators is smaller than 0.01 mm. Additionally the dielectric constant might be slightly different as well and most certainly vary slightly with frequency. While the resonance-frequencies were simulated for the closed system, the antennas actually open the system which also introduces small shifts in the resonance-frequencies. One other reason is that is actually only one experimental realization. Due to the varying contact between the resonator and the bottom plate upon replacing the same resonator at the same position, the resonance frequencies vary slightly. The variation of the resonance frequency depends on the sensitivity of the different modes, but can be as much as a few hundreds of MHz. A brief characterization of these fluctuations can be found in section 3.3.

Considering these factors we nevertheless find a good overall agreement, which allows us to identify the different modes in the experimental spectra. Having a detailed look at the three modes of interest (TE_{011} for both resonator diameters and the EH_{111} for the resonators with $D = 8\,\text{mm}$), we notice that these are some of the sharpest resonances present in the spectra and that we essentially only couple to them with the kink antenna and not with the monopole antenna. This is well expected for the TE_{011} modes, where we already have shown numerically that the separation in TE and TM modes is still valid for $n = 0$ even when the symmetry of the system is broken upon the introduction of an air gap above the resonator. But since we additionally do not couple to the EH_{111} with the monopole antenna, it experimentally confirms the strongly TE-dominant nature of this mode.

With these promising results we then continue to have a detailed look at the wavefunctions of the different modes, before characterizing experimental uncertainties.

3.2 Wavefunctions of a single resonator

3.2.1 The *s*-mode

We start with the TE_{011} mode that we measure and characterize using the resonators with $D = 6\,\text{mm}$. The resonators with $D = 8\,\text{mm}$ give similar results

and will not be presented. During this thesis all s-mode measurement were done with the resonators with $D = 6\,\mathrm{mm}$. Since their diameter is smaller, the overall size of the studied systems is significant smaller. This results in reduced errors that may arise due to eventually not perfectly aligned motion axis and/or bottom and top plates and the not perfect planarity of the metallic plates. Nevertheless many previous experiments have used the resonators with $D = 8\,\mathrm{mm}$ to perform s-mode tight binding experiments with great success and a detailed characterization of these resonators can be found, e.g. in [31].

According to (2.13), for the case where the total height of the cavity corresponds to the height of the resonator $h_{\mathrm{total}} = h_{\mathrm{reso}} = h$, the magnetic field in z-direction for the TE_{011} mode at frequency ν_0 takes the form

$$B_z(r,z) = B_0 \sin\frac{\pi z}{h} \begin{cases} J_0(q_{\mathrm{in}} r) & \text{for } r < r_0 \\ \frac{J_0(q_{\mathrm{in}} r_0)}{K_0(\gamma_{\mathrm{out}} r_0)} K_0(\gamma_{\mathrm{out}} r) & \text{for } r < r_0 \end{cases}, \tag{3.1}$$

where J_0 and K_0 are Bessel functions with the wave numbers $q_{in} = \sqrt{\epsilon_r \left(\frac{2\pi\nu_0}{c_0}\right)^2 - \left(\frac{\pi}{h}\right)^2}$ and $\gamma_{\mathrm{out}} = \sqrt{\left(\frac{\pi}{h}\right)^2 - \left(\frac{2\pi\nu_0}{c_0}\right)^2}$.

In the experiment we actually have an air gap between the resonator and the top plate inducing a change of the fields. As already shortly outlined in section 2.1.1, we assume that the symmetry is still sufficiently maintained, so that we can modify (3.1) by introducing an effective z-dependency $F(z)$ that respects the boundary conditions $F(0) = F(h) = 0$ and an effective q'_{in} that is defined using the function F [31]. Since the z-dependence inside the resonator is not a perfect sinus anymore, we can expect to couple to the first few radially evanescent modes in z-direction outside the resonator. This situation is described by

$$B_z(r,z) \approx B_0 \begin{cases} F(z) J_0(q'_{\mathrm{in}} r) & \text{for } r < r_0 \\ \sum_m a_m \sin\frac{m\pi z}{h} K_0(\gamma_m r) & \text{for } r > r_0 \end{cases}, \tag{3.2}$$

with $\gamma_m = \sqrt{\left(\frac{m\pi}{h}\right)^2 - \left(\frac{2\pi\nu_0}{c}\right)}$ and a_m are constants defined by the continuity equation at the surface of the resonator.

We scan the system by measuring reflection spectra using a loop antenna that is moved above the resonator in the x, y plane at a fixed height z_0. By including the z-dependence in the coefficients $\alpha_m = a_m \sin(\frac{m\pi}{h} z_0)/F(z_0)$, (3.2) can be rewritten as

$$B_z(r,z_0) \approx B'_0 \Psi_0(r) \propto \begin{cases} J_0(q'_{\mathrm{in}} r) & \text{for } r < r_0 \\ \sum_m \alpha_m K_0(\gamma_m r) & \text{for } r > r_0 \end{cases}, \tag{3.3}$$

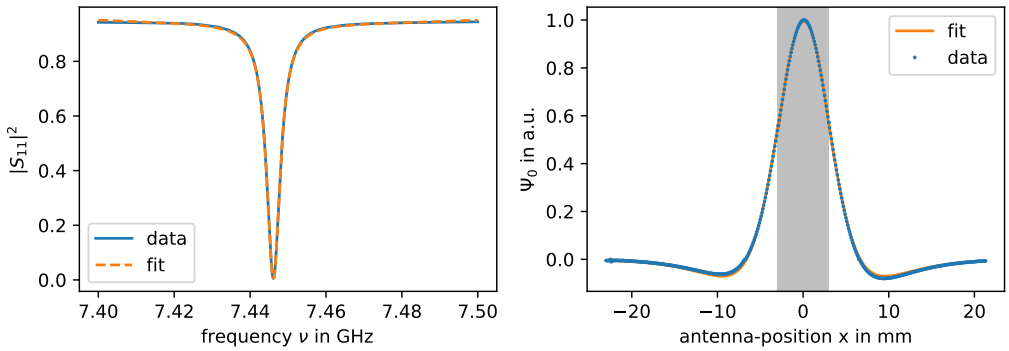

Figure 3.2 – (left) Reflection spectrum of single resonator, measured with the loop antenna over the center of the resonator (blue solid line). We extract the resonance frequency $\nu_0 = 7.446\,\text{GHz}$ and width $\gamma = 2.2\,\text{MHz}$ by fitting a Lorentz-line (dashed line). (right) Extracted single resonator wavefunction Ψ_0 measured on a line passing above the center of the resonator (dots). Inside the resonator, corresponding to the gray zone, we fit it with $f(x) = AJ_0(q'_{\text{in}}x)$ and outside of the resonator with $f(x) = \sum_{i=1}^{4} a_i K_0(\gamma_i x)$, where $\gamma_i = \sqrt{\left(\frac{i\pi}{h}\right)^2 - \left(\frac{2\pi\nu_0}{c}\right)^2}$ is defined using the measured resonance frequency ν_0. The obtained fit parameters are $A = 0.994$, $q'_{\text{in}} = 0.481\,\text{mm}^{-1}$, $a_1 = -1.47$, $a_2 = 22.3$, $a_3 = -58.2$, $a_4 = 46.9$ and $h = 11.6\,\text{mm}$ and the fit is shown as solid line.

where B'_0 is a constant and $\Psi_0(r)$ is the single resonator wavefunction. The constant B'_0 is chosen so that $\Psi_0(0) = 1$.

In order to extract the wavefunction $\Psi_0(r)$ we fit all spectra with a complex Lorentz-line and extract its resonance-amplitudes. Since s-modes should be completely rotational symmetric we limit our scan to a straight line in x direction passing over the center of the resonator with 0.1 mm-steps (a full 2D scan of the resonator wavefunction can be found in [31]).

Figure 3.2 shows the spectrum and wavefunction $\Psi_0(x)$ of the single resonator. One can note that $\Psi_0(x)$ is changing its sign outside of the resonator. Since actually a reflection measurement cannot give us access to the sign of the wavefunction, we compared the wavefunction $|\Psi_0(x)|$ extracted form the reflection experiment with the loop antenna to the wavefunction extracted from a transmission experiment using a second antenna, where we actually can access the phase of the wavefunction and thus directly see the change of sign. Since each antenna is a perturbation to the system, we decide to use $|\Psi_0(x)|$ extracted from the reflection measurement and manually change its sign at exactly the positions where the amplitudes are vanishing. We fit the extracted single disk wavefunction $\Psi_0(x)$ with (3.3) up to the order $m = 4$. Including higher orders does not improve the fit anymore. The fit parameters are

indicated in the figure caption. Since the loop antenna is not point-like, it integrates the magnetic field over a small surface therefore leading to effective parameters.

We find a good agreement between the measured resonance and the Lorentz-line fit, as well as between the fit-function (3.3) and the extracted wavefunction. The resonance is well isolated and has a quality factor $Q = \nu_0/\gamma \approx 3000$, which makes it suitable for tight-binding experiments. The fitted free parameter $h = 11.6\,\text{mm}$ corresponds reasonably well to the directly measured height of $h_{\text{meas}} \approx 12\,\text{mm}$ in between the bottom and top plate. The bottom and top plates are not perfectly parallel, leading to an inaccuracy of a few tenths of a millimeter when measuring directly their distance. One can see that the energy is well localized inside the resonator while outside the fields are decreasing fast with increasing distance from the center. This is an important property in order to be able to describe the system with a tight-binding model.

3.2.2 The p-mode

Next we have a look at the p-mode wavefunction. We start again by deriving the explicit expression of (2.13), for the case where the total height of the cavity corresponds to the height of the resonator $h_{\text{total}} = h_{\text{reso}} = h$. The magnetic field in z-direction for the EH_{111} mode at frequency ν_0 takes the form

$$B_z(r,\varphi,z) = B_0 e^{i\varphi} \sin\frac{\pi z}{h} \begin{cases} J_1(q_{\text{in}} r) & \text{for } r < r_0 \\ \frac{J_1(q_{\text{in}} r_0)}{K_1(\gamma_{\text{out}} r_0)} K_1(\gamma_{\text{out}} r) & \text{for } r < r_0 \end{cases}, \tag{3.4}$$

where J_0 and K_0 are Bessel functions with the wave numbers $q_{in} = \sqrt{\epsilon_r \left(\frac{2\pi\nu_0}{c_0}\right)^2 - \left(\frac{\pi}{h}\right)^2}$ and $\gamma_{\text{out}} = \sqrt{\left(\frac{\pi}{h}\right)^2 - \left(\frac{2\pi\nu_0}{c_0}\right)^2}$.

In a same way how (3.3) was derived for the s-mode, we again assume an effective z-dependency for the case, with an air gap above the resonator. We thus expect to couple again to the first few radially evanescent modes in z-direction outside the resonator and we get

$$B_z(r,\varphi,z) \approx B_0 e^{i\varphi} \begin{cases} f(z) J_1(q'_{\text{in}} r) & \text{for } r < r_0 \\ \sum_m a_m \sin\frac{m\pi z}{h} K_0(\gamma_m r) & \text{for } r > r_0 \end{cases}, \tag{3.5}$$

where $\gamma_m = \sqrt{\left(\frac{m\pi}{h}\right)^2 - \left(\frac{2\pi\nu_0}{c}\right)}$ and the constants a_m are defined by the continuity equation at the surface of the resonator, as for the s-mode.

Since we measure again at a fixed height z_0, we can include the z-dependence in the coefficients $\alpha_m = a_m \sin(\frac{m\pi}{h} z_0)/f(z_0)$ finally arriving at

$$B_z(r,\varphi,z_0) \approx B_0' \Psi_0(r,\varphi) \propto \mathrm{e}^{\mathrm{i}\varphi} \begin{cases} J_1(q_{\mathrm{in}}' r) & \text{for } r < r_0 \\ \sum_m \alpha_m K_1(\gamma_m r) & \text{for } r > r_0 \end{cases}, \tag{3.6}$$

where B_0' is a constant and $\Psi_0(r)$ the complex valued single resonator wavefunction.

It was convenient in section 2.1.1, to only give one solution of the Helmholtz-equation for each mode by implicitly restricting n to be positive. Since there is no physical reason that n should only be positive, modes with $|n| \geq 1$ are actually degenerated, with two linear independent solutions. This comes from the fact that when changing $n \to -n$, the characteristic equation (2.20) stays unchanged, since $J_{-n} = (-1)^n J_n$, $H_{-n}^{(2)} = (-1)^n H_n^{(2)}$ and one obtains a second solution, that differs only in the azimuthal-dependence $\mathrm{e}^{\mathrm{i}n\varphi} \to \mathrm{e}^{-\mathrm{i}n\varphi}$.

Since these are two linear independent solutions, any scalar combination of the two solutions is a solution as well. We thus decide to define the two real valued wave functions

$$\Psi_0^x(r,\varphi) \propto \sin\varphi \begin{cases} J_1(q_{\mathrm{in}}' r) & \text{for } r < r_0 \\ \sum_m \alpha_m K_1(\gamma_m r) & \text{for } r > r_0 \end{cases}, \tag{3.7}$$

$$\Psi_0^y(r,\varphi) \propto \cos\varphi \begin{cases} J_1(q_{\mathrm{in}}' r) & \text{for } r < r_0 \\ \sum_m \alpha_m K_1(\gamma_m r) & \text{for } r > r_0 \end{cases}, \tag{3.8}$$

since $\cos n\varphi = \frac{1}{2}\left(\mathrm{e}^{\mathrm{i}n\varphi} + \mathrm{e}^{-\mathrm{i}n\varphi}\right)$ and $\sin n\varphi = \frac{1}{2\mathrm{i}}\left(\mathrm{e}^{\mathrm{i}n\varphi} - \mathrm{e}^{-\mathrm{i}n\varphi}\right)$. The superscripts x and y are used to distinguish between the two modes that have their nodal line either along the x axis or the y-axis, respectively. Note, that the wavefunction of a mode with its nodal line along an arbitrary direction can be written as a superposition of the two modes $\Psi_0^x(r,\varphi)$ and $\Psi_0^y(r,\varphi)$

Since the system of a single resonator is completely rotational symmetric, there exists no preferred direction or axis and actually the origin of the φ-coordinate is not defined. Any excitation will excite both modes $\Psi_0^x(r,\varphi)$ and $\Psi_0^y(r,\varphi)$ simultaneously. Since ideally these two modes have the same resonance-frequency ν_0 we cannot distinguish between them, the two resonance-peaks share the same position and the same width. If one would then extract resonance-amplitudes from a reflection measurement scan, one could only access to the combined wavefunction intensity of both modes

$$|\Psi_0(r,\varphi)|^2 = \frac{1}{2}\left(|\Psi_0^x(r,\varphi)|^2 + |\Psi_0^y(r,\varphi)|^2\right) \propto \begin{cases} |J_1(q_{\mathrm{in}}' r)|^2 & \text{for } r < r_0 \\ |\sum_m \alpha_m K_1(\gamma_m r)|^2 & \text{for } r > r_0 \end{cases}. \tag{3.9}$$

In the experiments the degeneracy is lifted by imperfections as the resonator is slightly oval or tilted or simply by the presence of the antennas, breaking the rotational symmetry of the system.

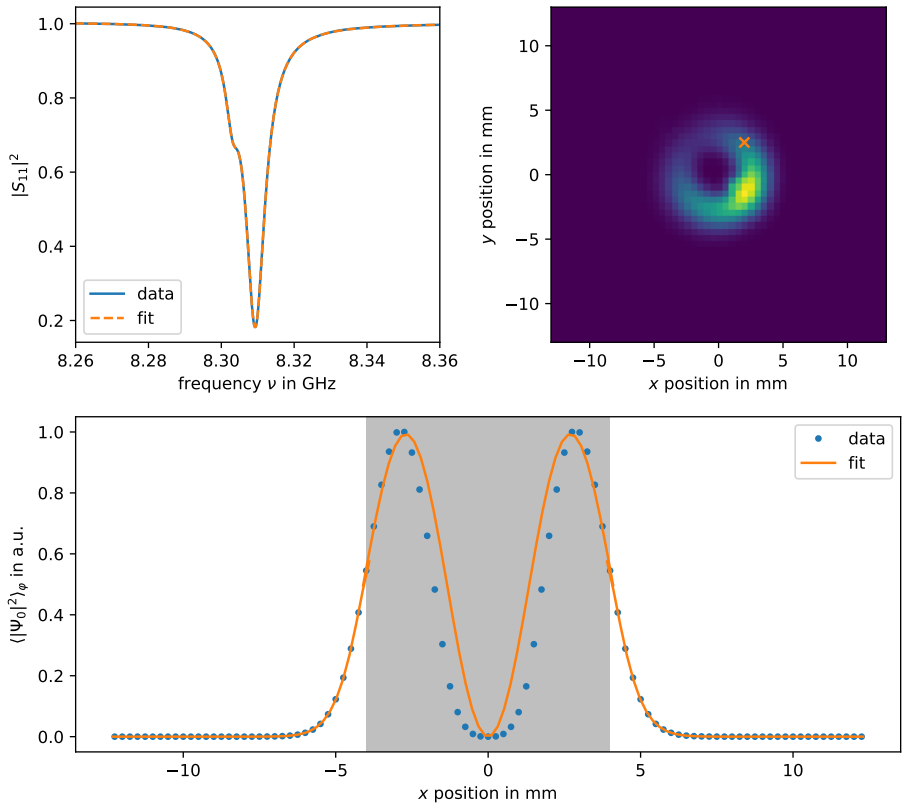

Figure 3.3 – (top,left) Reflection spectrum of a single resonator's p-mode resonance, measured with the loop antenna. The antenna position for this measurement in the x, y plane is marked as orange cross in the central figure. We fit it with a superposition of two Lorentz-lines and find the two resonances frequencies $\nu_1 = 8.303\,\mathrm{GHz}$ and $\nu_2 = 8.309\,\mathrm{GHz}$. (top, right) The extracted combined wavefunction intensity $|\Psi_0|^2$. (bottom) Angle averaged combined wavefunction intensity $\langle|\Psi_0|^2\rangle_\varphi$, calculated on a straight line passing through the center of the resonator. Inside the resonator, corresponding to the gray zone, we fit it with $f(x) = |AJ_1(q'_{\mathrm{in}}x)|^2$ and outside of the resonator with $f(x) = |\sum_{i=1}^{4} a_i K_1(\gamma_i x)|^2$, where $\gamma_i = \sqrt{\left(\frac{i\pi}{h}\right)^2 - \left(\frac{2\pi\nu_0}{c}\right)}$ is defined using the average measured resonance frequency $\nu_0 = (\nu_1 + \nu_2)/2 = 8.306\,\mathrm{GHz}$. The obtained fit parameters are $A = 1.71$, $q'_{\mathrm{in}} = 0.682\,\mathrm{mm}^{-1}$, $a_1 = 0.993$, $a_2 = -38.1$, $a_3 = 350$, $a_4 = -704$ and $h = 10.6\,\mathrm{mm}$.

Figure 3.3 shows the measured reflection spectrum and combined wave-

function intensity $|\Psi_0(r,\varphi)|^2 = |\Psi_1(r,\varphi)|^2 + |\Psi_2(r,\varphi)|^2$ of the single resonator's p-mode. The subscript x and y that were used to distinguish the two degenerated p-modes were replaced by 1 and 2 in the absence of a clear reference direction. Compared to the s-mode measurement we decide this time to measure on a full 2D grid with 0.5 mm step size. To emphasize the fact that there are actually two resonances associated with the p-mode of a single resonator, we present a spectrum for which one can directly observe the presence of two Lorentz-lines. Although we present a spectrum for which the degeneracy lift is the most visible, we do not see two separate peaks, since the two resonance frequencies are to close. We fit the spectrum with the superposition of two Lorentz-lines to extract their resonance-amplitudes and find the two resonances at $\nu_1 = 8.303\,\text{GHz}$, $\nu_2 = 8.309\,\text{GHz}$ with width $\gamma_1 = 2.2\,\text{MHz}$, $\gamma_2 = 3.2\,\text{MHz}$. Depending on the antenna position, the resonance frequencies can vary due to the perturbation induced by the antenna. While it might be possible to directly fit this spectrum with the superposition of two Lorentz-lines, it is not possible for many of the other antenna positions, where the two resonances are to close and appear as a single peak. Where the two-line fit does not converge, we actually fit the spectrum with a single Lorentzian, since $\frac{|\Psi_1|^2}{\nu-\nu_1+i\gamma_1/2} + \frac{|\Psi_2|^2}{\nu-\nu_2+i\gamma_2/2} = \frac{|\Psi_1|^2+|\Psi_2|^2}{\nu-\nu_0+i\gamma_0/2}$, for $\nu_1 = \nu_2 = \nu_0$ and $\gamma_1 = \gamma_2 = \gamma_0$. We suppose that this is still a good approximation, when the two resonance frequencies ν_1, ν_2 and width γ_1,γ_2 are sufficiently close. The extracted wavefunction-intensity $|\Psi_0|^2 = |\Psi_1|^2 + |\Psi_2|^2$ for all positions, whether it was obtained by fitting a single Lorentzian or the superposition of two Lorentzian, is then presented in the central part of figure 3.3.

As expected we find a ring shaped profile, but with varying intensity along the angular direction. Ideally, according to (3.9) it should be uniform in angular direction. We identify the antenna as cause, since upon turning the antenna by 90 degrees (in the x, y plane) within its fixture at the top plate and performing the same experiment, we basically find the same figure, but turned by 90 degrees. We did not investigate in detail how the antenna is causing this, but it is not surprising since the loop antenna itself is not rotational symmetric due to its horizontal part. Depending where this horizontal part is in respect to the center of the resonator and the center of the loop, the antenna's coupling to the mode most probably changes. One could further expect the antenna to sufficiently perturb the system so that the orientations of the two degenerate modes align along some axis. Since the antenna is moved, this axis probably changes for different positions and the antenna couples differently to the two modes.

We nevertheless want to compare the extracted combined wavefunction intensity to (3.5). Since (3.5) does not depend on φ, we angle-average the

extracted combined wavefunction intensity, by averaging over the different images, obtained by rotating the original image around a central point. We use a cubic spline interpolation, to evaluate intermediate points, when the grid points upon rotation do not align exact. We define the central point, by simply choosing the point, where the wavefunction intensity is the smallest. The obtained angle averaged combined wavefunction $\langle|\Psi_0|^2\rangle_\varphi$ can be seen in the right part of figure 3.3, where we fit it with (3.5) up to the order $m = 4$. The fit parameters can be found in the figure caption.

We generally find a good agreement between fit-function (3.5) and the angle averaged combined wavefunction, as well as for the the measured spectrum and the two-line fit. As for the s-mode, the fitted free parameter $h = 10.6\,\text{mm}$ again corresponds well to the measured height of $h_{\text{meas}} \simeq 10.5\,\text{mm}$ in between the bottom and top plate that we use for this experiment. One can see that the energy is again well localized inside the resonator while outside the fields are decreasing fast, making it a suitable mode for TB experiments.

3.3 Experimental incertitudes

In this section we will characterize the experimental incertitudes of the experiment. The metallic bottom and top plates are not perfectly flat and parallel, and the two motion axis might not be perfectly square to each other. But these factors can be easily measured and corrected with a accuracy of 0.1 mm and have not shown itself to be problematic in previous experiments. Resonators from the same series are not perfectly identical so they have slightly different resonance frequencies. This can be easily accounted for by characterizing each of the individual resonators and only choosing those whose frequencies are sufficiently close. The main source of experimental fluctuations is therefore the placing itself of the resonators onto the metallic plate.

3.3.1 Fluctuations of the resonance frequencies

As already outlined in section 2.1.1 and further confirmed with the FDTD simulations in section 2.1.2, the resonance-frequencies are very sensitive to the contact conditions at the resonator-metal interface. When the resonators are in contact with the metallic plates, a small air gap remains due to the surface roughness ($\approx 1\,\mu m$) of the two materials. Upon the re-placement of the same resonator at the same position, the air gap is not exactly the same and due to the low refractive index of air, resonance-frequencies will slightly change. We effectively get rid of the sensitive resonator-metal interface on top of the resonator by separating the two metallic plates by more than 8 mm. This

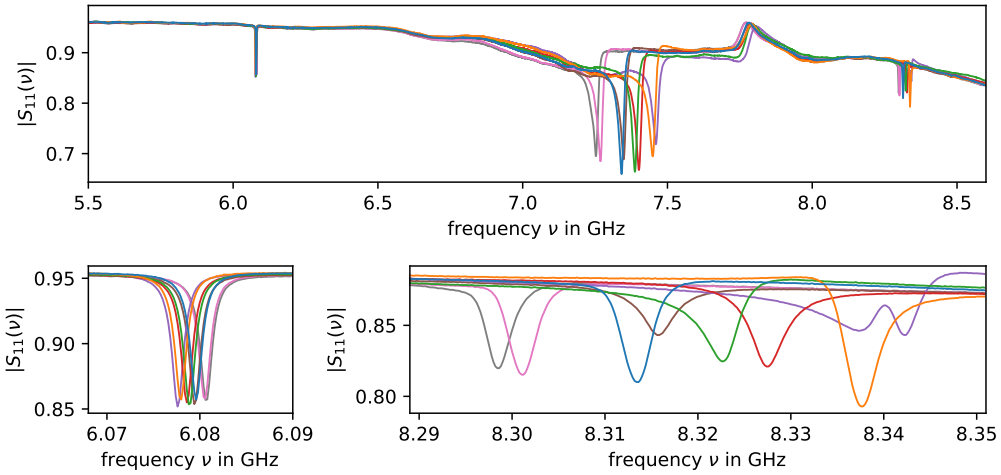

Figure 3.4 – (top) Measured reflection spectra of the same resonator ($D = 8\,\mathrm{mm}$) replaced several times at the same position. Each plot in a different color corresponds to a new placement. (bottom, left) Zoomed region for the s-mode and (bottom, right) zoomed region for the p-mode. The two figures at the bottom share the same scale, so that the figures can be directly compared to each other to reveal the difference in sensitivity between the s- and p-mode.

introduces a big enough air gap and relative changes become negligibly small. Nevertheless the sensitive resonator-metal interface underneath the resonator remains, where it is in contact with the bottom plate.

In figure 3.4 one can see the full reflection spectrum of the same resonator that was replaced several times at the same position. For this characterization, the resonators were placed by simply dropping them through a precision machined hole without any additionally step to estimate the worst case scenario. As one can see later on, it can be useful to apply a slight pressure down on to the resonators after placing them to ensure a better contact and therefore reduce the fluctuations in the resonance frequencies by almost one order of magnitude.

One can see that the resonance positions of different modes fluctuate to different extends. Different modes have a different sensitivity to the resonator-metal interface condition. The greatest fluctuations can be observed for the mode around 7.4 GHz, which is the order of $\approx 100\,\mathrm{MHz}$. Luckily we do not use this mode for our tight-binding experiments and it is sufficiently far away from the s- and p-modes to not affect their baselines. The fluctuations of the s-mode are reasonable small and of the same order as the resonance-width, which is acceptable. The fluctuations of the p-mode are of the order of a few $\approx$ 10 MHz, which is significantly more than their resonance width as one can see

in figure 3.4 (bottom, right). Upon later characterizing the coupling between two resonators in section 4.2.1 and 4.3.3 we find maximum coupling strengths of $\approx 100\,\mathrm{MHz}$. We can thus conclude that when the resonators are placed without any additionally steps, at least for the p-mode, the variance of the resonance frequencies are too important compared to the coupling strength and to its width. Consequently, running tight-binding experiments that do not explicitly expect disorder on the resonance-frequencies is not possible.

Fortunately, we have been able to improve the placing procedure. It still consists of dropping the resonator through a precision machined whole in the placement contrivance, but the latter was further improved so that the resonators fall from a smaller height and have less lateral play. Then we apply a light pressure with a slightly flexible plastic rod down on to the resonators before moving the contrivance away to ensure a better contact. As one can see in figure 3.5 the variance in the resonance frequencies have been significantly reduced. While in figure 3.4 (bottom) the s- and p-mode spectrum of the same resonator were presented, in figure 3.5 we measure and present the variations for the s-mode with a resonator with $D = 6\,\mathrm{mm}$, and the variations for the p-mode with a resonator with $D = 8\,\mathrm{mm}$, to be consistent with the latter tight-binding measurements, where all s-mode measurement were performed with the resonators with $D = 6\,\mathrm{mm}$ and all p-mode measurement with the resonators with $D = 8\,\mathrm{mm}$.

By fitting each spectrum with a Lorentz-line to extract the resonance-positions, we find a standard variation of $\sigma_s = 0.5\,\mathrm{MHz}$ for the s-mode and a standard variation of $\sigma_p = 3.5\,\mathrm{MHz}$ for the p-mode. For the p-mode the standard deviation is now similar to its resonance-width, while even smaller for the s-mode.

3.3.2 Fluctuations of the resonator positions

We place the resonator by letting them drop through a precision machined cylindrical hole. Since the diameter of the hole has to be slightly larger than the diameter of the resonator, in order for the resonators to fall down without getting stuck, we expect small variations for the position of the resonators. In order to characterize these variations we place a resonator with $D = 6\,\mathrm{mm}$, then scan its s-mode wavefunction on a fine 2D regular grid (with 0.1 mm stepsize) over the resonators center. We fit its wavefunction with $f(x,y) = J_0\left(\gamma\sqrt{(x-\Delta x)^2 + y - \Delta y)^2}\right)$ to extract the actual position $(\Delta x, \Delta y)$ of the resonator's center and then place it again and repeat the procedure. We repeat this 20 times and the results can be seen in figure 3.6, where we additionally perform a principal component analysis (PCA) to characterize the variations along the different directions. The variation along the x and y axis are differ-

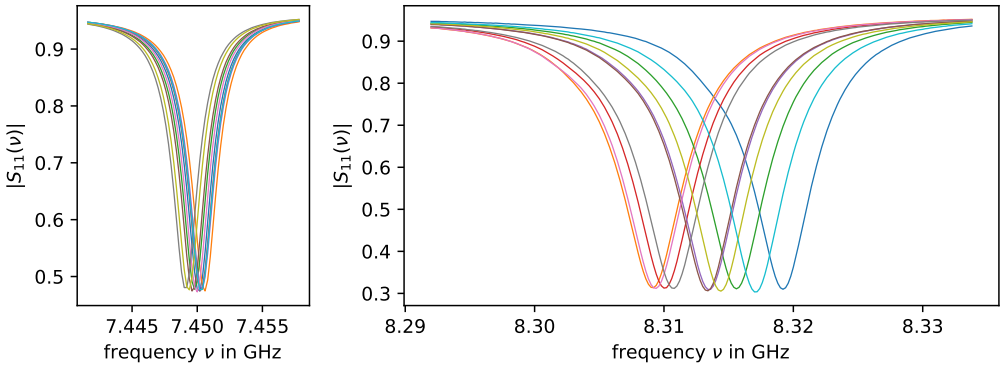

Figure 3.5 – Measured reflection spectra of the same resonator replaced several times at the same position. (left) A resonator with $D = 6\,\text{mm}$ was used to measure the s-mode, while (right) a resonator with $D = 8\,\text{mm}$ was used to measure the p-mode. This time a slight pressure was applied down onto the resonators after placing them, to ensure a better contact with the bottom plate. Both figures use the same scale on their frequency axis, so that the figures can be directly compared to each other.

ent. While we trust the roundness of the machined hole, through which we let the resonator drop, this difference is probably caused by other geometric features of our placing device, leading to more play between the different parts of the contrivance along the y-direction. Overall, the positional variations are smaller than expected and we can place the resonators very precisely, which is important for a consistent coupling strength between the different resonators.

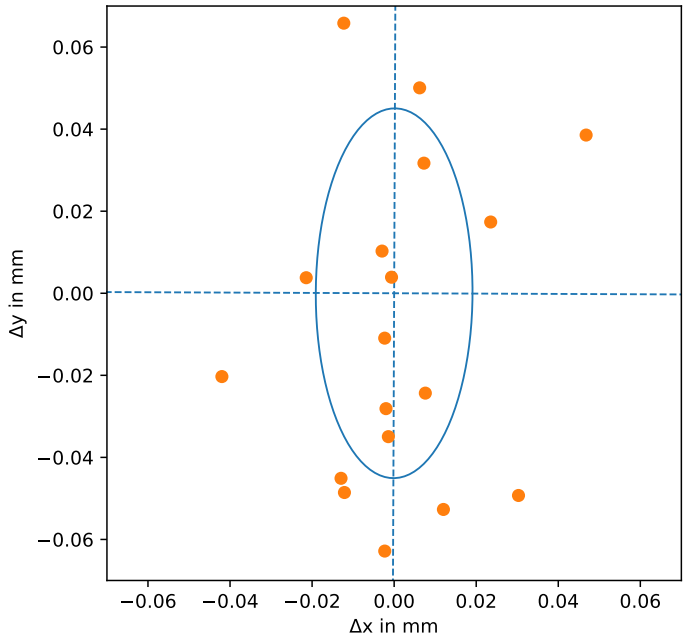

Figure 3.6 – Actual positions $(\Delta x, \Delta y)$ extracted by fitting the s-mode wavefunction for the same resonator placed several times (orange points). The average value was subtracted. We perform a PCA to find principal axis (dashed blue lines) that are so close to the actual x and y axis, that we will simply call them x and y as well. The standard-variation in x-direction is $\sigma_x = 0.019\,\text{mm}$ and in y-direction $\sigma_y = 0.045\,\text{mm}$. If we suppose a 2D normal distribution for the variations, the ellipse (solid blue line) is then indicating the standard deviation along other directions.

Chapter 4

Multiple resonators – a tight-binding system

The tight-binding formalism that we are going to use to describe systems of multiple resonators has its origin in the description of electrons in crystal lattices. Before we show how the model was adapted to fit photonic (dielectric) structures, we give a brief introduction to the original model [61].

We then proceed for both s- and p-mode to experimentally extract the coupling between two resonators as a function of their separation (and orientation), and then construct small test systems to verify the accuracy of our TB model.

Contents

4.1 The tight-binding formalism

The wavefunction Ψ of an electron with energy E in an atomic lattice is described by the stationary Schrödinger equation

$$\left(-\frac{\hbar^2}{2m}\Delta + U(\vec{r})\right)\Psi = E\Psi, \tag{4.1}$$

where $\left(-\frac{\hbar^2}{2m}\Delta + U(\vec{r})\right)$ is the systems Hamiltonian H. The potential $U(\vec{r}) = \sum_j V\left(\vec{r} - \vec{r}_j\right)$ is the superposition of the single atoms potential $V(\vec{r})$, where the $\{\vec{r}_j\}$ are the positions of the different atoms in the lattice.

With the use of the $H^j_{\text{at}} = \left(-\frac{\hbar^2}{2m}\Delta + V\left(\vec{r} - \vec{r}_j\right)\right)$, the Hamiltonian of a single atom at position $\vec{r}_j$, the systems Hamiltonian H can then be rewritten into

$$H = H^j_{\text{at}} + \sum_{k\neq j} V(\vec{r} - \vec{r}_k) = H^j_{\text{at}} + \Delta U^j(\vec{r}), \tag{4.2}$$

where $\Delta U^j(\vec{r})$ describes the differences between the single atom's potential and the true potential in the atomic lattice. We suppose that for all j, $\Delta U^j(0) \to 0$, so near the center of the atoms, the single atom potential is a good approximation of the true potential of the lattice.

Let $\psi(\vec{r})$ be the wavefunction of an electron bound to a single atom at position $\vec{r} = 0$, then

$$H^j_{\text{at}}\psi(\vec{r} - \vec{r}_j) = E_0\psi(\vec{r} - \vec{r}_j). \tag{4.3}$$

For simplicity we here consider only one solution, e.g. the ground state with energy E_0. Generally it is not difficult to expand the model to include all higher order atomic orbitals ψ_n, but the notations just become lengthier, while the essential idea stays the same.

One then supposes that the full systems wavefunctions Ψ can be written as linear superposition of the single atom wavefunctions $\{\psi(\vec{r} - \vec{r}_j)\}$

$$\Psi = \sum_j c_j\psi(\vec{r} - \vec{r}_j) \tag{4.4}$$

We assume that this basis of wavefunctions is orthogonal so that

$$\int \psi^*(\vec{r} - \vec{r}_i)\psi(\vec{r} - \vec{r}_j)\mathrm{d}r = \begin{cases} 1 & \text{if } i = j \\ 0 & \text{otherwise.} \end{cases} \tag{4.5}$$

We next proceed to calculate the matrix elements $\{H_{ij}\}$ of H in this new defined basis. We will make use of the simpler Dirac notation $\psi(\vec{r}-\vec{r}_j) \rightarrow |j\rangle$, $\Psi(\vec{r}) \rightarrow |\Psi\rangle = \sum_j c_j |j\rangle$.

$$H|\Psi\rangle = \sum_{i,j} |i\rangle\langle i|H|j\rangle\langle j|\Psi\rangle = \sum_i |i\rangle \sum_j H_{ij} c_j \tag{4.6}$$

With this notation (4.1) can be rewritten in matrix form:

$$\begin{bmatrix} H_{11} & H_{12} & \cdots & H_{1n} \\ H_{21} & H_{22} & \cdots & H_{2n} \\ \vdots & \vdots & \ddots & \vdots \\ H_{n1} & H_{n2} & \cdots & H_{nn} \end{bmatrix} \cdot \begin{bmatrix} c_1 \\ c_2 \\ \vdots \\ c_n \end{bmatrix} = E \begin{bmatrix} c_1 \\ c_2 \\ \vdots \\ c_n \end{bmatrix} . \tag{4.7}$$

The different matrix elements $\{H_{ij}\}$ are then defined as

$$H_{ij} = \langle i|H|j\rangle = \int \psi^*(\vec{r}-\vec{r}_i) H \psi(\vec{r}-\vec{r}_j) \mathrm{d}r \,. \tag{4.8}$$

The diagonal elements simplify to

$$H_{jj} = \int \psi^*(\vec{r}-\vec{r}_j) H^j_{\mathrm{at}} \psi(\vec{r}-\vec{r}_j) \mathrm{d}r + \int \psi^*(\vec{r}-\vec{r}_j) \Delta U^j \psi(\vec{r}-\vec{r}_j) \mathrm{d}r \tag{4.9}$$

$$= E_0 + \int \psi^*(\vec{r}-\vec{r}_j) \Delta U^j \psi(\vec{r}-\vec{r}_j) \mathrm{d}r \,. \tag{4.10}$$

The term $\beta_j = \int \psi^*(\vec{r}-\vec{r}_j) \Delta U^j \psi(\vec{r}-\vec{r}_j) \mathrm{d}r$ describes how the onsite energies shift due to the potential from the neighboring atoms. The non-diagonal ($i \neq j$) elements simplify to

$$H_{ij} = \int \psi^*(\vec{r}-\vec{r}_i) H^j_{\mathrm{at}} \psi(\vec{r}-\vec{r}_j) \mathrm{d}r + \int \psi^*(\vec{r}-\vec{r}_i) \Delta U^j \psi(\vec{r}-\vec{r}_j) \mathrm{d}r \tag{4.11}$$

$$= \int \psi^*(\vec{r}-\vec{r}_i) \Delta U^j \psi(\vec{r}-\vec{r}_j) \mathrm{d}r = -t_{i,j}, \tag{4.12}$$

where the coupling term $t_{i,j}$ describes the interaction between the two atomic sites i and j. If the basis functions $\{\psi(\vec{r}-\vec{r}_j)\}$ are not orthogonal, which most probably will be the case for real atoms, we have to keep the additional term $E_0 \int \psi^*(\vec{r}-\vec{r}_i)\psi(\vec{r}-\vec{r}_j)\mathrm{d}r = -\alpha_{i,j}$ in (4.12).

Often if a system can be well described by a tight-binding formalism the $\alpha_{i,j}$ and β_j are very small and one can typically neglect them or they can be taken into account through effective couplings $t_{i,j}$ and energies E_0. Additionally often

the $t_{i,j}$ for $|i-j| \geq 2$ become very small, so that one can consider only nearest neighbours and neglect the other interaction terms. The Hamiltonian H in matrix form becomes tridiagonal:

$$H = \begin{bmatrix} E_0 & -t_{1,2} & 0 & \cdots & 0 \\ -t_{1,2}^* & E_0 & -t_{2,3} & \ddots & \vdots \\ 0 & -t_{2,3}^* & E_0 & \ddots & 0 \\ \vdots & \ddots & \ddots & \ddots & -t_{n,n-1} \\ 0 & \cdots & 0 & -t_{n,n-1}^* & E_0 \end{bmatrix} \tag{4.13}$$

Its eigenvalues and -vectors can then be calculated and used to describe the wavefunctions and energies of the system.

Typically the different tight-binding parameters $\alpha_{i,j}$,β_j and $t_{i,j}$ are not explicitly calculated, since often the explicit forms of the single atom wavefunction $\psi(\vec{r})$ and/or the potential $V(\vec{r})$ are not known. Parameters might then be obtained from chemical bond energy data or adjusted to match measured band structure data.

Since our classical system of electromagnetic fields is essentially described by Helmholtz-equations, we will as a next step, outline the similarities between the Helmholtz- and Schrödinger equation and what "Hamiltonian" we will use in order to describe our system.

The Helmholtz equation for the electric field $\vec{E}$ in a dielectric resonator lattice can be written as

$$\left(\Delta + \frac{\omega^2}{c_0^2}\epsilon_r(\vec{r})\right)\vec{E} = 0 \quad \Longleftrightarrow \tag{4.14}$$

$$\left(-\Delta + \frac{\omega^2}{c_0^2}(1-\epsilon_r(\vec{r}))\right)\vec{E} = \frac{\omega^2}{c_0^2}\vec{E} \tag{4.15}$$

Here one can identify the term $\frac{\omega^2}{c_0^2}$ with the energy E of equation 4.1 and $\frac{\omega^2}{c_0^2}(1-\epsilon_r(\vec{r}))$ as a three-dimensional, energy-dependent potential, defined by the location-dependent dielectric constant $\epsilon_r(\vec{r}) = \sum_j \epsilon_r'\left(\vec{r}-\vec{r}_j\right)$ with $\epsilon_r'(\vec{r})$ the dielectric constant for a single resonator and $\vec{r}_j$ the position of the j-th resonator in the resonator-lattice. The factor ω^2/c_0^2 makes the potential energy-dependent, but since we are working within frequency ranges of approximately 0.4 GHz the relative change of ω and therefore ω^2/c_0^2 is small. It thus can be considered quasi constant.

While writing the Helmholtz equation under this form emphasizes the sim-

ilarity to the Schrödinger equation, we can also write it as

$$-\frac{\Delta}{\epsilon_r(\vec{r})}\vec{E} = \frac{\omega^2}{c_0^2}\vec{E}, \tag{4.16}$$

where we can identify the "Hamiltonian" $-\Delta/\epsilon_r(\vec{r})$ [62]. We reduce (4.16) to its scalar form [47] and calculate its matrix elements in the basis of our single resonator wavefunctions $\{\Psi_0\left(\vec{r}-\vec{r}_j\right)\}_j$ that we assume to be proportional to the magnetic field in z-direction. Actually (4.16) is a vectorial equation and it has to be full-filled for each individual field component of $\vec{B}$ and $\vec{E}$. Since all field components are related we expect to find the same result if one would use any of the other field components. We assume that the $\alpha_{i,j}$ and β_j can be neglected and only consider $t_{i,j}$, the nearest neighbour coupling terms. Instead of using ω^2 as measure of the systems "energy", as indicated in (4.16), we rather simply use the frequency ν, since it is the directly measured observable. For the small frequency range we are working with for each experiment, the difference caused by not taking the square of the frequency is sufficiently small. In the following two sections we will precisely characterize the systems abilities to be described with our TB formalism for both the s- and the p-mode, by performing simple benchmark experiments, mainly consisting of chains of resonators. Anticipating here the results obtained by these experiments we find the assumptions and simplification we made to formulate our model are indeed valid since we find a good overall agreement between the TB model and the measured resonance-frequencies and wave functions.

4.2 Benchmarking measurement with the *s*-mode

4.2.1 Two coupled resonators

We start by looking at the simple system consisting of two resonators. Bringing the two resonators sufficiently close together, we can observe a coupling that is depending on the separation d between the resonators, due to the evanescent nature of the excited mode outside the dielectric medium, as can be seen in Fig. 4.1. According to the tight-binding approach, the frequency splitting $\Delta\nu$ equals two times the coupling strength $|t|$ and can be calculated evaluating the overlap integral of the evanescent fields

$$t = \int \Psi_0^*(\vec{r}) H \Psi_0(\vec{r}+\vec{d})\mathrm{d}\vec{r} \tag{4.17}$$

with $H = -\vec{\nabla}^2/n^2(\vec{r})$ and $\Psi_0(\vec{r})$ is the 3D wavefunction of the system. However our setup only allows us to measure 2D scalar wavefunctions $\Psi_0(x, y, z_0)$,

making it impossible to evaluate (4.17) exactly. Note here, that in order to perform tight-binding experiments with our platform, we don't actually need an explicit function $|t(d)|$ since $|t|$ can be measured directly for any distance d and even an exponential fit for the intermediate d range works well [30, 63]. We nevertheless fit the coupling $|t|$ as a function of the separation d with a strongly simplified approximation of (4.17), taking into account only the first order evanescent mode outside, and replace the integration by a point-like evaluation at the exact center between the resonators:

$$t \simeq -\Psi_0\left(r=-\tfrac{d}{2}, z=z_0\right)\frac{\mathrm{d}^2\Psi_0\left(r=\frac{d}{2}, z=z_0\right)}{\mathrm{d}r^2} \tag{4.18}$$

$$\simeq K_0\left(\gamma_1\tfrac{d}{2}\right)\left[K_2\left(\gamma_1\tfrac{d}{2}\right)+K_0\left(\gamma_1\tfrac{d}{2}\right)\right], \tag{4.19}$$

where K_0, K_2 are Bessel functions. Since the two resonators have slightly different eigenfrequencies due to the fabrication process, we compensate for this by adding a constant frequency shift $\Delta\nu_0$ to the fit function $|t(d)| = A\{K_0(\gamma_1 d/2)[K_2(\gamma_1 d/2)+K_0(\gamma_1 d/2)]\}+\Delta\nu_0$. We only fit the two parameters A and $\Delta\nu_0$. We especially re-use the decay constant $\gamma_1 = 0.313\,\mathrm{mm}^{-1}$ obtained by fitting the outside part of a single resonator, in order to explicitly link the evanescent decay of the single resonator wavefunction to the coupling for increasing distance d. As one can see in Fig. 4.1 we find a good agreement between the experimental data and the fit function. Note that the constant frequency shift $\Delta\nu_0 = 1.55\,\mathrm{MHz}$ we found is smaller than the single resonator resonance width $\gamma = 2.2\,\mathrm{MHz}$, meaning that the resonance frequencies of the two used resonators are sufficiently close.

Another important requirement in order to describe our system with a tight-binding formalism, is that the wavefunctions of the system should be well approximated by superpositions of the single resonators wavefunctions. Still working with the two-resonator system, writing the tight-binding Hamiltonian under the form of a 2x2 matrix [1]

$$H = \begin{pmatrix} \nu_0 & -t \\ -t & \nu_0 \end{pmatrix} \tag{4.20}$$

we find the two eigenvectors $(1,1)/\sqrt{2}$ and $(1,-1)/\sqrt{2}$ corresponding to the eigenvalues $\nu_0 - t$ and $\nu_0 + t$ respectively. We expect a symmetric wavefunction $\Psi_{sym}(r) \propto \Psi_0(r)+\Psi_0(r-d)$ and an anti-symmetric wavefunction $\Psi_{antisym}(r) \propto \Psi_0(r)-\Psi_0(r-d)$.

1. We dropped the complex conjugate notation t^* and won't use it again during this manuscript, since we suppose that all wavefunction of the system are real valued and therefore we only have real couplings $t = t^*$.

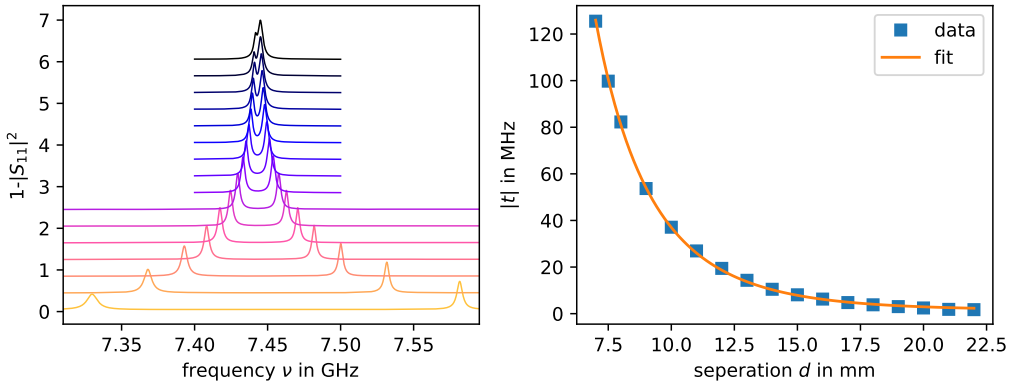

Figure 4.1 – (left) Reflection spectra of two coupled resonators with diameters of 6 mm for different separations d, ranging from 7 mm (yellow line, bottom spectrum) to 22 mm (red line, top spectrum), with a step-size of 1 mm, that are up-shifted for increasing distance between the resonators. The spectra are measured via the loop antenna over the center of the first resonator. (right) Measured coupling strength $|t|$ as a function of the separation d. We extract $|t| = \Delta\nu/2$ by fitting each spectrum with the superposition of two Lorentz lines in order to find the frequency-split $\Delta\nu$. Fitting (4.19) while fixing $\gamma_1 = 0.313\,\mathrm{mm}^{-1}$ gives $\Delta\nu_0 = 1.55\,\mathrm{MHz}$ and $A = 63.2\,\mathrm{MHz}$.

Similar to the wavefunction scan of a single resonator we perform a series of reflection measurements along an axis going through the center of both resonators. For each antenna-position we then fit the spectra with the superposition of two Lorentz lines in order to extract the two wavefunctions Ψ_{sym} and $\Psi_{antisym}$. In Fig. 4.2 one can see the measured wavefunction intensities for two resonators that are separated by a distance of $d = 10\,\mathrm{mm}$. We proceed to fit them with functions $f(x) = |A\Psi_{0,\mathrm{fit}}(x-x_1) \pm B\Psi_{0,\mathrm{fit}}(x-x_2)|^2$, where $\Psi_{0,\mathrm{fit}}(x)$ is the fit function obtained by fitting the wavefunction of a single resonator (see Fig. 3.2). Since the two resonators are not identical, we allow $A \neq B$ to compensate for that. We find a good agreement with the measurements, especially since the difference in fitted positions x_1, x_2 equals 10.0 mm, the exact spacing between the resonators. One may note that the antisymmetric state is occurring at the lower frequency and the symmetric state at the higher frequency, indicating that in our system the coupling-strength t is actually negative. This comes from the fact that we use the magnetic field $\vec{B}$ as a measure of the systems wavefunction which actually behaves as a pseudo vector. Geometrically, the direction of a reflected pseudo vector is opposite to its mirror image, but with equal magnitude. In contrast, the reflection of a true (or polar) vector is exactly the same as its mirror image. This means that if we would use the

electric field $\vec{E}$, which is a true vector, as measure of the systems wavefunction, we would actually find the symmetric state at the lower frequency and the antisymmetric state at the higher frequency, as it is normally the case for other photonic or electric structures. Since any state that is symmetric in $\vec{E}$, is antisymmetric in $\vec{B}$, and vise versa, the interpretation of the sign of t should always be made within the measure of the same field component, which in our case is naturally fulfilled since we exclusively use the loop antenna for scanning measurements and only use the kink antennas (that couples to the electric field) as fixed excitation for transmission measurements.

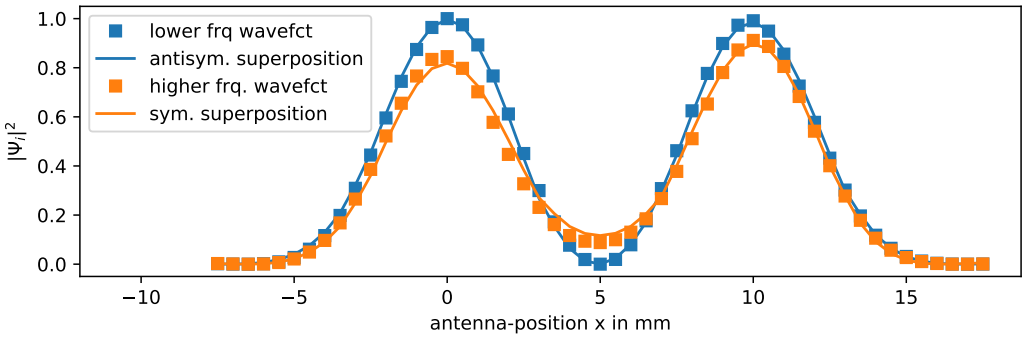

Figure 4.2 – Extracted wavefunctions of two coupled resonators with a separation of $d = 10\,\text{mm}$ between them (blue/orange squares). The blue squares correspond to the state that is occurring at the lower frequency. The orange squares correspond to the state that is occurring at the higher frequency. We identify the lower frequency state (blue) as the antisymmetric state, since its wavefunction is vanishing at the middle distance ($x = 5\,\text{mm}$) between the two resonators. It follows that the higher frequency state is the symmetric state. We then proceed to fit both wavefunction with symmetric and antisymmetric superpositions of the single resonator wavefunction $f(x) = |A\Psi_{0,\text{fit}}(x-x_1) \pm B\Psi_{0,\text{fit}}(x-x_2)|^2$ (solid blue/orange lines). The found fit parameters for the antisymmetric, symmetric superposition are $A = 0.69$, $B = 0.68$, $x_1 = 0.0\,\text{mm}$, $x_2 = 10.0\,\text{mm}$ and $A = 0.71$, $B = 0.75$, $x_1 = 0.0\,\text{mm}$,$x_2 = 10.0\,\text{mm}$, respectively.

Finding a good agreement in describing a coupled two-resonator system by a tight-binding formalism in the spectral-domain, i.e. eigenfrequencies, as well as in the spatial domain, i.e. wavefunctions, as symmetric and antisymmetric superpositions, we proceed now to investigate the next more complex system: a linear chain of equally spaced resonators.

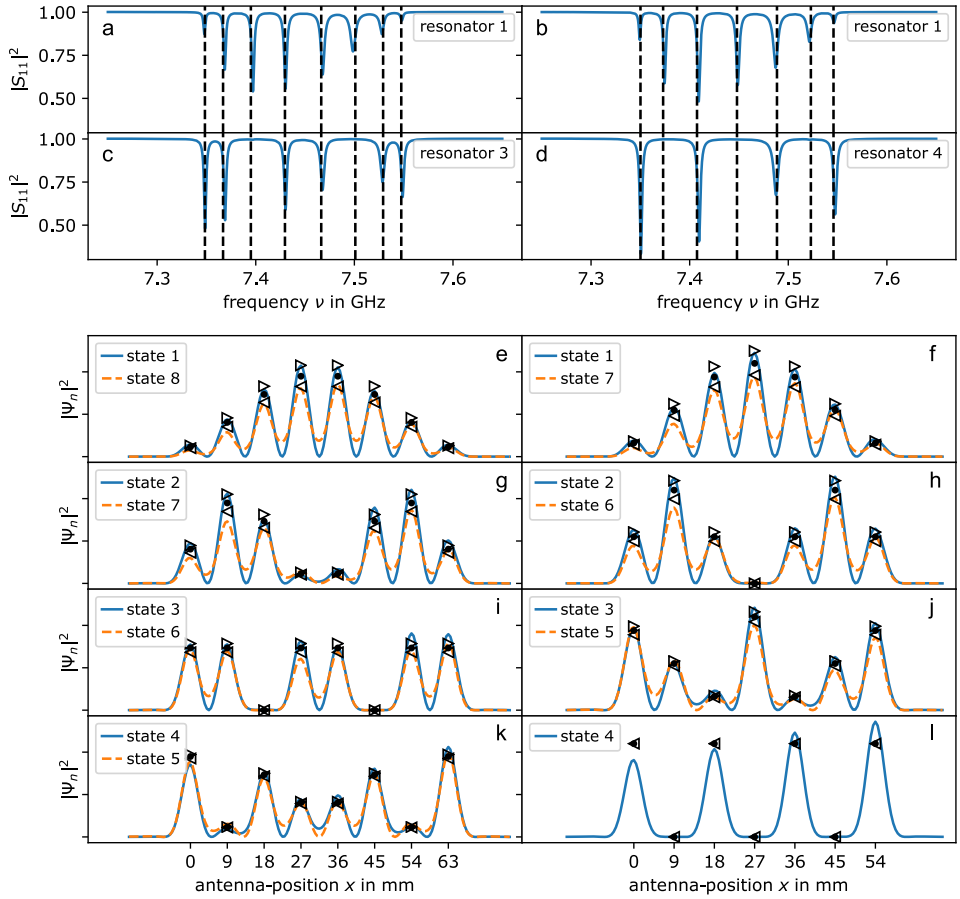

Figure 4.3 – The figures on the left (right) are corresponding to a chain with $N = 8$ ($N = 7$) resonators. Panel (a–d) present the reflection S_{11} measured over the central position of the indicated resonators (1,3, and 4). The vertical dashed lines indicate the eigenvalues ν_n of H_0. Panel (e–l) shows the extracted wavefunctions of the systems as a function of the antenna-position x (blue solid and orange dashed lines), as well as effective Hamiltonian simulations as left (higher frequency states) and right (lower frequency states) pointing triangles. The states are numbered increasingly according to their resonance-frequency. The antisymmetric and its corresponding symmetric state are presented in the same graph. We add the calculated eigenvectors of the closed systems Hamiltonian H_0 as black circles. The measured wavefunctions and effective Hamiltonian simulations share the same y-axis, while the eigenvectors of H_0 were adjusted by a global factor, chosen such that they match for state 4 for the $N = 7$ chain which is the state the least affected by neighboring sites, i.e. the dots and triangles in (l) are the same.

4.2.2 Linear chains

We chose to investigate two chains of resonators in detail, an even ($N = 8$) and an odd one ($N = 7$). Two neighboring resonators are separated by a distance of $d = 9\,\text{mm}$. As in the previous measurements, we measure the reflection along an axis passing through the centers of the resonators, in order to extract the spatially resolved wavefunctions of the N states of the system. In Fig. 4.3(a–d) we present two reflection spectra for each chain. For the chain with $N = 8$ ($N = 7$) resonators, we present the reflection measured exactly above the first (first) and third (fourth) resonator. In the spectra measured above the first resonator, we can identify N distinct and well isolated resonances for both chains. In the spectra above the third (forth) resonator one can see that several resonances are vanishing, since the associated wavefunctions have nodes at that resonator. We compare the spectra with the eigenvalues ν_n of the tight-binding Hamiltonian

$$H_0 = \sum_{i=1}^{N} \nu_0 |i\rangle\langle i| + \sum_{i=1}^{N-1} t\,|i\rangle\langle i+1| + h.c. \tag{4.21}$$

and find a good agreement. We re-use the single resonator resonance frequency $\nu_0 = 7.446\,\text{GHz}$ (see Fig. 3.2) and $t = -53.0\,\text{MHz}$, corresponding to the separation of 9 mm that we extracted from the two resonator measurement (see Fig. 4.1).

We then extract the wavefunctions for each state again by fitting each resonance individually with a Lorentz line and present them by pairs of symmetric and antisymmetric states [see Fig. 4.3(e–l)]. We further search to link the measured amplitude over a resonator to the tight-binding coefficient of that site. One problem that we encounter is the slight overlap of adjacent single resonator wavefunctions, meaning that the measured amplitude $\Psi(r_0)$ over the center of a resonator at position r_0 is not only proportional to a_0, the tight-binding coefficient of that site, but is actually proportional to $\Psi(r_0) = a_0\Psi_0(0) + \sum_i a_i\Psi_0(r_0 - r_i)$, where $\sum_i$ is the sum over the other resonators of the system and a_i and r_i their tight-binding coefficients and positions. This effect changes for each system and especially for each wavefunction individually. In order to illustrate and estimate the deviation we add the eigenstates $|v_n\rangle$ of the tight-binding Hamiltonian (4.21) as black circles to Fig. 4.3(e–l). In general, the biggest difference can be observed when comparing the complete symmetric with the complete antisymmetric wavefunctions of a system [see Fig. 4.3(e–f)], where the deviation is of the order of 10 %.

We still find a good overall agreement of the general structure of the different wavefunctions, but nevertheless we go one step further and compare our measurement with effective Hamiltonian simulations, that can account

for the overlapping between single resonator wavefunctions. The effective Hamiltonian theory has been introduced to describe open quantum system and suits perfectly to model our open tight-binding system (an overview is given in Refs [64, 65]). For a system of N resonators, where the openness is modeled via only one channel, the effective Hamiltonian takes the form [65, 66]

$$H_{eff} = H_0 - \frac{\mathrm{i}\sigma}{2} W W^T , \tag{4.22}$$

where W is a normalized vector of size N, containing the information on the exact nature of the coupling. σ is the overall coupling strength of the channel and H_0 is a $N \times N$ matrix representing the Hamiltonian of the corresponding closed (tight-binding) system (4.21). Modeling an excitation over the i-th resonator, not taking the overlap of the wavefunctions into consideration, only the i-th element of W is non zero and equals one. In our case the antenna is not only exciting the resonator at site i but also the neighboring sites, since their single resonator wavefunctions have not yet vanished completely at that distance. In order to model such an excitation we add a small term ϵ ($\epsilon \ll 1$) on the neighboring sites of the i-th element in W: $W = (..., 0, 0, 1, 0, 0, ...) \rightarrow W = (..., 0, \epsilon, 1, \epsilon, 0, ...)/\sqrt{1+2\epsilon^2}$. We further neglect next-nearest-neighbor contributions. We set $\epsilon \approx \Psi_0(0)/\Psi_0(d)$, where d is the distance between the resonators, which in our case turns out to be negative, since the measured single resonator wavefunction is negative at a distance of $d = 9\,\mathrm{mm}$ from the center.

The resulting reflection spectrum S_{11} as a function of the frequency ν is then given by [65–67]

$$S_{11}(\nu) = 1 - \mathrm{i}\sigma \left(W^T \frac{1}{\nu - H_{eff}} W \right) \tag{4.23}$$

We simulate the spectra over each resonator and extract the wavefunction the same way as for the measured spectra. The results are presented as triangles in Fig. 4.3. In order to match the measurements we are using $\sigma = 2.2\,\mathrm{MHz}$ and $\epsilon = -0.035$. ϵ does not correspond exactly to $\Psi_0(0)/\Psi_0(d) = -0.066$, but is the same order of magnitude. The difference can probably be explained by the fact that the antenna is not point-like, thus inducing a convolution operation, that is not commuting with the square-operation (in reflection measurement we only have direct access to $|\Psi|^2$). Apart from local fluctuations (due to small differences of the used resonators), we find a good agreement between the measured wavefunctions and the ones simulated using the effective Hamiltonian. The wavefunction of state 4 for the chain with $N = 7$ resonators [see Fig. 4.3(l)] actually shows a tendency of growing peak height for an increasing antenna position. This is probably due to not perfectly parallel bottom and

top plates, leading to different heights for different areas of the chain changing slightly the resonance-frequencies and couplings between the resonators. Since state 4 is occurring at the single resonator resonance frequency, we expect it to be the most sensitive one to those local fluctuations.

The results for the *s*-mode seem very promising. But before actually studying more complex and interesting systems, we will next present the same kind of systems for the *p*-mode.

4.3 Benchmarking measurement with the *p*-mode

4.3.1 Lifted degeneracy

Bringing two resonators close together, not only do their *s*-modes couple, but there is also a coupling in between the *p*-modes of the two resonators. As one can see in figure 4.4, due the degenerate nature of the single resonator *p*-mode, upon adding a second resonator at a distance of 10 mm the single resonator resonance peak splits into four peaks.

The fact that we observe four individual peaks in the two-resonator reflection spectrum confirms the expected different coupling, that arises from different overlap integrals depending on the alignment of the modes, that actually lift the degeneracy.

We proceed to extract the wavefunctions of the four different states by performing a full two dimensional reflection scan with the loop antenna and fitting the four individual resonances. The obtained two dimensional wavefunctions are plotted in Fig. 4.4(a–d). While it was not possible to individually visualize the two degenerate modes with a single resonator measurement (see figure 3.3), here one can clearly identify the two orthogonal *p*-modes Ψ_0^x and Ψ_0^y of the single resonators that form either a symmetric or antisymmetric superposition. Since the two resonator system is not rotational symmetric anymore, but actually has a distinct axis that is defined by the alignment of the two resonators, the nodal lines of the modes align either with the axis along which the resonators are aligned or with its perpendicular direction. One can identify the two higher frequency modes as symmetric and the two lower frequency modes as antisymmetric modes, which is consistent with the results obtained for the *s*-mode.

Since the coupling strength is in first approximation proportional to the mode overlap in between the two resonators, the modes that have their nodal line along the axis of alignment of the two resonators, are weaker coupled and therefore at the center of the spectrum. This property of an anisotropic coupling that depends on the orientation of the individual modes makes the

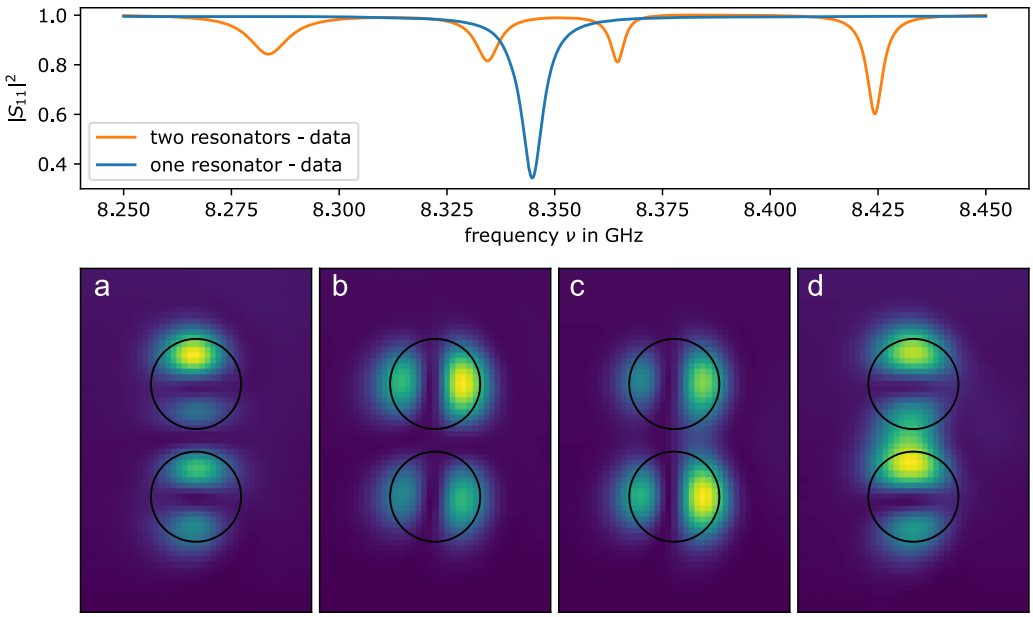

Figure 4.4 – (top) Reflection measurement for a single resonator (blue) and two coupled resonators (orange) separated by a distance of 10 mm (from center to center) measured at $d_x = d_y = 3$ mm from the center of the (first) resonator. (a–d) two dimensional wavefunctions $|\Psi|^2$ of the two resonator system (ordered according to their frequency) with a resolution of 0.5 mm. The black circles are corresponding to the perimeters of the two resonators with diameter $D = 8$ mm).

experiments with p-modes so interesting.

4.3.2 Adaption of the TB model for p-modes

While we have introduced the TB model for a unique, non degenerate single resonator wavefunction, it can be appropriately modified to account for the degenerate nature of the p-modes. While for the s-mode, a system of N resonators resulted in a $N \times N$ TB matrix (due to the basis of the N individual single resonator wavefunctions), it now results in a $2N \times 2N$ matrix, since we suppose that the wavefunctions $\Psi(\vec{r}) = \sum_i c_i^x \Psi_0^x(\vec{r}-\vec{r}_i) + c_i^y \Psi_0^y(\vec{r}-\vec{r}_i)$ of the system are now superpositions of the two basis functions $\Psi_0^x(\vec{r}-\vec{r}_i)$ and $\Psi_0^y(\vec{r}-\vec{r}_i)$ of each resonator at position $\vec{r}_i$. The tight binding coefficients $\{c_i^x, c_i^y\}$ form a vector $\vec{c} = (c_1^x, c_1^y, c_2^x, c_2^y, ..., c_N^x, c_N^y)$ of length $2N$, so that each element of the "original" TB matrix H_{ij} is replaced by a 2×2 matrix

$$H_{ij} \rightarrow \begin{pmatrix} H_{ij}^{xx} & H_{ij}^{xy} \\ H_{ij}^{yx} & H_{ij}^{yy} \end{pmatrix}. \tag{4.24}$$

Neglecting non leading order terms, the the onsite energies become

$$H_{ii} = \nu_i \rightarrow \begin{pmatrix} \nu_i^x & 0 \\ 0 & \nu_i^y \end{pmatrix}, \tag{4.25}$$

where ν_i^x and ν_i^y are the single resonator resonance frequencies associated with the two single resonator wavefunctions Ψ_0^x and Ψ_0^y of the resonator at site i, respectively. Theoretically they are identical, but as already seen in figure 3.3, the degeneracy might be slightly lifted due to experimental imperfections. The coupling term $t_{i,j}$ becomes

$$H_{i\neq j} = t_{i,j} \rightarrow \begin{pmatrix} t_{i,j}^{xx} & t_{i,j}^{xy} \\ t_{j,i}^{yx} & t_{i,j}^{yy} \end{pmatrix}, \tag{4.26}$$

where $t_{i,j}^{xx}$ and $t_{i,j}^{yy}$ describe the coupling between modes of sites i and j with the same orientation, while $t_{i,j}^{yx}$ and $t_{i,j}^{yx}$ describe the coupling between the modes Ψ_0^x and Ψ_0^y of the two sites i and j. For the two resonator system presented in figure 4.4, the orientation of the coordinate system in which one describes the system can be chosen in a way that the basis functions Ψ_0^x and Ψ_0^y align with the axis going through the resonators, so that the $t_{i,j}^{yx}$ and $t_{i,j}^{xy}$ are actually zero and one can therefore separate the system into $\Psi^x = \sum_i c_i^x \Psi_0^x(\vec{r} - \vec{r}_i)$ and $\Psi^y = \sum_i c_i^y \Psi_0^y(\vec{r} - \vec{r}_i)$ modes, sometimes also referred to as x-polarized and y-polarized modes, that then could actually be described completely independently. For systems with more resonators this is typically not possible anymore. Any structure, where resonators are not aligned along orthogonal axis, e.g. hexagonal or triangular lattices, have non zero $t_{i,j}^{yx}$ and $t_{i,j}^{xy}$ no matter how the systems coordinate system is orientated and the separation into an individual and independent description of x- and y-polarized modes is not possible.

Although during this theses for our description we only use the leading order onsite energies and nearest neighbour terms, for the sake of completeness any matrix element H_{ij}^{kl} with $k, l \in x, y$ and $i, j \in 1, 2, ...N$ for a system of N resonators is defined by the integral

$$H_{ij}^{kl} = \int \Psi_0^{k*}(\vec{r} - \vec{r}_i) H \Psi_0^l(\vec{r} - \vec{r}_j) \mathrm{d}r\,, \tag{4.27}$$

where $\vec{r}_i$ and $\vec{r}_j$ are the position of the i-th and j-th resonator, respectively.

As for the s-mode, the exact 3D experimental wavefunctions $\Psi_0^x(\vec{r})$, $\Psi_0^y(\vec{r})$ cannot be measured and therefore (4.27) cannot be evaluated. We therefore proceed as for the s-mode by determining the the single resonator resonance

frequencies ν_i and the coupling function $t_{i,j} = t(|\vec{r}_i - \vec{r}_j|) = t(d)$ experimentally.

While the $\{\nu_i^x\}$ and $\{\nu_i^y\}$ can be directly obtained by measuring the individual resonators resonance frequencies, the $t_{i,j}^{xx}$ and $t_{i,j}^{yy}$ as well as the $t_{i,j}^{xy}$ and $t_{i,j}^{yx}$ are actually described by functions $t^{xx}(d_{ij}, \theta_{ij})$, $t^{yy}(d_{ij}, \theta_{ij})$, $t^{xy}(d_{ij}, \theta_{ij})$ and $t^{yx}(d_{ij}, \theta_{ij})$, that not only depend on the distance d_{ij} of separation in between the two resonators at site i and j (as it was the case for the s-mode), but also an the angle θ_{ij}, that the line going through the centers of these two resonators forms with an fixed reference-axis, that we chose to be the x-axis.

The general Hamiltonian H of two coupled resonator separated by a distance d with resonance frequencies $\nu_0^x = \nu_0^y = \nu_0$ then takes the form

$$H = \begin{pmatrix} \nu_0 & 0 & -t^{xx}(d,\theta) & -t^{xy}(d,\theta) \\ 0 & \nu_0 & -t^{yx}(d,\theta) & -t^{yy}(d,\theta) \\ -t^{xx}(d,\theta) & -t^{xy}(d,\theta) & \nu_0 & 0 \\ -t^{yx}(d,\theta) & -t^{yy}(d,\theta) & 0 & \nu_0 \end{pmatrix} \tag{4.28}$$

If we now suppose that the two resonators are aligned along the x-axis, so that $\theta = 0$, the systems Hamiltonian can be simplified into

$$H = \begin{pmatrix} \nu_0 & 0 & -t^x(d) & 0 \\ 0 & \nu_0 & 0 & -t^y(d) \\ -t^x(d) & 0 & \nu_0 & 0 \\ 0 & -t^y(d) & 0 & \nu_0 \end{pmatrix}, \tag{4.29}$$

with $t^x(d) = t^{xx}(d, \theta = 0)$ and $t^y(d) = t^{yy}(d, \theta = 0)$. Because of the way one has chosen the alignment of the two resonators, $t^{xy}(d, \theta = 0) = t^{yx}(d, \theta = 0) = 0$. The eigenvalues of H then are $\nu_0 \pm t^x(d)$ with associated eigenstates $(\Psi_0^x(x,y,x) \mp \Psi_0^x(x-d,y,z))/\sqrt{2}$ and $\nu_0 \pm t^y(d)$ with eigenstates $(\Psi_0^y(x,y,x) \mp \Psi_0^y(x-d,y,z))/\sqrt{2}$.

With a two resonator measurements, where one varies the separation d in between the resonators, one can therefore obtain experimental estimates for $t^x(d)$ and $t^y(d)$. The resonance frequencies $\nu_1 < \nu_2 < \nu_3 < \nu_4$ of the 4 peaks can be experimentally determined for different separations d and one can calculate $|t^y(d)| = (\nu_4 - \nu_1)/2$ and $|t^x(d)| = (\nu_3 - \nu_2)/2$. We expect $|t^y(d)| > |t^x(d)|$ for all d since the nodal line of Ψ_0^x corresponds to the alignment axis of the two resonators and therefore its overlap integral is always smaller. The identification of the different modes as symmetric or antisymmetric can further give access to the sign of $t_0^x(d)$ and $t_0^x(d)$. We find $t^x(d) < 0$, while $t^y(d) > 0$. This seems a little surprising at first. As one can see in figure 4.4 we indeed find for both, the x and y polarized modes, that the symmetric

state is at the higher frequency, while the antisymetric state is at the lower frequency, in agreement with the results obtained for the s-mode. But since the single resonator wave functions Ψ_0^x and Ψ_0^y are not rotational symmetric and change their sign on their nodal lines, the overall symmetric state of the y polarized modes is actually described by the antisymetric vector $(0,1,0,-1)/\sqrt{2}$, since Ψ_0^y changes its sign along x-axis, on which the resonators are aligned.

When the $t^x(d)$ and $t^x(d)$ are known, one can then find general expressions for $t^{xx}(d,\theta)$, $t^{yy}(d,\theta)$, $t^{xy}(d,\theta)$, $t^{yx}(d,\theta)$ for any angle θ by rotating the Hamiltonian defined in (4.29) by θ in the x,y plane using the rotation matrix

$$R = \begin{pmatrix} \cos\theta & -\sin\theta & 0 & 0 \\ \sin\theta & \cos\theta & 0 & 0 \\ 0 & 0 & \cos\theta & -\sin\theta \\ 0 & 0 & \sin\theta & \cos\theta \end{pmatrix}. \tag{4.30}$$

Upon comparing the Hamiltonian RHR^{-1} in the new reference system with (4.28) we find the following expressions

$$t^{xx}(d,\theta) = t^x(d)\cos^2\theta + t^y(d)\sin^2\theta \tag{4.31}$$
$$t^{yy}(d,\theta) = t^y(d)\cos^2\theta + t^x(d)\sin^2\theta \tag{4.32}$$
$$t^{xy}(d,\theta) = (t^x(d) - t^y(d))\sin\theta\cos\theta \tag{4.33}$$
$$t^{yx}(d,\theta) = (t^x(d) - t^y(d))\sin\theta\cos\theta. \tag{4.34}$$

The terms $t^{xy}(d,\theta) = t^{yx}(d,\theta)$ that describe the interaction between the Ψ_x mode of one and the Ψ_y mode of the other resonator are actually zero when θ is a multiple of $\pi/2$. This is the case when the resonators are either aligned along the x or the y axis, and therefore the Hamiltonian can be separated into x and y polarized modes. One further finds that $t^{xx}(d,\theta \pm \pi/2) = t^{yy}(d,\theta)$, which is expected since the physics of the systems should not change upon interchanging the systems axis $x \longleftrightarrow y$.

Since the Hamiltonian for any angle θ is constructed with the use of unitary rotation matrices, we will always find its four eigenvalues $\nu_0 \pm t^x(d)$ and $\nu_0 \pm t^y(d)$. The corresponding eigenstates are $(\Psi_0^\theta(x,y,z) \mp \Psi_0^\theta(x - d\cos\theta, y - d\sin\theta, z))/\sqrt{2}$ and $(\Psi_0^{\theta\perp}(x,y,z) \mp \Psi_0^{\theta\perp}(x - d\cos\theta, y - d\sin\theta, z))/\sqrt{2}$, where one uses $\Psi_0^\theta(\vec{r}) = \cos\theta\Psi_0^x(r,\varphi,z) + \sin\theta\Psi_0^y(r,\varphi,z) = \sin(\varphi-\theta)\Psi_0(r,z)$ and $\Psi_0^{\theta\perp}(\vec{r}) = -\sin\theta\Psi_0^x(r,\varphi,z) + \cos\theta\Psi_0^y(r,\varphi,z) = \cos(\varphi-\theta)\Psi_0(r,z)$, where the function $\Psi_0(r,z)$ describes the r- and z-dependency of the single resonator p-mode wavefunctions. We find that they are superpositions of $\Psi_0^{\theta\parallel}$ and $\Psi_0^{\theta\perp}$, that are essentially the single resonator wavefunctions Ψ_0^x and Ψ_0^y rotated by an angle θ, so that their nodal lines align with the axis that goes through the centers of the two resonators and its perpendicular direction, respectively.

Although this is an intrinsic property of H arising from the construction via the rotation matrices, we preferred to write it down explicitly to emphasize the self-consistency of the adapted TB binding model, that can essentially be constructed in any reference coordinate system. To limit eventual confusion to a minimum and be consistent, throughout this thesis we will nevertheless limit ourselves to only use Ψ_0^x and Ψ_0^y as basis to construct further TB Hamiltonians.

4.3.3 Measuring the couplings $t^x(d)$ and $t^y(d)$

As a continuation of the experiment presented in figure 4.4, we will now measure the spectrum of the two resonator system for different distances d in order to experimentally extract $t^x(d)$ and $t^y(d)$. Instead of measuring a complete 2D-scan above the resonators, we decide to only measure at strategic points $\Delta x, \Delta y$ from the center of the two resonators to reduce the measurement time. We measure at $\Delta x = 0\,\text{mm}, \Delta y = 3\,\text{mm}$ in order to mainly couple to the x-polarization, since Ψ_0^y has its nodal line along the y-axis. Analogously, we measure at $\Delta x = 3\,\text{mm}, \Delta y = 0\,\text{mm}$ in order to mainly couple to the y-polarization. The measured spectrum can be seen in figure 4.5. One can see that the resonance peaks associated with the x-polarization (dashed lines) are on the inside, while the peaks associated with the y-polarization (solid lines) are on the outside of the spectrum, clearly confirming that $|t^y| > |t^x|$. As one can see the 4 resonance peaks do not converge into a single peak for increasing separation d as one would expect if all single resonator resonance frequencies would be equal, but actually converge into two distinct peaks. Due to the different colors used it becomes obvious that the 4 peaks converge into a lower frequency peak that is associated with the first resonator (orange lines) and a higher frequency peak that is associated with the second resonator (blue lines). It therefore seems that we have chosen two resonators for this experiment whose resonance frequencies do not match very well and their frequency difference seems to be around 25 MHz. For larger systems we can not avoid this problem totally, thus we decided to use this mismatch between the resonator's resonance frequencies to further test the robustness of the TB model, by formulating a TB Hamiltonian that actually accounts for the two different resonance frequencies ν_1 and ν_2

$$H = \begin{pmatrix} \nu_1 & 0 & -t^x(d) & 0 \\ 0 & \nu_1 & 0 & -t^y(d) \\ -t^x(d) & 0 & \nu_2 & 0 \\ 0 & -t^y(d) & 0 & \nu_2 \end{pmatrix}, \tag{4.35}$$

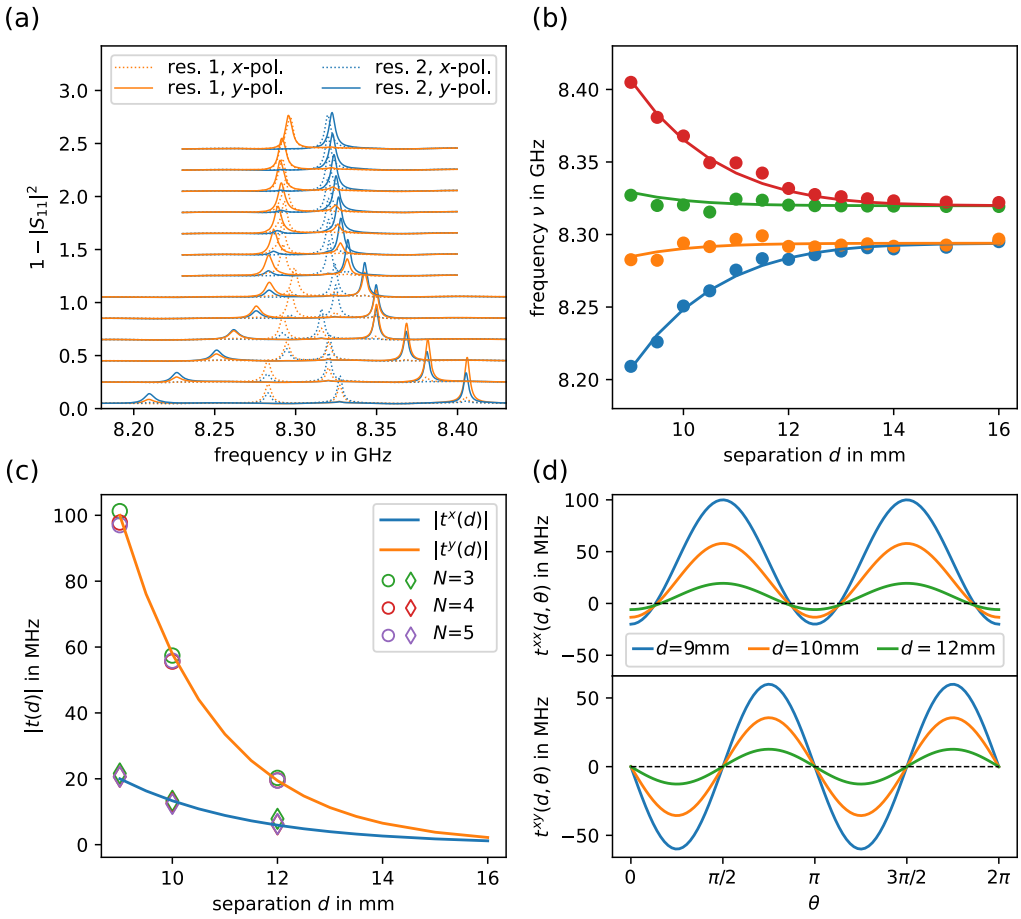

Figure 4.5 – (a) Reflection spectra of two coupled resonators for different separations d, ranging from 9 mm to 16 mm, that are up-shifted for increasing distance between the resonators. The spectra are measured via the loop antenna over 4 strategic points, that are then plotted in different colors and linestyles. (b) Extracted resonance frequencies (coloured dots) for the different separations d and the fit of (4.36) (solid lines). (c) The extracted functions $|t^x(d)|$ and $|t^y(d)|$ as a function of d. We further compare the coupling functions to coupling values extracted from linear chain measurement. We use chains with $N = 3, 4, 5$ total resonators separated by distances $d = 9, 10, 12$ mm. We plot the extracted $|t^x(d)|$ as diamonds and $|t^y(d)|$ as circles. (d) the general coupling functions $t^{xx}(d,\theta)$ and $t^{xy}(d,\theta)$ as a function of the angle θ for different distances $d = 9, 10, 12$ mm. The dashes black lines mark $t^{xx}(d,\theta) = 0$ and $t^{xy}(d,\theta) = 0$ and their only purpose is visual guidance.

with eigenvalues

$$\lambda_i = (\nu_1 + \nu_2 \pm \sqrt{4t^k(d)^2 + (\nu_1 - \nu_2)^2})/2, \text{ for } k \in \{x, y\}. \tag{4.36}$$

Assuming a simple exponential decay for both $t^x(d) = A_x e^{-\gamma_x(d-9\,\mathrm{mm})}$ and $t^y(d) = A_y e^{-\gamma_y(d-9\,\mathrm{mm})}$ (with $A_x < 0$ and $A_y > 0$), we proceed to fit the positions of the 4 resonance peaks (that we have beforehand extracted by fitting them with the superposition of Lorentz lines) with the expressions for the λ_i. We adjust all four curves at once minimizing their combined quadratic error by varying the parameters $\nu_1, \nu_2, A_x, A_y, \gamma_x, \gamma_y$. The result can be seen in figure 4.5. We find $\nu_1 = 8.294\,\mathrm{GHz}$, $\nu_2 = 8.320\,\mathrm{GHz}$, $A_x = -19.8\,\mathrm{MHz}$, $A_y = 98.4\,\mathrm{MHz}$, $\gamma_x = 0.406\,\mathrm{mm}^{-1}$. $\gamma_y = 0.546\,\mathrm{mm}^{-1}$. We generally observe a good agreement, but the extracted resonance positions show more fluctuations than it was the case for the *s*-mode (see figure 4.1). This is caused by the sensitivity of the resonance frequencies upon the re-placement of the same resonator, which is stronger for the *p*-mode than for the *s*-mode as already discussed in section 3.3. The decay constants γ_x and γ_y are slightly different, although both the Ψ^x and Ψ^y have the same radial decay. The different angular dependency of the modes leads to different decays within the overlap integral, as the resonators are not point-like, which explains the observed difference of γ_x and γ_y. In figure 4.5 one can see the extracted functions $|t^x(d)|$ and $|t^y(d)|$, where we further compare them to coupling values that we extracted from linear chain measurement (open symbols), which agree nicely with the extracted curves from the two resonator measurement. See section 4.3.4 for details on the extraction of coupling values from linear chain measurement. To help visualize the angle dependency of the general coupling functions we then proceed to plot in figure 4.5 $t^{xx}(d,\theta)$ and $t^{xy}(d,\theta)$ for different distances $d = 9, 10, 12\,\mathrm{mm}$. $t^{xx}(d,\theta)$ oscillates between $t^x(d)$ for $\theta = 0, \pi$ and $t^y(d)$ for $\theta = \pi/2, 2\pi/2$, while $|t^{xy}(d,\theta)|$ is maximal for multiple of $\pi/4$.

Using the now extracted general coupling functions $t^{xx}(d,\theta)$, $t^{yy}(d,\theta)$, and $t^{xy}(d,\theta)$, we can construct a TB Hamiltonian for any distribution of resonators. Before studying a more complex system in chapter 6, we test our formalism on systems consisting only of few resonators.

4.3.4 Linear chains

Before looking at non-separable systems, we study linear chains, where the *x*- and *y*-polarized modes can be described separately. Since the underlying TB Hamiltonians are equivalent, the wavefunctions and spectrum should be closely related to those measured for the linear chains presented in figure 4.3 for the *s*-mode.

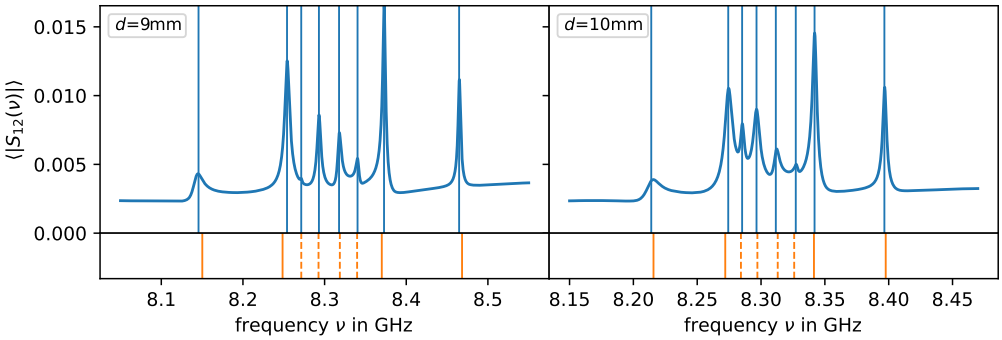

Figure 4.6 – Averaged transmission spectrum $\langle|S_{12}(\nu)|\rangle$ (in blue) for the linear chain of $N = 4$ resonators that are separated each by a distance of $d = 9\,\text{mm}$ (left) and $d = 10\,\text{mm}$ (right). Its extracted resonance-positions are plotted as blue vertical lines. We then fit the extracted positions with (4.39) for each polarization separately. The fitted positions are marked by dashed (for the x-polarization) and solid (for the y-polarization) orange lines.

We will limit ourself to spectral measurements at a few strategic points that allow to distinguish between x- and y-polarized modes and do not extract wavefunctions. For the s-modes a scan on a straight line was more than enough to fully visualize wavefunctions and actually measurements only over the centers of the resonators are enough to extract the TB coefficients of the wavefunctions. For the p-modes, on the other hand, we need at least a couple more measurements on strategic points and the TB coefficient cannot be extracted easily. In chapter 6 we will present a method to extract the TB coefficients for p-mode measurements, but it required a full 2D scan of the system, which is time consuming. While for those experiments their knowledge is actual necessary for further calculations, the aim of the following measurements is to characterize how the TB model works in describing small test systems. Here actually the comparison of the eigenvalues of the TB matrix with the position of the resonances within the spectra gives us enough information.

The linear chains are constructed out of $N = 3, 4, 5$ resonators separated by the same distance d. We study chains with $d = 9, 10, 12\,\text{mm}$. Assuming the same resonance frequencies ν_0 for all resonators, only considering nearest neighbour couplings t^x and t^y, their TB Hamiltonian (in Dirac notation) can be written as $H_0 = H_0^x + H_0^y$ with

$$H_0^x = \sum_{i=1}^{N} \nu_0 |i\rangle_x \langle i|_x + \sum_{i=1}^{N-1} t^x |i\rangle_x \langle i+1|_x + h.c. \tag{4.37}$$

and

$$H_0^y = \sum_{i=1}^{N} \nu_0 |i\rangle_y \langle i|_y + \sum_{i=1}^{N-1} t^y |i\rangle_y \langle i+1|_y + h.c. \tag{4.38}$$

and its eigenvalues are [68]

$$\nu_i^{x/y} = \nu_0 + 2t^{x/y} \cos\left(\frac{\pi k}{N+1}\right) \text{, with } k = 1, 2, ..., N. \tag{4.39}$$

Instead of comparing the measured spectrum to the eigenvalues that we calculate using the functions $t^x(d)$ and $t^y(d)$ extracted from the previous two resonator measurement, we actually decide to use the measured spectrum for the different linear chains to estimate t^x and t^y for the distances $d = 9, 10, 12\,\text{mm}$ and then compare them to the $t^x(d)$ and $t^y(d)$ extracted from the two resonator measurement.

In order to extract the couplings t^x and t^y for each chain measurement, we extract the position of all $2N$ resonance peaks in the measured spectra and identify them all as either belonging to a x or y-polarized mode. We then minimize the overall quadratic error between the positions of the resonance peaks and the eigenvalues predicted by (4.39) for each polarization individually by varying the parameters ν_0 and t^x, t^y.

The results are then added to figure 4.5, where we find a good agreement. Exemplary, we show in figure 4.6 the measured spectrum for the chain with $N = 4$, the distances $d = 9\,\text{mm}$ and $d = 10\,\text{mm}$ and the fitted resonance positions. The latter correspond to the measured position within a few MHz, which is the same order or even smaller than the fluctuations of the individual resonance frequencies upon the resonator placement and we cannot expect the model to be more precise.

4.3.5 Three-pointed star and hexagonal ring

Next we have a look at small test systems where one actually cannot separated the Hamiltonian in terms of x- and y-polarizations. Considering the good agreement of the TB model, the approximation to only consider the nearest neighbour coupling seems to work well for linear chains. Since the resonators are all aligned on a straight line with no direct line-of-sight between next nearest neighbours, one could eventually argument that there is some kind of effective shielding that minimizes the effect of the next nearest neighbours for these chains. For the two small test system that we are going to study next this is not the case anymore and there is a direct line-of sight not only for nearest neighbours but also in between the other resonators of the system. Additionally,

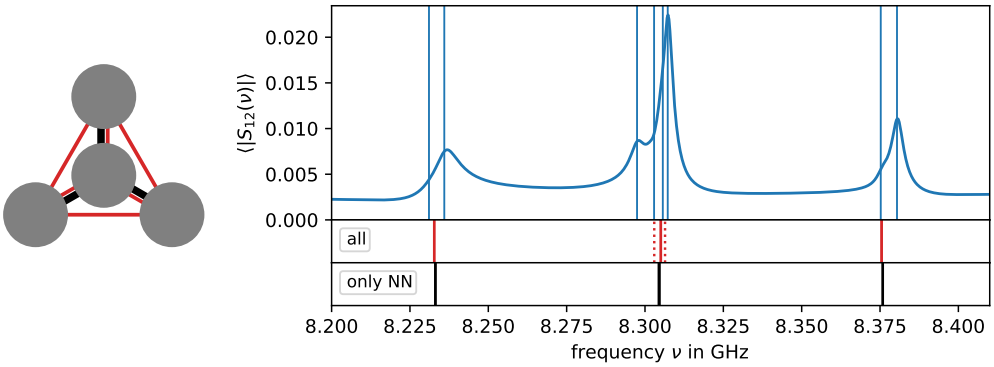

Figure 4.7 – (left) True to scale sketch of three-pointed star. Resonators are plotted as grey circles while the resonator-pairs that we consider for the theoretical model are marked by lines in between the resonators. All possible pairs are connected by red lines, while the nearest neighbours are connected by black lines. (right) Averaged transmission spectrum $\langle|S_{12}(\nu)|\rangle$ (in blue). The extracted resonance-positions of the experiment are plotted as blue vertical lines. Underneath the plot, the theoretically calculated eigenvalues are indicated as solid vertical lines for degenerate eigenvalues and as dashed vertical lines for singular eigenvalues. The eigenvalues for the model considering all possible coupling pairs are plotted in red, while the eigenvalues for the model that considers only the coupling between the nearest neighbours (NN) are plotted in black.

compared to the 1D chains, the 2D arrangement of the resonators naturally reduces the distance to the next nearest neighbours. We therefore try to extend our TB model in the most simple way possible to eventually account for next nearest neighbour couplings, by calculating the associated coupling terms with the same functions as for the nearest neighbour couplings that we determined experimentally in section 4.3.3.

Three-pointed star

The first system that we study is a three-pointed star, where one central resonator is symmetrically surrounded by three resonators. A true to scale sketch of the geometry can be seen on the left in figure 4.7. This structure is essentially the basic building block for honeycomb lattices, found for example in graphene nanoribbons and in boron nitride crystals. The system has a 120° rotational and mirror symmetry, i.e. belonging to the point group C_{3v}, that results in degenerate states.

We measure the transmission between a fixed kink antenna placed next to the central resonator and a loop antenna that we move over the different

resonators. For each resonator we measure at 16 equally spaced points on the circumference of a circle with radius $r = 3\,\text{mm}$ centered with respect to the resonator's center, so that we can be sure to not miss any state (by only measuring on its nodal lines). The averaged transmission spectrum can be seen in figure 4.7. We use the harmonic inversion method to extract the resonance-positions of the 8 states. We then compare them to the eigenvalues of the TB Hamiltonian, for the case, where we only consider the nearest neighbour (NN) couplings (plotted as black lines in figure 4.7) and the case, where we consider the coupling between all resonators (plotted as red lines in figure 4.7). For each resonator pair we calculate the coupling using the experimentally found coupling functions presented in figure 4.5.

For the Hamiltonian, where we only consider the nearest neighbour coupling, we find a 4 times degenerate eigenvalue at the center of the spectrum and two two-times degenerate eigenvalues at each end of the spectrum. By additionally considering the couplings between all resonators, the central eigenvalue splits up into two singular eigenvalues and a two times degenerate eigenvalue that remains at the center. While experimentally the degeneracy is slightly lifted for all resonances (either by the fluctuations of the resonance frequencies of the different resonators or simply by the presence of the antennas that break the rotational symmetry, we still find a good overall agreement with the predicted eigenvalues. Whether the model is more accurate by considering all possible resonator couplings is not really possible to tell, since experimentally the degeneracy lift of the central state is only slightly larger than the degeneracy lift for the outer states, which is of the same order as the single resonators resonance frequency fluctuations.

Hexagonal ring

Next we have a look at the system of 6 resonators that form a hexagonal ring. A true to scale sketch of the geometry can be seen in figure 4.8. This structure is closely related to the structure of benzene. The system again has a 120° rotational and mirror symmetry that results in degenerate states.

Similar to the experiment for the three-pointed star, we measure the transmission between a fixed kink-antenna that is placed on the outward facing side of one of the resonators and the movable loop antenna, that move again over several points per resonator. The averaged transmission spectrum can be seen in figure 4.8. We again use the harmonic inversion method to extract the resonance-positions of the 12 states and compare them to the eigenvalues of the TB Hamiltonian for the two cases of considering all possible resonator pairs or only the nearest neighbours, where we again use the coupling functions presented in figure 4.5.

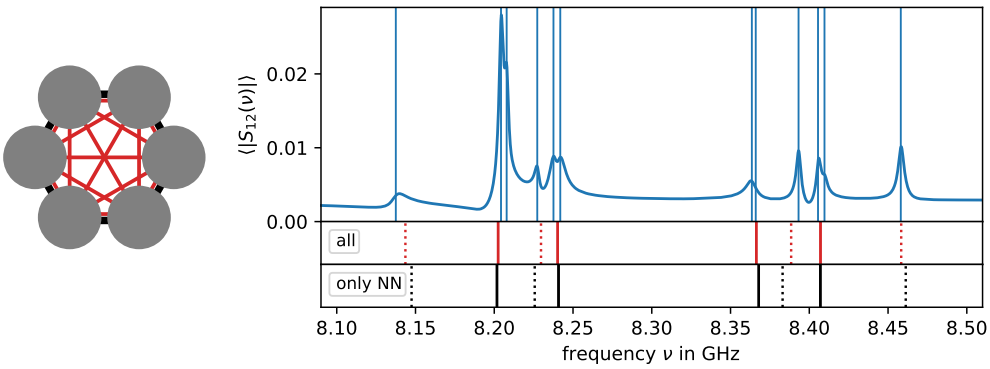

Figure 4.8 – (left) True to scale sketch of hexagonal ring. Resonators are plotted as grey circles while the resonator-pairs that we consider for the theoretical model are marked by lines in between the resonators. All possible pairs are connected by red lines, while the nearest neighbours are connected by black lines. (right) Averaged transmission spectrum $\langle|S_{12}(\nu)|\rangle$ (in blue). The extracted resonance-positions of the experiment are plotted as blue vertical lines. Underneath the plot, the theoretically calculated eigenvalues are plotted as solid vertical lines for degenerate eigenvalues and as dashed vertical lines for singular eigenvalues. The eigenvalues for the model considering all possible coupling pairs are plotted in red, while the eigenvalues for the model that considers only the coupling between the nearest neighbours (NN) are plotted in black.

For the Hamiltonian, where we only consider the nearest neighbour coupling, we find a symmetric spectrum consisting of four two-times degenerated eigenvalues and four singular eigenvalues. By additionally considering the couplings between all resonators, the degenerated eigenvalues remain degenerated, while all eigenvalues shift, some more than other, so that the spectrum becomes asymmetric. This is actually well expected for TB systems, where next nearest neighbour couplings are considered, since the $\mathscr{CT}$ symmetry of the system is broken.

As already seen previously for the three-pointed star, experimentally the degeneracy is again slightly lifted for all degenerate states, but this times it actually seems that the model that considers all possible resonator couplings is slightly more accurate. While the way how we calculate the couplings between all possible resonator pairs (by simply using the experimental coupling functions found for a two-resonator system) is a strong simplification of the actual overlap integrals in between the different resonators, it nevertheless gives qualitatively correct prediction about the direction in which the different eigenvalues get shifted. The overall agreement is good and more quantitative discussion is again not possible, since the found differences between the predicted eigenvalues and the found resonance-positions are of the same order as the single resonators resonance frequency fluctuations.

It thus seems indeed that the derived tight-binding model is well suited in describing systems of multiple coupled resonators. While it was already confirmed for the *s*-mode by many experiments throughout the recent years, it has now also been experimentally shown for the first time using the *p*-mode. With this promising results we will now continue to study more complex systems in chapter 5 and 6.

Chapter 5

1D quasiperiodic structures

After shortly outlining the basic concept of quasiperiodic structures and some interesting properties for waves propagating within such structures, like multifractal wavefunctions and spectra, we introduce the 1D Fibonacci model that we experimentally realize by chains of coupled resonators.

By measuring the systems local density of states (LDoS) we show that the self-similarity is revealed by reorganising the sites according to their local surrounding. We then calculate the fractal dimensions of the measured wavefunctions and find good agreement with theoretical formulations for the multifractality based on a perturbative description in the quasiperiodic limit. Studying different system sizes we are also able to verify recursive construction schemes for the LDoS for the two cases of dominant strong and dominant weak couplings. We end this chapter by presenting qualitative result for other quasi periodic structures, that a part of a generalization of the Fibonacci model to other metallic means, e.g. silver and bronze mean, where we take first steps towards formulating a generalized recursive construction scheme.

Contents

5.1 Quasiperiodic structures and multifractality

Quasiperiodic systems are non-periodic, while still maintaining some kind of order compared to disordered structures. A quasiperiodic lattice can tile all available space, and any subset can be found at some other position within the lattice. While mathematician and physicist Roger Penrose started investigated what will become the famous quasiperiodic Penrose tilings in the 1970s [69], it was only in 1982 that Dan Shechtmann observed unusual diffractograms for a certain aluminium-manganese alloys [70]. For this first revelation of quasicrystal structures in nature, Shechtmann was awarded with the Nobel Prize in Chemistry in 2011. According to the well-known crystallographic restriction theorem, periodic crystals can only exhibit two-, three-, four-, and six-fold rotational symmetries. While amorphous and disordered sample do not produce any sharp peaks in their diffraction pattern, the long range order, self-similarity and orientational symmetries of quasicrystals still produces sharp peaks in their Bragg diffraction pattern [71], but they cannot be associated to the classic crystal symmetries. The five-fold symmetry found by Dan Schechtmann in the diffraction pattern of his sample therefore proved that other symmetry was indeed possible.

For periodic crystals, justified by the use of Bloch theorem, the electronic states are typically extended. In disordered systems on the other hand states are typically localized when their dimension is low and/or their disorder strong enough [72]. Quasicrystals have a kind of intermediate "critical" character, that is very similar to the critical regime in the Anderson transition. In this regard, a lot of theoretical and experimental works have already been done. This transition from weak to strong disorder can be characterized by a multifractal distribution of wave amplitudes in real space and is associated with an anomalous diffusive propagation of wave packets [73–79], where several recent experiments have successfully revealing such a critical regime with multifractal waves[80–83]. Multifractality is used as a generalization for a fractal system, that cannot be described by a single fractal dimension and thus a continuous spectrum of exponents is needed [84]. This is often revealed by the scaling of a generalized fractal dimension D_q with a multifractal parameter q, as we will show in section 5.2.4.

Due to the fact that quasiperiodic structures lack periodicity and translational symmetry, while still showing some order and self-similarity on different scales, they may as well be classified as the transition between ordered and dis-

ordered systems. They therefore also generically have multifractal properties with the particularity of having tunable fractal dimensions[85–89]. Several works have linked these fractal properties of waves to the specific geometrical properties of quasiperiodic lattices (2D tilings and 1D chains) [90–101]. Nevertheless, nearly forty years after the discovery of quasicrystals, there is currently no experiment in real or meta materials that has clearly demonstrated these multifractal properties of waves, even in the simplest and most studied paradigmatic example, the Fibonacci chain [102]. However, a recent experiment using cavity polaritons propagating in a Fibonacci chain structure has succeeded in revealing the fractal character of the eigenfrequency spectrum and also in verifying the gap labeling in agreement with theoretical predictions [103].

As already mentioned the 1D Fibonacci model is the simplest and most studied model in terms of quasiperiodic structures, it therefore is not surprising that we have also decided to experimentally study variations of this system. We will present the first experiment that explicitly demonstrates the existence of a simple recursive scheme to reconstruct the fractal properties of the local density of states of the waves on the Fibonacci chain, where we further quantitatively characterize these multifractal properties and show good agreement between the measured fractal dimensions and theoretical predictions [92].

5.2 The 1D-Fibonacci chain

The Fibonacci 1D Chain is closely linked to the well known series of Fibonacci-numbers F_n, that follow the recursive construction law

$$F_n = F_{n-1} + F_{n-2}, \tag{5.1}$$

for $n \geq 2$, with initial values $F_0 = 0$ and $F_1 = 1$. This results in the series of numbers
$\{F_n\} = 0, 1, 1, 2, 3, 5, 8, 13, 21, 34, 55, 89, 144, ...$, where the ratio $\omega_n = F_{n-2}/F_{n-1}$ converges towards $\omega = \lim_{n\to\infty} \omega_n = (\sqrt{5}-1)/2$. ω is an irrational number and is the inverse of the well known golden ratio.

5.2.1 Fibonacci-sequence by concatenation and substitution

While this series of numbers is interesting on its own, it cannot be used directly to describe crystals or their lattices. In order to link these numbers to a lattice, we replace the sum in the recursive construction law 5.1 with a concatenation operation

$$S_n = S_{n-1}S_{n-2} \tag{5.2}$$

n	C_n	F_n	ω_n
1	B	1	
2	A	1	0/1
3	AB	2	1/1
4	ABA	3	1/2
5	ABAAB	5	2/3
6	ABAABABA	8	3/5
7	ABAABABAABAAB	13	5/8

Table 5.1 – The first six approximants C_n obtained by the substitution rule σ

with $S_1 = B$ and $S_2 = A$ and in the limit of $n \to \infty$ we find a quasiperiodic sequence S, constituted of the different letters A and B.

Another way to obtain such a sequence of letters A and B is by this substitution rule

$$\sigma : \begin{cases} A \to AB \\ B \to A. \end{cases} \tag{5.3}$$

Starting with the letter B and repeatedly applying the substitution rule we find a sequence of letters $C_n = \sigma^n(B)$ of increasing length. The first few C_n are shown in table 5.1. Up to only a permutation, C_n corresponds with the previous defined S_n and both are finite approximants of the quasiperiodic Fibonacci chain, which is obtained in the limit $n \to \infty$. The length of the sequence C_n is equal to the Fibonacci numbers F_n, and the ratio between the number of B and A is given by ω_n.

Additionally to the concatenation and substitution method, there exists another method to obtain the C_n, which is the cut and project (C&P) method.

5.2.2 Cut & Project method

The C&P method can be used to construct quasiperiodic lattice with dimension d (and their periodic approximants). The basic idea is that a d-dimensional quasicrystal may be viewed as the projection of a higher dimensional regular lattice along a d-dimensional cut. The projected points then define the new lattice and the angles under which the higher dimensional grid is cut by the lower dimensional object define whether the resulting lattice is periodic or aperiodic.

We will now use this method to construct all n-th periodic approximants c_n of the Fibonacci chain, up to its quasiperiodic structure for $n \to \infty$. We project the lattice sites within a given interval of a 2D regular grid onto a line that is cutting the grid with a slope ω_n as can be be seen in5.1. The upper

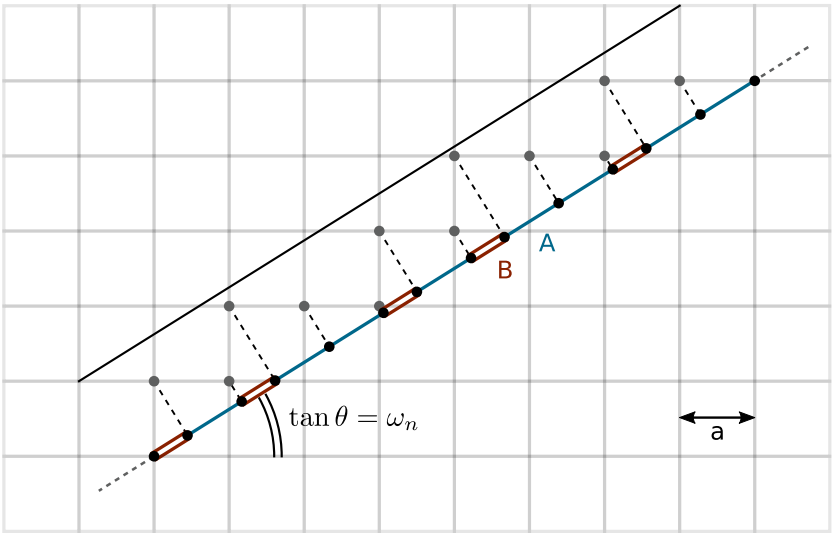

Figure 5.1 – Schema of the C&P method. Selected points of a 2D square lattice are projected onto a line with slope $\omega_7 = 5/8$, yielding to the binary sequence of two different length-interval between the projected points. A short distance, marked as red double binding that is assigned to the letter B and a long distance marked as blue single lines that is assigned to the letter A. While theoretically the resulting c_n is an infinite periodic sequence, for demonstration purposes, we projected only the grid points associated to one basic motif C_7 with length $F_7 = 13$.

line is positioned in such a way, that it delineates an interval encompassing all the grid points at a maximal distance $\sqrt{2}a$ to the cutting line, where a is the lattice constant. The positioning of the interval with respect to the cutting line is not unique (e.g. a symmetric configuration around the line is possible) but will always yield permutation of the same sequence c_n.

The projected points (black points in figure 5.1) divide the line in intervals that only have two different lengths A (blue line) and B (red double-line). For any rational approximation ω_n, the resulting infinite sequence of c_n is periodic with motif length F_n. Due to its rational slope, every F_n points the line will pass exactly through a grid point and the motif is repeated. The basic motifs of c_n correspond to all different permutations of A and B in the sequences C_n or S_n previously defined in section 5.2.1. The c_n are called the periodic approximants of the quasiperiodic Fibonacci-sequence $c = \lim_{n\to\infty} c_n$, that is obtained in the limit of $n \to \infty$ when the slope ω becomes irrational and no repetition occurs.

The off-diagonal tight-binding model

From there, different experimental strategies can be followed to formulate a tight-binding model: either the two letters are associated to two different couplings between resonators, called the off-diagonal model or they are used to account for two different resonant frequencies, called the diagonal-model. We will implement the first one here, thus introducing two coupling, t_A and t_B, or, equivalently, two distances d_A and d_B between the resonators. This experimental choice offers two scenarios: either $\rho = t_A/t_B > 1$, that corresponds to the dominant strong coupling scenario, or $\rho = t_A/t_B < 1$, the dominant weak coupling scenario. The main part of the study reported here will make use of the second scenario, but we will show at the end that inverting ρ yields interesting results too.

Conumbering

Compared to the construction of the Fibonacci sequence by concatenation or substitution, with the C&P method one additionally obtains further information about the system. This information is accessible by the projection of the grid points onto the axis that is orthogonal to the cut. As one can see in figure 5.2, the sites projected onto the perpendicular axis occupy equally spaced and reordered positions: The sites whose projection on the horizontal axis are surrounded by two A intervals (further referred to as atomic sites, since they are surrounded by two weak couplings) are clustered around the center, whereas those embedded in ABA sequences (further referred to as molecular

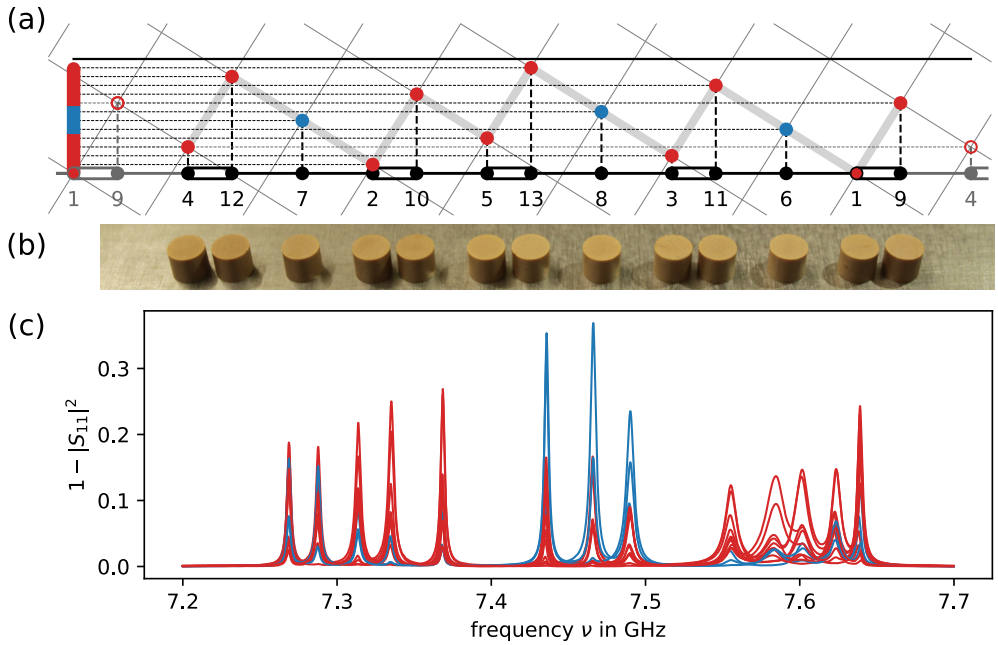

Figure 5.2 – (a) Cut and project method, for $\omega_7 = 8/5$, but additionally with the projections onto the perpendicular axis. In the off-diagonal TB Fibonacci model, the projection on the horizontal axis dictates the arrangement of the sites of the chain according to strong (black double-line) and weak (black line) couplings. Each site nomenclature is reordered according to its local environment on the perpendicular (vertical) axis, the resulting conumber $c(i)$ is indicated under each site at position i. Along the perpendicular axis, "atomic" (in blue) and "molecular" (in red) sites are clustered in 3 groups. (b) Photo of an experimental Fibonacci chain made of 13 resonators. (c) Measured reflection spectra $1-|S_{11}|^2$ for each resonator in the chain shown in (b), where the colors differentiate the atomic (blue) and molecular (red) sites.

sites, due to the strong coupling in between the sites) are grouped outside the center – at the bottom for the sites between *AB* and at the top for *BA*.

This way of referring to the sites not by their index i, that orders them according to their position within the chain, but by the order $c(i)$ of the projections onto the perpendicular axis [see figure 5.2(a)] is called conumbering and was first introduced by Mosseri et al [104, 105].

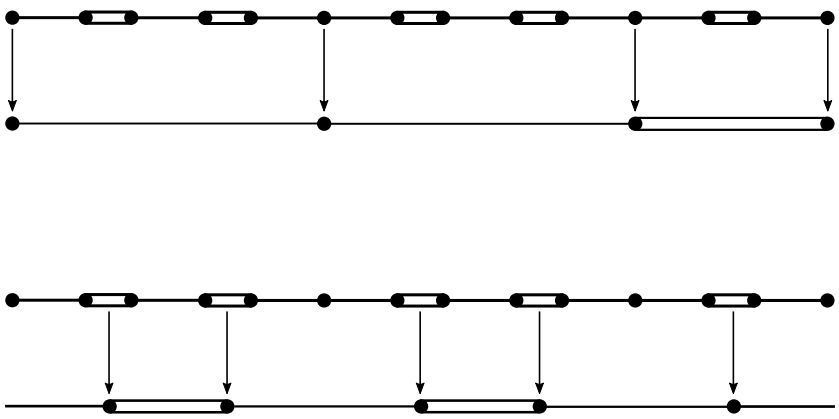

Figure 5.3 – (top) *atomic deflation* The 7th approximant (presented as a permutation that starts and ends with a weak coupling) is transformed into the 4th approximant. (bottom) *molecular deflation* The 7th approximant is transformed into the 5th. (figure reproduced from [92])

Renormalization scheme to show the equivalence of conumbers and frequencies

To further understand the role of the conumbers $c(i)$, we will now describes the basic idea behind the perturbative renormalization scheme, first introduced by Kalugin, Kitaev and Levitov [106] and independently by Niu and Nori [99].

The renormalization scheme is formulated in the strong modulation regime $\rho \ll 1$. When $\rho = 0$ ($t_A = 0$), the atoms and the molecules decouple and the spectrum consists of three degenerate levels: $\nu = \pm t_B$, corresponding to molecular bonding and anti-bonding states, and $\nu = 0$, for the isolated atomic state. For a chain of $N = F_n$ sites, the degeneracy of the $\nu = 0$ level is given by the number of atomic sites, F_{n-3}. The degeneracy of the $\nu = \pm t_B$ levels is given by the number of molecules F_{n-2}. When ρ is non-zero, but still small, the states in these three degenerate levels couple weakly to each other, therefore lifting the degeneracy. Before we have a detailed look on how the atomic sites and molecular sites couple separately, we can draw a first connection between the arrangement of states in the frequency domain and the clustering of states by conumbering. In both cases atomic states/sites are at the center, while molecular states are on the sides.

For the atomic sites and states, at first order, each atomic energy level, localized on an atomic site couples to the atomic levels localized on the two neighboring atomic sites (figure 5.3). Within perturbation theory, the effective bond coupling between any two neighboring atomic sites takes only two

possible values, a strong and a weak one, that are arranged according to a Fibonacci sequence. The atomic frequency level is therefore split up into 3 levels again. A central level associated with the atomic sites that couple via the weak effective coupling and two levels at the sides, associated to the atomic sites that couple via the strong effective coupling. In a similar fashion, any state localized on a molecular site, is coupled to the neighboring molecules through only two possible effective couplings, that themselves also follow a Fibonacci sequence and the molecular levels also split up in three sub-levels.

This consecutive deflation of the chain can be repeated until the chain is fully deflated. When the values of the effective couplings are known, the full spectrum of the Fibonacci-chain can be obtained. Similar to how the atomic and molecular states couple via their effective bonds and the spectrum is split up, the conumbering orders the sites within the molecular and atomic cluster further by their local environment. It is therefore not surprising that the more isolated atomic site (the left most) is at the center of the atomic cluster with $c(i) = 7$, while the two other sites form the "molecule" of the atomic sites, being closer to each other and are therefore at the side of the atomic cluster with $c(i) = 6$ and $c(i) = 8$. It becomes clear that in the conumber index $c(i)$ the sites are ordered in exactly the same way as the frequency bands.

Before we start building longer chains in the next section, we measure a short chain of 13 resonators using the direct pattern created by the C&P procedure, to illustrate this equivalence of the frequency index j of states and the conumbering $c(i)$ of sites. A picture of the chain can be seen in figure 5.2(b). In this case, as it is the case for the main part of this section, the dominant weak coupling regime is implemented. Since a chain of 13 resonators only has 12 couplings in between the nearest neighbours, the last weak coupling is suppressed. This ensures that the chain only ends on a strong coupling and there are no localized edge states. This procedure has also the advantage that the experimental chain reproducing an elementary motif of a c_n Fibonacci-approximant generates F_n collective resonance peaks, as can be seen in the spectra plotted on figure 5.2(c), where each spectrum is measured individually by the movable loop antenna placed directly over each resonator. The spectra measured at molecular site positions are plotted in red, and in blue for atomic sites. Indeed, one can clearly see that the three resonances within the central band are mainly localized on atomic sites, while the two side bands are dominated by states located at the molecular sites.

5.2.3 Revealing the self-similarity using conumbers

We want to realize the highest approximant, where we can still extract the wavefunctions of the system. We therefore chose to implement the 10th

approximant with a motif length of $F_{10} = 55$, since for the next higher approximant the spectrum becomes to dense in some frequency ranges to resolve all states anymore. The c_n are actually periodic sequences of infinite length. In order to still investigate the system with finite size chains, we limit the chains to a single motif C_n with size F_n, but realize all possible permutations of the basic motif C_n. Since generally linear chains of length N only have $N-1$ couplings, we are confronted with the choice whether to use $F_{10}+1 = 56$ resonators, so that we would have $F_{10} = 55$ couplings, as defined by the single motif C_n, or to use $F_{10} = 55$ resonators, which would result in neglecting a coupling of the sequence. Both approaches will suffer equally from localized edge states, we thus decide us for the latter, since in this case at least the number of resonances/states will still correspond to the number of bands, that one expects for the infinite long approximant c_n. We further decide to neglect only weak coupling links and constrain the experiment to permutations that impose that the elementary chain ends on both sides by a strong coupling. This should get rid of strongly localized edge states at the two ends of the chain [1]. In practice, for a motif of $F_{10} = 55$ resonators, in the dominant weak coupling regime ($\rho < 1$), there are 8 different permutations that start and end on a strong coupling.

We measure the spectrum over each resonator for all permutations for the coupling strengths $t_A = 81\,\text{MHz}$ and $t_B = 126\,\text{MHz}$, corresponding to distances $d_A = 8\,\text{mm}$ and $d_B = 7\,\text{mm}$. The relation between coupling strength t and separation d that we use was extracted from a two resonators measurements (see section 4.2.1). We chose these values in order to have the least possible overlap between resonances in the spectra, while keeping $\rho = 0.64$ as small as possible, for the best visible contrast. A picture of one configuration can be seen in figure 5.4(a) and the spectrum measured above the center of the resonator at position $i = 33$ of this permutation can be seen in figure 5.4(b). Here one can clearly observe the overlapping between resonance peaks, which would make it impossible to study higher order approximants or system with smaller ρ, since for smaller ρ the frequency-gaps would become greater and there-

1. Limiting the permutations to those, that start and end on a strong coupling does not completely get rid of localized states. Actually any permutation has states that are spectrally localized in the band-gaps of the infinite long approximant c_n. While neglecting those permutations that end on weak couplings gets rid of the strongly localized states that are expected to be spectrally localized within the large band-gaps, we expect to find localized states in the smaller band-gaps for all remaining permutations. While we cannot spectrally resolve these smaller band gaps, clear evidence of these remaining localized states can be found in figures B.3-B.5 in Appendix B.1 (under the form of a few very bright pixels), where we present the individual measurements for the different permutations. Nevertheless, the averaging over the different permutations seems to effectively reduce these remaining localization/edge-state effects, as can be seen in figure 5.5 and further in chapter 5.2.4, where we compare quantitative calculations of the fractal dimensions to analytic formulations.

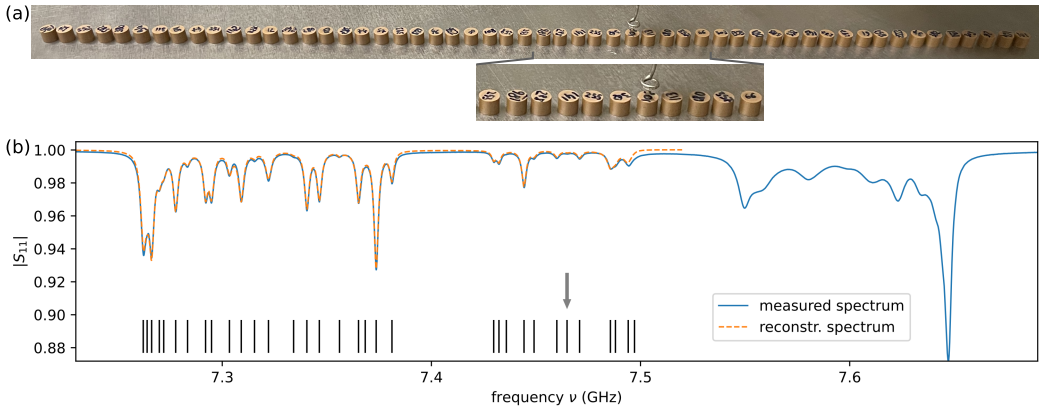

Figure 5.4 – (a) picture of the experimental chain for a given configuration in the case of dominant weak coupling ($\rho = t_A/t_B < 1$). The metallic top plate that is normally placed above the resonators to reduce the system to two dimensions was removed to take the picture. Above the resonator at position 33 (counted from the left) we position the loop antenna through which we measure the reflection spectra above each resonator. (b) reflection spectrum measured at position 33 and the reconstructed spectrum using the resonances obtained via the harmonic inversion method. The black vertical lines mark the extracted resonance positions and the grey arrow marks the central state ($j = 28$), around which we symmetrize the LDoS(i, j) in order to span the whole frequency range.

fore the bands more densely packed with resonances. For all permutations, we extract all resonance amplitudes $\psi_j(i)$ of each peak j of the measured spectrum [2] above resonator i with the harmonic inversion method and a density-based clustering algorithm [60]. In this way we can obtain a discretized form of the local density of states LDoS$(i, j) = |\psi_j(i)|^2$, where $|\psi_j(i)|^2$ represents the wavefunction intensity of state j evaluated over resonator i.

While a detailed description of the procedure from raw-data to final wavefunctions can be found in Appendix B.1, in figure 5.4 one can see the partial reconstruction of the spectrum using resonance-amplitudes and -frequencies obtained with the harmonic inversion algorithm, where the black vertical lines are indicating the extracted resonance frequencies. The quality of the reconstruction is excellent. We limit the reconstructed spectrum to the lower and central frequency bands only, since the higher frequency states have larger resonance-widths due to different effective antenna-couplings and larger ohmic losses, and even with the harmonic inversion method, we cannot resolve them anymore. If only nearest-neighbour couplings are present, the system has a CT-

2. The index j is the frequency-index of a state and orders the states as a function of their resonance-frequency

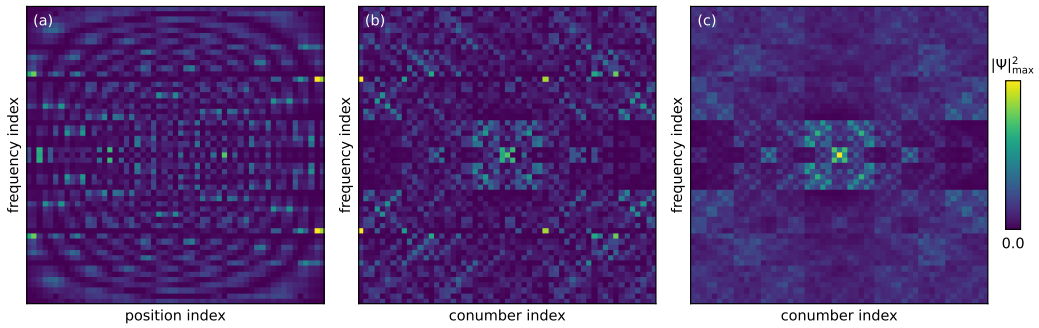

Figure 5.5 – Experimentally extracted LDoS of a single configuration of 55 resonators arranged according to their position index i (a), rearranged according to the conumber index $c(i)$ (b) and the average over all 8 permutations (c).

symmetry [107] imposing that the spectrum is symmetric around the eigenfrequency of a single resonator. In our experiment we have a next-nearest-neighbour coupling of the order of 5 % of the nearest-neighbour coupling. By consequences, the latter symmetry is almost preserved. We thus restrict our analysis to the first 28 states (the 28th state is the central state and indicated by a gray arrow in figure 5.4) and symmetrize the result to expand over the higher-frequency states. Theoretically the eigenvectors c_i^j of the tight-binding Hamiltonian are normalized in both direction ($\sum_i |c_i^j|^2 = \sum_j |c_i^j|^2 = 1$), the experimentally extracted LDoS(i,j) should then also be normalized along both the frequency and position axis ($\sum_i \text{LDoS}(i,j) = \sum_j \text{LDoS}(i,j) = 1$). Since the antenna-coupling σ is slightly dependent on the frequency and the single resonance wavefunctions are overlapping, the sum of the raw resonance amplitudes over all positions (states) vary about 10 percent for different states (positions). We thus normalize the extracted wavefunction intensities in both dimensions by repeatedly normalizing them along one direction and then the other, until the difference in normalization along the two directions is of the order of 10^{-6}. We then consider that the extracted LDoS(i,j) is properly normalized along the two dimensions, which is especially important for the calculation of the fractal dimensions.

Figure 5.5(a) shows the local density of states LDoS(i,j) extracted and normalized according to the procedure described above for a single configuration of a chain made with 55 resonators. Figure 5.5(b) shows a rearranging of the LDoS according to their conumber: LDoS$(c(i),j)$, and (c) the average over the 8 permutations identified in this situation of dominant weak coupling. In figure 5.5(a), LDoS exhibit typical standing-wave interference patterns due to the finite-size of the chain[44], but no hierarchical structure is visible. It is only upon the reordering the LDoS based on the conumber index that we

gain insight into fractal structures, that are completely revealed by the average over all permutations [see figure 5.5(c)]. Additionally the symmetry between frequency index j and conumber index $c(i)$ is clearly visible: The plot in figure 5.5(c) is almost invariant under the exchange of the conumber/frequency axis.

5.2.4 The multifractal dimension of wavefunctions

In order to give a more quantitative characterization of the fractality, and especially the multifractal aspect of the wavefunctions, we investigate the fractal dimensions $D_q^{\psi}(j)$ of the wavefunctions [92], that are defined via an exponential scaling of the generalized inverse participation number with the motif length F_n as follows

$$\chi_q^{(n)}(j) = \sum_i |\psi_j^{(n)}(i)|^{2q} \underset{n\to\infty}{\sim} F_n^{-(q-1)D_q^{\psi}(j)}. \tag{5.4}$$

For systems that exhibit multifractal wavefunctions like quasicrystal or disordered systems at criticality, the fractal dimensions $D_q^{\psi}(j)$ decrease when q increases. This property is related to the fact that the region with high wave function probability are rarer [77, 78].

One can further define the frequency-averaged fractal dimension of wavefunctions $\overline{D_q^{\psi}}$ by averaging over all states [92]

$$\left\langle \chi_q^{(n)}(j) \right\rangle_j = \frac{1}{F_n} \sum_j \chi_q^{(n)}(j) \underset{n\to\infty}{\sim} F_n^{-(q-1)\overline{D_q^{\psi}}}. \tag{5.5}$$

In order to investigate the scaling behaviour as a function of the system size one would have to perform the experiment for different system sizes F_n, which is impractical in our case, because the maximal possible system size in order to resolve all wavefunction is 55, which is far from the quasiperiodic limit. Fortunately there is another approach that is commonly used to calculate (fractal) dimensions in various fields of physics and mathematics, which is a box-counting algorithm that we apply on the LDoS$(c(i), j)$ presented in figure 5.5(c). The method that we use and present in the following section has already proven itself in the characterization of chaotic system and multifractal wavefunctions at critical transitions and in quasiperiodic structures [74, 76, 88, 108].

Calculation via a box-counting algorithm

The main idea behind the box-counting method is to divide the system into small "boxes" and analyse them individually. By changing the box size and con-

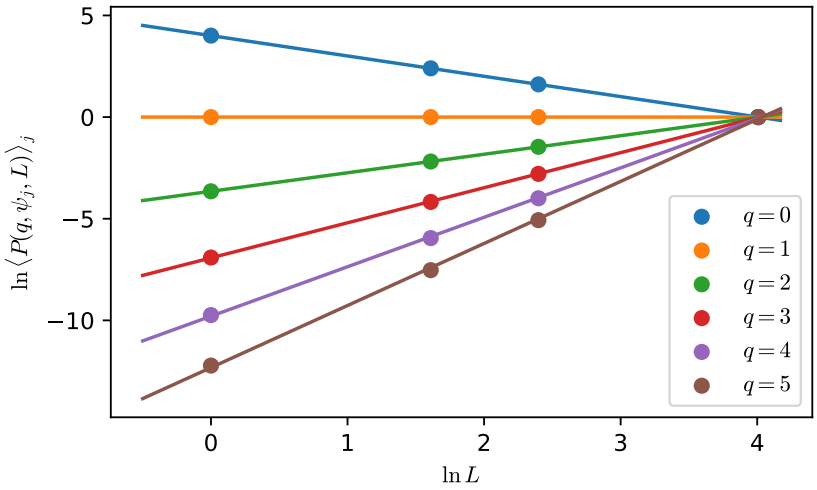

Figure 5.6 – Calculated $\ln\left\langle P(q,\psi_j,L)\right\rangle_j$ for the different box sizes L and some example values of q. For each q the data points are fitted individually (solid lines), in order to extract their slope.

sidering smaller and smaller boxes, one can thus deduce scaling properties for the system. We use in the following the notations and formalism presented in reference [108]. We start by dividing our system of size F_n into $B = F_n/L$ boxes of size L. Since the system is one dimensional the boxes are actually intervals of length L. We then study the spatial distribution of each wavefunction $\psi_j(i)$ by calculating the probability

$$\mu_b(\psi_j, L) = \sum_{i \in \text{box } b} |\psi_j(i)|^2 \tag{5.6}$$

to find a “ball" inside box b. Repeating this procedure for different box-sizes L, one can then compute the mass exponent

$$\tau_q = \lim_{L\to 0} \frac{\ln\left\langle P(q,\psi_j,L)\right\rangle_j}{\ln L/N} = \lim_{L\to 0} \frac{\ln\left\langle \sum_{b=1}^{B} \mu_b(\psi_j,L)^q\right\rangle_j}{\ln L/N} \tag{5.7}$$

by performing a linear fit of the spectrally averaged quantity $\ln\left\langle P(q,\psi_j,L)\right\rangle_j$ versus $\ln L$ and extracting the slope. For our system of size $F_n = 55$, we consider all box sizes $L = 1, 5, 11, 55$ with integer ration F_n/L. In figure 5.6 we plot and fit $\ln\left\langle P(q,\psi_j,L)\right\rangle_j$ versus the box-size $\ln L$ for some typical values of q. We find an excellent agreement between the data points and fit. From the mass exponents τ_q one can then easily obtain the spectrally averaged fractal dimension $D_q = \tau_q/(q-1)$.

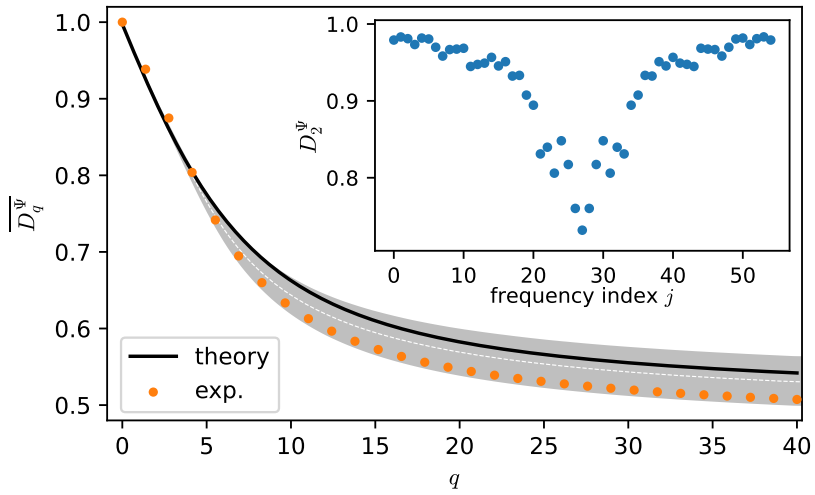

Figure 5.7 – Frequency averaged fractal dimension $\overline{D_q^\psi}$ versus the multifractal parameter q, experimentally extracted using a box-counting method (orange points) compared to theoretical predictions (solid black line). The grey area highlights the 90 % confidence interval obtained from tight-binding simulations (see Appendix C.1 for details), the dashed line indicates the mean expectation value. The inset shows $D_2^\psi(j)$ for all states j.

Comparison to analytic and numeric results

In figure 5.7 one can see the extracted frequency-averaged fractal dimension $\overline{D_q^\psi}$ as a function of the multifractal parameter q (orange points). The inset shows the fractal dimensions, $D_2^\psi(j)$ for all states j, which is proportional to the logarithm of the inverse participation ratio. There are large fluctuations with respect to the mean value with a very distinct dip for the central state. Thus, the central state is the most localized and has the lowest fractal dimensions, while the highest/lowest states are the most extended ones.

We compare the frequency-averaged fractal dimension $\overline{D_q^\psi}$ obtained experimentally with a theoretical prediction based on a renormalization group approach, formulated in the limit $\rho \ll 1$ and developed until the order ρ^{4q} [92]; in the experiment $\rho = 0.64$. We further estimate a 90 % confidence interval for the experiment, by performing tight-binding simulations of the system that account for the variances in the positioning of the resonators and the fluctuations of their resonance frequency. Details on the procedure can be found in Appendix C.1. Although far from the strong modulation limit ($\rho \ll 1$), a good agreement between experimental and theoretical values of $\overline{D_q^\psi}$ is ob-

tained, both curves lie within the estimated confidence interval (see figure 5.7). For large q, an offset is noticeable between theory and experiment, that could eventually be explained by experimental fluctuations, but even the average value of the simulated $\overline{D_q^{\psi}}$ (white dashed line) shows an offset. This is mainly due to the finite system size, since the theory was formulated in the quasiperiodic limit, as we demonstrate in Appendix C.2, where we numerically study the convergence for increasing order n. Note that, although equation (5.5) is invariant to inverting index $c(i)$ and j, our method to calculate $\overline{D_q^{\psi}}$ via a box counting algorithm is not. Nevertheless, interchanging the conumbering index $c(i)$ with the frequency index j upon the calculation of $\overline{D_q^{\psi}}$ leads to two hardly distinguishable curves (not shown in figure 5.7), further emphasizing the equivalence between conumbers and frequencies.

5.2.5 The recursive construction of the LDoS

Another aspect often refereed to fractality is the self similarity of structures [90, 91, 93, 94, 96–98]. Similar to the recursive construction of the Fibonacci numbers F_n, the complete LDoS can be constructed recursively. The procedure is based on the renormalization of atomic and molecular sites [92]

$$|\psi_j^{(n)}(c_i)|^2 = \overline{\lambda} \cdot |\psi_{j'}^{(n-3)}(c_{i'})|^2 \quad \text{if } j \text{ is atomic,} \tag{5.8}$$

$$|\psi_j^{(n)}(c_i)|^2 = \lambda \cdot |\psi_{j'}^{(n-2)}(c_{i'})|^2 \quad \text{if } j \text{ is molecular,} \tag{5.9}$$

where $\overline{\lambda}$ and λ are renormalization factors that depend on ρ.

We investigate this recursive construction by experimentally realizing the first periodic approximants (i.e. $F_n = 3, 5, 8, 13, 21$). Due to the small F_n and thus the lower number of possible permutations, we here now employ a different strategy to mimic the periodic approximants c_n, than in section 5.2.3, where we averaged over the different permutations of the basic motif of length 55. We use circular chains, where we repeat the basic motif C_n of length F_n N_p times. Since the circular chains are closed, the number of couplings now corresponds to the number of resonators $N = F_n N_p$ and peaks in the spectrum. The number of iteration N_p is chosen such that a ring of around 100 resonators is build for each F_n-motif. In figure 5.8 one can see a photo of the circular chain of resonators for a motif length of $F_n = 13$, that was repeated 8 times.

Extracting the LDoS$(c(i), j)$ for the circular chains

Compared to the linear chains, where we have been able to identify each state individually and extract its wavefunction, we employ a different approach

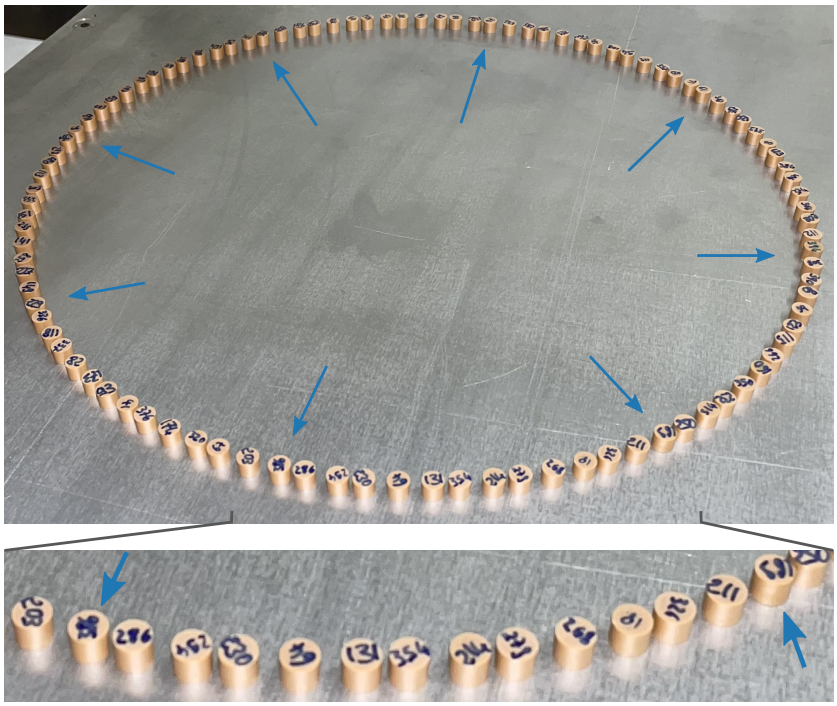

Figure 5.8 – (top) Photo of one circular chain, where the basic motif with length $F_n = 13$ is repeated $N_p = 8$ times, resulting in a total of 104 resonators. To emphasize the periodicity the first resonator of each repeated motif is marked with a blue arrow. (bottom) Zoomed in photo of one motif, where one can identify the "molecules" (dimers) and "atoms" (single resonator) that make up the chain.

to extract the LDoS$(c(i), j)$ of the measurement. Since over 100 resonances are to much even for the harmonic inversion method to identify the individual states, we instead extract averaged values for equivalent states and sites resulting from the repetition of the basic motif. Due to the N_p repetitions, the F_n frequency bands expected for an infinite chain c_n are each populated with N_p states, and can be individually identified in each reflection spectrum $S_{11}(\vec{r}_i, \nu)$ measured over each resonator i. We can recall from section 2.3.3

$$1 - \Re S_{11}(\vec{r}_i, \nu) \propto \rho(\vec{r}_i, \nu) = \sum_{k}^{N} f_{\nu_k,\Gamma_k}(\nu) \cdot |\psi_k(\vec{r}_i)|^2, \tag{5.10}$$

where $f_{\nu_n,\Gamma_n}(\nu)$ are normalized Cauchy distributions around ν_n with width Γ_n. Rearranging the sum over the different states, one can re-write

$$\rho(\vec{r}_i, \nu) = \sum_{j=1}^{F_n} \sum_{p=1}^{N_p} f_{\nu_{j,p},\Gamma_{j,p}}(\nu) \cdot |\psi_{j,p}(i)|^2, \tag{5.11}$$

where $\nu_{j,p}$ and $\Gamma_{j,p}$ are the resonance-frequency and -width of the p-th state within the j-th frequency band and $|\psi_{j,p}(i)|^2$ the corresponding wavefunction intensity measured over resonator i.

Supposing that the bands are sufficiently isolated, by integrating each frequency band j individually, one can then find

$$\mathrm{LDoS}(i,j) \propto \int_{\text{band } j} [1 - \Re S_{11}(i,\nu)]\,\mathrm{d}\nu, \tag{5.12}$$

where we can further average over all indices i that have the same conumbering $c(i)$. Essentially each n-th site in each of the N_p repetitions of the basic motif are equivalent and have the same conumber, since they have exactly the same (local) environment. Unlike the procedure for linear chains, we do not need to symmetrize our results since this approach allows to analyse the whole frequency range, but we still use the same procedure to assure the normalization of the LDoS.

Compared to the linear chains, where the lowest overlap was sought after in between the individual resonances, we now want to create F_n energy bands that are as dense as possible, while having the greatest gaps in between them, so we can easily identify each band. We therefore enhanced the stronger coupling to $t_B = 148\,\mathrm{MHz}$ and reduced the weaker coupling to $t_A = 55\,\mathrm{MHz}$, in order to obtain a smaller $\rho = 0.37$ and thus better isolated bands. Experimentally this was done by increasing the longer distance d_A to 9 mm (we keep the shorter distance at 7 mm) and by reducing the distance between the two metallic plates that sandwich the resonators from $\approx 12\,\mathrm{mm}$ to 8 mm. This alters the evanescent decay of the electromagnetic fields outside of the resonators.

Determining the integration borders of each band is obvious for $F_n = 3$ and 5, where the 3 or 5 frequency bands are isolated and well separated by clearly visible gaps. Unfortunately even with the improved coupling values, for higher n the direct identification of all frequency-bands, and therefore the determination of integration borders is not possible and we use a method bases on the normalization of each state, to further define the integration border for bands that are not separated by a clear gap. Further information on this method and a details step by step illustration of the whole data treatment process from spectrum to final LDoS can be found in Appendix B.2.

In figure 5.9 we present the LDoS for the first approximants. Especially highlighted for $F_{10} = 55, F_8 = 21$ and $F_7 = 13$ (Fig. 5.9(f), (e) and (d), respectively], the central square (marked in red), which gathers atomic sites and their corresponding states, of the LDoS at order n resembles at the complete LDoS of order $n-3$, and the four squares in the corners (molecular sites and frequencies, one marked in green) of the LDoS at order n resemble at the complete

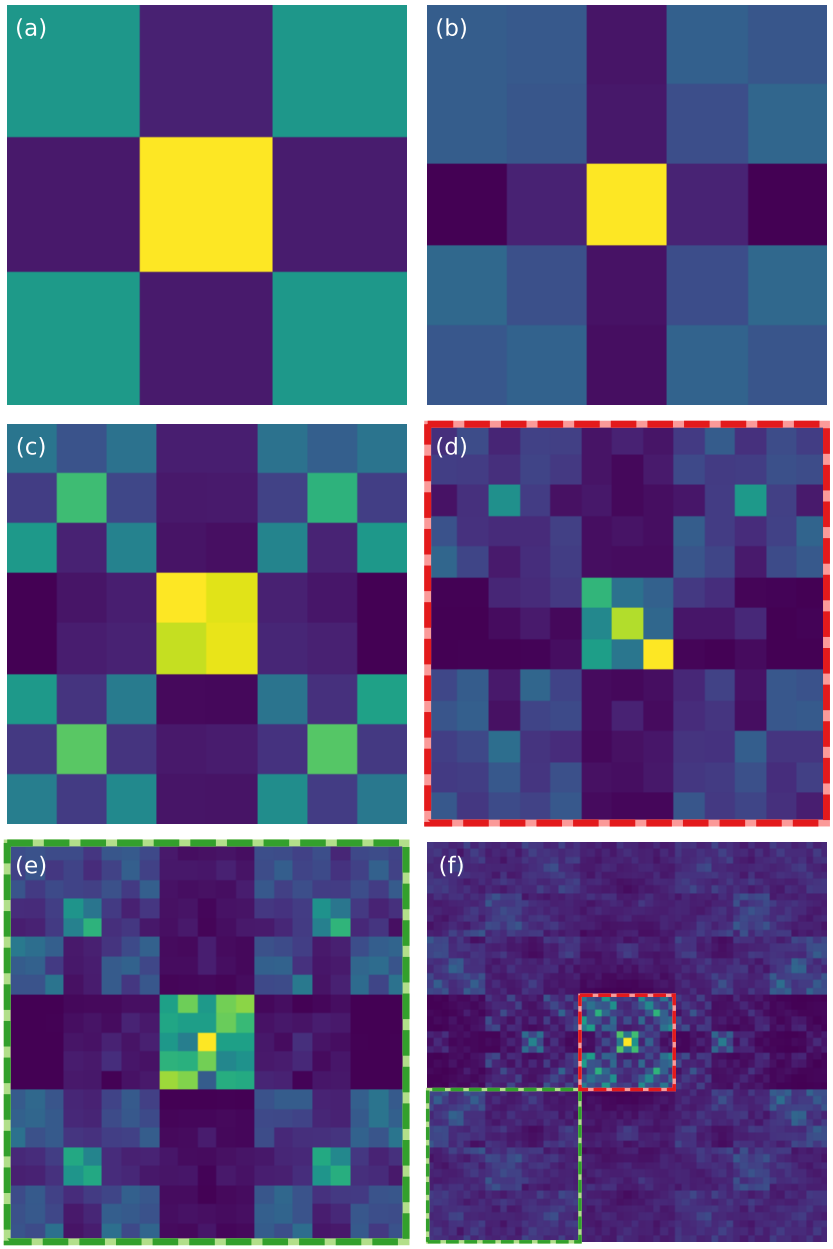

Figure 5.9 – Conumber-averaged LDoS for different motif length F_n: (a) $F_4 = 3$, (b) $F_5 = 5$, (c) $F_6 = 8$, (d) $F_7 = 13$, (e) $F_8 = 21$ and (f) $F_n = 55$ (already presented in figure 5.5). For all plots the horizontal axis corresponds to the conumber index $c(i)$ and the vertical axis to the frequency index j, and the same colormap as in figure 5.5 is used. The green and red squares highlight the recursive construction.

LDoS of order $n-2$. The recursive construction is also well visible for smaller n. This recursive construction can be well explained by the renormalization scheme outlined in section 5.2.2. The effective bond couplings between atomic and molecular sites themselves follow a Fibonacci sequence that explains the self similarity of the internet structure within the atomic and molecular clusters.

Renormalization factors $\lambda(\rho)$ and $\tilde{\lambda}(\rho)$

As a next step we now calculate the renormalization factors λ and $\tilde{\lambda}$, that are used to define the recursive construction laws in (5.8) and (5.9). The two renormalization factors depend on the ratio of the coupling strength ρ,

$$\tilde{\lambda}(\rho) = \frac{2}{(1+\rho^2)^2 + \sqrt{(1+\rho^2)^4 + 4\rho^4}} \tag{5.13}$$

and

$$\lambda(\rho) = \frac{1}{1+\rho^2\gamma(\rho) + \sqrt{1+(\rho^2\gamma(\rho))^2}} \tag{5.14}$$

with $\gamma(\rho) = 1/1(1+\rho^2)$[92].

In order to experimentally estimate the renormalization factors we make use of the fact that the sum over all states and positions of the LDoS for a system with motif length F_n, sums up to F_n because each of the F_n states were properly normalized ($\sum_i |\psi_j(i)|^2 = 1$).

We can thus sum up all the pixels that contribute to the central square of the LDoS (corresponding to atomic sites and states) and divide it by the side length of that square (i.e. the number of atomic sites within the chain) to find the renormalization factor $\tilde{\lambda}$ for the atomic sites/states. For the molecular sites/states we proceed in the same way, but additionally we average over the four corner squares (corresponding to molecular sites and states).

Since we have chosen to use different couplings for the linear chains and the circular chains, we experimentally can investigate the renormalization factor for two different values of ρ: $\rho = 0.64$ for the linear chains of $F_n = 55$ resonators and $\rho = 0.37$ for the circular chains with smaller motif length. In figure 5.10 one can see the two theoretical curves for $\lambda(\rho)$ and $\tilde{\lambda}(\rho)$ as a function of ρ, that we compare to the experimentally extracted values (black symbols).

The experimentally extracted renormalization factors $\lambda(\rho)$ and $\tilde{\lambda}(\rho)$ correspond reasonably well with their theoretical prediction, though the extracted $\lambda(\rho)$ for the molecular sites vary for the different motif length F_n and generally show a slight offset. This can be explained by the small system sizes F_n, since the theoretical predictions were formulated in the quasi periodic limit.

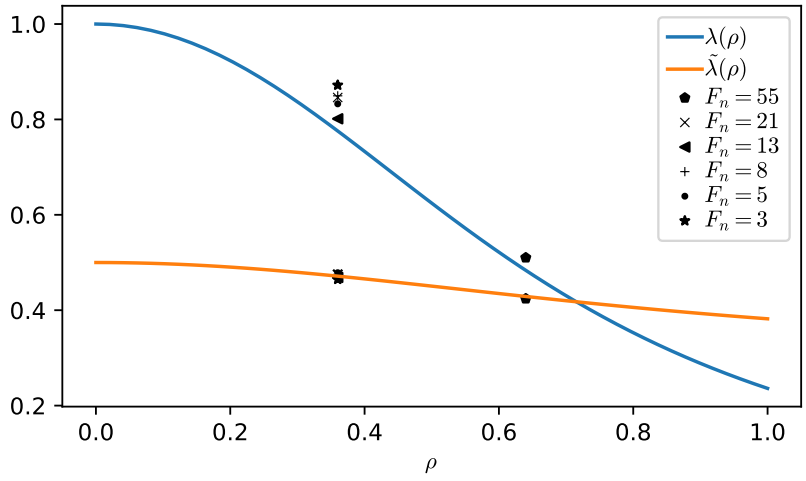

Figure 5.10 – The theoretical renormalization factors λ (blue line) and $\tilde{\lambda}$ (orange line) as a function of ρ. The experimentally extracted renormalization factors for the different motif lengths F_n are plotted at their corresponding ρ with different black symbols.

5.2.6 Inverted weak and strong couplings

Although we have mainly focused our quantitative analyses on the common case of $\rho < 1$, we also experimentally investigate the system with interchanged couplings: t_B is now the weaker coupling and t_A the stronger, $\rho > 1$, thus the strong coupling dominates. As for the system with $\rho < 1$ we investigate the large system ($F_n = 55$) by averaging over the 21 different permutations that meet the constraints, and smaller systems by means of circular chains. Note that over the 21 possible permutations, 10 of them are actually mirrored sequences of the others. Since they are experimentally equivalent, we measure only the 11 different permutations that are not mirrored sequences of each other, but average over all 21 permutations by inverting the position axis for the mirrored ones. The averaged LDoS can be seen in figure 5.11. Instead of single atoms and dimers, as for $\rho < 1$, the chains are now composed by dimers and trimers. This results in a different renormalization scheme [99].

For vanishing weak coupling ($t_B = 0$), the dimers and the trimers decouple and the spectrum consists now of five degenerate levels: $\nu = \pm t_A$, corresponding to molecular bonding and anti-bonding states, and $\nu = 0$, $\nu = \pm\sqrt{2}t_A$ corresponding to the central and bonding and anti- bonding states of the timers. Similarly the sites can be clusters in 5 clusters, according to their conumbers. From small to large conumbers: The right atoms of trimers, the right atoms of dimers, the central atom of trimers, the left atoms of dimers and the left

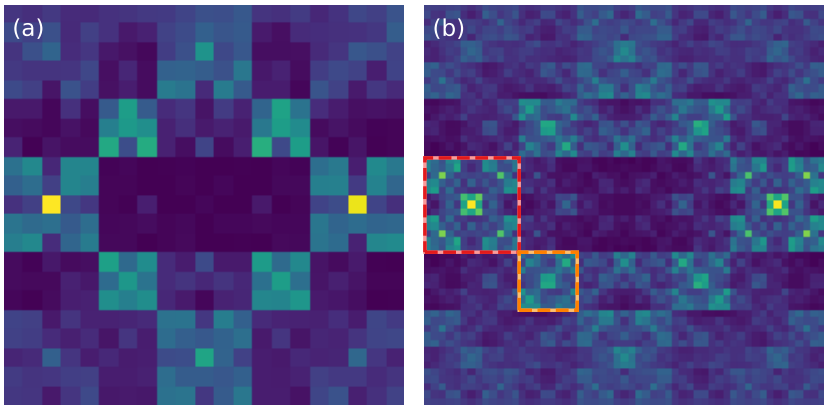

Figure 5.11 – LDoS for motif length $F_8 = 21$ (a) and $F_{10} = 55$ (b) for $\rho > 1$. The x-axis corresponds to the conumber index $c(i)$ and the y-axis to the frequency index j and the same colormap as in figure 5.5 is used. The red and orange square highlight the basic motifs.

atom of trimers. This again reveals the equivalence between conumbers and frequencies, since in both cases dimer and trimer states/sites are arranged the same way.

When t_B is non-zero, but still small, the states in these five degenerate levels couple again weakly to each other, therefore lifting the degeneracy. As can be seen in figure 5.12, the effective bond couplings between two neighboring trimers take on only two possible values, arranged again according to a Fibonacci sequence but with inverted strong and weak couplings. One thus passes from the chain c_n to the chain c_{n-3} with $\rho \to 1/\rho$ when appropriately renormalizing their couplings. In the same way one passes from the chain c_n to the chain c_{n-4} again with $\rho \to 1/\rho$ for the dimers. All further deflation steps then follow the renormalization laws for $\rho < 1$. This explains why the general structure in figure 5.11 is quite different, but we find the same basic motifs as in figure 5.9. The red square in figure 5.11(b) highlights the basic motif associated with the trimers, that can be found in figure 5.9(d,f), while the orange square highlights the basic motif associated with the dimers, which again can be found in figure 5.9(c).

5.3 Other metallic means

The Fibonacci Chains are part of a greater family of quasicrystals, known as the metallic mean chains. Similar to how the Fibonacci chains are related to the golden mean, the other chains of this family are related to the other

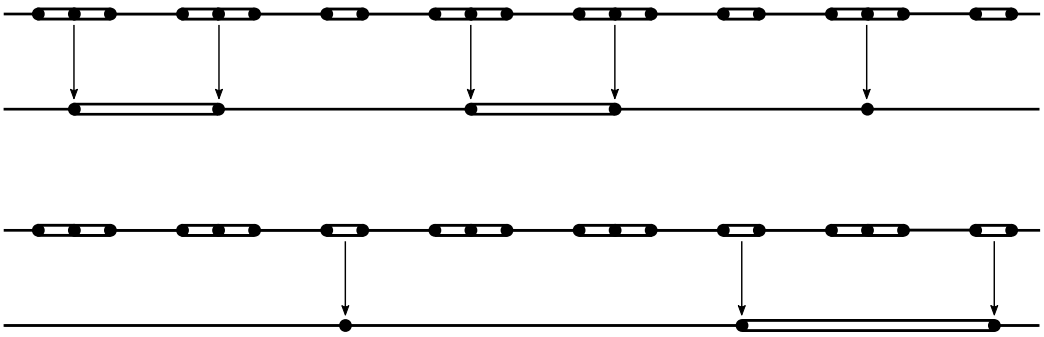

Figure 5.12 – (top) *trimer deflation* The 8th approximant with dominant strong coupling is transformed into the 5th approximant with dominant weak coupling. (bottom) *dimer deflation* The 8th approximant with dominant strong coupling is transformed into the 4th approximant with dominant weak coupling.

metallic means. The metallic means for an integer m are given by

$$\frac{m+\sqrt{m^2+4}}{2}, \tag{5.15}$$

where $m=1$ gives the golden mean, $m=2$ the silver mean, $m=3$ the bronze mean, etc.

Similar to the Fibonacci-series of numbers (for $m=1$) one can construct a generalized series of numbers $F_n^{(m)}$, that follow the recursive construction

$$F_n^{(m)} = mF_{n-1}^{(m)} + F_{n-2}^{(m)}, \tag{5.16}$$

with the initial values $F_0^{(m)}=0$, $F_1^{(m)}=1$. For $m=2$ one then finds a series of numbers, also known as Pell numbers. For higher m the series do not have special names anymore.

Based on these series of numbers, quasiperiodic sequences of A and B can then be generated, as for the Fibonacci-sequence. There exist generalized concatenation and substitution rules, but we decide to only present the adaption of the cut and project method, since this methods can gives us at the same time access to the conumbers, that make us of later in order to reveal the fractality of the LDoS.

It is not surprising that the adaption is rather straight forward. A generalized slope $\omega_n^{(m)}$ can be defined as ratio of two consecutive numbers

$$\omega_n^{(m)} = \frac{F_{n-2}^{(m)}}{F_{n-1}^{(m)}}, \tag{5.17}$$

n	$F_n^{(2)}$	$C_n^{(2)}$	$L_n^{(2)}$	$\omega_n^{(2)}$
1	1	B		
2	2	A	1	0/1
3	5	AAB	3	1/2
4	12	AABAABA	7	2/5
5	29	AABAABAAABAABAAAB	17	5/12
6	70	AABAABAAABAABAAABAABAABAAABAABAAABAABAABA	41	12/29
7	169	AABAABAAABAABAAABAABAABAAABAABAAABAABAA ...	99	29/70

Table 5.2 – The first seven Pell numbers $F_n^{(2)}$, together with the approximants $C_n^{(2)}$ of the silver mean sequence. They have a length $L_n^{(2)}$ and are created by a C&P method with slope $\omega_n^{(2)}$.

that is then used instead of ω_n in the Cut and Project method presented in section 5.2.2. The projected points divide the line again in intervals that only have two different lengths A and B. For any rational approximation $\omega_n^{(m)}$, the resulting infinite sequence $c_n^{(m)}$ is periodic with a motif $C_n^{(m)}$ of length $L_n^{(m)} = F_{n-2}^{(m)} + F_{n-1}^{(m)}$, and the ratios of the numbers of B and A correspond to $\omega_n^{(m)}$. In the limit $n \to \infty$, the slopes $\omega^{(m)}$ become the inverse of the metallic means defined in (5.15) and due to their irrational character one finds quasiperiodic sequences, that then can be used to construct the metallic mean chains.

We decide to implement again the off-diagonal model. We concentrate on the silver mean chains and study here both cases of weak and strong dominant coupling.

5.3.1 Silver mean chains

We investigate the silver mean chains by means of circular chains, where the basic motif is eventually repeated several times to form a closed ring of ≈ 100 resonators, as we did in section 5.2.5 for the Fibonacci chains. We use the same technique of directly integrating each frequency-band in $1 - \Re S_{11}(i, \nu)$, where $S_{11}(i, \nu)$ is the reflection spectrum measured over resonator i, in order to average over equivalent states (and additionally over equivalent sites i with the same conumber $c(i)$).

The first few approximants can be found in table 5.2. Differently to the Fibonacci chain, the length of the basic motifs does not correspond to Pell numbers anymore, since $F_n^{(m)} = mF_{n-1}^{(m)} + F_{n-2}^{(m)} \neq F_{n-1}^{(m)} + F_{n-2}^{(m)} = L_n^{(m)}$ for $m \geq 2$. This will later become important upon the formulation of the renormalization scheme.

The experimental results that will be presented in the following were ob-

tained with the help of Louise Morleas as part of her Master's internship, that I supervised together with Fabrice Mortessagne and Ulrich Kuhl.

As for the Fibonacci chains we use two different couplings strengths t_A and t_B, or equivalently two different distances d_A and d_B between the resonators. In the aim of treating now chains for a motif length of up to $L_7^{(2)} = 99$, compared to the circular chains for the Fibonacci chains, we further increase both coupling values, which increases the overall frequency-span of the measured spectra and since the width of the individual resonances stays the same, the separation between the individual frequency-bands is more visible. We use a short distance of 6.8 mm, corresponding to a strong coupling of 165 MHz and a long distance of 8 mm corresponding to a weak coupling of 87 MHz. For shorter distances between the resonators, their coupling becomes exponentially stronger, but since the precision with which one can position the resonators is about 0.05 mm (see section 3.3), the fluctuations of the coupling strengths becomes more important as well. While for the measurements for the circular Fibonacci chains a short distance of 7 mm was enough to identify the maximum $F_8 = 21$ integration borders upon the data-treatment, for the silver mean chains, in order to identify the maximum $L_7^{(2)} = 99$ integration borders, we now need the overall increased frequency-span of the spectra that we achieve with a shorter distances between the resonators, with the expense of stronger fluctuations of the coupling strengths. While for $n = 3$ and $n = 4$ is was still possible to identify the $L_3^{(2)} = 3$ and $L_4^{(2)} = 7$ individual frequency bands, for higher n this is not the case anymore and we used the same method to determine the $L_n^{(2)}$ integration borders, as for the higher order circular Fibonacci-chains, that is presented in Appendix B.2.

Dominant weak coupling: $\rho < 1$

For the case of dominant weak coupling, $d_A = 8$ mm and $d_B = 6.8$ mm, and thus $t_A < t_B$. For vanishing weak coupling t_A, the chains consist of isolated atomic sites and molecular sites. Frequency and conumbering axis can therefore be grouped into three clusters, two molecular clusters at the side and one atomic cluster at the center. The size of the molecular clusters is given by the number of molecules present in the basic motif, which is equal to the numbers of B in $C_n^{(2)}$, which is $F_{n-2}^{(2)}$. The size of the atomic clusters is then given by $L_n^{(2)} - 2F_{n-2}^{(2)} = \left[F_{n-1}^{(2)} + F_{n-2}^{(2)}\right] - 2F_{n-2}^{(2)} = \left[\left(2F_{n-2}^{(2)} + F_{n-3}^{(2)}\right) + F_{n-2}^{(2)}\right] - 2F_{n-2}^{(2)} = F_{n-3}^{(2)} + F_{n-2}^{(2)} = L_{n-1}^{(2)}$. For non-zero t_A, there are effective bond couplings between the different atomic and molecular states/sites.

As can be seen in figure 5.13, upon the deflation of the atomic cluster of a silver mean chain $c_n^{(2)}$ one finds again a silver mean chain $c_{n-1}^{(2)}$ with dominant

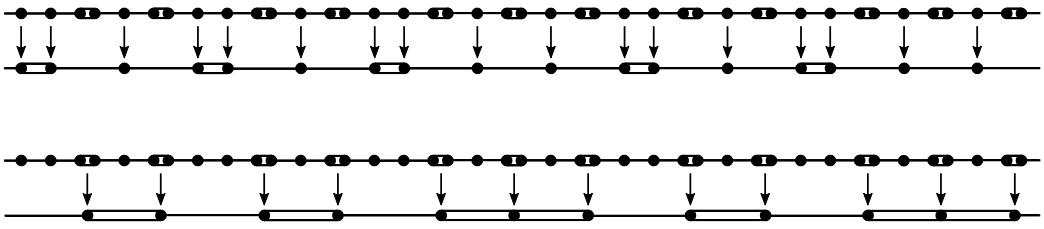

Figure 5.13 – Dominant weak coupling: (top) *atomic deflation* The 6th approximant $C_6^{(2)}$ is transformed into the 5th approximant $C_5^{(2)}$. (bottom) *molecular deflation* The 6th approximant $C_6^{(2)}$ is transformed into the 5th companion sequence $\hat{C}_5^{(2)}$ with dominant strong coupling.

weak coupling [109], while for the molecular cluster the deflation is less obvious. There cannot exist a direct recursive inflation scheme, since the size of the molecular clusters $F_{n-2}^{(2)}$ does not correspond to any of the basic motifs of the periodic approximants $C_n^{(2)}$ with length $L_n^{(2)}$. Nevertheless it can be shown, that there is a weak effective coupling corresponding to the *AAA* sequence and a strong effective coupling corresponding to the *AA* sequence in $c_n^{(2)}$. The frequency with which the sequence *AAA* occurs in $C_n^{(2)}$, corresponds to the number of B in $C_{n-1}^{(2)}$, which is $F_{n-3}^{(m)}$. The frequency of the sequence *AA* in $C_n^{(2)}$ is then $F_{n-2}^{(2)} - F_{n-3}^{(m)} = L_{n-2}^{(m)}$. We next introduce the set of companion sequences $\hat{c}_n^{(2)}$, that are generated using the C&P method with slope $\hat{\omega}_n^{(2)} = F_{n-2}^{(m)}/L_{n-1}^{(m)}$ and whose basic motifs $\hat{C}_n^{(2)}$ then have the length $\hat{L}_n^{(2)} = F_{n-1}^{(2)}$. The arrangement of the weak and strong effective bond couplings in between the molecular sites is then given by the companion sequence $\hat{c}_{n-1}^{(2)}$, where the letter A corresponds to a strong and the letter B to a weak coupling.

To be able to describe the full recursive construction of the LDoS, one would has to continue to study the deflation rules of the companion chains $\hat{c}_n^{(2)}$, but we actually stop our analysis here and present the experimental results.

In figure 5.14 one can see the measured LDoS for the first few approximants. Similar to the case of weak dominant coupling for the Fibonacci chains, we find the atomic cluster at the center, and the molecular cluster at the 4 corners of the LDoS (highlighted in figure 5.14(c) with orange and pink squares respectively). The direct recursive construction of the atomic clusters is well visible. Especially highlighted for $L_4^{(2)} = 7$ and $L_5^{(2)} = 17$, the central square (marked in orange), which gathers atomic sites and their corresponding states, of the LDoS at order n resembles the complete LDoS of order $n-1$.

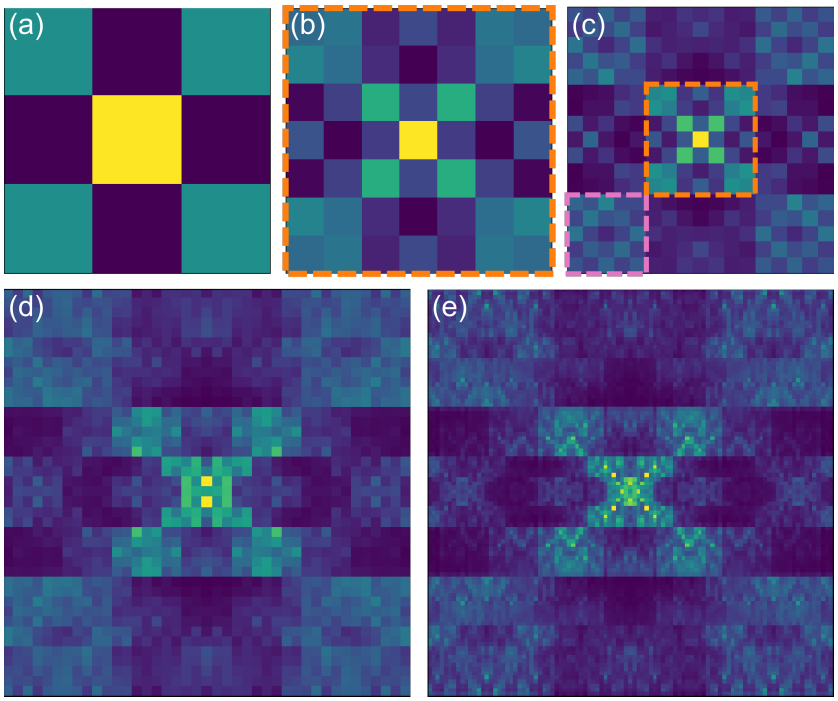

Figure 5.14 – Conumber-averaged LDoS for different approximants $c_n^{(2)}$ with dominant weak couplings, that were measured by means of circular chains, where the basic motif $C_n^{(2)}$ was repeated several times. (a) motif $C_3^{(2)}$ of length $L_3^{(2)} = 3$, repeated 32 times, (b) motif $C_4^{(2)}$ of length $L_4^{(2)} = 7$, repeated 14 times, (c) motif $C_5^{(2)}$ of length $L_5^{(2)} = 17$, repeated 6 times, (d) motif $C_6^{(2)}$ of length $L_6^{(2)} = 41$, repeated 2 times and (e) motif $C_7^{(2)}$ of length $L_7^{(2)} = 99$, that was actually not repeated, since the motif was already long enough to form a ring of ≈ 100 resonators. The plots were symmetrized along both axis. For all plots the horizontal axis corresponds to the conumber index $c(i)$ and the vertical axis to the frequency index j, and the same colormap as in figure 5.5 is used. The orange and pink squares in (c) mark the single atom and molecular clusters respectively, while the orange square around (b) additionally highlights the recursive construction.

Dominant strong coupling: $\rho > 1$

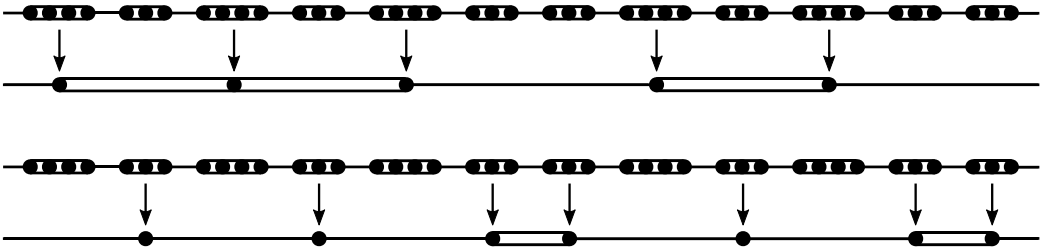

Figure 5.15 – Dominant strong coupling: (top) *tetramer deflation* The 6th approximant $C_6^{(2)}$ is transformed into the 4th companion sequence $\hat{C}_4^{(2)}$ with dominant strong coupling. (bottom) *trimer deflation* The 6th approximant $C_6^{(2)}$ is transformed into the 4th approximant $C_4^{(2)}$ with dominant weak coupling.

Similar to the case for dominant weak coupling, before presenting the measurements, we will start by formulating the renormalization scheme for inverted strong and weak coupling.

For the case of dominant strong coupling, $d_A = 6.8\,\text{mm}$ and $d_B = 8\,\text{mm}$, and thus $t_A > t_B$. For vanishing weak coupling t_B, the chains consist now of isolated trimers (three atom molecules) and tetramers (four atom molecules). The spectrum/conumbers then consist of 7 clusters. Four clusters associated with the tetramers at $\nu = \pm\frac{1}{2}\left(\sqrt{5}-1\right)t_B$ and $\nu = \pm\frac{1}{2}\left(\sqrt{5}+1\right)t_B$, and three clusters associated with the trimers at $\nu = 0$, $\nu = \sqrt{2}t_B$, that lay in between the tetramer clusters. The size of the trimer clusters corresponds to the frequency with which the sequence *AA* appears in $C_n^{(2)}$ and is $L_{n-2}^{(m)}$, while the size of the tetramer clusters corresponds to the frequency with which the sequence *AAA* appears in $C_n^{(2)}$ and is $F_{n-3}^{(m)}$. For non-zero t_B, there are again effective bond couplings between the different trimer and tetramer states/sites. The effective bond couplings between two neighboring trimers take on only two possible values, arranged again according to a silver mean sequence but with inverted strong and weak couplings. One thus passes from the chain $c_n^{(2)}$ to the chain $c_{n-2}^{(2)}$ with $\rho \to 1/\rho$. The effective bond couplings between two neighboring tetramers also only take two possible values, arranged according to the companion sequence $\hat{c}_{n-2}^{(2)}$, where the letter *A* corresponds again to a strong and the letter *B* to a weak coupling.

In figure 5.16 one can see the measured LDoS for the first few approximants. Similar to the case of the strong dominant coupling for the Fibonacci chains, we find a general structure that is quite different form the weak dominant case, but we find the same basic motifs as in figure 5.14. The orange

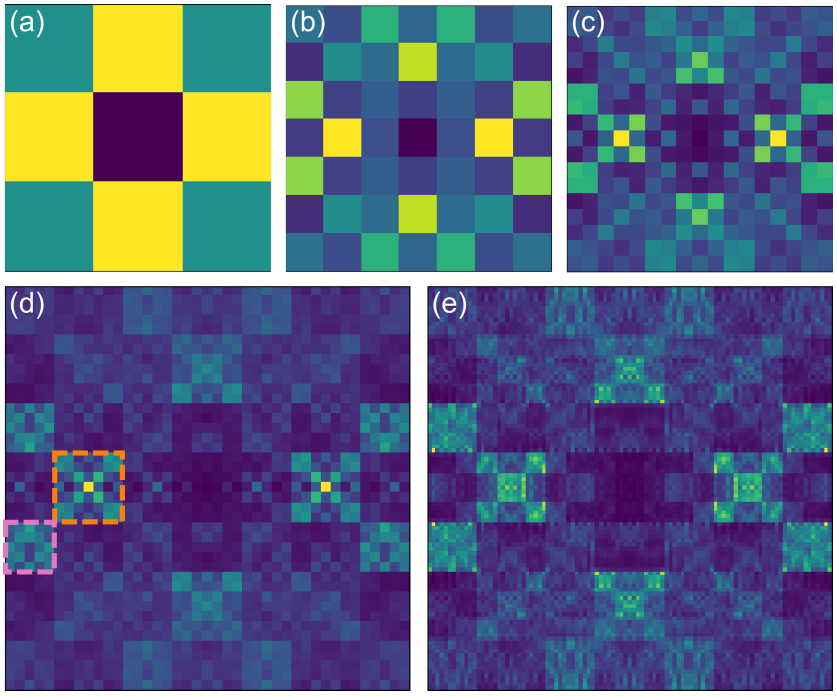

Figure 5.16 – Conumber-averaged LDoS for different approximants $c_n^{(2)}$ with dominant strong couplings, that were measured by means of circular chains, where the basic motif $C_n^{(2)}$ was repeated several times. (a) motif $C_3^{(2)}$ of length $L_3^{(2)} = 3$, that was repeated 32 times, (b) motif $C_4^{(2)}$ of length $L_4^{(2)} = 7$, that was repeated 14 times, (c) motif $C_5^{(2)}$ of length $L_5^{(2)} = 17$, that was repeated 6 times, (d) motif $C_6^{(2)}$ of length $L_6^{(2)} = 41$, that was repeated 2 times and (e) motif $C_7^{(2)}$ of length $L_7^{(2)} = 99$, that was actually not repeated, since the motif was already long enough to form a ring of ≈ 100 resonators. The plots were symmetrized along both axis. For all plots the horizontal axis corresponds to the conumber index $c(i)$ and the vertical axis to the frequency index j, and the same colormap as in figure 5.5 is used.

square in figure 5.16(d) highlights the basic motif associated with the trimers, that can also be found in figure 5.14(b,c), while the pink square highlights the basic motif associated with the tetramers, which again can be found in figure 5.14(c).

5.4 Conclusion

In this chapter we have investigated different 1D-quasiperiodic structures, with the main focus on the classical off-diagonal Fibonacci-model with dominant weak coupling. For the studied quasiperiodic structures the self-similarity of the LDoS can be revealed by reorganising the sites according to their conumber index, that is directly accessible via the cut and project construction method.

We also experimentally studied the different recursive construction schemes for the LDoS of the different quasiperiodic structures. The recursive construction schemes are based on a renormalization group theory, that was already well known for the classical (golden mean) Fibonacci model, for both cases of dominant strong and weak couplings. To our knowledge, a complete renormalization theory for the generalization of the Fibonacci-model to other metallic means did not exist. We thus took the first steps into at least qualitatively formulating a complete renormalization scheme for the generalized model. For all structures studied, we found a good qualitative agreement. Additionally, we have found good quantitaive agreement between the experimentally extracted renormalization factors and the theoretical predictions for the classical off-diagonal Fibonacci-model.

The main result of this chapter is the multifractal analysis that we performed for the classical off-diagonal Fibonacci-model with dominant weak coupling. By experimentally calculating the fractal dimension via a box-counting method, we found good agreement with theoretical and numerical predictions. These measurements actually provide the first experimental demonstration of multifractal properties of wavefunctions. While a lot of work on quasicrystal structures and its wavefunctions was done theoretically and numerically, only a few experimental works exists. We have explicitly shown that one can already extract multifractal properties in real systems of finite size, which will hopefully motivate others to perform further experiments on these highly interesting states.

Chapter 6

Topological transition in p-mode SSH-chains

In the realm of topological photonics, the standard SSH model is one of the simplest 1-D systems with a topological transition from a trivial to a non-trivial phase, associated with the appearance of edge states [110]. Motivated by the recent improvements in the experimental platform that allowed for a controlled employment of the resonators p-mode in TB experiments we decide to study a very similar system, but instead of staggered distances, we employ the anisotropic coupling in between the p-modes of the resonators to generate dimerization. We arrange the resonators on a zigzag pattern, and experimentally and analytically study the transition, that occurs when the zigzag bond angle θ in between the resonators is varied. After a short general introduction, we present our experimental results which shows the opening of a bandgap at a critical angle θ_c. The topological nature of the band gap leads to localized edge states at each end of the chains, that can be characterized by their inverse participation ratio (IPR). We end this chapter with a detailed analytic description of the system in the limit $N \to \infty$ that confirms the topological nature of the transition.

Contents

6.1 Introduction

In recent years, topological photonics appeared as a rapidly growing field of study, with the aim to explore the physics of topological phases of matter, originally discovered in solid-state electron systems, with the use of photonic platforms [17]. Topological phases of matter are characterized by a global property – a topological invariant – which make them insensitive to continuous deformation and disorder. Since 1980 with the discovery of the integer quantum Hall effect [1, 2], they have triggered an extensive research area in condensed matter physics.

The salient feature of topological materials is the *bulk-edge correspondence* [111–114]: At the contact of two materials with different topological invariants, there exist states that are spatially localized at the interface at energies/frequencies within the gap of the surrounding bulk materials dispersion relations. The integer topological invariant of a system, cannot change its value under perturbations or deformations of the system, unless the energy gap is closed. When two materials with different topological invariants are put in contact, the energy gap must be closed, leading to the appearance of localized states. In a finite-size topologically nontrivial system, the edge of the sample can be considered as an interface between a region with a nonzero topological invariant and the topologically trivial vacuum, which results in localized edge states.

One of the simplest 1D model with a topological band structure is a chain of sites with alternating couplings (i.e. a dimer chain). This model was originally introduced by Su, Schrieffer and Heeger (SSH) [110] to describe fractionalized charges in polyacetylene, which appear in the presence of a dimerization defect. It is therefore not surprising that analogies of this model were extensively studied with the use of various different photonic platforms, such as photonic superlattices [115], plasmonic metal nanoparticles [116–118], coupled optical waveguides [119–122], polariton micropillars [123], a hybrid silicon platform [124], and chains of dielectric resonators [37].

We study a very closely related system, a zigzag array of equidistantly spaced resonators (see figure 6.1), where the dimerization of the system occurs due to the polarization-dependent coupling between the two orthogonal

p-modes of the individual resonators. Such a topological system was first proposed theoretically [125] and later realized experimentally for plasmonic [27] nanoparticles.Its topologically protected edge modes have been used to realize photonic spin-Hall effect [126] and zigzag structures were utilized in polaritonics [127–130] and in the first demonstration of topological lasing [18]. Such arrays have also proven itself useful in controlling photoluminescence emissions [131] and for non-linear generation of light [24].

While the vast majority of research was done exclusively on right-angle zigzag chains, we are especially interested in the topological transition and more precisely the transition from the topological trivial linear chains to the topological non-trivial right-angle zigzag chains by a continuous homogeneous deformation of the chains. It is expected that at some point in the transition from linear to zigzag chains, a critical configuration is reached, where a gap is opening in the bulk band structure and edge modes arise within the bandgap (see section 6.3).

Only very recently we became aware of other works studying this transition analytically [132] and experimentally [133]. Due to the large absorption within their samples, the researchers have not been able to experimentally observe the opening of a bandgap, nor have they been able to individually resolve the edge states spectrally, but rather used the relative contrast of the measured intensity at a given wavelength between the first and the last resonator to follow the transition. The measured relative contrast is in good agreement with analytical predictions, but it lacks distinct features to determine this critical point. With our experimental platform we can individually resolve all different states spectrally and spatially (for small systems). Thus we have full access to the wavefunctions associated with the two central frequency states, that upon the transition will emerge into the two (degenerate) topologically protected edge modes. Apart from the direct observation of the formation of a band-gap within the spectra, we propose the inverse participation ratio (IPR) of the central frequency states as a better measure to follow the topological transition.

Other topological transitions in zigzag chains that were studied experimentally and analytically, are induced by staggered distances [129] between the resonators and/or disorder [134].

6.2 Zigzag chains of coupled resonators

A sketch of the arrangement of the resonators for different angles θ can be seen in figure 6.1(b). We use the same separation of 9 mm in between each resonator, but the angles with which the line in between two neighboring res-

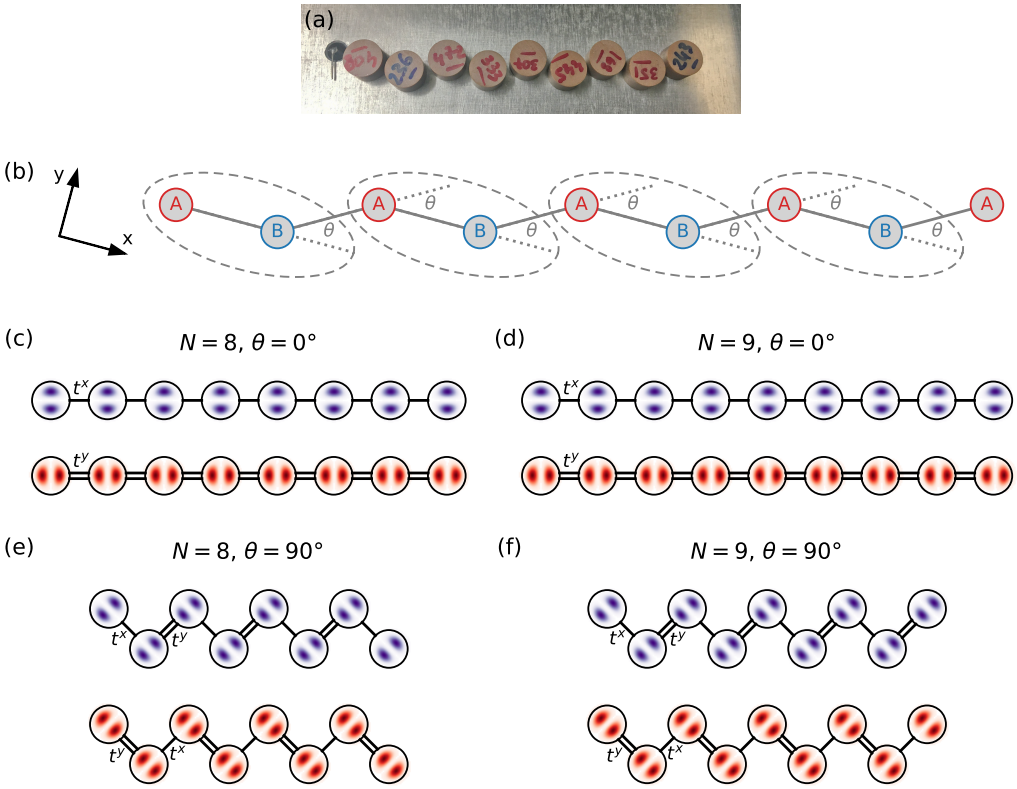

Figure 6.1 – (a) Photo of an experimental chain of $N = 9$ resonators. We use a stationary kink antenna that couples to the left-most resonator and a movable loop antenna (not shown) in order to probe the system. (b) General sketch of the arrangement. The angle θ is used to describe the transition form linear chains ($\theta = 0°$) to right-angle zigzag chains ($\theta = 90°$). We describe the system with the use of two sublattices A and B, so that each unit cell (encircled by dashed ellipses), contains two resonators, one of the A and and one of B sublattice. For the case of $\theta = 0°$ (c),(d) and $\theta = 90°$ (e),(f) the system can be completely separated into its x- (blue) and y-polarized (red) components. For $\theta = 0°$(c),(d) this results in two topological trivial linear chains, while for $\theta = 90°$, the system becomes non-trivial due to the staggered couplings t^x (single black line) and t^y (double black line) with $|t^y| > ^x$ and we expect edge states on each side of the chain.

onators intersect the x-axis are following a $\{0, \theta, 0, \theta, 0, \theta, \cdots\}$ sequence. As we will explicitly show in section 6.3.1, the TB Hamiltonian of such chains possesses a chiral symmetry [7]. We thus introduce the two sublattices A and B to describe the system. Due to this symmetry we expect different results, when using an even or odd number N of resonators. We thus study the cases of $N = 8$ and $N = 9$ in detail. When not explicitly interested in finite-size effects, it is always preferred to study the largest possible chains. But the increased resonance-width and the slightly smaller coupling of the p-mode compared to the s-mode, together with the fact that in the case of p-modes, a chain of N resonators produced $2N$ resonance peaks, made it more challenging to identify all individual states in the spectra compared to s-mode measurements. The clear identification of the two central frequency states was especially challenging for intermediate values of θ. Before the gap is finally opening, the density of states around the central frequency is actually increasing, making it harder to identify the different resonance peaks in the spectra. $N = 9$ was the maximum system size, where we still could identify $2N$ resonance peaks for all studied angles θ and extract the associated wave functions of the system.

We experimentally study the system for angles $\theta = 0°, 15°, 30°, 45°, 60°, 75°$ and $90°$. The case $\theta = 0°$ (see figure 6.1(c) and (d)) corresponds to linear chains, where the x and y-polarization can be separated and treated individually, as we have already shown in section 4.3.4. The case $\theta = 90°$ corresponds to a right-angle zigzag chain, where the system once more can be separated into its x- and y-polarization. Due to the different coupling strength t^x, t^y, this case can be described by the standard SSH model, where both topological phases are present at once. In the limit of $n \to \infty$ the sub-system in y-polarization is in the topological trivial phase, where the parity of the winding number $P = 0$, while the sub-system in x-polarization is in the topological non-trivial phase, where $P = 1$, since $|t^y| > |t^x|$. We thus expect localized edge states with a localization length $\zeta \approx \ln|t^y/t^x|$ on both sides of the chain. For finite systems, if the total number of resonators N is even, we expect the edge state at each end of the chain to be in the x-polarization, but each supported by the different sublattices A or B (see figure 6.1(e)). If N is odd, we expect the left edge state to be in the x-polarization, while the right edge state is in the y-polarization and both modes are now supported only by the A sublattice (see figure 6.1(f)).

For both cases of even and odd number of resonators, the polarized edge states for $\theta = 90°$ have been well observed with the use of various different photonic platforms [18, 24, 27, 126–138]. We are thus especially interested in intermediate values of θ, in order to explicitly study the transition from the topological trivial case of decoupled linear chains ($\theta = 0°$) to the non-trivial case, with localized edge states for $\theta = 90°$. The general Hamiltonian of this

system as a function of the angle θ is described by

$$H = H_0 + H_{\text{intra}} + H_{\text{inter}}(\theta). \tag{6.1}$$

H_0 describes the on-site energies

$$H_0 = \sum_j \nu_0 (a^\dagger_{x,j} a_{x,j} + b^\dagger_{y,j} b_{y,j}) + h.c.,$$

where $a^\dagger_{l,j}$ ($a_{l,j}$) is the creation (annihilation) operator of the l-polarized mode at site A_j, and $b^\dagger_{l,j}$ ($b_{l,j}$) is the creation (annihilation) operator of the l-polarized eigenmode at site B_j, respectively with $l \in \{x, y\}$. ν_0 is the single resonator resonance frequency. H_{intra} describes the intra-cell coupling

$$\begin{aligned} H_{\text{intra}} &= \sum_j t^{xx}(0) b^\dagger_{x,j} a_{x,j} + t^{yy}(0) b^\dagger_{y,j} a_{y,j} + t^{xy}(0)(b^\dagger_{y,j} a_{x,j} + b^\dagger_{x,j} a_{y,j}) + h.c. \\ &= \sum_j t^x b^\dagger_{x,j} a_{x,j} + t^y b^\dagger_{y,j} a_{y,j} + h.c. \end{aligned}$$

and $H_{\text{inter}}(\theta)$ the inter-cell coupling

$$H_{\text{inter}}(\theta) = \sum_j t^{xx}(\theta) a^\dagger_{x,j+1} b_{x,j} + t^{yy}(\theta) a^\dagger_{y,j+1} b_{y,j} + t^{xy}(\theta)(a^\dagger_{y,j+1} b_{x,j} + a^\dagger_{x,j+1} b_{y,j}) + h.c.,$$

where the functions $t^{xx} = t^x \cos^2(\theta) + t^y \sin^2(\theta)$, $t^{yy} = t^y \cos^2(\theta) + t^x \sin^2(\theta)$ and $t^{xy} = (t^x - t^y)\cos(\theta)\sin(\theta)$, describe the different co- and cross-polarized couplings, that depend on the two parameters t^x, the weak coupling between two x-polarized modes of aligned resonators, and t^y, the strong coupling between two y-polarized modes of aligned resonators. For simplicity, compared to the notations introduced in section 4.3.2, we drop the minus sign before the coupling terms and integrate them in the t^x and t^y factors. We thus have $t^x > 0$, while $t^y < 0$, but still $|t^y| > |t^x|$.

As we will later demonstrate in section 6.3, the topological phase transition occurs at a critical angle θ_c, where $t^{xx}(\theta)$ changes its sign, defined by $\tan(\theta_c/2) = \sqrt{|t^x/t^y|}$.

We scan the experimental chains by measuring the transmission and reflection spectra between two antennas: a fixed kink antenna, that couples to the first resonator of the chain, as can be seen in figure 6.1(a), and a movable loop antenna, that we move on a 2D regular grid with a step size of 1 mm in the (x, y)-plane over the resonators. In order to achieve a better spatial resolution of the wavefunctions, we use a loop antenna with a smaller loop than the one used to s-mode measurements and reduce the overall cavity height to 9 mm. The reason why we have not used the small loop antenna for the s-mode measurements is due to an internal resonance of the antenna that coincides with the resonance frequencies of the s-modes.

6.2.1 Spectrum

The local density of states LDoS(i, ν), averaged over each resonator i, can be directly obtained from the reflection spectra $\{S_{11}(r_j, \nu)\}$, measured at the loop antenna for the different antenna positions $\{r_j\}$.

$$\text{LDoS}(i, \nu) = \left\langle 1 - \Re\left(S_{11}(r_j, \nu)\right)\right\rangle_{r_j \text{ over resonator } i} . \tag{6.2}$$

In order to separate the different contributions coming from the bulk and the edges of the chains, we define a "bulk" density of states as the sum of the LDoS of all resonators, except the first and last resonator.

In figure 6.2 one can see the measured "bulk" density of states (blue), and the local density of states at the first (orange) and last (green) resonator for both cases $N = 8$ and $N = 9$ and different angles θ.

Highlighted in grey, for both cases $N = 8$ and $N = 9$, one can clearly obverse the opening of a band-gap in the "bulk" density of states for $\theta = 60°$, accompanied by the formation of two edge states that lay within the gap and that are localized on either side of the chain. The degeneracy of the edge two states is lifted in the experiment, which can be explained by slightly different resonance frequencies of the two resonators at each end. Also the kink-antenna that is coupled to the first resonator of the chain induces an additional small frequency shift of the resonance localized at that resonator.

By extracting all resonance-positions for the linear chains ($\theta = 0°$) we can estimate the two couplings strengths $|t^x|$ and $|t^y|$ for our experiment, as we already did in section 4.3.4. We cannot directly use the functions $t^x(d)$ and $t^y(d)$, obtained in section 4.3.3, since we are now working at a different height in between bottom and top plate and thus the evanescent decay of the modes is not the same. We extract the resonance-positions with the harmonic inversion method and fit them with (4.39) and find $t^x = 24\,\text{MHz}$ and $t^y = -102\,\text{MHz}$. Thus the transition should occur at $\theta_c = 2\tan^{-1}(\sqrt{t^x/|t^y|}) \approx 51.7°$. This is consistent with the experimental observation, where the gap is opening in between $\theta = 45°$ and $\theta = 60°$.

One can further notice that the two peaks associated with the edge states can also be found to a small extent in the "bulk" density of states. This comes from the finite localisation length of the edge states, which still have small amplitudes on the sites that we have assigned to the "bulk" region. The effect is the strongest for $\theta = 60°$, just after the opening of the gap, and is less visible for $\theta = 75°$ and $\theta = 90°$, showing that the edge states become more and more localized, the further we are from the transition.

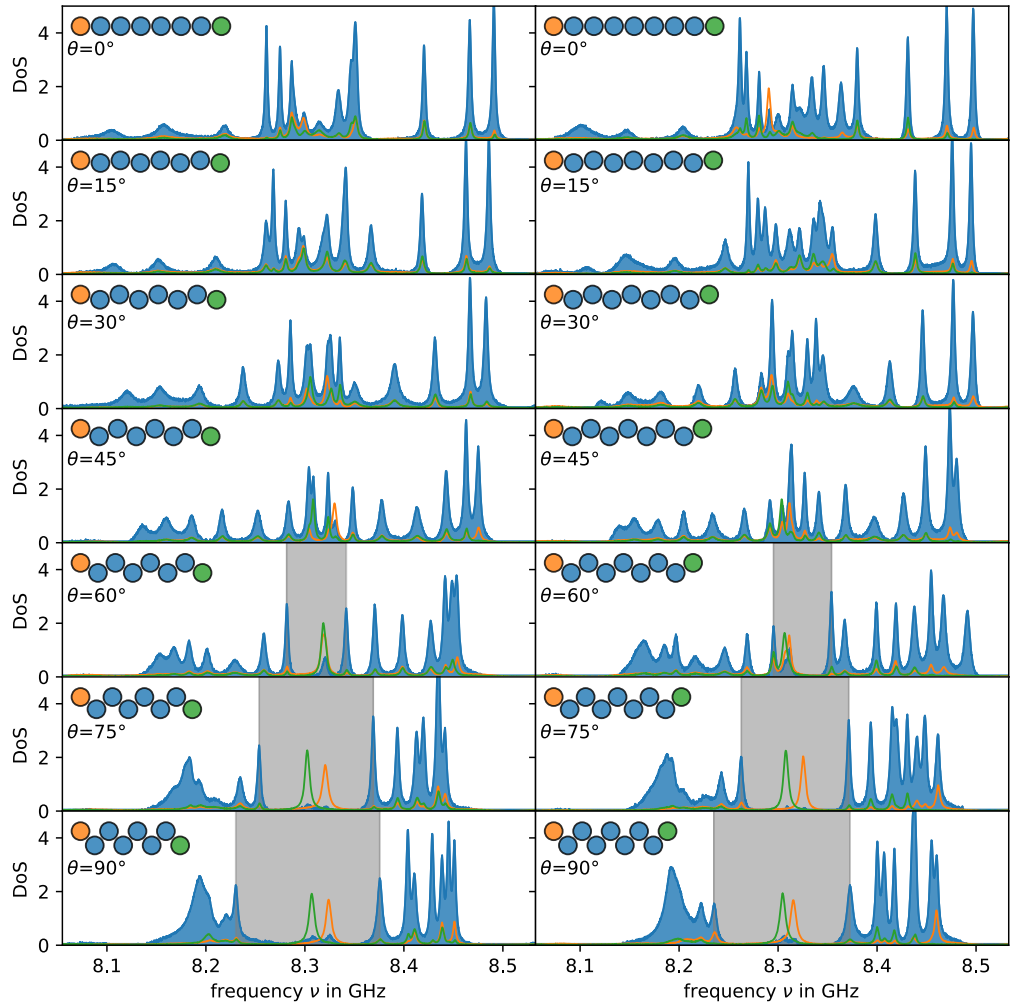

Figure 6.2 – Measured "bulk" density of states (DoS) (in blue) for different angles and both cases $N = 8$ (left) and $N = 9$ (right). The grey areas highlight the band-gaps, that are opening for $\theta \geq 60°$. We additionally plot the local density of states measured over the first resonator in orange and over the last resonator in green.

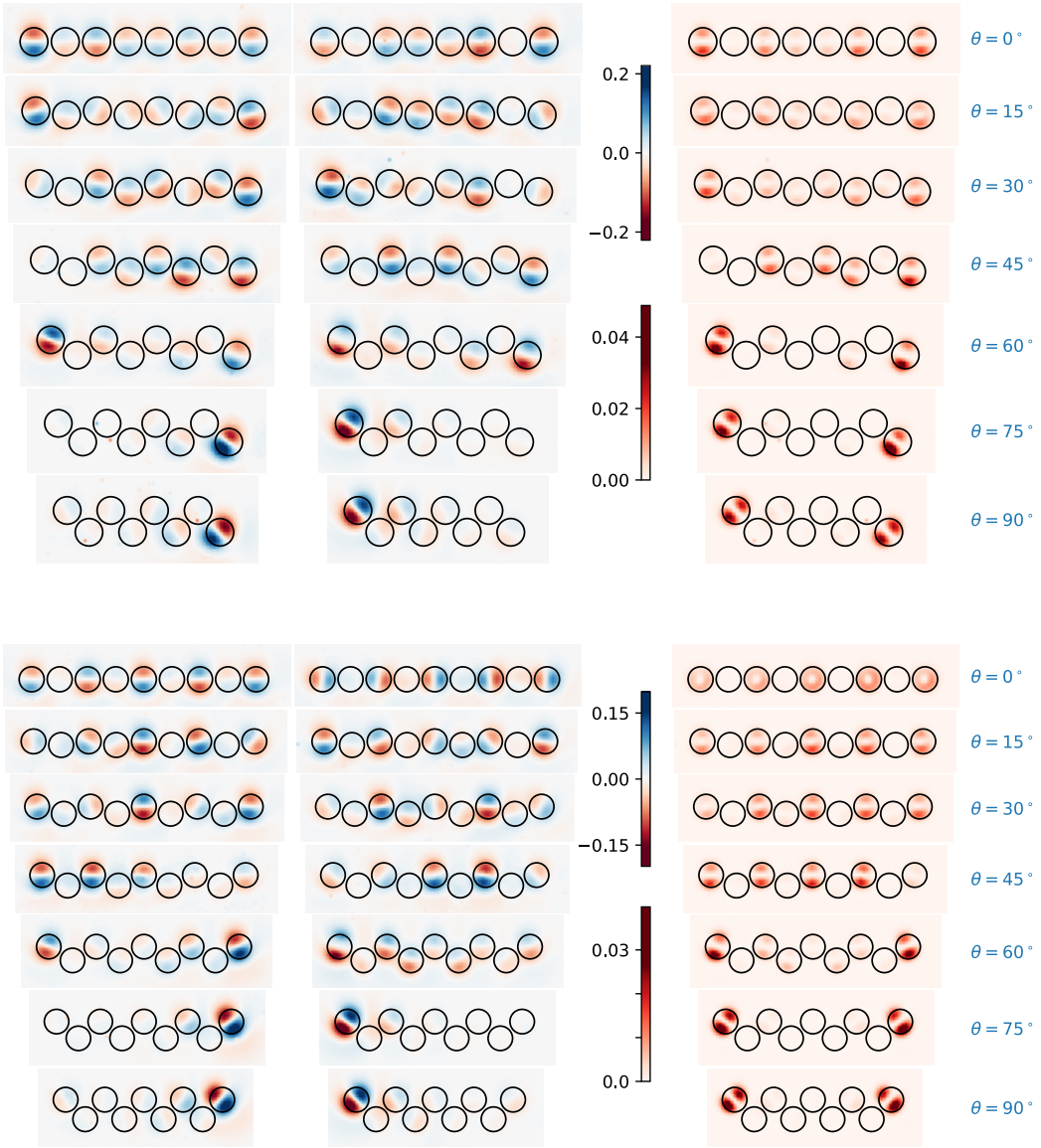

Figure 6.3 – Extracted wavefunction amplitude of the two central frequency states (left and center columns), together with its combined wavefunction intensity (right column) for the chains of $N = 8$ resonators (top) and $N = 9$ resonators (bottom).

6.2.2 Wavefunctions of the central frequency states

To further study the spatial evolution of the two central frequency states, we are going to compare their associated wavefunctions for different angles θ. In order to extract the wavefunctions $\psi_1(r)$ and $\psi_2(r)$ of the two central frequency states, we use the harmonic inversion method to extract and cluster all resonance-frequencies and -amplitudes in each transmission spectrum. We further normalize each wavefunction $\psi(r)$, so that the sum of the wavefunction-intensity over all measured positions $\{r_j\}$ equals 1, $\sum_j |\psi(r_j)|^2 = 1$.

The extracted wavefunctions $\psi_1(r)$ and $\psi_2(r)$ for each angle θ can be seen in figure 6.3. We additionally plot the combined wavefunction intensity $|\psi_1(r)|^2 + |\psi_2(r)|^2$, as it allows to compare the wavefunctions of the chains more easily. Due to the degenerate nature of the two central frequency states, in the presence of slightest variations of resonance-frequencies and/or couplings, they hybridize. This effect is sensitive to experimental imperfection such as the tiny difference in the resonance-frequencies of each resonator and the marginally varying coupling strength due to small variations in the positioning of the resonators. This effect is indeed so sensitive, that even standard double precision numerical simulations of the TB Hamiltonian where all resonance frequencies and couplings are the same throughout the chain, still show some hybridization for the degenerate central frequency states. For small disorder, one can assume, that the combined wavefunction intensity $|\psi_1(r)|^2 + |\psi_2(r)|^2$ is conserved. This can be understood as a kind of energy conservation. The overall intensity at a given frequency (here it is the central frequency, which plays the role of the systems "energy" in the TB framework) at each site must be conserved, although it may be distributed differently onto the two degenerate states. Of course for strong disorder, the combined wavefunction intensity will be altered as well, but it is much more robust than the individual wave functions $\psi_1(r)$) and $\psi_2(r)$.

Due to the chiral symmetry of the Hamiltonian we expect a symmetric spectrum $\{\nu_0 \pm \nu_n\}$ around ν_0, the single resonator resonance frequency, associated with pairs of symmetric and antisymmetric states. Despite the hybridization, traces of this symmetry can still be found in some pairs $\psi_1(r)$, $\psi_2(r)$, for example for $\theta = 0°$, $N = 8$ and $\theta = 60°$, $N = 8$ and $N = 9$. Another property arising from this symmetry is that for a finite chain of an even number of resonators, without experimental fluctuations and considering only nearest neighbour couplings, the two central frequency states are at frequencies $\nu_c = \nu_0 \pm \epsilon$ around ν_0. ϵ becomes smaller for increasing θ and in the limit $N \to \infty$, $\epsilon \to 0$ for all θ. On the other hand, for an odd number of resonators, even for finite chains, both central states are at $\nu_c = \nu_0$ for any value of θ. This parity anomaly breaks the sublattice symmetry for any θ and both central frequency states are supported

by only the A sublattice. While we cannot resolve the parity anomaly spectrally due to experimental fluctuations in the resonance-frequencies of the individual resonators, that are larger then the expected ϵ, we can still observe the broken sublattice symmetry for the chains of $N = 9$ resonators, despite experimental fluctuations and next nearest neighbour coupling. Except for $\theta = 60°$, where we probably are in an unfavorable case concerning the individual resonance frequencies of the resonators, all states have vanishing amplitudes on the B-sublattice sites.

Overall, as expected, one can clearly see the transformation of bulk-modes that have amplitude all over the chains to localized edge states at each side of the chain. As expected the edge state for the chains of $N = 8$ resonators are both x-polarized, with the left edge state being supported mainly by the A-sublattice and the right edge state being supported mainly by the B sublattice. For the chains of $N = 9$ resonators, both edge states are mainly supported by the A sublattice, and the left edge state is x-polarized, while the right edge state is y-polarized.

We do not restrict ourselves to these qualitative observations, but additionally extract the tight-binding coefficients $|C_i|^2 = |c_i^x|^2 + |c_i^y|^2$ for both central frequency states, to compare our experimental results to numerical TB simulations. In the TB formalism the wavefunction $\psi(r)$ of any state can be approximated as a superposition of the individual single resonator wave functions $\psi_0^x(r - r_i)$ and $\psi_0^y(r - r_i)$, $\psi(r) = \sum_i c_i^x \psi_0^x(r - r_i) + c_i^y \psi_0^y(r - r_i)$, where the coefficients $\{c_i^x, c_i^y\}$ are given by the associated eigenvector $\vec{c} = (c_1^x, c_1^y, c_2^x, c_2^y, ..., c_N^x, c_N^y)$ of the TB Hamiltonian in matrix form and the $\{r_i\}$ are the positions of the individual resonators.

If we assume the overlap between adjacent single resonator wavefunction $\psi_0^x(r)$ and $\psi_0^y(r)$ to be negligible, we can extract the $|C_i|^2$ by integrating the wavefunction intensities $|\psi(r)|^2$ over each resonator i at position r_i with radius r_{reso}

$$\begin{aligned}\int_{|r-r_i|<r_{\text{reso}}} |\psi(r)|^2 dr &= \int_{|r-r_i|<r_{\text{reso}}} \left| \sum_i c_i^x \psi_0^x(r - r_i) + c_i^y \psi_0^y(r - r_i) \right|^2 dr \\ &\approx \int_{|r-r_i|<r_{\text{reso}}} \left| c_i^x \psi_0^x(r - r_i) + c_i^y \psi_0^y(r - r_i) \right|^2 dr \\ &= (|c_i^x|^2 + |c_i^y|^2) \int_{|r|<r_{\text{reso}}} \left| \psi_0^{x/y}(r) \right|^2 dr \propto |C_i|^2 .\end{aligned}$$

The normalizing of the single resonator wavefunction assures $\int \left| \psi_0^{x/y}(r) \right|^2 dr = 1$, we thus expect $\int_{|r|<r_{\text{reso}}} \left| \psi_0^{x/y}(r) \right|^2 dr < 1$, but this can be accounted for by

renormalizing the obtained coefficients $|C_i|^2$, so that $\sum_i |C_i|^2 = 1$. The extracted coefficients for both central frequency states $|C_i^{(1)}|^2$, $|C_i^{(2)}|^2$ together with their sum $|C_i^{(1)}|^2 + |C_i^{(2)}|^2$ is presented in figure 6.4.

We additionally compare the extracted combined coefficients, to tight-binding simulations of the systems Hamiltonian, using the $t^x = 24\,\mathrm{MHz}$ and $t^y = -102\,\mathrm{MHz}$ that we extracted earlier from the spectra of the linear chains. We simulate the ideal case of only nearest neighbour interactions (black plus symbols), but since we experimentally cannot get rid of the small next nearest neighbour couplings in between the resonators, we also try to evaluate this contribution by including all possible couplings in between the resonators in the TB Hamiltonian (red circles), as already done in section 4.3.5 and 4.3.5. While we have not explicitly measured $t^x(d)$ and $t^y(d)$ as a function of the separation d in between the resonators for this specific cavity height, we recall that for the s-mode, as demonstrated in section 4.2.1, the resonators mainly couple via their first evanescent mode. We therefore use $t^{x/y}(d) = t^{x,y} K_1(\gamma_1 d)/K_1(\gamma_1 9\,\mathrm{mm})$, where the $t^{x,y}$ are the measured couplings extracted from the spectra of the linear chains, and $\gamma_1 = \sqrt{\left(\frac{\pi}{h}\right)^2 - \left(\frac{2\pi\nu_0}{c_0}\right)^2} \approx 0.30\,\mathrm{mm}^{-}1$ is the decay rate of the first evanescent TE_1 mode outside of the resonators. Of course the actual dependency most likely also involves small contributions from higher order modes, but the dependency we use is a justified simplification, considering that the aim of the next nearest neighbour simulations is to reveal and roughly estimate its effects on the wave functions.

Generally we find a good quantitative agreement between the measurement and the TB simulations, especially considering that the experimental fluctuation of the resonance-frequencies (see section 3.3 for details) are of the order of $\approx 15\%$ of the weaker coupling strength t^x. For $N = 9$ the sublattice polarization becomes even clearer than in figure 6.3 and we experimentally find ratios of $\approx 2 - 15\%$ in between the averaged intensities on the B and A-sublattice for the different θ. A part from the already mentioned variations of the single resonator resonance frequencies that might explain the highest ratio of 15% for $\theta = 60°$, other effects that lead to a ratio that differs from zero are the spatial overlap of the individual wave functions and non negligible next nearest neighbour couplings.

Especially visible for $\theta > \theta_c$ due to the logarithmic scale, the next nearest neighbour simulations show the breaking of the sublattice polarization of the edge states for both cases $N = 8$ and $N = 9$, and we observe amplitudes even on the sublattice, that in the nearest neighbour regime do not support the edge states. For both cases ($N = 8$ and $N = 9$), however, we experimentally and numerically still observe much greater amplitudes on the sublattices that support the edge states in the nearest neighbour regime, then on the other sublat-

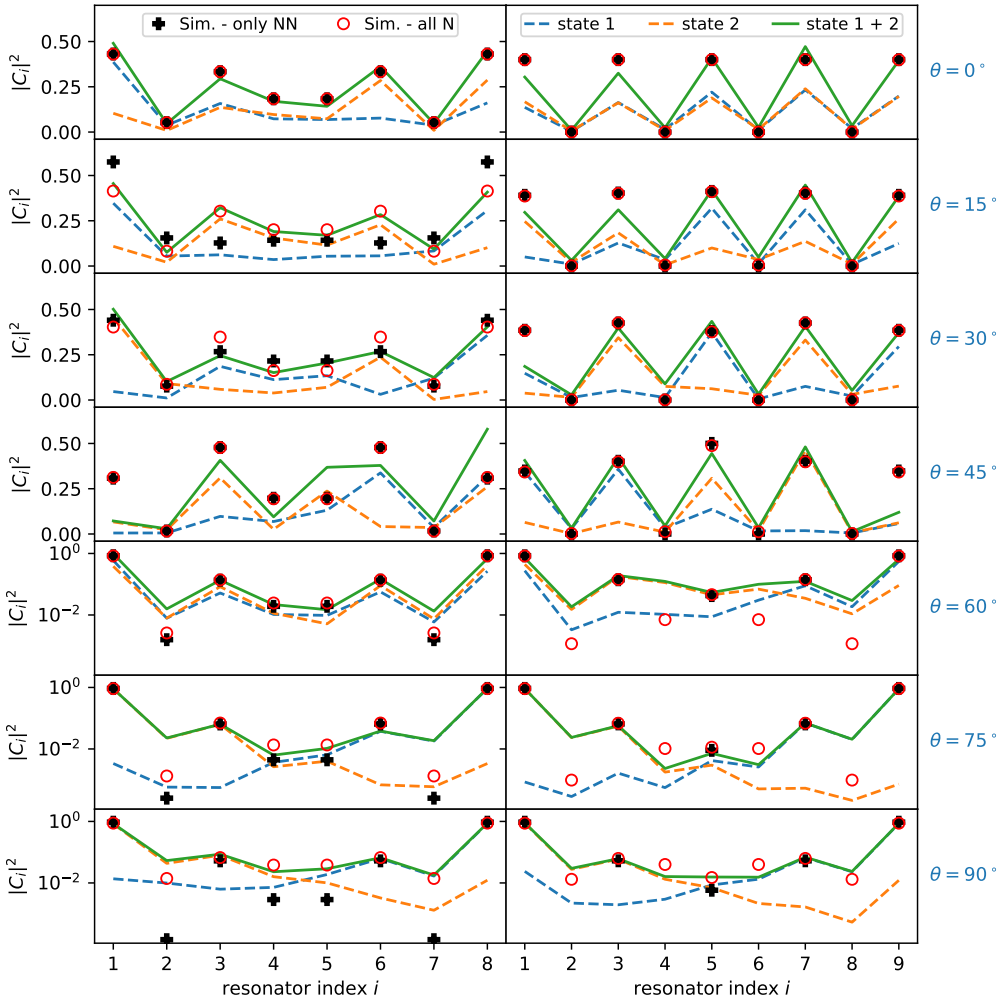

Figure 6.4 – The extracted coefficients for both central frequency states $|C_i^{(1)}|^2$ (blue dashed line) and $|C_i^{(2)}|^2$ (orange dashed line) together with their sum $|C_i^{(1)}|^2 + |C_i^{(2)}|^2$ (green solid line) for the chains of $N = 8$ resonators (left) and $N = 9$ resonators (right) are shown. The first 4 rows ($\theta < \theta_c$) are plotted with the same linear (y-axis) scale, while the last 3 rows ($\theta > \theta_c$) are plotted with the same logarithmic scale, to help visualize the exponential decay of the edge states. We additionally compare them to TB simulations, considering only nearest neighbours couplings (black plus symbols) or considering all couplings (red circles).

tice. It seems that the next nearest neighbour simulations tend to overestimate the experimental next nearest neighbour couplings. This is especially visible for $\theta \geq 75°$ and in the center of the chains, where the simulated coefficients are even higher then the experimentally extracted ones on the not supporting sublattice in the nearest neighbour regime. Nevertheless the amount of next-nearest neighbour coupling present in the experiment does not seem to be negligible, since some states (e.g. for $N = 8, \theta = 15°$) seem to be in much better agreement with the next-nearest neighbour simulations, then with the simulation that only consider the nearest neighbours.

Underlined by the use of the logarithmic scale for $\theta > \theta_c$, one can observe the exponential decay of the edge states. This exponential localization of the edge-state inspired us to further extract the inverse participation ratio (IPR) of the central frequency states, which can be interpreted as a measure of localisation of wavefunctions [139]. We expect it to show significant different behaviour for the bulk modes before and for the edge states after the transition.

6.2.3 The IPR as marker of the transition

For normalized eigenstates, the IPR of a certain state is defined as the square of its intensity summed over all sites. Consequently, for an extended (bulk) state the IPR is close to zero, while for a state that is completely localized at a single site the IPR$= 1 : 0 <$ IPR ≤ 1. Due to the observed hybridization in the experiment we define a combined $\overline{\text{IPR}}$, calculated with the combined central frequency states intensities

$$\overline{\text{IPR}} = \frac{1}{2}\sum_i (|C_i^{(1)}|^2 + |C_i^{(2)}|^2)^2. \tag{6.3}$$

Bulk modes are expected to have $\text{IPR}_{\text{bulk}} \propto 1/N \xrightarrow{N\to\infty} 0$, since their intensity is distributed more or less evenly through out the whole chain of length N. The edge states on the other hand are expected to not depend on the systems size but only on their localization length, when their localization length is (much) smaller than the length of the chain. For even N, both edge state are expected to be supported by different sublattices. So for $\theta > \theta_c$ the combined $\overline{\text{IPR}}$ can be separated into $\overline{\text{IPR}} = \frac{1}{2}\sum_i (|C_i^{(1)}|^2 + |C_i^{(2)}|^2)^2 = \frac{1}{2}(\sum_i |C_i^{(1)}|^4 + \sum_i |C_i^{(2)}|^4) = (\text{IPR}_1 + \text{IPR}_2)/2 = \text{IPR}_{\text{edge}}$, since in the absence of hybridization, $\text{IPR}_1 = \text{IPR}_2 = \text{IPR}_{\text{edge}}$. Similar reasoning can be made for odd N, when the localization length is (much) smaller then the length of the chains and in the vicinity of $\theta = 90°$, where both edge states are orthogonally polarized to each other.

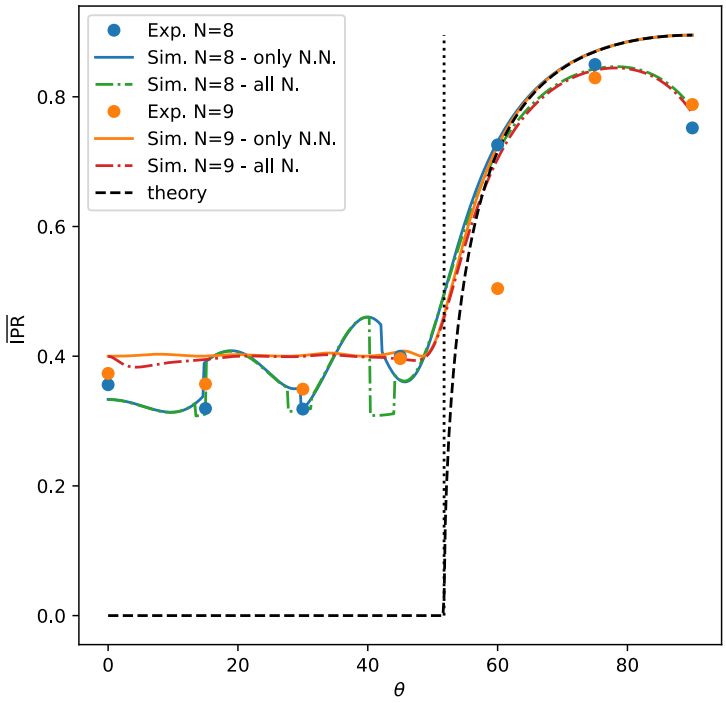

Figure 6.5 – Experimental $\overline{\text{IPR}}$ as a function of the different θ for $N = 8$ (blue dots) and $N = 9$ (orange dots). We compare them to TB simulations considering only nearest neighbours (blue and orange line) and all neighbours (green and red dash-dotted lines) and an analytical theoretical expression obtained in the limit $N \to \infty$ (black dashed line). The vertical black dotted line marks the critical angle θ_c of the transition.

In figure 6.5 one can see the experimental $\overline{\text{IPR}}$ (blue and orange dots) for different θ, where we compare it again to TB simulations considering only nearest neighbours (blue and orange line) and all neighbours (green and red dash-dotted lines) and an analytical theoretical expression obtained in the limit $N \to \infty$ (black dashed line). For more details on the theoretical expression see section 6.3.4.

For $\theta < \theta_c$, before the transition, while the analytic expression for $N \to \infty$ is zero, one can see that the both the experimental, as well as the simulated $\overline{\text{IPR}}$ fluctuate around a constant value, that depends on the system size. The simulated $\overline{\text{IPR}}$ for $N = 9$ fluctuates significantly less, which directly results from the breaking of the sublattice symmetry. Without the exact knowledge of the

systems wavefunctions, if one assumes an equidistribution of the intensity on all 5 sites of the A sublattice (for $N = 9$), one would expect that $\overline{\text{IPR}} = 0.4$ before the transition, which is in good agreement with the simulations. The amount of fluctuations in the experimental $\overline{\text{IPR}}$ is similar for the case of $N = 8$ and $N = 9$, which indicate that their origin is dominated by the experimental uncertainties and fluctuations that are similar for both cases.

Around and after the transition, $\theta \gtrapprox \theta_c$, both the experimental and simulated $\overline{\text{IPR}}$ quickly increase and converge towards the analytic expression for $N \to \infty$. While one would expect a monotonous increase until $\theta = 90°$, the experimental $\overline{\text{IPR}}$ is maximal for $\theta = 75°$ and actually decreases again for $\theta = 90°$, which indicates that within the experiment, the edge states are maximal localized for $\theta = 75°$, and not as expected for $\theta = 90°$. We find that this can essentially be explained by next nearest neighbour couplings, that become more important for large θ, since the resonators become closer to each other. While the TB simulations considering only nearest neighbour couplings are in perfect agreement with the theoretical expression for $\theta \gtrapprox 60°$, that was actually formulated in the very same approximation, the TB simulations that consider all possible interaction between the resonators actually shows the same behaviour as the experimental $\overline{\text{IPR}}$. There is actually one experimental data point for $N = 9$ at $\theta = 60$, that is not in as good agreement with the simulations as the rest. As already discussed earlier, for this experimental chain, we measured non negligible amplitudes on the B sublattice, which is not in agreement with the expected sublattice polarization of the edge-states and then results in a reduced $\overline{\text{IPR}}$. We explain this by an unfavorable distribution of the individual resonance frequencies due to the fluctuation of the resonance frequencies upon the placing of the resonators.

Overall one can see two clearly different behaviours of the $\overline{\text{IPR}}$ before and after the transition, which makes the $\overline{\text{IPR}}$ a good marker, also experimentally, to follow the topological transition. For larger systems, where the extraction of the individual resonance-amplitudes is not possible anymore, one still can approximate the combined TB coefficients $|C_i^{(1)}|^2 + |C_i^{(2)}|^2$ in order to calculate the $\overline{\text{IPR}}$ by integrating the LDoS(i, ν) within a small interval around the central frequency ν_0. We already used such method with great success in section 5. When the gap is open for $\theta > \theta_c$, the peak(s) associated with the central frequency states should be well isolated and when the gap is closed for $\theta < \theta_c$, the frequency-overlap with resonance peaks of other bulk states should not affect the $\overline{\text{IPR}}$.

6.3 Analytic description

While the system's Hamiltonian in its real-space representation can be directly formulated knowing the relative arrangement of the resonators, for an analytic description (in the limit of $N \to \infty$) it is convenient to transform the Hamiltonian into its momentum-space representation. Without sacrificing generality we suppose $\nu_0 = 0$ for the theoretical description of the system. Assuming Bloch periodic boundary conditions (e.g. when the chains form a closed loop) and using

$$a_{x,j} = \frac{1}{\sqrt{N}} \sum_k \mathrm{e}^{\mathrm{i}kj} \hat{a}_{x,k} \tag{6.4}$$

$$a_{y,j} = \frac{1}{\sqrt{N}} \sum_k \mathrm{e}^{\mathrm{i}kj} \hat{a}_{y,k} \tag{6.5}$$

$$b_{x,j} = \frac{1}{\sqrt{N}} \sum_k \mathrm{e}^{\mathrm{i}kj} \hat{b}_{x,k} \tag{6.6}$$

$$b_{y,j} = \frac{1}{\sqrt{N}} \sum_k \mathrm{e}^{\mathrm{i}kj} \hat{b}_{y,k}, \tag{6.7}$$

we can express the systems Hamiltonian (6.1) as $H = \sum_k^\dagger \psi_k H(k) \psi_k$, where ψ_k is defined as $\psi_k = (\hat{a}_{x,k}, \hat{a}_{y,k}, \hat{b}_{x,k}, \hat{b}_{y,k})^T$ and $H(k)$ is the momentum-space Hamiltonian

$$H(k) = \begin{pmatrix} 0 & h(k) \\ h^\dagger(k) & 0 \end{pmatrix}, \tag{6.8}$$

with

$$h(k) = \begin{pmatrix} t^x + \mathrm{e}^{-\mathrm{i}k} t^{xx}(\theta) & \mathrm{e}^{-\mathrm{i}k} t^{xy}(\theta) \\ \mathrm{e}^{-\mathrm{i}k} t^{xy}(\theta) & t^y + \mathrm{e}^{-\mathrm{i}k} t^{yy}(\theta) \end{pmatrix}. \tag{6.9}$$

This way the Hamiltonian's dimension is effectively reduced from a $2N \times 2N$ matrix into a 2×2-matrix, that contains all information about the system.

6.3.1 Chiral symmetry

A Hamiltonian H is said to be chiral symmetric if there exists a unitary and Hermitian operator Γ (so that $\Gamma^2 = \mathbb{1}$), which anticommutes with the Hamiltonian [140], $\Gamma H \Gamma = -H$. In our case

$$\Gamma = \begin{pmatrix} \mathbb{1} & 0 \\ 0 & -\mathbb{1} \end{pmatrix} \tag{6.10}$$

and since $H(k)$ can be written as a completely block-off-diagonal matrix, it is easy to show that the system possesses a chiral symmetry, $\Gamma H(k) \Gamma = -H(k)$.

Actually, any system whose Hamiltonian can be written as a block-off-diagonal matrix possesses a chiral symmetry.

One property of a system with chiral symmetry is its symmetric spectrum, which is a direct result of the block-off-diagonal form of the Hamiltonian. Given a generic block anti-diagonal matrix $M = \begin{pmatrix} 0 & M_{12} \\ M_{21} & 0 \end{pmatrix}$, we have $M^2 = \begin{pmatrix} M_{12}M_{21} & 0 \\ 0 & M_{21}M_{12} \end{pmatrix}$. The eigenvalues of M are therefore $\{\pm\sqrt{m_i}\}$, the square roots of the eigenvalues $\{m_i\}$ of $\hat{M} = M_{12}M_{21}$.

The states associated with a pair of energies $\pm\varepsilon$ are related via the chiral operator Γ. If $|\psi\rangle$ is an eigenstate of H with eigenvalue ε, then $\Gamma|\psi\rangle$ is also an eigenstate of H with eigenvalue $-\varepsilon$.

6.3.2 Bulk dispersion relation $E(k)$

The eigenvalues of $H(k)$ define the energy spectrum of the system, also refereed to as the bulk dispersion relation $E(k)$. We find the 4 eigenvalues

$$E_1(k) = \Delta\cos\theta\cos\frac{k}{2} + \sqrt{t^2\cos^2\frac{k}{2} + \Delta^2\sin^2\frac{k}{2}\sin^2\theta} \tag{6.11}$$

$$E_2(k) = \Delta\cos\theta\cos\frac{k}{2} - \sqrt{t^2\cos^2\frac{k}{2} + \Delta^2\sin^2\frac{k}{2}\sin^2\theta} \tag{6.12}$$

$$E_3(k) = -\Delta\cos\theta\cos\frac{k}{2} + \sqrt{t^2\cos^2\frac{k}{2} + \Delta^2\sin^2\frac{k}{2}\sin^2\theta} \tag{6.13}$$

$$E_4(k) = -\Delta\cos\theta\cos\frac{k}{2} - \sqrt{t^2\cos^2\frac{k}{2} + \Delta^2\sin^2\frac{k}{2}\sin^2\theta}, \tag{6.14}$$

where $t = t^x + t^y$ and $\Delta = t^x - t^y$. We find that the spectrum is gaped for $\cos\theta > \left|\frac{t^x+t^y}{t^x-t^y}\right|$, which gives us the critical angle of the transition

$$\theta_c = \arccos\left|\frac{t^x + t^y}{t^x - t^y}\right| = 2\arctan\sqrt{|t^x/t^y|}. \tag{6.15}$$

As one would expect it is the ratio t^x/t^y that determines the angle θ_c of the zigzag chains at which the transition occurs. In figure 6.6 one can see the calculated spectrum of the system for different θ and ratios t^x/t^y. The red line separates the plots into two regions : $\theta \leq \theta_c$, where the spectrum is gapless, and $\theta > \theta_c$, where the spectrum is gaped.

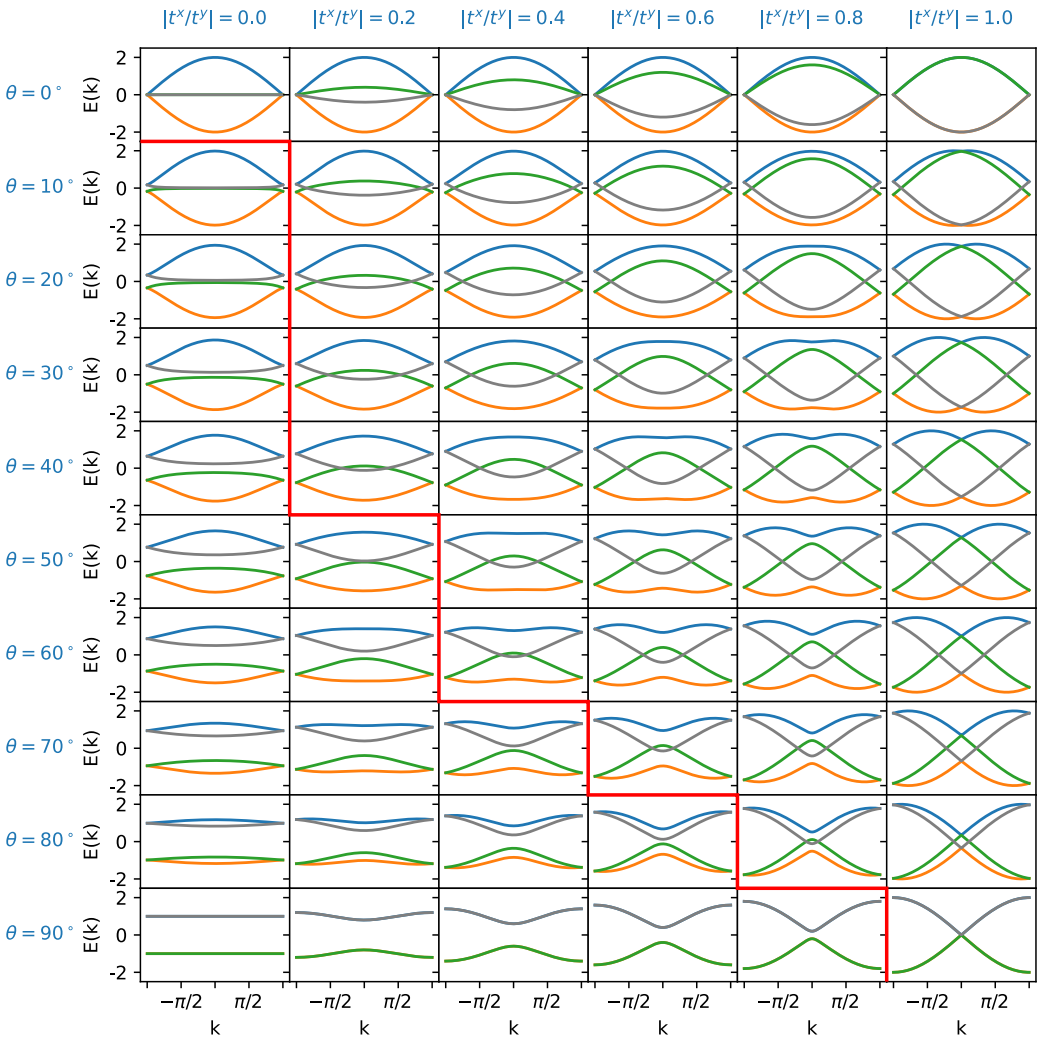

Figure 6.6 – Bulk Dispersion Relation $E(k)$ for different θ and ratios $|t^x/t^y|$. t^y was fixed to -1 and t^x varied from 0 to 1. Each eigenvalue $E(k)$ of $H(k)$ is plotted in a different color, $E_1(k)$ in blue, $E_2(k)$ in orange, $E_3(k)$ in green and $E_4(k)$ in grey. The added red line in between the plots separates them into two domains : $\theta \leq \theta_c$, where the spectrum is gapless, and $\theta > \theta_c$, where the spectrum is gaped.

6.3.3 The topological invariant P

We will now investigate the nature of this transition and show that it is indeed a topological transition from a trivial to a non-trivial phase, by calculating the systems topological invariant P, which is defined as the parity of the winding number $P = W \mod 2$ [132]. Due to bulk-edge correspondence the number of protected edge states per edge that appear when edges are inserted into a topological insulating system is exactly equal to $|W|$. The system's Zak phase γ [141] is equal to $W\pi$. The winding number W can be found in various equivalent ways. We will calculate it in terms of the winding of the lower-left block h of the off-diagonal Hamiltonian $H(k)$ [142–144],

$$W = \oint \frac{\mathrm{d}k}{2\pi \mathrm{i}} \log\left[\mathrm{Det}(h)\right] = \oint \frac{\mathrm{d}k}{2\pi} \partial_k \arg\left[\mathrm{Det}(h)\right], \tag{6.16}$$

where $\oint \mathrm{d}k = \int_{\pi}^{\pi} \mathrm{d}k$ indicates the contour integral over the whole Brillouin zone, and the determinant is given by

$$\mathrm{Det}(h) = \mathrm{e}^{-\mathrm{i}k}\left[t^2 \cos^2\frac{k}{2} + \Delta^2\left(\sin^2\frac{k}{2} - \cos^2\theta\right)\right]. \tag{6.17}$$

The calculated parity P of the winding number for different θ and ratios $|t^x/t^y|$ can be seen in figure 6.7. For $\theta > \theta_c$, hence $|\Delta|\cos\theta < |t|$ and $\mathrm{Det}(h)$ is non-zero for any k, which results in $\mathrm{Det}(h)$ making exactly one turn around zero and therefore leads to a winding number of $W = 1 = P$, which can be seen in figure 6.7 (a). For $\theta < \theta_c$, since the spectrum is not gaped, the individual energy bands $E_i(k)$ are intersecting each other and thus $\mathrm{Det}(h)$ passes exactly two times through zero, as can be seen in figure 6.7 (c) and (d). Since the phase of the point $\mathrm{Det}(h) = 0$ is undefined, in order to calculate P, one can shift the whole contour an infinitesimal amount to the left or to the right. If one shift the whole contour to the left, one finds $W = 0$ and if one shifts the whole contour to the right and finds $W = 2$, which both result in the same parity of $P = 0$. As can be seen in figure 6.7 (b), for $\theta = \theta_c$, $\mathrm{Det}(h)$ passes again trough the origin, but only a single time. If we then shift the whole contour an infinitesimal amount in order to calculate P, we find $P = 0$, when we shift to the left, but $P = 1$, when we shift to the right, confirming that the topological invariant is actually undefined for this critical point.

This change of the systems topological invariant from $P = 0$ to $P = 1$, passing through the critical point at θ_c indeed confirms the topological nature of this transition.

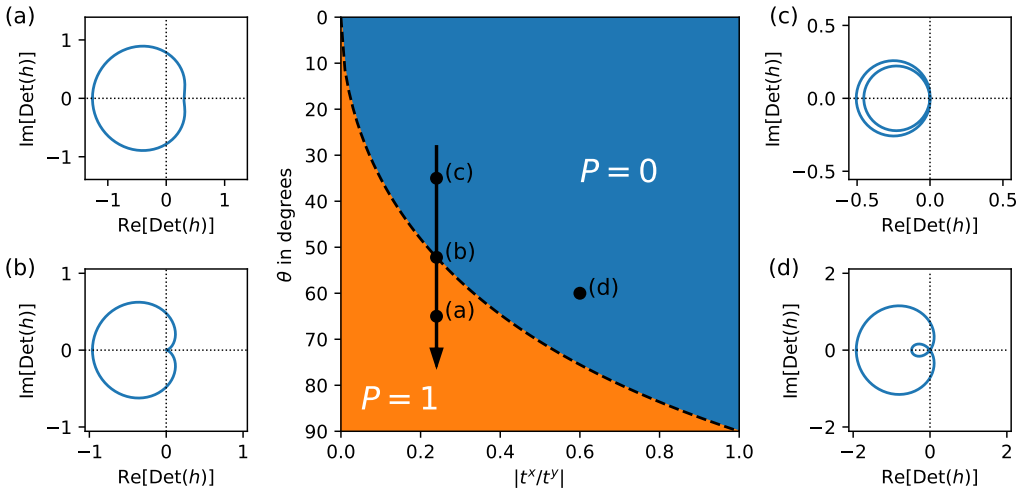

Figure 6.7 – (center) Parity P of the winding number W as a function of θ and the ratio $|t^x/t^y|$. The black dashed line indicate the critical angle of the transition $\theta_c = 2\arctan\sqrt{|t^x/t^y|}$ and separate the topological trivial region with $P = 0$, where no edge-states occurs and the topological non-trivial region with $P = 1$, where one topological edge state occurs at each end of the chain. (a)-(d) illustrate the winding of Det(h) in the complex plane (as k is varied from $-\pi$ to π) for a fixed $t_y = -1$ and values of t_x and θ that are marked by the corresponding letter in the central figure. (a)-(c) show the different cases for ratios of $|t^x/t^y| = 0.24$, which corresponds the our experimental case, were (c) is right at transition with $\theta = \theta_c$. The black arrow going trough the points in the central figure indicates the direction, from small to large θ, that we followed when presenting the experimental results.

6.3.4 Zero-energy edge state

We next derive the analytic solution for the wavefunction of the edge states in the limit of $N \to \infty$. With zero-energy, the wavefunctions can be derived without solving the eigenvalue problem. When the Hamiltonian (6.1) acts on the zero-energy state $|\psi\rangle$, it yields

$$H|\psi\rangle = 0. \tag{6.18}$$

The associated wavevector can be written as

$$|\psi\rangle = \sum_{j=1}^{N} A_j^x a_{x,j}^\dagger + A_j^y a_{y,j}^\dagger + B_j^x b_{x,j}^\dagger + B_j^y b_{y,j}^\dagger |0\rangle, \tag{6.19}$$

where j enumerates the unit cells, and the A_j^x (A_j^y) and B_j^x (B_j^y) are the coefficients of the x-(y-)polarized wavefunction on sublattice A and B of the j-th unit cell respectively. N is now the number of unit cells and not the number of resonators which is $2N$. Substituting (6.19) in (6.18), every single term must be zero, we therefore find a set of $4N$ linear equations:

$$A_j^x t^x + A_{j+1}^x t^{xx}(\theta) + A_{j+1}^y t^{xy}(\theta) = 0 \tag{6.20}$$
$$A_j^y t^y + A_{j+1}^x t^{xy}(\theta) + A_{j+1}^y t^{yy}(\theta) = 0 \tag{6.21}$$
$$B_j^x t^{xx}(\theta) + B_j^y t^{xy}(\theta) + B_{j+1}^x t^x = 0 \tag{6.22}$$
$$B_j^x t^{xy}(\theta) + B_j^y t^{yy}(\theta) + B_{j+1}^x t^y = 0 \tag{6.23}$$

for the bulk ($j = 1, 2, ..., N-1$), and

$$A_N^x t^x = 0 \tag{6.24}$$
$$A_N^y t^y = 0 \tag{6.25}$$
$$B_1^x t^x = 0 \tag{6.26}$$
$$B_1^y t^y = 0 \tag{6.27}$$

at the the boundary. Due to the inversion symmetry, it is sufficient to only solve for the amplitudes on sublattice A, $\{A_j^x, A_j^y\}$, and the $\{B_j^x, B_j^y\}$ can be obtained by labeling the indices from the opposite direction.

This gives us the following recurrence formula

$$\begin{pmatrix} A_{j+1}^x \\ A_{j+1}^y \end{pmatrix} = M \begin{pmatrix} A_j^x \\ A_j^y \end{pmatrix} \tag{6.28}$$

with

$$M = \begin{pmatrix} \frac{-t^{yy}(\theta)}{t^y} & +\frac{t^{xy}(\theta)}{t^x} \\ \frac{t^{xy}(\theta)}{t^y} & -\frac{t^{xx}(\theta)}{t^x} \end{pmatrix} = 2\Delta \sin\theta \begin{pmatrix} \frac{\sin\theta}{\Delta - t} & \frac{\cos\theta}{\Delta + t} \\ \frac{-\cos\theta}{\Delta - t} & \frac{\sin\theta}{\Delta + t} \end{pmatrix} - \mathbb{1}. \tag{6.29}$$

The amplitude at the jth unit cell $(A_j^x, A_j^y)^T$, can then be expressed as

$$\begin{pmatrix} A_j^x \\ A_j^y \end{pmatrix} = M^{j-1} \begin{pmatrix} A_1^x \\ A_1^y \end{pmatrix} \tag{6.30}$$

In order to study the dynamics of the system one has to find the eigenvalues λ_1 and λ_2 of M with their associated eigenvectors $\vec{\Lambda}_1$,$\vec{\Lambda}_2$. The general solution can then we written as

$$\begin{pmatrix} A_j^x \\ A_j^y \end{pmatrix} = \alpha \lambda_1^j \vec{\Lambda}_1 + \beta \lambda_2^j \vec{\Lambda}_2, \tag{6.31}$$

where the factors α and β are defined by the boundary conditions (and constrained by the normalization of the wavefunction).

With $\sin^2(\theta_c) = \frac{\Delta^2 - t^2}{\Delta^2}$, we can express the two eigenvalues λ_1 and λ_2 of M, as a function of θ and θ_c,

$$\lambda_1(\theta) = \left(2\frac{\sin^2(\theta)}{\sin^2(\theta_c)} - 1\right) - \sqrt{\left(2\frac{\sin^2(\theta)}{\sin^2(\theta_c)} - 1\right)^2 - 1}, \tag{6.32}$$

$$\lambda_2(\theta) = \left(2\frac{\sin^2(\theta)}{\sin^2(\theta_c)} - 1\right) + \sqrt{\left(2\frac{\sin^2(\theta)}{\sin^2(\theta_c)} - 1\right)^2 - 1}. \tag{6.33}$$

After the transition, $\theta > \theta_c$ both eigenvalues are real-valued. We have $|\lambda_1(\theta > \theta_c)| < 1$, associated with an exponentially decreasing behaviour and $|\lambda_2(\theta > \theta_c)| > 1$ associated with an exponentially increasing behaviour. Only the decreasing solution can fulfill the boundary conditions $A_N^x = A_N^y = 0$ and for $N \to \infty$, we finally get

$$\begin{pmatrix} A_j^x \\ A_j^y \end{pmatrix} = \sqrt{\frac{1-\lambda^2}{\lambda^2}} \lambda^j \vec{\Lambda}, \tag{6.34}$$

where $\lambda = \lambda_1$ and the factor α was determined from the wavefunctions normalization $|\alpha|^2 = \left(\sum_{j=1} \lambda^{2j}\right)^{-1} = \frac{1-\lambda^2}{\lambda^2}$. The localization length of the mode is then given by $\zeta = -1/\ln(\lambda)$, which for $\theta = 90°$, converges to $\zeta = -1/\ln(|t^x/t^y|)$, the localization length of the standard SSH-model, that can be formulated by separating the x- and y-polarization.

The associated eigenvector $\vec{\Lambda} = \vec{\Lambda}_1$, that we supposed to be properly normalized, $||\vec{\Lambda}|| = 1$, indicates the polarization of the mode. It is more convenient to calculate $\vec{\Lambda}$ in a different reference system (x', y'), that can be obtained by turning the original orthogonal coordinate system (x, y) by an angle $\theta/2$ anticlockwise, so that the new x' axis is now in line with the first sublattice, as

indicated by the small coordinate systems on the left of figure 6.8. In this reference system

$$\vec{\Lambda} = \sqrt{2}\begin{pmatrix}\sqrt{1+\frac{\cos\theta}{\cos\theta_c}}\\ \sqrt{1-\frac{\cos\theta}{\cos\theta_c}}\end{pmatrix}. \tag{6.35}$$

We define the polarization $p = \arctan(-A^y/A^x)$ of the mode as the angle under which the nodal line of the mode intersects the x' axis. We get

$$p(\theta) = -\arctan\left(\sqrt{1-\cos\theta/\cos\theta_c}/\sqrt{1+\cos\theta/\cos\theta_c}\right). \tag{6.36}$$

In figure 6.8 one can see the analytically calculated edge-states for some angles $\theta > \theta_c$, and plots of the modes polarization p and localisation length ζ as a function of θ. One can also observe that the localization length ζ diverges for $\theta = \theta_c$. For $\theta > \theta_c$, ζ exhibits a sharp initial decrease followed by a steady evolution.

Confirmed by the drastic change of ζ right after the transition, the inverse participation ratio (IPR), which can be used to measures the amount of localization of any state [139], has the potential to be a good marker of the transition. The IPR of the zero-energy edge state in the limit $N \to \infty$ is given by

$$\mathrm{IPR}(\theta) = \sum_{j=1}^{\infty}(|A_j^x|^2 + |A_j^y|^2)^2 = \sum_{j=1}^{\infty}|\alpha|^4\lambda^{4j} = \frac{1-\lambda(\theta)^2}{1+\lambda(\theta)^2}. \tag{6.37}$$

As one can see in figure 6.5, the IPR is zero for bulk modes and drastically increases at $\theta = \theta_c$. This large increase, combined with its simple calculation and straightforward measurement procedure, makes it indeed an excellent marker of the transition, which has already been confirmed in the experiment (see chapter 6.2.3).

The polarization p of the edge-state changes throughout the transition. At the transition $\theta = \theta_c$ $\vec{\Lambda} = (1,0)^T$, which results in $p = 0$ and the edge-state is therefore fully x'-polarized. For $\theta = 90°$, $\vec{\Lambda} = \sqrt{2}(1,1)^T$ and thus $p = -\pi/4$, which translates to a fully x-polarized mode in the earlier used reference system (x, y). This change of polarization throughout the transition can also be observed experimentally in figure~6.3). In order to extract the polarization of the experimentally measured left and right edge-state, we individually fit the combined wavefuntion-intensity above the first and last resonator (encircled by black lines) with $f(x,y) = [A\sin(\tan^{-1}(\frac{y-y_0}{x-x_0}) - \phi_0)J_1(\gamma\sqrt{(x-x_0)^2+(y-y_0)^2})]^2$. The fit parameter ϕ_0 gives the alignment of the nodal line, which up to a (sign and interval) convention then corresponds to the polarization p. For both edge states of the chain with $N = 8$

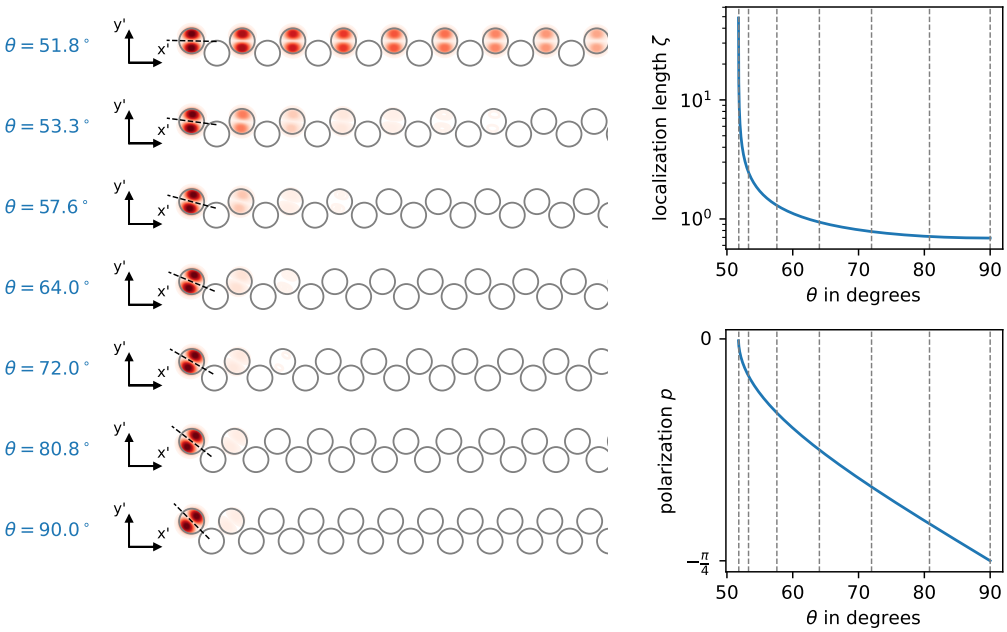

Figure 6.8 – (left) Plots of the analytically calculated wavefunction-intensities in the limit of $N \to \infty$ of the zero-energy edge state, localized at the left-edge of the zigzag array. We use the same coupling-ratio $|t^x/t^y| = 24/102$, as in the experiments, which gives $\theta_c \approx 51.7°$. We plot different θ, from right after to transition with $\theta = 51.8°$ up to $\theta = 90°$ with a non-uniform spacing, to help visualize the turning of the wavefunctions polarization. We chose the spacing in between the different values of θ, so that between two consecutive plots the polarization of the mode always gets turned by the same amount and we additionally highlight the modes polarization at the first resonator with a black dashed line. (right) Plots of the localization length ζ (top) of the zero-energy-mode and its polarization p (bottom) as a function of θ after the transition ($\theta > \theta_c$). The polarization is defined as the angle in between the nodal line and the x' axis in the new defined x'-y' coordinate system. The grey vertical lines mark the angles θ, for which we have explicitly visualized the modes wavefunctions on the (left) part of the figure.

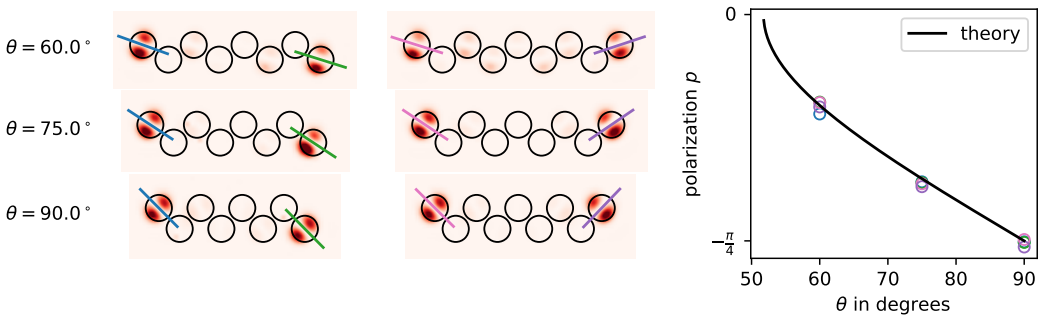

Figure 6.9 – Experimentally extracted polarization of the edge-states after the transition. We plot the wavefunction intensity for both cases of $N = 8$ (left) resonators and $N = 9$ (center) resonators, for angles $\theta = 60°$, $75°$ and $90°$. We extract the polarization of the edge state by individually fitting the area over the first and last resonator of each chain (encircled by the black lines). The found orientation of the nodal lines is then highlighted by differently coloured line above the corresponding resonators. (right) We compare the experimentally extracted (coloured circles) edge-state polarizations p to the theoretical formulation obtained in the limit of $N \to \infty$ (black solid line). In order to distinguish the different edge-states the same colors as for highlighting the fitted nodal lines in the other subplots are used.

resonates and the left edge state for the chain of $N = 9$ resonators, we get $p = \phi_0 \mathrm{mod}\pi - \pi$, but in order to include the right edge state of the chain of $N = 9$ resonators in the comparison, we use $p = -\phi_0 \mathrm{mod}\pi$ due to the chains symmetry. The results can be seen in figure 6.9, where we compare them to the theoretical formulation (6.36).

This turning of the edge-states polarization throughout the transitions seems to be less sensible to next-nearest neighbour coupling contributions compared to the localization length. While one could observe a disagreement between the measured IPR and the analytic formulation for $\theta = 90°$ in figure 6.5, the agreement between the experimental points and the theory in figure 6.9 is generally very good. It also seems that the finite system size does not have strong effects on the edge-states polarization.

The polarization of the edge states turns steadily for increasing bond angles θ, while right after the transition, the localization length shows a drastic change, which is followed by a steady and slow evolution for larger angles θ. When operating in this latter range of bond angles, changing θ will mainly change the edge states polarization, but its amplitude will only slightly change. This could lead to an application of such structure as polarizers. When engineering the couplings t^x and t^y in such a polarizer so that the critical angle

θ_c comes closer to 90°, only a small range of effective bond angles θ would be needed to describe the full accessible range of polarization from 0 to $-\pi/4$. Depending on the used materials of such photonic structures, a simple stretching and compressing along the principal axis of such a device could be enough to effectively modulate the zigzag bond angle θ. Thinking about optical applications, one could excite the edge states in such systems with unpolarized light, but the polarization of the resulting emission on each end of the chain could then be controlled by the its bond angle θ. In such optical applications, where typical length scales are much smaller and therefore precise manufacturing more challenging, the protection and robustness against disorder provided by these topological modes is also a huge advantage.

6.4 Conclusion

In this chapter we have investigated in detail the emergence of topological edge states in zigzag chains of coupled resonators, closely related to the well known SSH model. While the dimerization in the classical SSH model comes from alternating distances, we here used the anisotropic nature of the coupling between higher order p-modes of the resonators to induce a topological transition at a critical angle θ_c.

Zigzag arrays with a bond angle of $\theta = 90°$ have already been investigated by various groups, using many different photonic platforms. [27, 125–138] To recall a few works of special interest, a zigzag structure of polaritons was used in the first experimental realization of a topological laser [18] and in nanophotonics the robustness and spatial localization provided by the topological edge states, combined with the intrinsic non-linearity of silica was used to generate higher order harmonics [24]. While these are excellent examples of recent accomplishments and possible applications of topological photonics, only one other group has actually studied the topological transition experimentally [133], that can be described by deforming linear chains continuously into zigzag chains upon varying the zigzag bond angle from 0° to 90°.

We thus were not the first to study this transition experimentally, but the current advances in the control of the experimental platform, combined with new data treatment methods, allow us to obtain results that are unprecedented in terms of spatial and frequency resolutions. We were thus able to actually observe the opening of the band gap at the critical angle θ_c, accompanied by the emergence of localized edge states at each end of the chain.

Motivated by the observations of these strong hints of a topological transition, we performed an analytic study of the model and found that the system is indeed in a topological non-trivial phase for $\theta > \theta_c = 2\arctan\sqrt{|t^x/t^y|}$.

In order to quantitatively compare our results, we further investigated this model analytically, and formulated an expressions for the edge-state of the semi-infinite chains. These edge-states can essentially be described by their localization-length $\zeta(\theta)$ and their polarization $p(\theta)$.

Combining these analytic results with our experimental findings, we proposed the inverse participation ratio (IPR) of the central-frequency states as a good quantitative measure to follow the transition. Due to the divergence of the localization length ζ at the transition, the IPR shows a drastic increase at the transition, which we observed experimentally. For large bond angles we found discrepancies between experiment and theory. Modeling the system numerically, while considering all possible couplings between the resonators and not only the nearest neighbour coupling terms, we found that these discrepancies can be essentially explained by next nearest neighbour contributions that become more important for larger bond angles θ.

At the end of this chapter we compared the experimentally extract polarization p of the edge-states with the theoretical formulation, where we found a good agreement. The state's polarization is actually less sensible to next-nearest neighbour contributions. Engineering such photonic structures in a way, where the bond-angle θ could be easily changeable, may lead to further possible applications of such structures in controlling the polarization of electromagnetic radiation emitted from such type of arrays.

Chapter 7

General conclusion and outlook

In this thesis we have shown that with coupled microwave resonators, which act as simple photonic system, remarkable results can be achieved in the field of topological photonics. Compared to other highly engineered photonic systems, like cold atoms or polaritons, our platform is much simpler, and consequently more limited, yet very versatile. Despite this apparent simplicity, we had to invest a lot of work, in order to understand and control all the different aspects of the experiment. Starting with the unit cell of our platform, the single resonator, we performed analytic and numerical calculations of the single resonator's resonant modes that helped us to better understand the spatial profile of the modes, especially with the perturbation of the cylindrical symmetry by the additional airgap above the resonator.

Mechanical changes of the setup reduced experimental uncertainties, like the variance of the resonance frequencies or the precision with which we can place the resonators. It's especially due to these improvements that we were finally able to interpret our results and especially the extracted wavefunction amplitudes in quantitative ways, compared to qualitative comparisons done before. Another crucial aspect that allowed us to further push the boundaries of what is possible with the platform was the improvement in data-treatment methods. Besides the losses in our system, we can extract individual wavefunction with a great spectral and spatial resolution. It is due to this improved resolutions, that we were able to extract such fine quantities like the multifractality of Fibonacci chains in chapter 5. In chapter 6, where we followed a topological transition in zizzag chains, this improved resolution also allowed us to follow the central frequency states IPR and polarization throughout the transition. These latter two achievements can be seen as the major experimental results of this thesis.

Since each of these chapters 5 and 6, comes already with an individual conclusion, to avoid repetition, we will now rather focus on further possibili-

ties to make use of the experimental platform, which go beyond the systems presented in this thesis.

All systems studied during this thesis were 1D structures. A possible next step could therefore be to study similar quasi periodic and topological structures, but using two dimensional lattices. In the context of quasiperiodic systems, first steps in this direction have already been taken. The platform has already been used to study the famous 2D Penrose tilings, but with the infinite amount of possible 2D quasiperiodic tilings there is still a lot more that can be done in this regard. One family of 2D tilings, that may be of special interest are 2D tiling that still have a one dimensional codimensional/perpendicular space [105], as for example the Rauzy tiling [145]. Due to the physical couplings that are not constrained to the edges of the tiles, the tight-binding model implemented in our lattices is not the one usually theoretically and numerically studied and one can expect it to exhibit richer multifractal properties. One could also think of, as a next step, to introduce disorder into the systems. In the context of quasiperiodic systems, the effects of on-site disorder in the Fibonacci lattice were already studied theoretically [146]. Implementing on-site disorder with our platform is possible, but not simple, since we typically uses series of identical resonators, that all have very similar resonance-frequencies. One could think of other types of disorder, which are more easily implementable with our experimental platform. Either a coupling disorder, induced by small variations of distances between the resonators, or a phason disorder, resulting from a local inversion of short and strong bond and giving birth to configurations that cannot be obtained by permutations of the original sequence.

In recent years the interplay between topology and disorder has also gained much interest. While one could introduce disorder for example to test the robustness of topological protection [19, 20, 37, 134], it was also shown that for strong enough disorder, the system's topological invariant can change, thus transitioning into a new topological phase [134, 147–151]. Such disorder-induced topological transitions have not been studied a lot experimentally, and our experimental platform with its flexibility and reconfigurability seems suitable to tackle such interesting systems.

It would be also great to further use of the resonators p-mode. Only very few other experimental tight binding platforms make use of these higher order modes and it is especially the anisotropic nature of the coupling that could led to some very interesting systems, especially if extended to two dimensions. And of course it would also be possible to combine quasiperiodicity with these higher order modes.

Another aspect of the experimental platform, that was only shortly mentioned in the introduction is the fact, that we can generate non-linear systems by coupling the resonators to diodes. A few measurements in that direction

have already been done. By coupling a diode to a defect-site in a classical SSH chain, we have been able to realize a topological reflective power limiter [39, 152]. As a next step in that direction of combining nonlinearity and topology could be to employ several diodes and couple them for example only to a single sublattice of the system. A simple 1D chiral system with distinct sublattices could be SSH chains, but simple 2D lattices should also be possible. Of course one could also think of systems, that are not directly related to topology, but which still benefit from the richness that non-linear interactions can provide. Already a single resonator strongly coupled to two antennas leads to a very interesting dynamical system with an exceptional point. When close to this exceptional point, we were able to observe broadband nonlinear perfect coherent absorption [28, 153]. Next steps in this direction could be to embed this single non-linear resonator into more complex structures, which could be other resonators, or network structures like graphs [154], that could result in chaotic systems. In this latter context, the interplay between non-linearity, chaos [155] and exceptional points [156, 157] can give access to very interesting physical phenomena. Only few experimental works have been done in this regard[158, 159], but the understanding of such effects can be crucial for our modern world and its communication systems, where we make us of all types of waves propagating inside highly complex networks.

Appendix A

Baseline calibration for reflection spectra

We can calibrate the VNA using terminations at the end of the cables with well known impedances, hereby correcting phase and amplitude modulations coming from the waves propagating inside the cable. But this does not get rid of the phase and amplitude modulation created by the antennas themselves and its surrounding in the near-field.

Fortunately there is a simple solution to that. Assuming the ideal reflection spectrum of the system is $S(\nu)$. The amplitude and phase modulation caused by the antenna can be modeled as a factor $m(\nu)$, so that the measured signal can be written as $S_{\text{meas}}(\nu) = m(\nu)S(\nu)m(\nu) = m(\nu)^2 S(\nu)$. Since the empty cavity should ideally have $S(\nu) = 1$, the measured spectrum of the empty cavity gives us access to $S_{\text{meas}}^{\text{empty}}(\nu) = m(\nu)^2$. Therefore in order to correct our measured data, we simply have to divide it by the reflection spectrum of the empty cavity $S(\nu) = S_{\text{meas}}/S_{\text{meas}}^{\text{empty}}(\nu)$. Measuring the reflection spectrum of the empty cavity locally, for each antenna position separately, we can additionally account for small changes within the local environment of the antenna (such as other antenna holes or a slightly varying cavity height) and compensate deficits of the VNA's calibration. The VNA is calibrated for a certain curvature of its cables. When the antenna is moved, this curvature is changed, which additionally induces very small modulations in phase and amplitude.

In figure A.1 one can see the measured spectrum of a single resonator, the reflection spectrum of the empty cavity, measured at the same antenna-position and its corrected spectrum. As one can see, with the correction, we effectively get rid of the varying phase factor, and also correct modulation in the amplitude, which result in a much cleaner baseline. We can observe that, in a first approximation, the phase-factor shows a linear frequency-dependency. We assume this comes mainly comes from the propagation within the antennas and

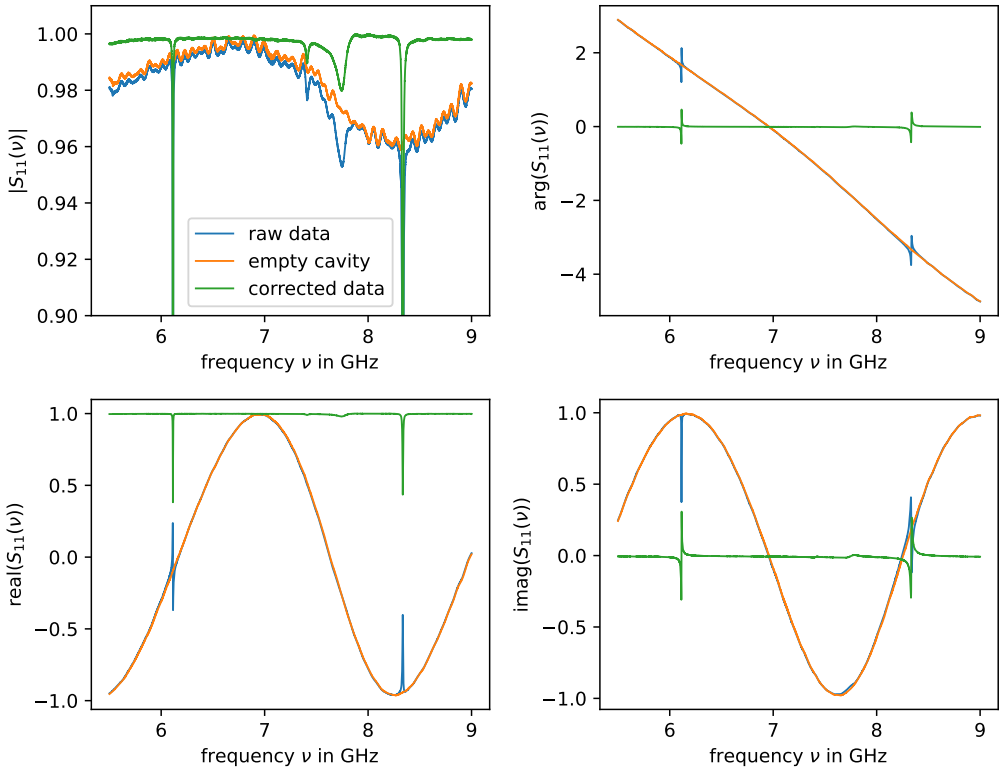

Figure A.1 – Raw reflection spectrum of the empty cavity (orange line) and of a single resonator (blue line), measured at the same antenna-positions, together with its corrected spectrum (green line).

the phase factor is then given by $\phi = 2\pi\nu L/c_0$, where L is approximately two times the effective antenna length. By performing a linear fit of the phase, we find $L = 10.6\,\text{cm}$, which is consistent with the expected effective antenna length. Waves will travel only at about 2/3 of the speed of light inside coaxial cables. Since the antenna mainly consists of a bend coaxial cable, the fitted $L = 10.6\,\text{cm}$ results in a one-way geometrical length of $\approx 3.5\,\text{cm}$, which equals more or less the combined length of the loop, the vertical part of the antenna and its SMA connector.

Appendix B

Extraction of wavefunctions for the Fibonacci chains

For small system where the resonance peaks in the spectrum are sufficiently separated, the wavefunctions of the system can be obtained by direct fitting the spectra with a sum of complex Lorentz lines. For the long chains of resonators, studies in chapter 5, this is not possible as the overlap between individual resonances peaks is to strong. To extract the LDoS(i, j), we thus developed two different techniques depending weather we work with the linear chains of 55 resonators or the circular chains of around 100 resonators. For the linear chains we use a harmonic inversion method to extract all resonances and then use a clustering algorithm to assign the resonances to the different states. For the circular chains we directly integrate $1 - \Re S_{11}(i, \nu)$ using different, non overlapping frequency windows for each state. The latter technique is also used to extract the LDoS for the silver mean chains.

Contents

B.1 Linear chains

The linear chains are constituted of 55 resonators. To average over different permutations we measure different configurations of the chain, as detailed in

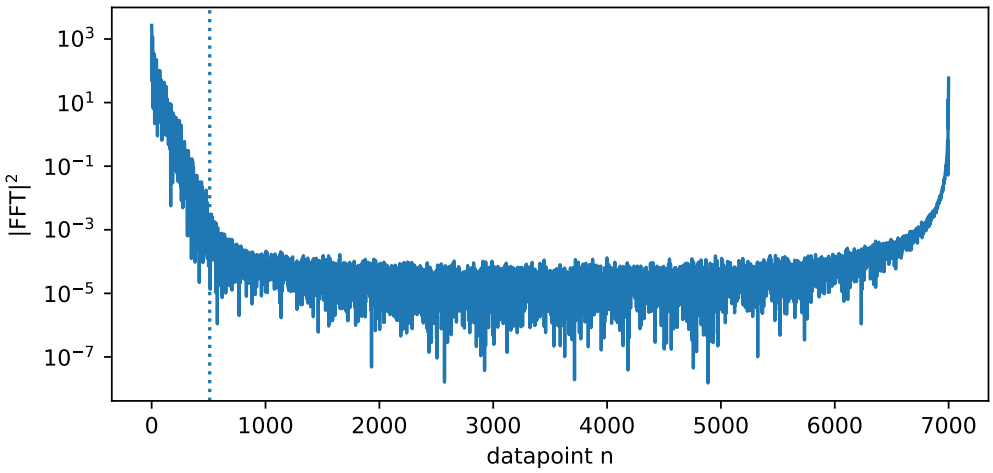

Figure B.1 – Fast Fourier Transform of the spectrum presented in figure 5.4, which results in a discrete time-signal. The dotted vertical line marks N_{trunc}, the number of points that we use to formulate the non-linear set of equations.

section 5.2.3. A picture of one configuration, with dominant weak coupling and its measured spectrum can bee seen in figure 5.4, where one can clearly see the overlapping between resonance peaks.

B.1.1 Harmonic inversion and clustering

In order to extract all resonance-amplitudes for each configuration we use a method based on an algorithm called Harmonic Inversion [53, 58, 59]. The basic idea of this method is also outlines in section 2.3.2. It is based on the fact that in the time-domain a complex Lorentz-line gives rise to an exponential function. Supposing that the time-signal (discrete signal with 2N points) only consists of N exponential functions with different complex amplitude and exponents, one can establish a set of non-linear equations in order to determine all of their parameters.

The first step therefore consists of Fourier transforming the spectrum using the FFT method in order to obtain a discrete time-signal. The Fourier transform of the spectrum presented in 5.4 can bee seen in figure B.1.

The spectra are measured from 7.1 GHz to 7.8 GHz with a step size of 100 kHz resulting in 7001 data-points. Due to the typical resonance-widths of a few MHz, which is one order of magnitude greater than the frequency step size the time signals decays rapidly within a few hundred data-points. The rather linear decay that can be observed (on the left) in the logarithmic scaled plot

in figure B.1, confirms the exponential decay expected for Lorentzian shaped resonances. All information about the systems resonances can be extracted from this decay. In order to establish the set of non-linear equation to extract all complex resonance-positions and amplitudes, we therefore select only the first N_{trunc} data-points. For this series of experiments, we chose $N_{\text{trunc}} = 510$. For other experiments, N_{trunc} typically ranges from 200 to 650. We always chose N_{trunc} in a way that we include most of the exponential decay, without it being unnecessarily large, since the greater N_{trunc}, the more time is needed for the computation. Additionally due to the way the set of non-linear equations is formulated, the algorithm always finds $N_{\text{trunc}}/2$ "resonances". A huge portion of these "resonances" have vanishing amplitudes and/or are "resonances" that form the baseline or mimic the small variations in the spectra induced by noise. We thus have to proceed and filter out resonances according to their width, frequency, phase and intensity to reduce the result to real resonances only. Here, a small N_{trunc} is also desired so that we have less resonances that we have to filter out.

We choose the filters such that we typically still find more resonances than actually should be present in the spectra, so we can be sure to not accidentally filter out real resonances of the system. We thus use a clustering algorithms [60] that regroup resonances that are appearing for different antenna positions around one frequency with similar width and assign them to a state. False "resonances" typically appear as noise in between the clusters, since their origins are not the intrinsic resonant structure of the system, but rather fluctuations and baseline effects that are different for each measured spectrum.

In figure B.2 one can see the extracted resonances from reflection spectra measured over each resonator for one configuration, where the different clusters are visualized using different colors. As already explained in 5.2.3, we limit the extraction to the lower and central frequency band, since for the higher frequency band, due to an increase in the resonance-widths the resonances are stronger overlapping making the data treatment impossible. The resonances were already filtered by their width and intensity, but a few false "resonances" remains. These false "resonances" where successfully omitted in the clustering process and the final clusters only contain real resonances.

For each cluster j, we then expect to have only one resonance for each antenna-position. The amplitudes of the resonance found in the spectrum measured over resonator i then corresponds to $|\psi_j(i)|^2$, the wavefunction intensity of state j at resonator i. In practice there are some rare cases where within the same cluster there are two resonances for the the same position. In such cases we decide to use the resonance, with the greater resonance-amplitudes.

We use this method to extract the wavefunctions for all measured configurations. In section 5.2.3, we only present the LDoS for one configuration and

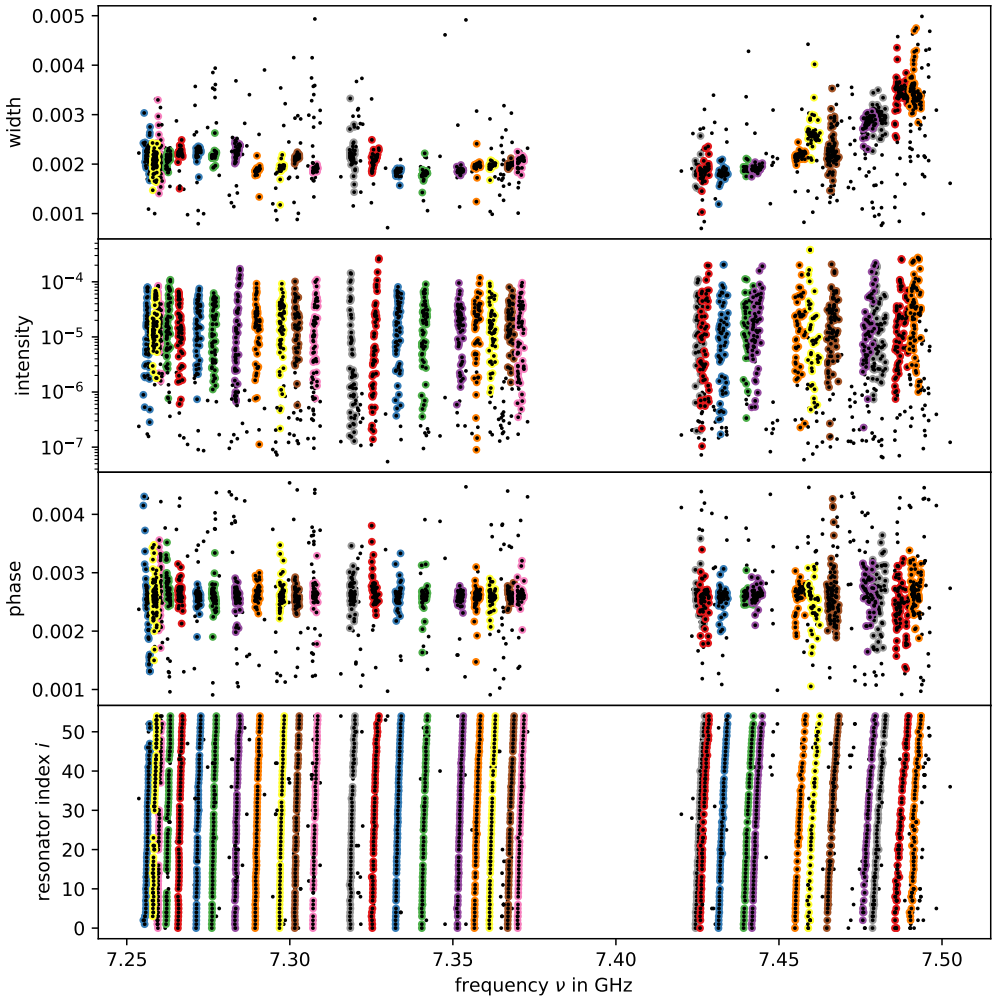

Figure B.2 – Filtered resonances, extracted using the harmonic inversion method applied to reflection measurements taken over each resonator of one configuration. From top to bottom we plot the resonance-width, the resonance-intensity, the phase of the resonance-amplitude and the index i of the resonator over which the measurement were taken, all as a function of the resonance-frequency. With the use of an clustering algorithm, we can group resonances that are appearing for different antenna positions around one frequency with similar width and assign them to a state. The found clusters are then highlighted by different colors.

the mean LDoS, obtained by averaging over all configuration. In the following one can thus find the LDoS (arranged according to their position index i and rearranged according to the conumber index $c(i)$) for all measured configurations for the both cases of weak and strong dominant coupling.

B.1.2 LDoS of all configurations: Dominant weak coupling

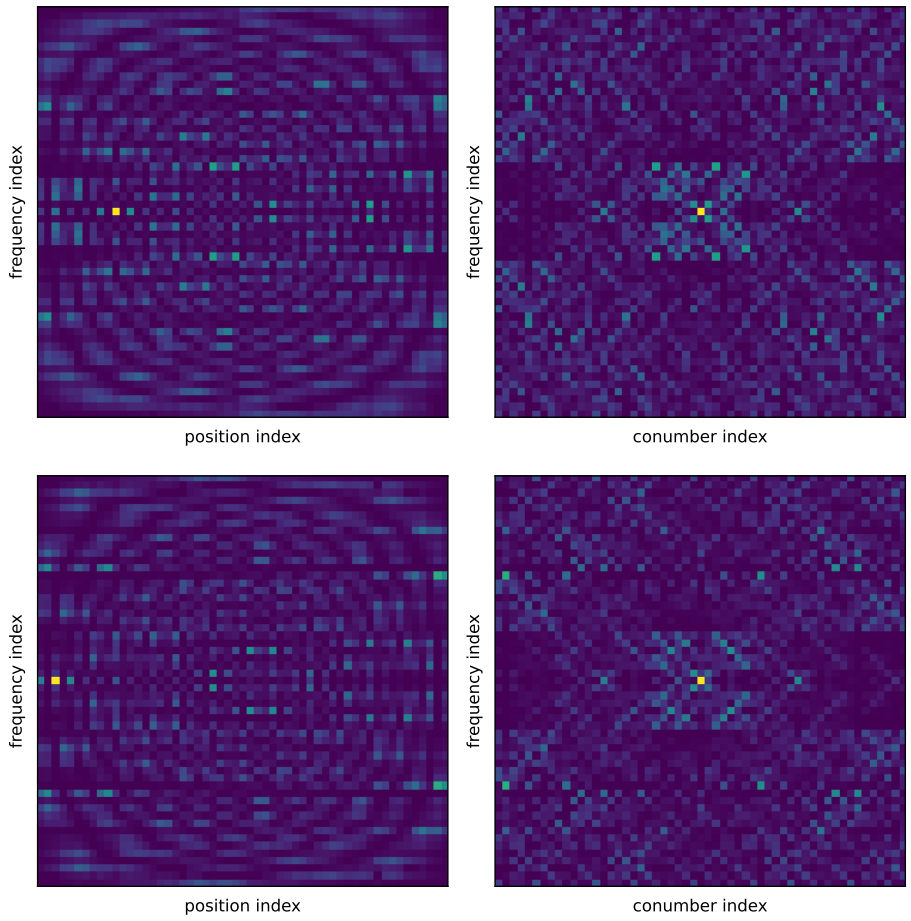

Figure B.3 – Experimentally extracted LDoS for configuration 1 (top) and configuration 2 (bottom) for $\rho < 1$, arranged according to their position index (left) and rearranged according to their conumber index (right).

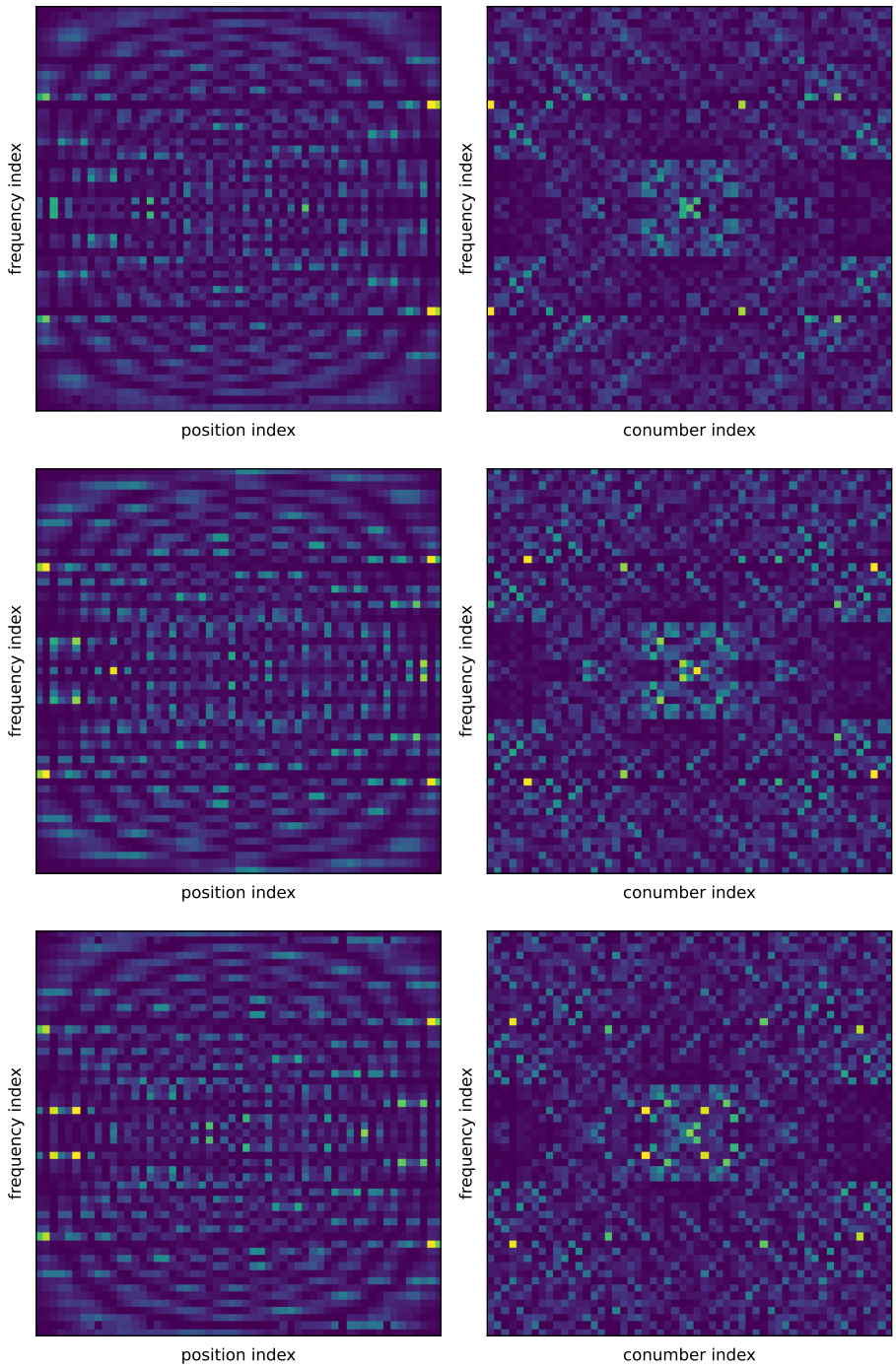

Figure B.4 – Experimentally extracted LDoS for configuration 3 (top), configuration 4 (center) and configuration 5 (bottom) for $\rho < 1$, arranged according to their position index (left) and rearranged according to their conumber index (right).

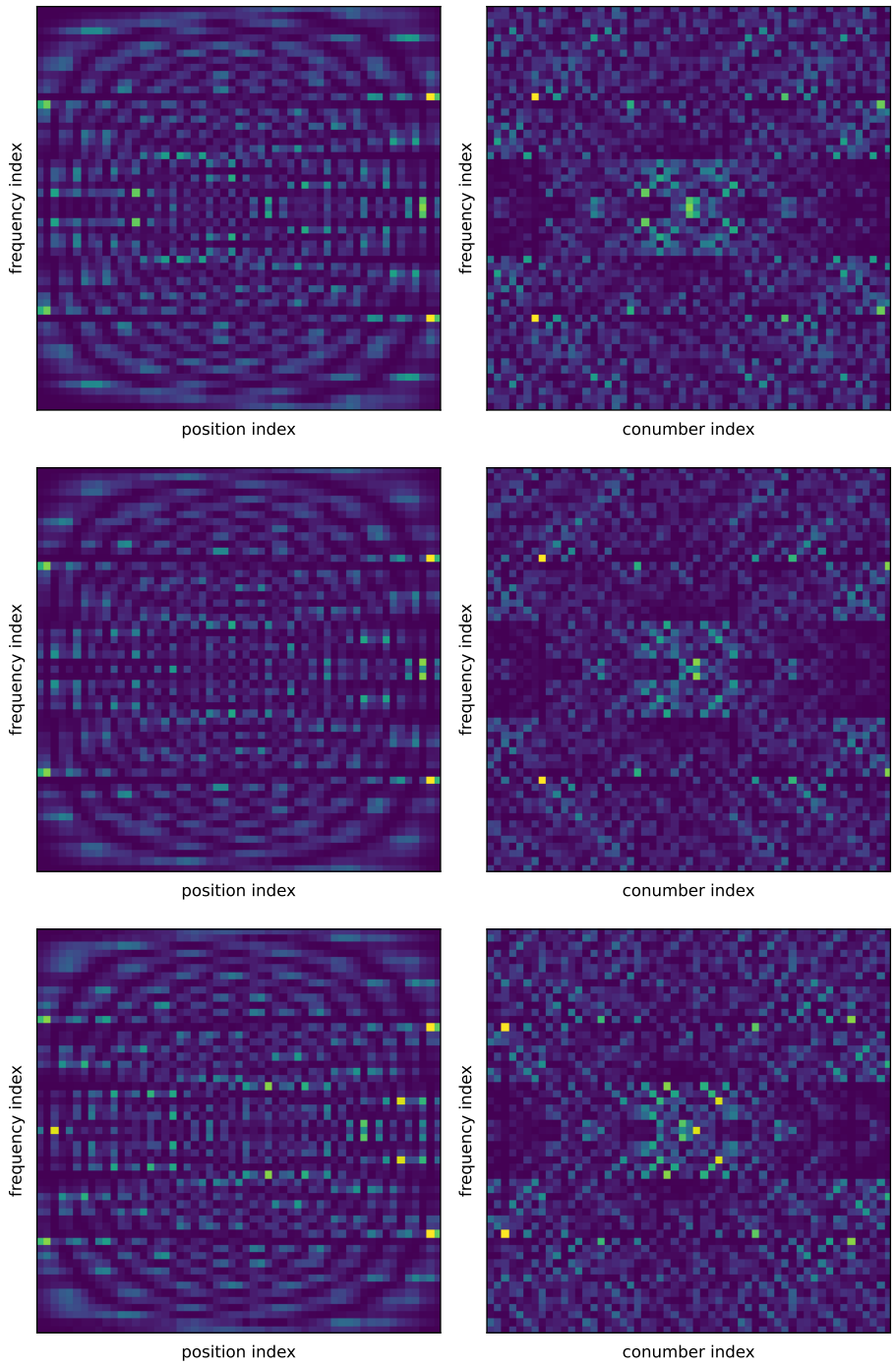

Figure B.5 – Experimentally extracted LDoS for configuration 6 (top), configuration 7 (center) and configuration 8 (bottom) for $\rho < 1$, arranged according to their position index (left) and rearranged according to their conumber index (right).

B.1.3 LDoS of all configurations: Dominant strong coupling

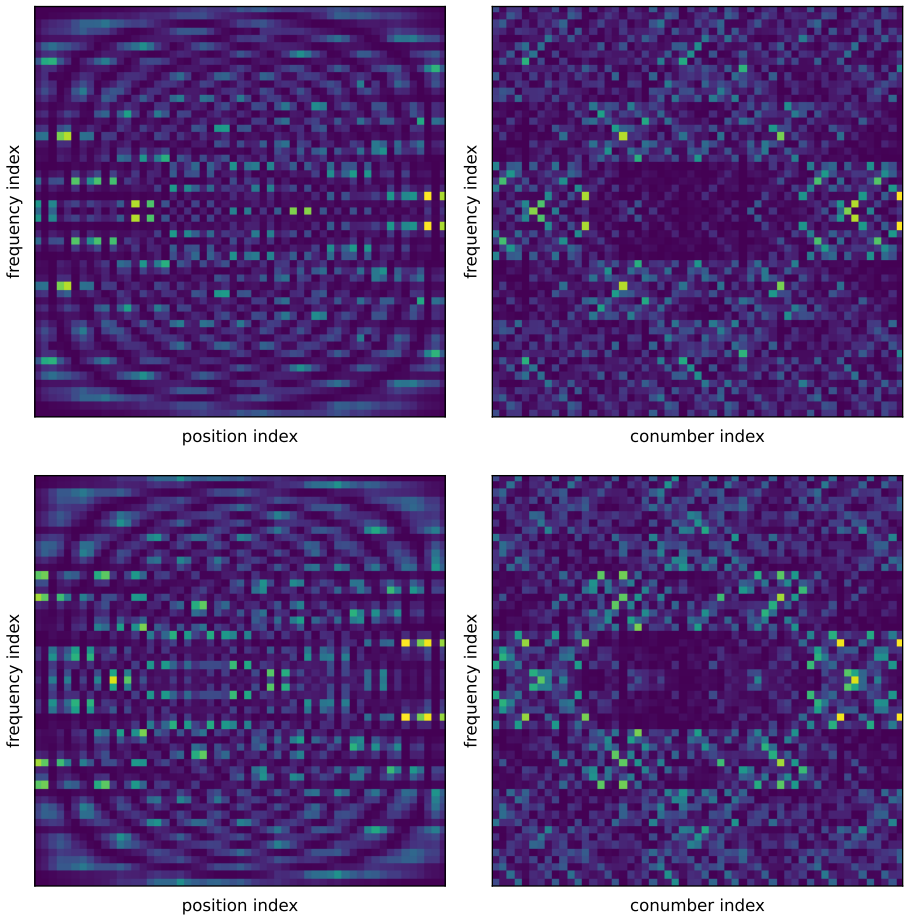

Figure B.6 – Experimentally extracted LDoS for configuration 1 (top), configuration 2 (bottom) for $\rho > 1$, arranged according to their position index (left) and rearranged according to their conumber index (right).

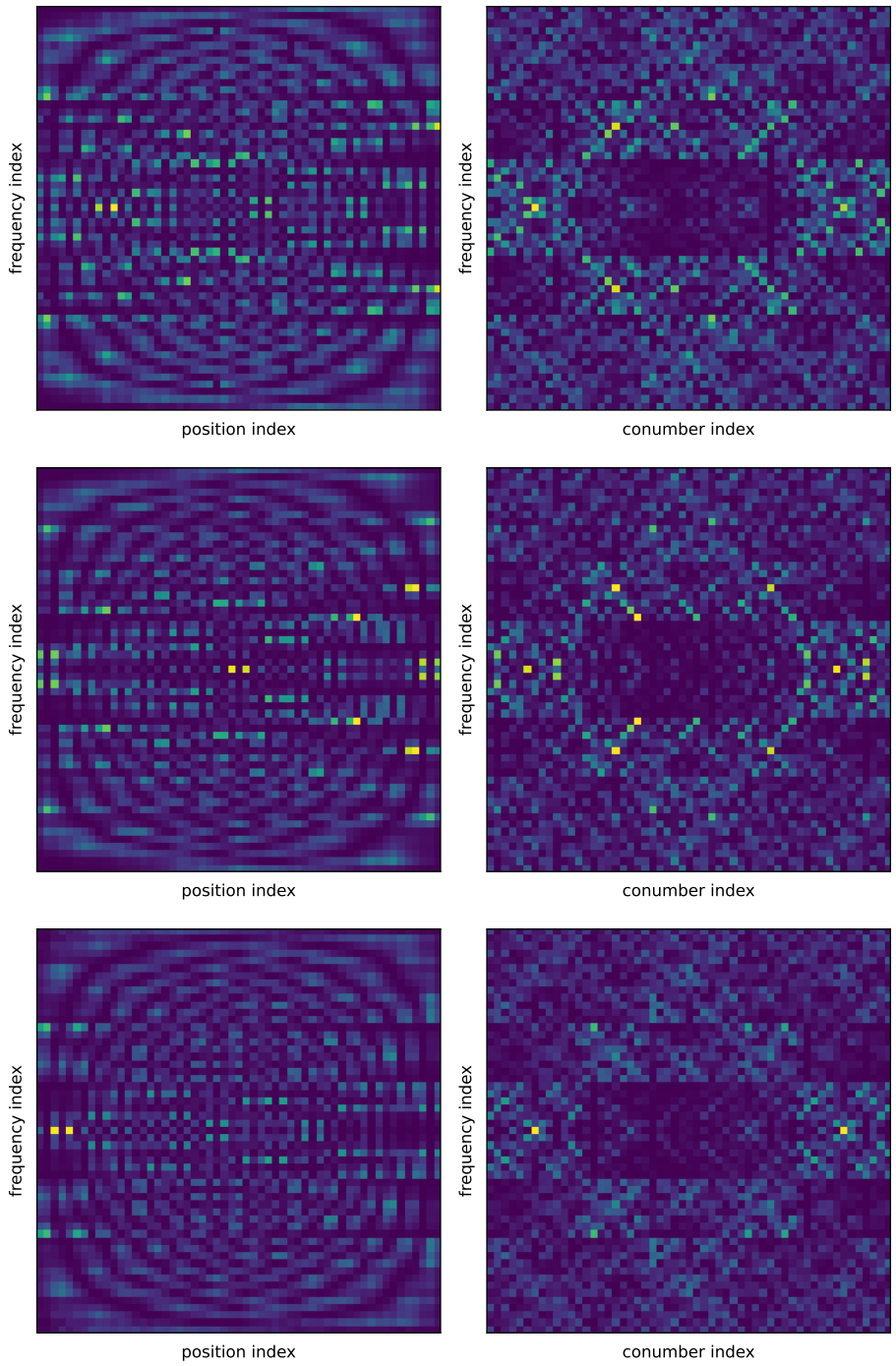

Figure B.7 – Experimentally extracted LDoS for configuration 3 (top), configuration 4 (center) and configuration 5 (bottom) for $\rho > 1$, arranged according to their position index (left) and rearranged according to their conumber index (right).

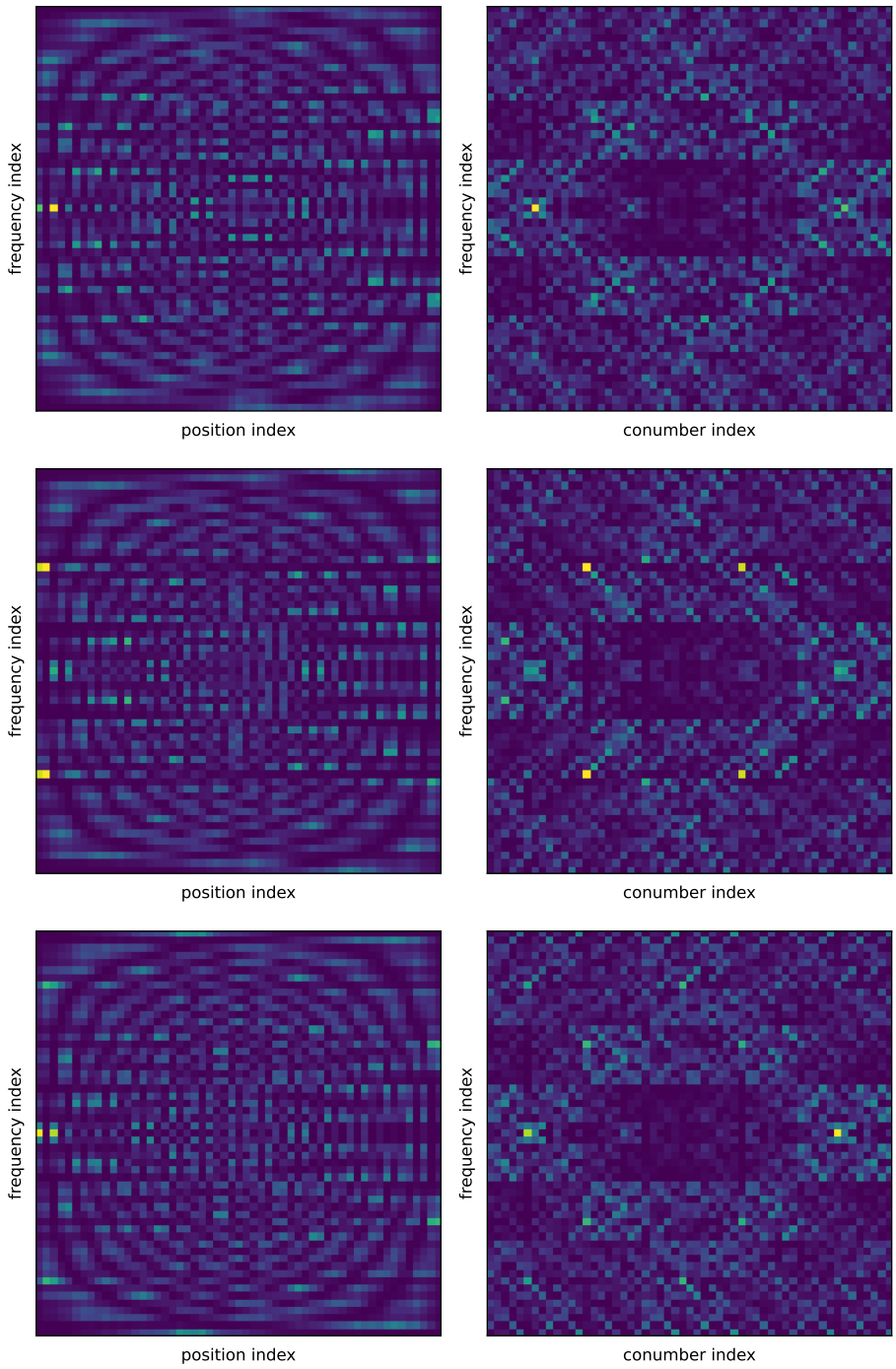

Figure B.8 – Experimentally extracted LDoS for configuration 6 (top), configuration 7 (center) and configuration 8 (bottom) for $\rho > 1$, arranged according to their position index (left) and rearranged according to their conumber index (right).

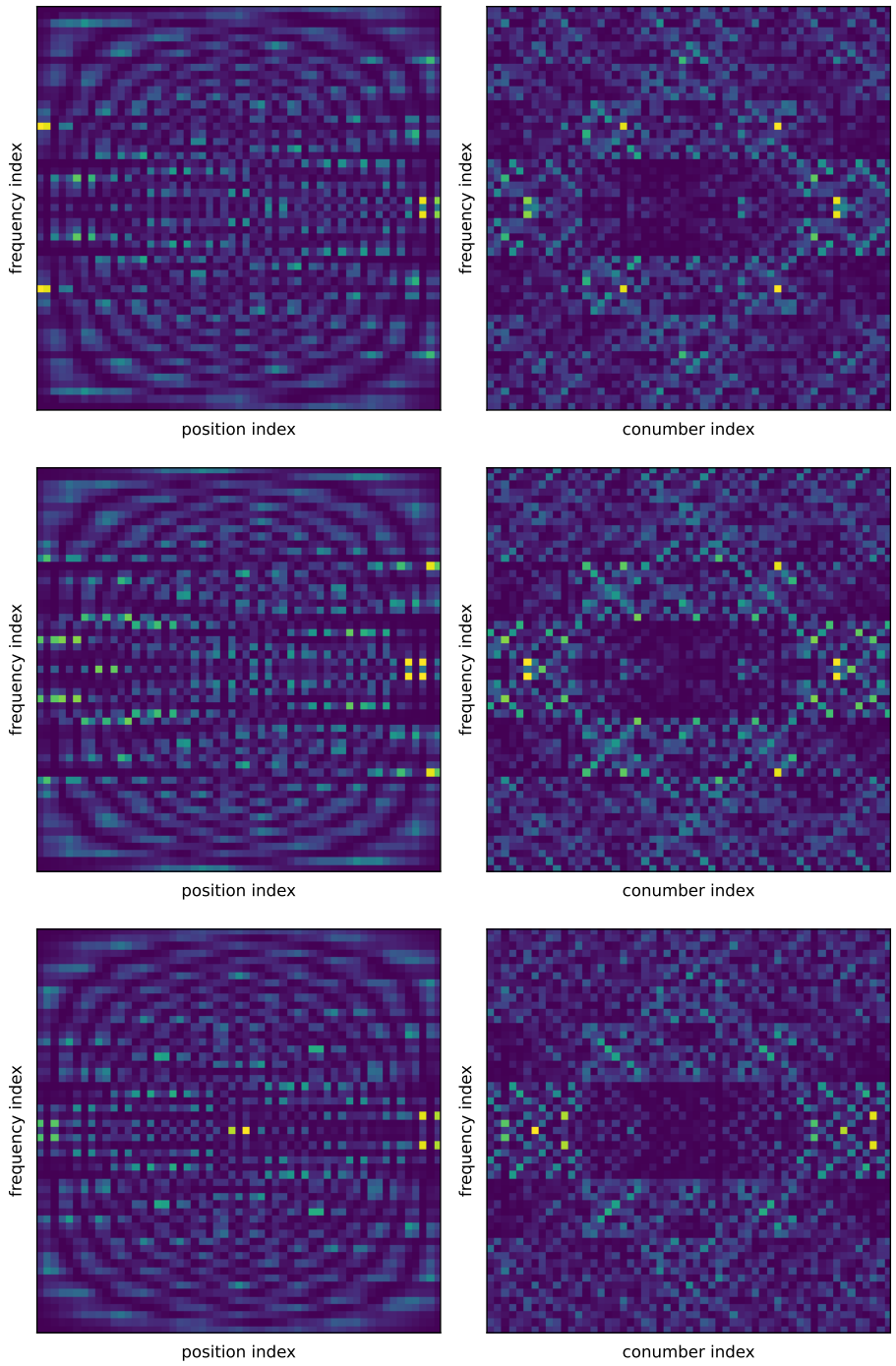

Figure B.9 – Experimentally extracted LDoS for configuration 9 (top), configuration 10 (center) and configuration 11 (bottom) for $\rho > 1$, arranged according to their position index (left) and rearranged according to their conumber index (right).

B.2 Circular chains

The circular chains are made up of smaller motifs (i.e. $F_n = 3, 5, 8, 13, 21$), that we repeat N_p times, while imposing a weak coupling between two consecutive repetitions. The number of iteration N_p is chosen such that a ring of around 100 resonators is build for each F_n-motif. In this way, the F_n frequency bands expected for an infinite chain C_n are each populated with N_p states, and can be individually identified in each reflection spectrum $S_{11}(i, \nu)$ measured over each resonator i.

We can recall from section 2.3.3

$$1 - \Re S_{11}(\vec{r}_i, \nu) \propto \rho(\vec{r}_i, \nu) = \sum_k^N f_{\nu_k,\Gamma_k}(\nu) \cdot |\psi_k(\vec{r}_i)|^2, \tag{B.1}$$

where $f_{\nu_n,\Gamma_n}(\nu)$ are normalized Cauchy distributions around ν_n with width Γ_n. Rearranging the sum over the different states, one can re-write

$$\rho(\vec{r}_i, \nu) = \sum_{j=1}^{F_n} \sum_{p=1}^{N_p} f_{\nu_{j,p},\Gamma_{j,p}}(\nu) \cdot |\psi_{j,p}(i)|^2, \tag{B.2}$$

where $\nu_{j,p}$ and $\Gamma_{j,p}$ are the resonance-frequency and -width of the p-th state within the j-th frequency band and $|\psi_{j,p}(i)|^2$ the corresponding wavefunction intensity measured over resonator i.

Supposing that the bands are sufficiently isolated, by integrating each frequency band j individually, one can then find

$$\mathrm{LDoS}(i, j) \propto \int_{\text{band } j} [1 - \Re S_{11}(i, \nu)] \, \mathrm{d}\nu, \tag{B.3}$$

where we can further average over all indices i that have the same conumbering $c(i)$.

In figure B.10 (left column) one can see the measured density of states $\mathrm{DoS}(\nu) = \langle 1 - \Re S(i, \nu) \rangle_i$ for all $F_n = 3, 5, 8, 13, 21$. Determining the integration borders of each band j is obvious for $F_n = 3$ and 5, where the F_n frequency bands are isolated and well separated by clearly visible gaps. While for $F_n = 8$ one could eventually still identify 8 bands, although some gaps in between are closing, it becomes impossible for higher n to directly identify all frequency-bands. We therefore use a method that exploits the normalization of each state, to further define the integration border for bands that are not separated by a clear gap.

B.2.1 Defining integration borders

We calculate the integrated density of states $\mathrm{iDoS}(\nu) = \int^{\nu} \mathrm{DoS}(\nu')\mathrm{d}\nu'$, that we normalize so that when integrating over all states the $\mathrm{iDoS}(\nu)$ equals F_n, the total number of bands ($\int \mathrm{DoS}(\nu')\mathrm{d}\nu' = F_n$). Theoretically in the limit of $\Gamma \to 0$ and perfectly normalized wave functions, we would obtain a staircase function where we would have F_n big steps with step-height 1, that are constituted of N_p smaller steps, with height $1/N_p$. Since the step corresponding to a single band has a height of 1, one could think of intersecting the $\mathrm{iDoS}(\nu)$ with a set of horizontal lines that have a spacing of 1 in between them. The found intersecting points ν_k^* ($\mathrm{iDoS}(\nu_k^*) = k$, for all $k \in (0, 1, 2, ..., F_n)$ could then define the integration intervals for each band.

Due to the non-zero linewidth of our resonances, the N_p smaller steps within a band are completely blurred, while only the plateaus corresponding to the well visible gaps, remain. Since the antenna-coupling σ is slightly dependent on the frequency, and the single resonance wavefunctions are slightly overlapping [29], the different states are not properly normalized in the experiment, which translates to slighlty different step-heights in the iDoS. So just intersecting the experimental iDoS with equally spaced lines, does not work very well, as can be seen for the case of $F_n = 3$, where the two clearly visible plateaus are not at $\mathrm{iDoS}(\nu) = 1$ and $\mathrm{iDoS}(\nu) = 2$, as expected if properly normalized, but slightly higher. We thus use a hybrid approach where we take the frequency-positions of the clearly visible gaps as fixed references and find the frequency-position of the vanished gaps in between by intersecting the iDoS in between with equally spaced lines. The position of the visible gaps are extracted by hand and marked as solid black vertical lines in the first two columns of figure B.10. At the positions where the solid black lines intersect the iDoS we draw solid blue horizontal lines. For $F_n = 3, 5, 8$ we were able to identify all gaps, so the solid blue lines divide the iDoS in F_n intervals, but as explained earlier for $F_n = 13, 21$ not all gaps can be identified. Whenever we could not identify a gap, we draw additional blue dashed horizontal lines, that equally divide the space in between the two solid blue lines by the number of bands that we expected to be in between the clearly visible gaps. In order to not adjust our results by our expectations we estimate the number of bands in between two clearly visible gaps (solid blue lines), by rounding the position where the blue lines intersect the iDoS-axis to the nearest integer value and suppose that this is the number of bands below that gap. That way we determine the number of bands in between two solid blue lines. At the frequencies where the dashed blue lines intersect the iDoS we draw dashed black vertical line. The black vertical (solid and dashed) lines then define the integration boundaries, that we use to integrate each individual spectrum measured over

each resonator, leading to LDoS(i, j).

The results can be seen in figure B.10, where LDoS(i, j) is plotted ordered according to the resonator position indexes i (third column) and to the conumber indexes $c(i)$ (forth column). By averaging LDoS$(c(i), j)$ over all sites that share the same conumber index, one obtains the smoothed patterns plotted on figure 5.9.

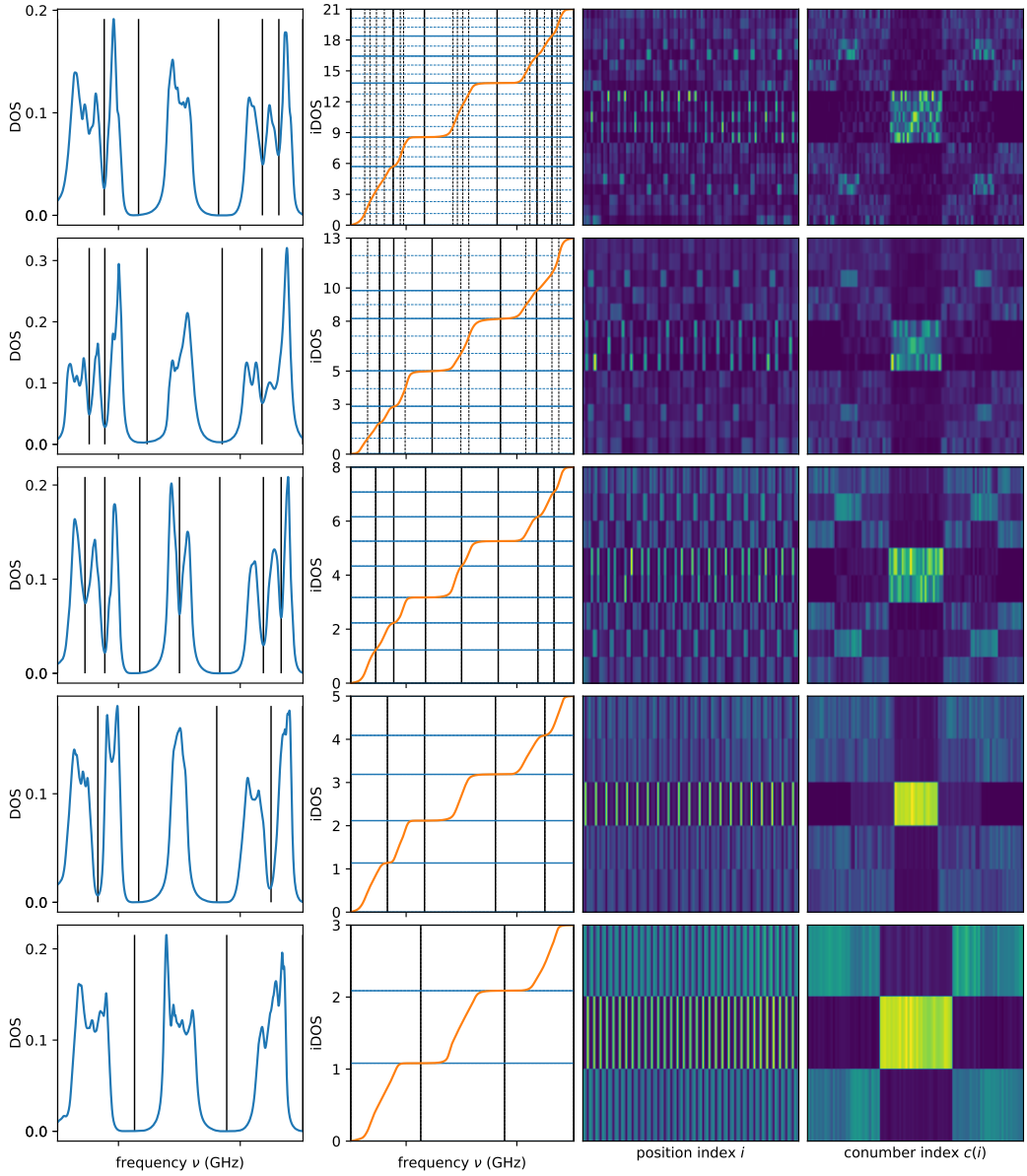

Figure B.10 – The different steps of the data treatment procedure for the circular chains with (first row) $F_n = 21$, (second row) $F_n = 13$, (third row) $F_n = 8$, (forth row) $F_n = 5$ and (fifth row) $F_n = 3$. For each chain we plot (from the left the right) (first column) the density of states DoS(ν) and (second column) the integrated density of states iDoS(ν) as a function of the frequency ν. The black and blue horizontal and vertical lines define the integration boundaries to extract LDoS(i, j), that are arranged according to the position index i (third column) and conumber index $c(i)$ (forth column). The vertical axis of the third and forth column corresponds to the frequency-index j.

Appendix C

Numerical results for the fractal dimensions of wavefunctions

In this appendix we explain in detail how the confidence interval (grey area in figure 5.7) for the experimentally extracted fractal dimension was calculated by simulating the experimental chains with simple TB Hamitonians, that account for fluctuations in the resonance frequencies and positions of the resonators. We also numerically calculate the fractal dimensions for large n. This reveals that the noticeable offset for large q between the theoretical curve and the experiment data in figure 5.7 arises mainly from finite-size effect.

Contents

C.1 Calculation of the confidence interval

In Fig. 5.7 one can see the calculated experimental fractal Dimension $\overline{D_q^{\psi}}$, the theoretical prediction as well as an confidence interval for our measurement. Both the positioning of the resonators as well as the resonance frequency of each resonator have a small variance (see section 3.3 for a details characterization of the experimental fluctuations), which leads to slightly different tight-binding Hamiltonians, wavefunctions and thus fractal dimensions each time one would perform the experiment.

The fluctuation of the resonance frequencies have two origins. To place the resonators, we let them drop through a small precision machined down-

tube and then apply slight pressure via an plastic rod on top of the dielectric cylinders. This ensures a good electrical contact between the bottom plate and the resonator, but upon replacing the same resonator several times, the measured resonance frequencies of the very same resonator still vary slighly with a standard deviation of $\approx 0.5\,\mathrm{MHz}$. Further, the resonators are not identical, resulting in different resonance frequencies as well. Out of a series of 500 resonators, whose resonance frequencies follow approximately a normal distribution with a width of 40 MHz, we chose the 55 resonators that have the closest resonance frequencies. This results in a difference between the extreme resonance frequencies of $\approx 3\,\mathrm{MHz}$. Since the span of 3 MHz is small compared to the width of the distribution of resonance frequencies for the whole series, we suppose that they follow a quasi linear distribution. In addition, we have small variations within the positions upon placing the resonators, that result in slightly varying coupling strength's. In space, these fluctuations are of the order of 0.05 mm, that induces in the worst case (smallest distance between resonators) a variation of 4% of the coupling strength.

In order to estimate the impact of these experimental fluctuation on the extracted fractal dimensions, we simulate the experiment by formulating simple tight binding Hamitonians for the 11 different permutations. We model the resonators resonance frequencies $\nu^* \sim 7.454\,\mathrm{MHz} + \mathcal{U}(-1.5\,\mathrm{MHz}, 1.5\,\mathrm{MHz}) + \mathcal{N}(0, \sigma_\nu)$ by employing a uniform distribution $\mathcal{U}$ with a span of 3 MHz combined with a normal distribution $\mathcal{N}$ with $\sigma_\nu = 0.5\,\mathrm{MHz}$ centered around 7.454 GHz, that accounts for the variation of the resonance frequencies upon the placing of the resonators. With $\{\vec{r}_i\}$ being the exact positions that follow the Fibonacci sequence, we suppose that the actual positions of the resonators $\{\vec{r}_i^*\}$ follow $\vec{r}_i^* \sim \vec{r}_i + \mathcal{N}(0, \sigma_{\mathrm{pos}})$, supposing a normal distribution with a standard deviation of $\sigma_{\mathrm{pos}} = 0.5\,\mathrm{mm}$ in the x and y direction. We then calculate the coupling strength between all nearest neighbours i and k, by calculating their distances $d_{ik} = |\vec{r}_i^* - \vec{r}_k^*|$ and using the relation $t(d) = 63.2\,\mathrm{MHz} \cdot K_0(0.481\,\mathrm{mm}^{-1} \cdot d/2) \cdot [K_2(0.481\,\mathrm{mm}^{-1} \cdot d/2) + K_0(0.481\,\mathrm{mm}^{-1} \cdot d/2)]$ between coupling strength t and separation d between two resonators that was extracted from two-resonator measurements in section 4.2.1. We diagonalize the Hamitonians in order to find the wavefunctions, average over the different permutations and determine the fractal Dimensions D_q^* via the same box-counting method that we use for the experiment. We perform this procedure 10000 times and then for each q the 5-th percentile and 95-th percentile of the distribution of D_q^* are used as the lower and higher contour line of the grey area in Fig. 5.7 respectively, defining a sort of 90% confidence interval.

There is a noticeable offset for large values of q between the experimental $\overline{D_q^\psi}$ and the theory. The fact the values for one experimental realization

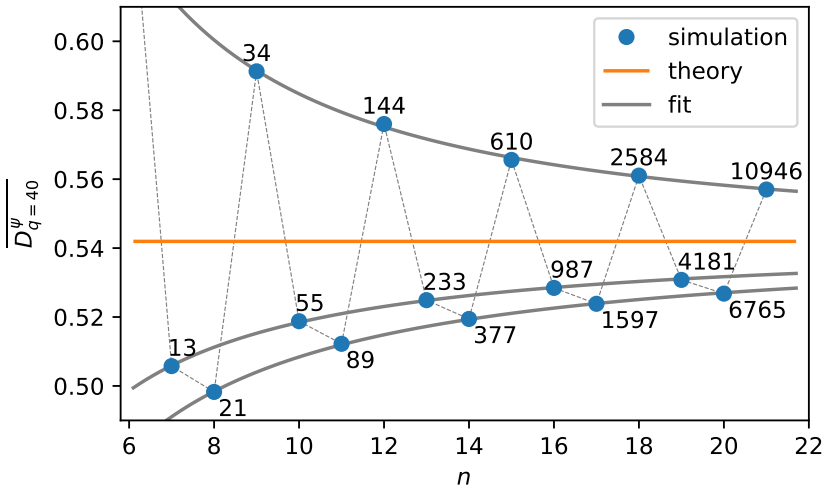

Figure C.1 – Simulated spectrally averaged fractal dimension $\overline{D_{q=40}^\psi}$ for a high value of $q = 40$ as a function of the iteration index n (blue points). The numbers near the blue points are the system size/motif length F_n for each iteration. The orange line presents the theoretical value of the fractal Dimension of the quasiperiodic system $\overline{D_{q=40}^{\text{theo}}}$. The grey solid lines are fits of the form $D(n) = An^B - y_0$.

have an offset could be explained by experimental fluctuation, since both the experimental points as well as the theoretical curve lie within the confidence interval, but the average values of the simulated D_q^* (white dashed line within the grey area in Fig. 5.7) shows an offset compared to the theoretical curve as well. Next-neighbour couplings within the actual experiment and the way we average over the 11 permutations play certainly a small role, but this offset mainly arises form the finite system size of $F_n = 55$ as we will show in the following.

C.2 Convergence of $\overline{D_q^\psi}$ to the theoretical prediction for increasing order n

In Fig. C.1 one can see calculated fractal dimensions $\overline{D_{q=40}^\psi}$ for different system sizes F_n for a high value of $q = 40$ and $\rho = 0.64$. Since here we only want to compare the effect of the system size, we simulate the only-nearest neighbour tight-binding system of the n-th periodic approximant of infinite size by formulating a closed chain of F_n resonators (one single motif) and F_n couplings where we vary over the phase of the connecting coupling between

the first and last resonator to account for the periodicity. One can see that the fractal dimensions converge to the theoretical value in the quasi periodic limit $n \gg 1$, with an oscillating behaviour. A quick explanation of this feature can be given, when looking into the central/most localized state. If the system size is an uneven number the central state is localized only at the central site, while for an even system size, the central state is localized at the two central positions of $c(i)$. It is thus less localized and therefore it has a greater fractal dimension. Since numerically it is very costly to diagonalize very large matrices, we stop ourself at a system size of $F_{21} = 10946$, which still has a noticeable offset compared to the theoretical value. Then in order to verify that the values converge to the theoretical one, we fit the apparent three different subsets with an algebraic decay $D(n) = An^B - y_0$, where we suppose the same exponent B and offset y_0 for all subsets but with different amplitudes A. We find $B = -1.298$ and $y_0 = 0.540$, which corresponds reasonably well to the theoretical value $\overline{D^{\text{theo}}_{q=40}} = 0.542$, considering that the theory was formulated in the strong modulation regime $\rho \ll 1$, where we are far off with $\rho = 0.64$.

Bibliography

[1] K. v. Klitzing, G. Dorda, and M. Pepper. « New method for high-accuracy determination of the fine-structure constant based on quantized Hall resistance ». *Phys. Rev. Lett.* **45**, 494 (1980).

[2] K. v. Klitzing, T. Chakraborty, P. Kim, V. Madhavan, X. Dai, J. McIver, Y. Tokura, L. Savary, D. Smirnova, A. M. Rey, C. Felser, J. Gooth, and X. Qi. « 40 years of the quantum Hall effect ». *Nat. Rev. Phys.* **2**, 397 (2020).

[3] T. Ando, Y. Matsumoto, and Y. Uemura. « Theory of Hall Effect in a Two-Dimensional Electron System ». *Journal of the Physical Society of Japan* **39**, 279 (1975).

[4] J.-i. Wakabayashi and S. Kawaji. « Hall Effect in Silicon MOS Inversion Layers under Strong Magnetic Fields ». *Journal of the Physical Society of Japan* **44**, 1839 (1978).

[5] M. Z. Hasan and C. L. Kane. « Colloquium: Topological insulators ». *Rev. Mod. Phys.* **82**, 3045 (2010).

[6] M. Franz and L. Molenkamp. *Topological insulators*. Elsevier, (2013).

[7] J. K. Asbóth, L. Oroszlány, and A. Pályi. *A Short Course on Topological Insulators*. Springer International Publishing, (2016). DOI: 10.1007/978-3-319-25607-8.

[8] F. D. M. Haldane and S. Raghu. « Possible Realization of Directional Optical Waveguides in Photonic Crystals with Broken Time-Reversal Symmetry ». *Phys. Rev. Lett.* **100**, 013904 (2008).

[9] J. D. Joannopoulos, S. G. Johnson, J. N. Winn, and R. D. Meade. *Photonic Crystals: Molding the Flow of Light*. Princeton University Press, (2008).

[10] N. R. Cooper, J. Dalibard, and I. B. Spielman. « Topological bands for ultracold atoms ». *Rev. Mod. Phys.* **91**, 015005 (2019).

[11] W. S. Gan. « Topology in Acoustics and Topological Sound Waves ». In: *Time Reversal Acoustics*. Singapore: Springer Singapore, (2021), 77. DOI: 10.1007/978-981-16-3235-8_11.

[12] L. Xin, Y. Siyuan, L. Harry, L. Minghui, and C. Yanfeng. « Topological mechanical metamaterials: A brief review ». *Current Opinion in Solid State and Materials Science* **24**, 100853 (2020).

[13] Y. Wu, J. Lu, X. Huang, Y. Yang, L. Luo, L. Yang, F. Li, W. Deng, and Z. Liu. « Topological materials for full-vector elastic waves ». *National Science Review* (2022).

[14] Z. Wang, Y. Chong, J. D. Joannopoulos, and M. Soljačić. « Observation of unidirectional backscattering-immune topological electromagnetic states ». *Nature* **461**, 772 (2009).

[15] M. C. Rechtsman, J. M. Zeuner, A. Tünnermann, S. Nolte, M. Segev, and A. Szameit. « Strain-induced pseudomagnetic field and photonic Landau levels in dielectric structures ». *Nature Photon.* **7**, 153 (2013).

[16] M. Hafezi, S. Mittal, J. Fan, A. Migdall, and J. M. Taylor. « Imaging topological edge states in silicon photonics ». *Nature Photonics* **7**, 1001 (2013).

[17] T. Ozawa, H. M. Price, A. Amo, N. Goldman, M. Hafezi, L. Lu, M. C. Rechtsman, D. Schuster, J. Simon, O. Zilberberg, and I. Carusotto. « Topological photonics ». *Rev. Mod. Phys.* **91**, 015006 (2019).

[18] P. St-Jean, V. Goblot, E. Galopin, A. Lemaître, T. Ozawa, L. Legratiet, I. Sagnes, J. Bloch, and A. Amo. « Lasing in topological edge states of a one-dimensional lattice ». *Nature Photonics* **11**, (2017).

[19] M. A. Bandres, S. Wittek, G. Harari, M. Parto, J. Ren, M. Segev, D. N. Christodoulides, and M. Khajavikhan. « Topological insulator laser: Experiments ». *Science* **359**, eaar4005 (2018).

[20] G. Harari, M. A. Bandres, Y. Lumer, M. C. Rechtsman, Y. D. Chong, M. Khajavikhan, D. N. Christodoulides, and M. Segev. « Topological insulator laser: Theory ». *Science* **359**, eaar4003 (2018).

[21] D. Leykam and Y. D. Chong. « Edge solitons in nonlinear photonic topological insulators ». *Phys. Rev. Lett.* **117**, 143901 (2016).

[22] S. Mukherjee and M. C. Rechtsman. « Observation of Floquet solitons in a topological bandgap ». *Science* **368**, 856 (2020).

[23] L. J. Maczewsky, M. Heinrich, M. Kremer, S. K. Ivanov, M. Ehrhardt, F. Martinez, Y. V. Kartashov, V. V. Konotop, L. Torner, D. Bauer, and A. Szameit. « Nonlinearity-induced photonic topological insulator ». *Science* **370**, 701 (2020).

[24] S. Kruk, A. Poddubny, D. Smirnova, L. Wang, A. Slobozhanyuk, A. Shorokhov, I. Kravchenko, B. Luther-Davies, and Y. Kivshar. « Nonlinear light generation in topological nanostructures ». *Nature Nanotechnology* **14**, (2019).

[25] S. Mittal, E. Goldschmidt, and M. Hafezi. « A topological source of quantum light ». *Nature* **561**, (2018).

[26] S. Yves, R. Fleury, T. Berthelot, M. Fink, F. Lemoult, and G. Lerosey. « Crystalline metamaterials for topological properties at subwavelength scales ». *Nature Communications* **8**, (2017).

[27] I. Sinev, I. Mukhin, A. Slobozhanyuk, A. Poddubny, A. Miroshnichenko, A. Samusev, and Y. Kivshar. « Mapping plasmonic topological states at the nanoscale ». *Nanoscale* (2015).

[28] S. Suwunnarat, Y. Tang, M. Reisner, F. Mortessagne, U. Kuhl, and T. Kottos. « Non-linear coherent perfect absorption in the proximity of exceptional points ». *Communications Physics* **5**, (2022).

[29] M. Reisner, M. Bellec, U. Kuhl, and F. Mortessagne. « Microwave resonator lattices for topological photonics [Invited] ». *Opt. Mater. Express* **11**, 629 (2021).

[30] U. Kuhl, S. Barkhofen, T. Tudorovskiy, H.-J. Stöckmann, T. Hossain, L. de Forges de Parny, and F. Mortessagne. « Dirac point and edge states in a microwave realization of tight-binding graphene-like structures ». *Phys. Rev. B* **82**, 094308 (2010).

[31] M. Bellec, U. Kuhl, G. Montambaux, and F. Mortessagne. « Tight-binding couplings in microwave artificial graphene ». *Phys. Rev. B* **88**, 115437 (2013).

[32] J. A. Franco-Villafañe, E. Sadurni, S. Barkhofen, U. Kuhl, F. Mortessagne, and T. H. Seligman. « First Experimental Realization of the Dirac Oscillator ». *Phys. Rev. Lett.* **111**, 170405 (2013).

[33] T. Stegmann, J. A. Franco-Villafañe, Y. P. Ortiz, U. Kuhl, F. Mortessagne, and T. H. Seligman. « Microwave emulations and tight-binding calculations of transport in polyacetylene ». *Phys. Lett. A* **381**, 24 (2016).

[34] T. Stegmann, J. A. Franco-Villafañe, U. Kuhl, F. Mortessagne, and T. H. Seligman. « Transport gap engineering by contact geometry in graphene nanoribbons: Experimental and theoretical studies on artificial materials ». *Phys. Rev. B* **95**, 035413 (2017).

[35] J. Böhm, M. Bellec, F. Mortessagne, U. Kuhl, S. Barkhofen, S. Gehler, H.-J. Stöckmann, I. Foulger, S. Gnutzmann, and G. Tanner. « Microwave Experiments Simulating Quantum Search and Directed Transport in Artificial Graphene ». *Phys. Rev. Lett.* **114**, 110501 (2015).

[36] P. Vignolo, M. Bellec, J. Böhm, A. Camara, J.-M. Gambaudo, U. Kuhl, and F. Mortessagne. « Energy landscape in a Penrose tiling ». *Phys. Rev. B* **93**, 075141 (2016).

[37] C. Poli, M. Bellec, U. Kuhl, F. Mortessagne, and H. Schomerus. « Selective enhancement of topologically induced interface states in a dielectric resonator chain ». *Nature Comm.* **6**, 6710 (2015).

[38] C. Poli, M. Bellec, U. Kuhl, F. Mortessagne, and H. Schomerus. « Partial chiral symmetry-breaking as a route to spectrally isolated topological defect states in twodimensional artificial materials ». *2D Mater.* **4**, 025008 (2017).

[39] M. Reisner, F. Mortessagne, E. Makri, T. Kottos, and U. Kuhl. « Microwave limiters implemented by coupled dielectric resonators based on a topological defect mode and CT-symmetry breaking ». *Acta Physica Polonica A* **136**, 790 (2019).

[40] D. H. Jeon, M. Reisner, F. Mortessagne, T. Kottos, and U. Kuhl. « Non-Hermitian $\mathscr{C}\mathscr{T}$-Symmetric Spectral Protection of Nonlinear Defect Modes ». *Phys. Rev. Lett.* **125**, 113901 (2020).

[41] M. Bellec, U. Kuhl, G. Montambaux, and F. Mortessagne. « Topological Transition of Dirac Points in a Microwave Experiment ». *Phys. Rev. Lett.* **110**, 033902 (2013).

[42] M. Bellec, U. Kuhl, G. Montambaux, and F. Mortessagne. « Manipulation of edge states in microwave artificial graphene ». *New Journal of Physics* **16**, (2014).

[43] M. Bellec, C. Poli, U. Kuhl, F. Mortessagne, and H. Schomerus. « Observation of supersymmetric pseudo-Landau levels in strained microwave graphene ». *Light Sci. Appl.* **9**, 146 (2020).

[44] C. Dutreix, M. Bellec, P. Delplace, and F. Mortessagne. « Wavefront dislocations reveal the topology of quasi-1D photonic insulators ». *Nature Communications* **12**, 3571 (2021).

[45] G. J. Aubry, L. S. Froufe-Pérez, U. Kuhl, O. Legrand, F. Scheffold, and F. Mortessagne. « Experimental Tuning of Transport Regimes in Hyperuniform Disordered Photonic Materials ». *Phys. Rev. Lett.* **125**, 127402 (2020).

[46] D. Laurent, O. Legrand, P. Sebbah, C. Vanneste, and F. Mortessagne. « Localized Modes in a Finite-Size Open Disordered Microwave Cavity ». *Phys. Rev. Lett.* **99**, 253902 (2007).

[47] S. Rotter and S. Gigan. « Light fields in complex media: Mesoscopic scattering meets wave control ». *Rev. Mod. Phys.* **89**, 015005 (2017).

[48] Y. Kobayashi and S. Tanaka. « Resonant Modes of a Dielectric Rod Resonator Short-Circuited at Both Ends by Parallel Conducting Plates ». *IEEE Transactions on Microwave Theory and Techniques* **28**, 1077 (1980).

[49] C. C. Johnson. *Field and Wave Electrodynamics*. McGraw-Hill, (1965), 173.

[50] W. Courtney. « Analysis and Evaluation of a Method of Measuring the Complex Permittivity and Permeability Microwave Insulators ». *IEEE Transactions on Microwave Theory and Techniques* **18**, 476 (1970).

[51] J. Sheen. « Microwave Measurements of Dielectric Properties Using a Closed Cylindrical Cavity Dielectric Resonator ». *IEEE Transactions on Dielectrics and Electrical Insulation* **14**, 1139 (2007).

[52] A. F. Oskooi, D. Roundy, M. Ibanescu, P. Bermel, J. Joannopoulos, and S. G. Johnson. « Meep: A flexible free-software package for electromagnetic simulations by the FDTD method ». *Computer Physics Communications* **181**, 687 (2010).

[53] V. A. Mandelshtam and H. S. Taylor. « Harmonic inversion of time signals and its applications ». *The Journal of Chemical Physics* **107**, 6756 (1997).

[54] S. G. Johnson. *Harmonic Inversion of Time Signals by the Filter Diagonalization Method (FDM)*. URL: `https://github.com/NanoComp/harminv`.

[55] J. Barthélemy, O. Legrand, and F. Mortessagne. « Complete S matrix in a microwave cavity at room temperature ». *Phys. Rev. E* **71**, 016205 (2005).

[56] U. Kuhl, O. Legrand, and F. Mortessagne. « Microwave experiments using open chaotic cavities in the realm of the effective Hamiltonian formalism ». *Fortschritte der Physik* **61**, 404 (2013).

[57] J. Stein, H.-J. Stöckmann, and U. Stoffregen. « Microwave Studies of Billiard Green Functions and Propagators ». *Phys. Rev. Lett.* **75**, 53 (1995).

[58] J. Main. « Use of harmonic inversion techniques in semiclassical quantization and analysis of quantum spectra ». *Physics Reports* **316**, 233 (1999).

[59] U. Kuhl, R. Höhmann, J. Main, and H.-J. Stöckmann. « Resonance Widths in Open Microwave Cavities Studied by Harmonic Inversion ». *Phys. Rev. Lett.* **100**, 254101 (2008).

[60] G. J. Aubry, L. S. Froufe-Pérez, U. Kuhl, O. Legrand, F. Scheffold, and F. Mortessagne. « Experimental Tuning of Transport Regimes in Hyperuniform Disordered Photonic Materials ». *Phys. Rev. Lett.* **125**, 127402 (2020).

[61] N. Ashcroft and N. Mermin. *Solid State Physics*. Saunders College Publishing, (1976).

[62] E. Lidorikis, M. M. Sigalas, E. N. Economou, and C. M. Soukoulis. « Tight-Binding Parametrization for Photonic Band Gap Materials ». *Phys. Rev. Lett.* **81**, 1405 (1998).

[63] S. Barkhofen, M. Bellec, U. Kuhl, and F. Mortessagne. « Disordered graphene and boron nitride in a microwave tight-binding analog ». *Phys. Rev. B* **87**, 035101 (2013).

[64] I. Rotter. « A non-Hermitian Hamilton operator and the physics of open quantum systems ». *Journal of Physics A: Mathematical and Theoretical* **42**, 153001 (2009).

[65] U. Kuhl, O. Legrand, and F. Mortessagne. « Microwave experiments using open chaotic cavities in the realm of the effective Hamiltonian formalism ». *Fortschritte der Physik* **61**, 404 (2013).

[66] J. Barthélemy, O. Legrand, and F. Mortessagne. « Complete S-matrix in a microwave cavity at room temperature ». *Phys. Rev. E* **71**, 016205 (2005).

[67] T. Tudorovskiy, R. Höhmann, U. Kuhl, and H. Stöckmann. « On the theory of cavities with point-like perturbations: part I. General theory ». *Journal of Physics A* **41**, 275101 (2008).

[68] S. Noschese, L. Pasquini, and L. Reichel. « Tridiagonal Toeplitz matrices: properties and novel applications ». *Numerical Linear Algebra with Applications* **20**, 302 (2013).

[69] R. Penrose. « The role of aesthetics in pure and applied mathematical research ». *Bull.Inst.Math.Appl.* **10**, 266 (1974).

[70] D. Shechtman, I. Blech, D. Gratias, and J. W. Cahn. « Metallic Phase with Long-Range Orientational Order and No Translational Symmetry ». *Phys. Rev. Lett.* **53**, 1951 (1984).

[71] P. J. Steinhardt and S. Ostlund. *The Physics of Quasicrystals*. WORLD SCIENTIFIC, (1987). DOI: 10.1142/0391.

[72] P. W. Anderson. « Absence of Diffusion in Certain Random Lattices ». *Phys. Rev.* **109**, 1492 (1958).

[73] F. Wegner. « Inverse participation ratio in 2+ϵ dimensions ». *Zeitschrift für Physik B Condensed Matter* **36**, 209 (1980).

[74] M. Schreiber and H. Grussbach. « Multifractal wave functions at the Anderson transition ». *Phys. Rev. Lett.* **67**, 607 (1991).

[75] U. Fastenrath, M. Janßen, and W. Pook. « Multifractal analysis of disorder induced metal-insulator transitions ». *Physica A: Statistical Mechanics and its Applications* **191**, 401 (1992).

[76] M. Schreiber. « Multifractal Characteristics of Electronic Wave Functions in Disordered Systems ». In: *Computational Physics*. Ed. by K. H. Hoffmann and M. Schreiber. Springer, Berlin, Heidelberg, (1996). DOI: 10.1007/978-3-642-85238-1_9.

[77] T. Brandes, B. Huckestein, and L. Schweitzer. « Critical dynamics and multifractal exponents at the Anderson transition in 3d disordered systems ». *Annalen der Physik* **508**, 633 (1996).

[78] B. Huckestein and R. Klesse. « Spatial and spectral multifractality of the local density of states at the mobility edge ». *Phys. Rev. B* **55**, R7303 (1997).

[79] F. Evers and A. D. Mirlin. « Anderson transitions ». *Rev. Mod. Phys.* **80**, 1355 (2008).

[80] M. Morgenstern, J. Klijn, C. Meyer, and R. Wiesendanger. « Real-Space Observation of Drift States in a Two-Dimensional Electron System at High Magnetic Fields ». *Phys. Rev. Lett.* **90**, 056804 (2003).

[81] K. Hashimoto, C. Sohrmann, J. Wiebe, T. Inaoka, F. Meier, Y. Hirayama, R. A. Römer, R. Wiesendanger, and M. Morgenstern. « Quantum Hall Transition in Real Space: From Localized to Extended States ». *Phys. Rev. Lett.* **101**, 256802 (2008).

[82] S. Faez, A. Strybulevych, J. H. Page, A. Lagendijk, and B. A. van Tiggelen. « Observation of Multifractality in Anderson Localization of Ultrasound ». *Phys. Rev. Lett.* **103**, 155703 (2009).

[83] B. Jäck, F. Zinser, E. J. König, S. N. P. Wissing, A. B. Schmidt, M. Donath, K. Kern, and C. R. Ast. « Visualizing the multifractal wave functions of a disordered two-dimensional electron gas ». *Phys. Rev. Research* **3**, 013022 (2021).

[84] D. Harte. *Multifractals: Theory and Applications*. Chapman and Hall/CRC, (2001). DOI: 10.1201/9781420036008.

[85] M. Kohmoto, L. P. Kadanoff, and C. Tang. « Localization Problem in One Dimension: Mapping and Escape ». *Phys. Rev. Lett.* **50**, 1870 (1983).

[86] T. Fujiwara, M. Arai, T. Tokihiro, and M. Kohmoto. « Localized states and self-similar states of electrons on a two-dimensional Penrose lattice ». *Phys. Rev. B* **37**, 2797 (1988).

[87] T. Fujiwara, M. Kohmoto, and T. Tokihiro. « Multifractal wave functions on a Fibonacci lattice ». *Phys. Rev. B* **40**, 7413 (1989).

[88] A. Chhabra and R. V. Jensen. « Direct determination of the f(α) singularity spectrum ». *Phys. Rev. Lett.* **62**, 1327 (1989).

[89] H. Tsunetsugu, T. Fujiwara, K. Ueda, and T. Tokihiro. « Electronic properties of the Penrose lattice. I. Energy spectrum and wave functions ». *Phys. Rev. B* **43**, 8879 (1991).

[90] M. Kohmoto and B. Sutherland. « Electronic States on a Penrose Lattice ». *Phys. Rev. Lett.* **56**, 2740 (1986).

[91] P. Repetowicz, U. Grimm, and M. Schreiber. « Exact eigenstates of tight-binding Hamiltonians on the Penrose tiling ». *Phys. Rev. B* **58**, 13482 (1998).

[92] N. Macé, A. Jagannathan, and F. Piéchon. « Fractal dimensions of wave functions and local spectral measures on the Fibonacci chain ». *Phys. Rev. B* **93**, 205153 (2016).

[93] N. Macé, A. Jagannathan, P. Kalugin, R. Mosseri, and F. Piéchon. « Critical eigenstates and their properties in one- and two-dimensional quasicrystals ». *Phys. Rev. B* **96**, 045138 (2017).

[94] B. Sutherland. « Self-similar ground-state wave function for electrons on a two-dimensional Penrose lattice ». *Phys. Rev. B* **34**, 3904 (1986).

[95] Q. Niu and F. Nori. « Renormalization-Group Study of One-Dimensional Quasiperiodic Systems ». *Phys. Rev. Lett.* **57**, 2057 (1986).

[96] M. Kohmoto, B. Sutherland, and C. Tang. « Critical wave functions and a Cantor-set spectrum of a one-dimensional quasicrystal model ». *Phys. Rev. B* **35**, 1020 (1987).

[97] B. Sutherland. « Critical electronic wave functions on quasiperiodic lattices: Exact calculation of fractal measures ». *Phys. Rev. B* **35**, 9529 (1987).

[98] T. Tokihiro, T. Fujiwara, and M. Arai. « Exact eigenstates on a two-dimensional Penrose lattice and their fractal dimensions ». *Phys. Rev. B* **38**, 5981 (1988).

[99] Q. Niu and F. Nori. « Spectral splitting and wave-function scaling in quasicrystalline and hierarchical structures ». *Phys. Rev. B* **42**, 10329 (1990).

[100] M. Holzer. « Multifractal wave functions on a class of one-dimensional quasicrystals: Exact f(α) curves and the limit of dilute quasiperiodic impurities ». *Phys. Rev. B* **44**, 2085 (1991).

[101] F. Piéchon. « Anomalous Diffusion Properties of Wave Packets on Quasiperiodic Chains ». *Phys. Rev. Lett.* **76**, 4372 (1996).

[102] A. Jagannathan. « The Fibonacci quasicrystal: Case study of hidden dimensions and multifractality ». *Rev. Mod. Phys.* **93**, 045001 (2021).

[103] D. Tanese, E. Gurevich, F. Baboux, T. Jacqmin, A. Lemaître, E. Galopin, I. Sagnes, A. Amo, J. Bloch, and E. Akkermans. « Fractal Energy Spectrum of a Polariton Gas in a Fibonacci Quasiperiodic Potential ». *Phys. Rev. Lett.* **112**, 146404 (2014).

[104] R. Mosseri. « Contribution to the Theory of Quasicrystal Approximants ». In: *Universalities in Condensed Matter*. Ed. by R. Jullien, L. Peliti, R. Rammal, and N. Boccara. Berlin, Heidelberg: Springer Berlin Heidelberg, (1988). DOI: 10.1007/978-3-642-51005-2_3.

[105] Sire, Clément and Mosseri, Rémy. « Excitation spectrum, extended states, gap closing: some exact results for codimension one quasicrystals ». *J. Phys. France* **51**, 1569 (1990).

[106] P. Kalugin, A. Kitaev, and L. Levitov. « Electron spectrum of a one-dimensional quasicrystal ». *Sov. Phys. JETP* **64**, 410 (1986). URL: http://www.jetp.ras.ru/cgi-bin/dn/e_064_02_0410.pdf.

[107] A. Rehemanjiang, M. Richter, U. Kuhl, and H.-J. Stöckmann. « Microwave Realization of the Chiral Orthogonal, Unitary, and Symplectic Ensembles ». *Phys. Rev. Lett.* **124**, 116801 (2020).

[108] S. Thiem and M. Schreiber. « Wavefunctions, quantum diffusion, and scaling exponents in golden-mean quasiperiodic tilings ». *Journal of Physics: Condensed Matter* **25**, 075503 (2013).

[109] S. Thiem and M. Schreiber. « Renormalization group approach for the wave packet dynamics in golden-mean and silver-mean labyrinth tilings ». *Phys. Rev. B* **85**, 224205 (2012).

[110] W. Su, J. Schrieffer, and A. Heeger. « Solitons in polyacetylene ». *Phys. Rev. Lett.* **42**, 1698 (1979).

[111] R. Jackiw and C. Rebbi. « Solitons with fermion number ½ ». *Phys. Rev. D* **13**, 3398 (1976).

[112] Y. Hatsugai. « Chern number and edge states in the integer quantum Hall effect ». *Phys. Rev. Lett.* **71**, 3697 (1993).

[113] Y. Hatsugai. « Edge states in the integer quantum Hall effect and the Riemann surface of the Bloch function ». *Phys. Rev. B* **48**, 11851 (1993).

[114] X.-L. Qi, Y.-S. Wu, and S.-C. Zhang. « General theorem relating the bulk topological number to edge states in two-dimensional insulators ». *Phys. Rev. B* **74**, 045125 (2006).

[115] N. Malkova, I. Hromada, X. Wang, G. Bryant, and Z. Chen. « Observation of optical Shockley-like surface states in photonic superlattices ». *Opt. Lett.* **34**, 1633 (2009).

[116] C. W. Ling, M. Xiao, C. T. Chan, S. F. Yu, and K. H. Fung. « Topological edge plasmon modes between diatomic chains of plasmonic nanoparticles ». *Opt. Express* **23**, 2021 (2015).

[117] C. Liu, M. G. Dutt, and D. Pekker. « Robust manipulation of light using topologically protected plasmonic modes ». *Opt. Express* **26**, 2857 (2018).

[118] S. R. Pocock, X. Xiao, P. A. Huidobro, and V. Giannini. « Topological Plasmonic Chain with Retardation and Radiative Effects ». *ACS Photonics* **5**, 2271 (2018).

[119] F. Bleckmann, Z. Cherpakova, S. Linden, and A. Alberti. « Spectral imaging of topological edge states in plasmonic waveguide arrays ». *Phys. Rev. B* **96**, 045417 (2017).

[120] S. Weimann, M. Kremer, Y. Plotnik, Y. Lumer, S. Nolte, K. Makris, M. Segev, M. C. Rechtsman, and A. Szameit. « Topologically protected bound states in photonic parity–time-symmetric crystals ». *Nature Materials* **16**, (2016).

[121] E. Saei Ghareh Naz, I. C. Fulga, L. Ma, O. G. Schmidt, and J. van den Brink. « Topological phase transition in a stretchable photonic crystal ». *Phys. Rev. A* **98**, 033830 (2018).

[122] J. M. Zeuner, M. C. Rechtsman, Y. Plotnik, Y. Lumer, S. Nolte, M. S. Rudner, M. Segev, and A. Szameit. « Observation of a Topological Transition in the Bulk of a Non-Hermitian System ». *Phys. Rev. Lett.* **115**, 040402 (2015).

[123] N. Pernet, P. St-Jean, D. Solnyshkov, G. Malpuech, N. Carlon Zambon, Q. Fontaine, B. Real, O. Jamadi, A. Lemaitre, M. Morassi, L. Le Gratiet, T. Baptiste, A. Harouti, I. Sagnes, A. Amo, S. Ravets, and J. Bloch. « Gap solitons in a one-dimensional driven-dissipative topological lattice ». *Nature Physics* **18**, 678 (2022).

[124] H. Zhao, P. Miao, M. Teimourpour, S. Malzard, R. Elganainy, H. Schomerus, and L. Feng. « Topological Hybrid Silicon Microlasers ». *Nature Communications* **9**, (2018).

[125] A. Poddubny, A. Miroshnichenko, A. Slobozhanyuk, and Y. Kivshar. « Topological Majorana States in Zigzag Chains of Plasmonic Nanoparticles ». *ACS Photonics* **1**, 101 (2014).

[126] A. Slobozhanyuk, A. Poddubny, I. Sinev, A. Samusev, Y. F. Yu, A. Kuznetsov, A. Miroshnichenko, and Y. Kivshar. « Enhanced photonic spin Hall effect with subwavelength topological edge states ». *Laser & Photon. Rev.* **10**, 656 (2016).

[127] C. E. Whittaker, E. Cancellieri, P. M. Walker, B. Royall, L. E. Tapia Rodriguez, E. Clarke, D. M. Whittaker, H. Schomerus, M. S. Skolnick, and D. N. Krizhanovskii. « Effect of photonic spin-orbit coupling on the topological edge modes of a Su-Schrieffer-Heeger chain ». *Phys. Rev. B* **99**, 081402 (2019).

[128] T. Harder, M. Sun, O. Egorov, I. Vakulchyk, J. Beierlein, P. Gagel, M. Emmerling, C. Schneider, U. Peschel, I. Savenko, S. Klembt, and S. Höfling. « Coherent Topological Polariton Laser ». *ACS Photonics* **8**, (2021).

[129] M. Pieczarka, E. Estrecho, S. Ghosh, M. Wurdack, M. Steger, D. W. Snoke, K. West, L. N. Pfeiffer, T. C. H. Liew, A. G. Truscott, and E. A. Ostrovskaya. « Topological phase transition in an all-optical exciton-polariton lattice ». *Optica* **8**, 1084 (2021).

[130] R. Su, S. Ghosh, T. C. H. Liew, and Q. Xiong. « Optical switching of topological phase in a perovskite polariton lattice ». *Science Advances* **7**, eabf8049 (2021).

[131] A. Tripathi, S. Kruk, Y. Shang, J. Zhou, I. Kravchenko, D. Jin, and Y. Kivshar. « Topological nanophotonics for photoluminescence control ». *Nanophotonics* **10**, 435 (2021).

[132] A. P. Slobozhanyuk, A. N. Poddubny, A. E. Miroshnichenko, P. A. Belov, and Y. S. Kivshar. « Subwavelength Topological Edge States in Optically Resonant Dielectric Structures ». *Phys. Rev. Lett.* **114**, 123901 (2015).

[133] S. Kruk, A. Slobozhanyuk, D. Denkova, A. Poddubny, I. Kravchenko, A. Miroshnichenko, D. Neshev, and Y. Kivshar. « Edge States and Topological Phase Transitions in Chains of Dielectric Nanoparticles ». *Small* **13**, 1603190 (2017).

[134] L. Lin, S. Kruk, Y. Ke, C. Lee, and Y. Kivshar. « Topological states in disordered arrays of dielectric nanoparticles ». *Phys. Rev. Res.* **2**, 043233 (2020).

[135] L. Wang, R.-Y. Zhang, B. Hou, Y. Huang, S. Li, and W. Wen. « Subwavelength topological edge states based on localized spoof surface plasmonic metaparticle arrays ». *Opt. Express* **27**, 14407 (2019).

[136] Y. Moritake, M. Ono, and M. Notomi. *Nanophotonics* **11**, 2183 (2022).

[137] G. Kurganov, D. Dobrykh, E. Puhtina, I. Yusupov, A. Slobozhanyuk, Y. S. Kivshar, and D. Zhirihin. « Temperature control of electromagnetic topological edge states ». *Applied Physics Letters* **120**, 233105 (2022).

[138] M.-X. Zhang, Z. Zhou, L. Yan, L. Zhang, and J.-Y. Yan. « Polarization-induced topological phase transition in zigzag chains composed of metal nanoparticles ». *Journal of Applied Physics* **129**, 243103 (2021).

[139] B. Kramer and A. MacKinnon. « Localization: theory and experiment ». *Reports on Progress in Physics* **56**, 1469 (1993).

[140] C.-K. Chiu, J. C. Y. Teo, A. P. Schnyder, and S. Ryu. « Classification of topological quantum matter with symmetries ». *Rev. Mod. Phys.* **88**, 035005 (2016).

[141] J. Zak. « Berry's phase for energy bands in solids ». *Phys. Rev. Lett.* **62**, 2747 (1989).

[142] M. Maffei, A. Dauphin, F. Cardano, M. Lewenstein, and P. Massignan. « Topological characterization of chiral models through their long time dynamics ». *New Journal of Physics* **20**, 013023 (2018).

[143] S. Ryu and Y. Hatsugai. « Topological Origin of Zero-Energy Edge States in Particle-Hole Symmetric Systems ». *Phys. Rev. Lett.* **89**, 077002 (2002).

[144] S. Ryu, A. P. Schnyder, A. Furusaki, and A. W. W. Ludwig. « Topological insulators and superconductors: tenfold way and dimensional hierarchy ». *New Journal of Physics* **12**, 065010 (2010).

[145] J. Vidal and R. Mosseri. « Generalized Rauzy tilings: construction and electronic properties ». *Materials Science and Engineering: A* **294-296**, 572 (2000).

[146] A. Moustaj, S. Kempkes, and C. M. Smith. « Effects of disorder in the Fibonacci quasicrystal ». *Phys. Rev. B* **104**, 144201 (2021).

[147] J. Li, R.-L. Chu, J. K. Jain, and S.-Q. Shen. « Topological Anderson Insulator ». *Phys. Rev. Lett.* **102**, 136806 (2009).

[148] P. Titum, N. H. Lindner, M. C. Rechtsman, and G. Refael. « Disorder-induced Floquet topological insulators ». *Phys. Rev. Lett.* **114**, 056801 (2015).

[149] S. Stützer, Y. Plotnik, Y. Lumer, P. Titum, N. H. Lindner, M. Segev, M. C. Rechtsman, and A. Szameit. « Photonic topological Anderson insulators ». *Nature* **560**, 461 (2018).

[150] W. Zhang, D. Zou, Q. Pei, W. He, J. Bao, H. Sun, and X. Zhang. « Experimental Observation of Higher-Order Topological Anderson Insulators ». *Phys. Rev. Lett.* **126**, 146802 (2021).

[151] S. E. Skipetrov and P. Wulles. « Topological transitions and Anderson localization of light in disordered atomic arrays ». *Phys. Rev. A* **105**, 043514 (2022).

[152] M. Reisner, D. H. Jeon, C. Schindler, H. Schomerus, F. Mortessagne, U. Kuhl, and T. Kottos. « Self-Shielded Topological Receiver Protectors ». *Phys. Rev. Applied* **13**, 034067 (2020).

[153] D. Baranov, A. Krasnok, T. Shegai, A. Alu, and Y. Chong. « Coherent perfect absorbers: Linear control of light with light ». *Nature Reviews Materials* **2**, 17064 (2017).

[154] L. Chen, T. Kottos, and S. M. Anlage. « Perfect absorption in complex scattering systems with or without hidden symmetries ». *Nature Communications* **11**, (2020).

[155] H. Li, S. Suwunnarat, R. Fleischmann, H. Schanz, and T. Kottos. « Random Matrix Theory Approach to Chaotic Coherent Perfect Absorbers ». *Phys. Rev. Lett.* **118**, 044101 (2017).

[156] W. R. Sweeney, C. W. Hsu, S. Rotter, and A. D. Stone. « Perfectly Absorbing Exceptional Points and Chiral Absorbers ». *Phys. Rev. Lett.* **122**, 093901 (2019).

[157] C. Wang, W. R. Sweeney, A. D. Stone, and L. Yang. « Coherent perfect absorption at an exceptional point ». *Science* **373**, 1261 (2021).

[158] C. Ferise, P. del Hougne, S. Félix, V. Pagneux, and M. Davy. « Exceptional Points of PT-Symmetric Reflectionless States in Complex Scattering Systems ». *Phys. Rev. Lett.* **128**, 203904 (2022).

[159] X. Jiang, S. Yin, H. Li, J. Quan, M. Cotrufo, J. Kullig, J. Wiersig, and A. Alù. *Coherent Perfect Absorption in Chaotic Optical Microresonators for Efficient Modal Control*. (2022). arXiv: 2211.08727.